

ISSN 1451 - 9372(Print)
ISSN 2217 - 7434(Online)
JULY-SEPTEMBER 2017
Vol.23, Number 3, 293-440

Chemical Industry & Chemical Engineering Quarterly



**The AChE Journal for Chemical Engineering,
Biochemical Engineering, Chemical Technology,
New Materials, Renewable Energy and Chemistry**

www.ache.org.rs/ciceq



Journal of the
Association of Chemical Engineers of
Serbia, Belgrade, Serbia

**Chemical Industry &
Chemical Engineering
CI&CE Quarterly**

EDITOR-In-Chief

Vlada B. Veljković

*Faculty of Technology, University of Niš, Leskovac, Serbia
E-mail: veljkovicvb@yahoo.com*

ASSOCIATE EDITORS

Jonjaua Ranogajec

*Faculty of Technology, University of
Novi Sad, Novi Sad, Serbia*

Srđan Pejanović

*Department of Chemical Engineering,
Faculty of Technology and Metallurgy,
University of Belgrade, Belgrade, Serbia*

Milan Jakšić

*ICEHT/FORTH, University of Patras,
Patras, Greece*

EDITORIAL BOARD (Serbia)

**Đorđe Janačković, Sanja Podunavac-Kuzmanović, Viktor Nedović, Sandra Konstantinović, Ivanka Popović
Siniša Dodić, Zoran Todorović, Olivera Stamenković, Marija Tasić, Jelena Avramović**

ADVISORY BOARD (International)

Dragomir Bukur

*Texas A&M University,
College Station, TX, USA*

Milorad Dudukovic

*Washington University,
St. Luis, MO, USA*

Jiri Hanika

*Institute of Chemical Process Fundamentals, Academy of Sciences
of the Czech Republic, Prague, Czech Republic*

Maria Jose Cocero

*University of Valladolid,
Valladolid, Spain*

Tajalli Keshavarz

*University of Westminster,
London, UK*

Zeljko Knez

*University of Maribor,
Maribor, Slovenia*

Igor Lacik

*Polymer Institute of the Slovak Academy of Sciences,
Bratislava, Slovakia*

Denis Poncelet

ENITIAA, Nantes, France

Ljubisa Radovic

*Pen State University,
PA, USA*

Peter Raspor

*University of Ljubljana,
Ljubljana, Slovenia*

Constantinos Vayenas

*University of Patras,
Patras, Greece*

Xenophon Verykios

*University of Patras,
Patras, Greece*

Ronnie Willaert

*Vrije Universiteit,
Brussel, Belgium*

Gordana Vunjak Novakovic

*Columbia University,
New York, USA*

Dimitrios P. Tassios

*National Technical University of Athens,
Athens, Greece*

Hui Liu

China University of Geosciences, Wuhan, China

FORMER EDITOR (2005-2007)

Professor Dejan Skala

University of Belgrade, Faculty of Technology and Metallurgy, Belgrade, Serbia



Journal of the
Association of Chemical Engineers of
Serbia, Belgrade, Serbia

**Chemical Industry &
Chemical Engineering
CI&CE Quarterly**

Vol. 23

Belgrade, July-September 2017

No. 3

Chemical Industry & Chemical Engineering
Quarterly (ISSN 1451-9372) is published
quarterly by the Association of Chemical
Engineers of Serbia, Kneza Miloša 9/I,
11000 Belgrade, Serbia

Editor:
Vlada B. Veljković
veljkovic@yahoo.com

Editorial Office:
Kneza Miloša 9/I, 11000 Belgrade, Serbia
Phone/Fax: +381 (0)11 3240 018
E-mail: shi@yubc.net
www.ache.org.rs

For publisher:
Tatijana Duduković

Secretary of the Editorial Office:
Slavica Desnica

Marketing and advertising:
AChE Marketing Office
Kneza Miloša 9/I, 11000 Belgrade, Serbia
Phone/Fax: +381 (0)11 3240 018

Publication of this Journal is supported by the
Ministry of Education, Science and
Technological Development of the Republic of
Serbia

Subscription and advertisements make payable
to the account of the Association of Chemical
Engineers of Serbia, Belgrade, No. 205-2172-
71, Komercijalna banka a.d., Beograd

Computer typeface and paging:
Vladimir Panić

Printed by:
Faculty of Technology and Metallurgy,
Research and Development Centre of Printing
Technology, Karnegijeva 4, P.O. Box 3503,
11120 Belgrade, Serbia

Abstracting/Indexing:
Articles published in this Journal are indexed in
Thompson Reuters products: *Science Citation
Index - Expanded™* - access via *Web of
Science®*, part of *ISI Web of Knowledge™*

CONTENTS

- Lina Lv, Jianbin Yang, Zhigang Shen, Yanbo Zhou, Jun Lu, **Optimizing the characteristics of calcium sulfate dihydrate in the flue gas desulfurization process: Investigation of the impurities in slurry - Cl⁻, Fe³⁺ and Mn²⁺**293
- Wenyuan Fan, Xiaohong Yin, **Bubble formation in shear-thinning fluids: Laser image measurement and a novel correlation for detached volume**301
- R.A.F. Oliveira, G.H. Justi, G.C. Lopes, **Grid convergence study of a cyclone separator using different mesh structures**311
- Shaobai Li, Jungeng Fan, Shuang Xu, Rundong Li, Jingde Luan, **The influence of pH on gas-liquid mass transfer in non-Newtonian fluids**321
- Bojana Ž. Bajić, Damjan G. Vučurović, Siniša N. Dodić, Zorana Z. Rončević, Jovana A. Grahovac, Jelena M. Dodić, **The biotechnological production of xanthan on vegetable oil industry wastewaters. Part I: Modelling and optimization**329
- Nilgün Ertaş, **A comparison of industrial and homemade bulgur in turkey in terms of physical, chemical and nutritional properties**341
- Jelena Filipović, Shahin Ahmetxhekaj, Vladimir Filipović, Milenko Košutić, **Spelt pasta with increased content of functional components**349
- A. Sudha, V. Sivakumar, V.Sangeetha, K.S. Priyenka Devi, **Improving enzymatic saccharification of Cassava stem using peroxide and microwave assisted pre-treatment techniques**357
- Didem Özçimen, M. Ömer Gülyurt, Benan İnan, **Optimization of biodiesel production from *Chlorella protothecoides* oil via ultrasound assisted transesterification**367
- Liangchao Li, Bin Xu, **CFD simulation of gas-liquid floating particles mixing in an agitated vessel**377
- Zixia Li, Yin Ran, Wenqi Zhang, Wei Sun, Tinghai Wang, **Industrial application of gasoline aromatization and desulfurization technology in Hohhot refinery**391
- Muhammad Imran Din, Kiran Ijaz, Khalida Naseem, **Bio-sorption potentials of acid modified *Saccharum bengalense* for removal of methyl violet from aqueous solutions**399
- Petar Stojanovic, Marija Savic, Dusan Trajkovic, Jovan Stepanovic, Miodrag Stamenkovic, Mirjana Kostic, **The effect of false-twist texturing parameters on the structure and crimp properties of polyester yarn**411

CONTENTS Continued

Meng Peng, Xiaojun Yang, Jiaxiong Wu, Hua Yuan, Chaofan Yin, Yuanxin Wu, Application of vanadium-incorporated phosphomolybdate supported on the modified kaolin in synthesis of diphenyl carbonate by oxidative carbonylation with phenol	421
Mohsen Beigi, Numerical simulation of potato slices drying using a two-dimensional finite element model	431

Activities of the Association of Chemical Engineers of Serbia are supported by:

- Ministry of Education, Science and Technological Development, Republic of Serbia
- Hemofarm Koncern AD, Vršac, Serbia
- Faculty of Technology and Metallurgy, University of Belgrade, Belgrade, Serbia
- Faculty of Technology, University of Novi Sad, Novi Sad, Serbia
- Faculty of Technology, University of Niš, Leskovac, Serbia
- Institute of Chemistry, Technology and Metallurgy, University of Belgrade, Belgrade, Serbia

LINA LV¹
JIANBIN YANG²
ZHIGANG SHEN²
YANBO ZHOU¹
JUN LU¹

OPTIMIZING THE CHARACTERISTICS OF CALCIUM SULFATE DIHYDRATE IN THE FLUE GAS DESULFURIZATION PROCESS: INVESTIGATION OF THE IMPURITIES IN SLURRY - Cl⁻, Fe³⁺ AND Mn²⁺

¹Key Laboratory of Coal Gasification and Energy Chemical Engineering of Ministry of Education, East China University of Science and Technology, Shanghai, People's Republic of China
²R&D Center, Shanghai Oriental Enviro-Industry Co., Ltd., Shanghai, People's Republic of China

SCIENTIFIC PAPER

UDC 66.094.522.091.8:502/504:54

Article Highlights

- Limestone with a high CaCO₃ content and a low content of MgCO₃, Al₂O₃ and Fe₂O₃ was expected
- Cl⁻ were found to distort crystal structure by increasing the induction period
- Fe³⁺ and Mn²⁺ can catalysis oxidation of SO₂ to increase desulphurization efficiency
- Fe³⁺ and Mn²⁺, especially Fe³⁺, can slow the crystal growth of all faces except {011} and {111}
- Cl⁻, Fe³⁺ and Mn²⁺ concentration should be controlled for optimizing the characteristics of DH

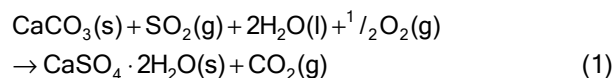
Abstract

The effects of limestone, Cl⁻, Fe³⁺ and Mn²⁺ in slurry on the characteristics of calcium sulfate dehydrate (DH) in flue gas desulfurization (FGD) process were investigated. The moisture content, particle size distribution, and crystal morphology were considered as end use characteristics of DH. As a result, the number of needle-like DH crystals was increased with increasing total contents of MgCO₃, Al₂O₃ and Fe₂O₃ in limestone. Cl⁻ ions were reported to distort the crystal structure and change the crystals from orthorhombic to irregular. Mn²⁺ can increase the desulfurization efficiency by catalyzing the oxidation of SO₂. Finally, Fe³⁺ will inhibit crystal growth of all faces, except {011} and {111}.

Keywords: calcium sulfate dehydrate, flue gas desulfurization, limestone, chloride ion, iron ion, manganese ion.

The limestone-gypsum wet flue gas desulfurization (FGD) process is the most widely used desulfurization technology in Chinese coal-power plants for removing acidic compounds (SO₂, HCl, and HF) from flue gases [1-3]. In FGD systems, acidic flue gases are captured by alkaline slurry at an absorber. An absorber is costly and time-consuming. Thus, bubbling reactors are often used in lab-scale experiments for FGD studies [4]. In the bubbling reactor, flue gases bubble through the slurry, and SO₂ is absorbed by the slurry. A

slurry holding tank is an integrated part of the bubbling reactor. In this tank, SO₂ are dissociated to HSO₃⁻ and then oxidized to SO₄²⁻ by the injected oxygen. Finally, the SO₄²⁻ combine with Ca²⁺ to produce calcium sulfate dehydrate (DH), which can be refined for commercial applications. The moisture content, particle size distribution (PSD), and crystal morphology were usually considered as end use characteristics of DH products [5-7]:



The characteristics of DH will be affected by impurity ions, such as, chlorine ion, Fe³⁺, Mn²⁺ and so on. The crystallization of DH in CaCl₂-H₂SO₄-H₂O system and CaCl₂-Na₂SO₄-H₂O system has been investigated in detail previously. The effects of Mg²⁺ and Al³⁺ on DH crystallization in a CaCl₂-Na₂SO₄-H₂O sys-

Correspondence: J. Lu, Key Laboratory of Coal Gasification and Energy Chemical Engineering of Ministry of Education, East China University of Science and Technology, No. 130, Meilong Road, Shanghai 200237, People's Republic of China.

Paper received: 12 June, 2016

Paper revised: 16 August, 2016

Paper accepted: 24 August, 2016

<https://doi.org/10.2298/CICEQ160612043L>

tem have been investigated by many authors [5,8,9]. In the presence of Mg^{2+} , the growth rate of DH crystal was reduced and the crystals were elongated, while the growth rate of DH crystal increased in the presence of Al^{3+} .

However, no detailed study focuses on the effects of impurities on crystallization of DH in a wet FGD system. The characteristic of DH is the key factor for the re-utilization of the FGD gypsum. In the FGD slurry, there are many kinds of impurities, such as Cl^- , Mg^{2+} , Fe^{3+} , Mn^{2+} , SiO_2 and so on. Mg^{2+} and SiO_2 mainly come from limestone, so the limestone style and components should be researched. Chlorine ion [10] is the highest content impurity in the FGD slurry, which come from fuel coal, limestone and supplemental water. Fe^{3+} [9,11] and Mn^{2+} [9,12] are the major metal impurities in the FGD slurry, which were reported to catalyze the oxidation of SO_2 .

Hence, this study investigated the influences of limestone, Cl^- , Fe^{3+} and Mn^{2+} , on desulfurization efficiency and DH product quality in a lab-scale FGD system. Great efforts were devoted to optimize the characteristics of DH and increase FGD gypsum utilization rate in engineering application. The DH with low moisture content, concentrated PSD, and plate-like morphology is desired.

EXPERIMENTAL

Chemicals and materials

N_2 (purity >99.9%), O_2 (purity >99.9%), and SO_2 (purity >99.99%), used in the study were purchased from Shanghai Shenkai Gases Technology Co., Ltd. (Shanghai, China). Analytical pure $CaCO_3$, $CaCl_2$, HCl , $Fe_2(SO_4)_3$ and $MnSO_4 \cdot H_2O$ were supplied by Sino-pharm Chemical Reagent Co., Ltd. (Shanghai, China). Limestone 1, Limestone 2 and Limestone 3 were supplied by R&D Center, Shanghai Oriental Enviro-Industry Co., Ltd. (China). All solutions were prepared from deionized water.

The gas composition was measured by using a Testo 350 gas analyzer, and the pH of the solution was monitored by using a BANTE 901b pH meter. The PSD analysis was measured by using a LS-POP (VI) laser particle size analyzer, the crystal morphology structure was observed by using a SEM Quanta 250 scanning electron microscope, and the components of limestone were determined by using a XRF-1800.

Experimental setup and procedure

The bubbling experiment is often used in the laboratory to simulate the limestone-gypsum wet FGD process [13–16]. Experiments were carried out in a

closed, 2 L volume, flat-bottom glass reactor with a thermostatic jacket (4), a gas inlet (6) and an axial two blade stirrer (5). A sketch of the experiment is shown in Figure 1.

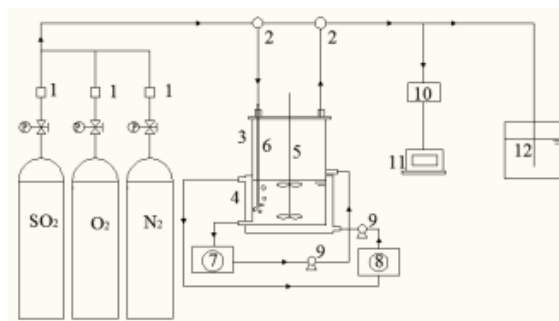


Figure 1. Sketch of bubbling experimental setup used to simulate wet FGD (arrows show gas and liquid flow directions); 1. rotameter, 2. valve, 3. bubble reactor, 4. thermostatic jacket, 5. digital mixer, 6. gas inlet, 7. slurry circulating tank, 8. thermostatic water bath, 9. peristaltic pump, 10. flue gas analyzer, 11. computer, 12. NaOH solution.

Artificial flue gas, which consists of 21% O_2 and 1500 mg/m^3 SO_2 , was bubbled into the reactor at a flow rate of 1.05 m_n^3/h . The flue gas composition was adjusted by rotameters (1) and measured by using a Testo 350 gas analyzer (10). Between the adjustment of the flue gas composition and the bubbling of flue gas into the reactor, a peristaltic pump (9) was used to circulate the slurry at a flow rate of 270 mL/min. The experiments were performed at 323 K. Fe^{3+} and Mn^{2+} were added in the form of sulfate salts, and Cl^- were added in the form of calcium salts.

At the beginning of each experiment, 20 g limestone was added into the reactor with 980 mL deionized water. During the bubbling experiment, the off-gas composition and pH value of the slurry were monitored and controlled consistently. The desulfurization efficiency was determined at $pH\ 5.5 \pm 0.1$. When the pH value of the slurry dropped to 4.6 ± 0.1 , the bubbling reaction was stopped. The slurry after the reaction should be maintained in oxidation for 24 h to ensure that the concentration of SO_3^{2-} was below the detection limit. Then, the slurry samples were taken for analyses of moisture content, PSD, and crystal morphology.

Analytical methods

The four types of limestone were ground to 325 meshes (44 μm). The dry limestone was analyzed by using a XRF-1800 to determine the components.

The quality of produced gypsums was analyzed in the experiments. Moisture content, PSD and crystal morphology were the three targeted characteristics of FGD gypsum. The moisture content was analyzed with

the help of a vacuum pump. A 100 mL slurry sample was compressed by suction filtration at 0.1 MPa for 10 min. Then, the moisture content was obtained by measuring the reduction of water at 313 K for 24 hours. The dried samples were stored in a dryer. The PSD was analyzed by using a laser particle size analyzer, and the crystal morphology was analyzed by using a scanning electron microscope. 1.0 mg dried samples were needed for PSD analysis and crystal morphology structure analysis, respectively.

RESULTS AND DISCUSSIONS

Selection of limestone types

In the limestone-gypsum wet FGD system, SO₂ removal efficiency and gypsum characteristics were directly related to limestone. The limestone's components change with the producing area. The major impurities of limestone were MgCO₃, SiO₂, Al₂O₃ and Fe₂O₃ [4,17-19]. The data in Figure 2 indicated that the CaCO₃ contents reached up to 90% and contained impurities of MgCO₃, SiO₂, Al₂O₃ and Fe₂O₃.

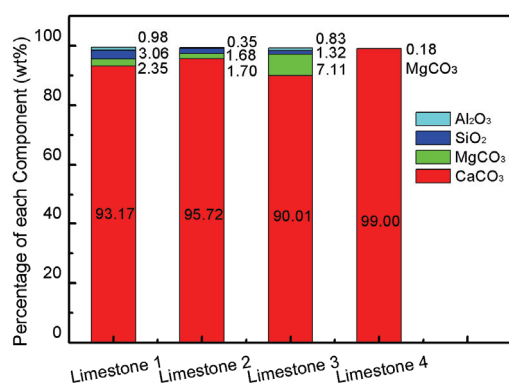


Figure 2. The percentage of each component in four types of limestone.

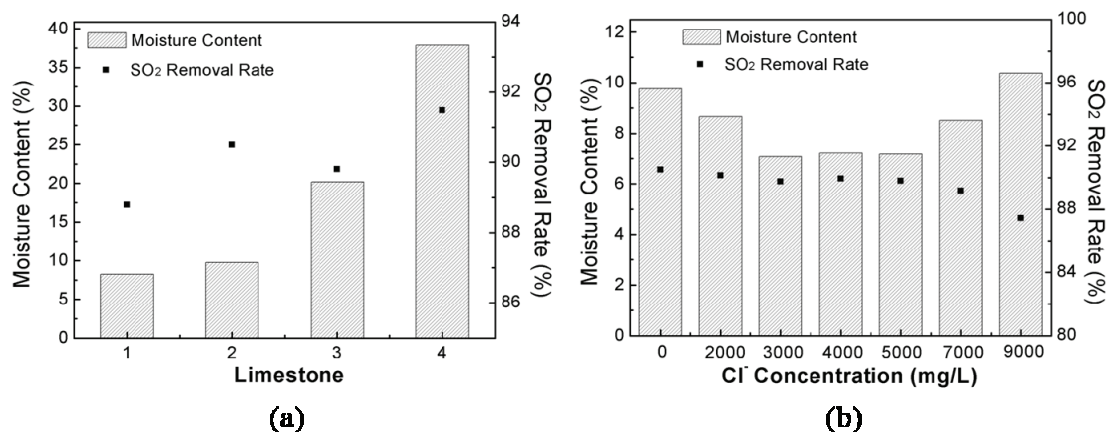


Figure 3. Desulfurization efficiency and moisture content of produced gypsums with: a) four types of limestone as absorbents; b) different Cl⁻ concentration.

The investigation of the four types of limestone indicated that limestone components had significant effects on the moisture content of DH products and moderate effects on desulfurization efficiency (relevant data is shown in Figure 3a). The desulfurization efficiency likely increased when the contents of CaCO₃ and MgCO₃ increased, and impurities had significant effects on the moisture content of DH products. Mg²⁺ were reported to cause the elongation of crystals and reduced the growth rate of gypsum [5,20], while Al³⁺ and Fe³⁺ were reported to change the morphology from thin plates to thick crystals [5,9]. Thus, Limestone 3 had the largest particle size and the highest total contents of MgCO₃, Al₂O₃ and Fe₂O₃, as shown in Figure 4. The crystal morphology of Limestone 3 partly changed from plate-like (such as Limestones 1 and 2) to needle-like, as shown in Figure 4.

The moisture content of gypsum was related to its particle size distribution and crystal morphology [7,21]. Large and regular particles were better for moisture removal. Figure 4 shown that the moisture contents were similar, and the crystal morphology and particle size of Limestones 1 and 2 were not different significantly. The moisture content of Limestone 3 was higher than the Limestones 1 and 2 (Figure 3a) because of the inhomogeneous morphology of gypsum crystals. Among the four types of limestone that were investigated, Limestone 4 had the highest moisture content because of the small and irregular gypsum crystals, with a D_{50} of 12.71 μm . Thus, the free waters between gypsum crystals were not extracted by vacuum equipment easily.

In consideration of desulfurization efficiency and end use gypsum characteristics, Limestone 2 was selected as the best absorbent material for the following experiments.

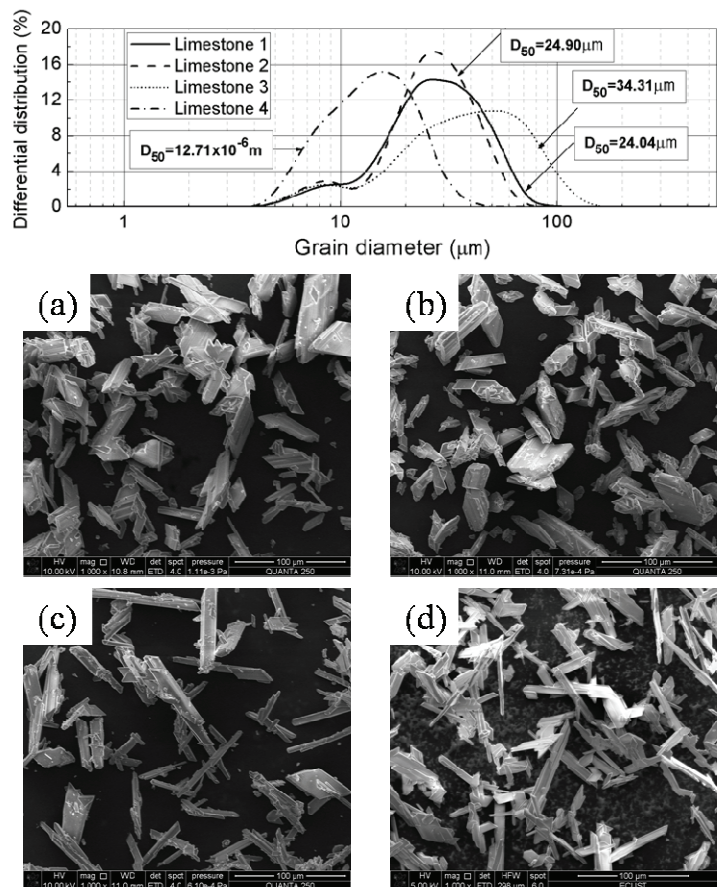


Figure 4. PSD and SEM images of gypsum crystals produced by Limestones: a) 1, b) 2, c) 3 and d) 4.

Influence of Cl⁻ concentration

Chlorine ion is the highest content impurity in the FGD slurry. The chlorine ions come from fuel coal, limestone and supplemental water, with contents of approximately 0.1 and 0.01%, and 10-150 mg/L, respectively.

The chlorine ions dissolved into the slurry, thereby increasing the concentration of Ca²⁺ and lowering the decomposition rate of CaCO₃. As a result, the absorption rate of SO₂ was reduced.

In Figure 3b, when Cl⁻ concentration increased to 5000 mg/L, SO₂ removal rate remained nearly cons-

tant, but when Cl⁻ concentration increased up to 9000 mg/L, SO₂ removal rate declined evidently. Interestingly, a certain concentration range of Cl⁻ was helpful to the combination of gypsum crystals through the formation of CaCl₂·6H₂O. The Cl⁻ ions [7] changed the DH crystals from being plate-like to elongated, as shown in Figure 5. As a result, at a concentration below 5000 mg/L (Figure 6), the moisture content was decreased. However, Cl⁻ exhibited a distortion effect on the crystal structure by increasing the induction period and retarding nucleation kinetics [10]. At a Cl⁻ concentration of 9000 mg/L, the distortion influence was pro-

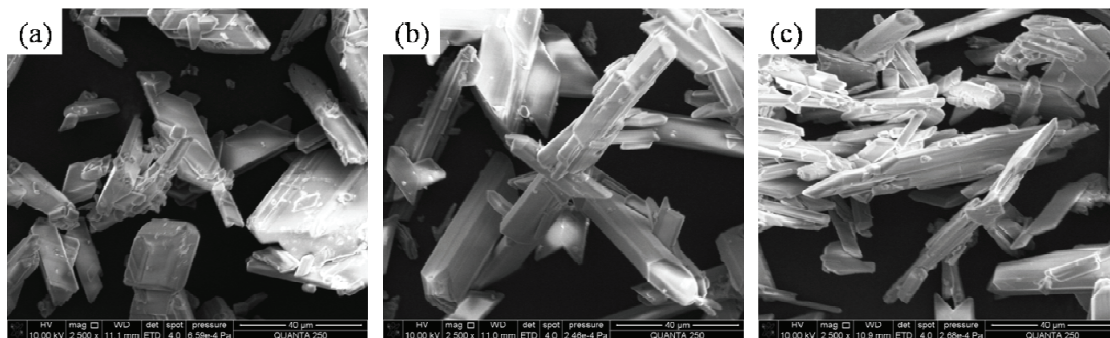


Figure 5. SEM of gypsum crystals grown under different Cl⁻ concentrations; a) 0, b) 2000 and c) 9000 mg/L.

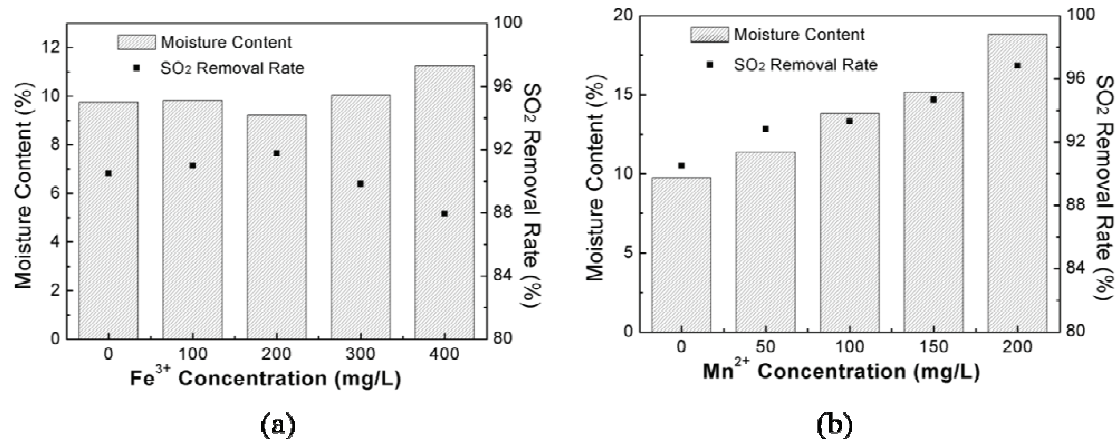


Figure 6. Desulfurization efficiency and moisture content of gypsums under different concentrations of: a) Fe³⁺ and b) Mn²⁺.

minent. The crystal morphology changed from orthorhombic to irregular (Figure 5c), the particle size reduced sharply, and specific surface areas increased, thereby increasing the moisture content. Therefore, the maximum limited content of Cl⁻ in FGD slurry, for industrial application is 5000 mg/L.

Influence of Fe³⁺ concentration

Fe³⁺ is one of the major metal impurities in the FGD slurry. Fe³⁺ was reported as a catalyst for the oxidation of SO₂ [22,23]. The mechanism for the catalysis was shown in Eq. (2). Fe³⁺ was combined with HSO₃⁻, which was generated by the dissolution of SO₂, to form a coordination compound of ferric sulfite. The coordination compound of ferric sulfite was quickly broken down to Fe²⁺ and HSO₃. After a series of reactions, the HSO₃⁻ changed to form SO₄²⁻.

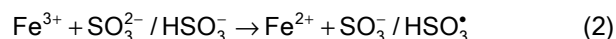


Figure 6a shows an obvious influence, which increased desulfurization efficiency, with the Fe³⁺ concentration increasing to 200 mg/L. However, when the concentration was above 200 mg/L, the desulfurization efficiency declined rapidly. This condition was related to the pH of the FGD slurry, which remained at 5.4±0.2. In an acidic condition, Fe³⁺ will agglomerate visibly, thereby reuniting the limestone particles and minimizing the contact area between limestone and liquid. SEM evaluation showed a flocculent aggregate on the surface of gypsum crystals at a high Fe³⁺ concentration (Figure 7). In the meantime, the dissolution rate of limestone and removal of SO₂ was greatly reduced.

Fe³⁺ affected gypsum crystal significantly, as shown in Figure 8b. The PSD of gypsum crystals were widened (Figure 8), and the crystal morphology become elongated and needle shaped (Figure 8b) when the Fe³⁺ concentration was 200 mg/L. The change in the

crystals indicates that the Fe³⁺ slowed the crystal growth of all faces, except {011} and {111} [7].

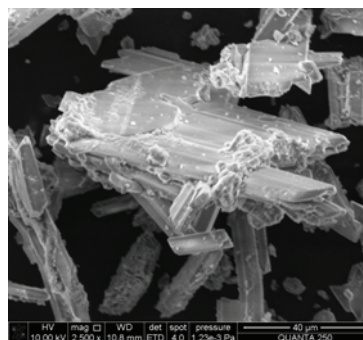
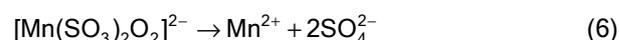
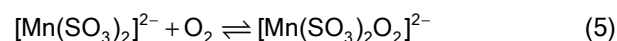
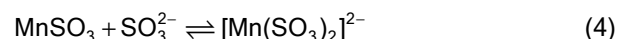


Figure 7. SEM image of crystal surface at high Fe³⁺ concentration.

The Fe³⁺ concentration of FGD slurry in coal-power plants was about 300 mg/L. The Fe³⁺ in the slurry should be removed for optimizing the characteristics of DH. The Fe³⁺ mainly came from fuel coal and limestone, so selecting fuel coal and limestone with low Fe³⁺ content was an effective method.

Influence of Mn²⁺ concentration

Similar to Fe³⁺, Mn²⁺ can catalyze the oxidation of SO₂ [23,24]. The mechanism for the catalysis is shown in Eqs. (3)-(6) [25]:



Mn²⁺ was combined with SO₃²⁻ to form [Mn(SO₃)₂]²⁻. The [Mn(SO₃)₂]²⁻ combined with the O₂ and was finally broken down to Mn²⁺ and SO₄²⁻. The

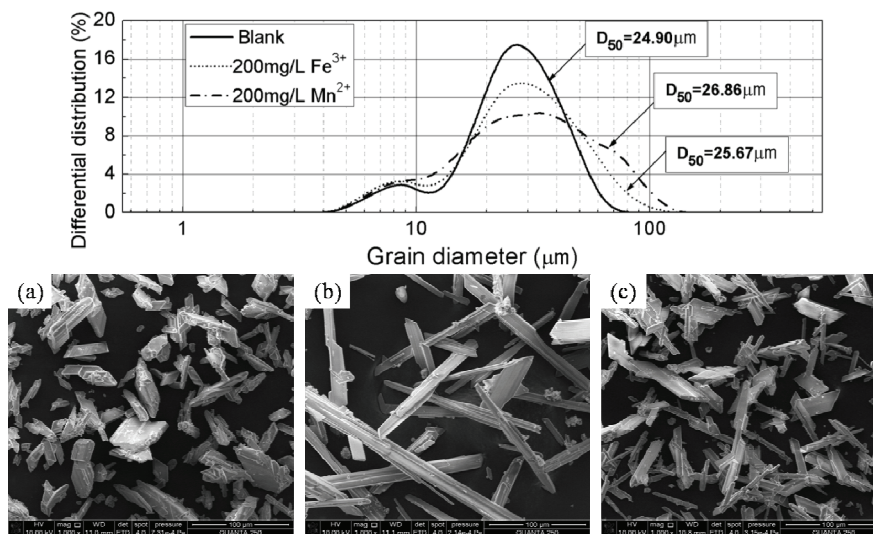


Figure 8. PSD and SEM images of gypsum crystals grown in the presence of impurities: a) blank; b) Fe^{3+} , 200 mg/L; c) Mn^{2+} , 200 mg/L.

data in Figure 6b indicate that the desulfurization efficiency and moisture content of gypsum increased with the increase in Mn^{2+} concentration. The increased moisture content implied the deterioration of gypsum crystals; an evaluation of the SEM image and PSD of the crystals are shown in Figure 8, respectively. Figure 8c shows that the presence of Mn^{2+} gave rise to partly needle-like crystallites and a PSD of crystals that was wider than that in the presence of Fe^{2+} . A comparison among the data indicates that the Fe^{3+} had a stronger inhibiting effect than Mn^{2+} on the crystal growth of all faces except {011} and {111}. The presence of Mn^{2+} caused the crystals to become more irregular than Fe^{3+} . This finding was confirmed by the PSDs and SEM images.

The Mn^{2+} concentration of FGD slurry in coal-power plants was about 30 mg/L. The Mn^{2+} in the slurry should also be removed for optimizing the characteristics of DH. The Mn^{2+} mainly came from fuel coal, so selecting fuel coal with low Mn^{2+} content was an effective method.

CONCLUSIONS

The effect of slurry compositions on desulfurization efficiency and the characteristics of DH in the FGD process were investigated in this paper. In the FGD system, high desulfurization efficiency and low moisture content of gypsum were expected. This study will help coal-power plants in selecting raw limestone and in reducing the cost of the gypsums dewatering process. The results of this study can be summarized as follows:

- Limestone with a high CaCO_3 content and a low of MgCO_3 , Al_2O_3 and Fe_2O_3 content was the expected product.

- Cl^- distorted the crystal structure by increasing the induction period.

- Fe^{3+} and Mn^{2+} , especially Fe^{3+} , can slow the crystal growth of all faces except {011} and {111}.

- The concentration of Cl^- , Fe^{3+} and Mn^{2+} in FGD slurry should be controlled, especially Fe^{3+} , and Mn^{2+} for optimizing the characteristics of DH.

Acknowledgement

The authors would like to express their sincere gratitude to Shanghai Oriental Enviro-Industry Co., Ltd. for their financial support of this study.

REFERENCES

- [1] C. Feng, X. Gao, Y. Tang, J. Cleaner Prod. **68** (2014) 81-92
- [2] F. Yu, J. Chen, F. Sun, Energy Policy **39** (2011) 1586-1599
- [3] H. Qi, B. Zhao, Cleaner Combustion and Sustainable World, Springer-Verlag, Berlin, 2013, p. 207
- [4] C. Zheng, C. Xu, X. Gao, Y. Zhang, J. Zhang, Z. Luo, K. Cen, Environ. Prog. Sustainable Energy **33** (2014) 1171-1179
- [5] T. Feldmann, G. P. Demopoulos, Ind. Eng. Chem. Res. **52** (2013) 6540-6549
- [6] X. Mao, X. Song, G. Lu, Y. Sun, Y. Xu, J. Yu, Ind. Eng. Chem. Res. **54** (2015) 4781-4787
- [7] T. Feldmann, G.P. Demopoulo, J. Chem. Technol. Biotechnol. **89** (2014) 1523-1533
- [8] B. Guan, L. Yang, Z. Wu, Ind. Eng. Chem. Res. **49** (2010) 5569-5574
- [9] X. Mao, X. Song, G. Lu, Y. Sun, Y. Xu, J. Yu, Ind. Eng. Chem. Res. **53** (2014) 17625-17635

- [10] M. Prisciandaro, A. Lancia, D. Musmarra, Ind. Eng. Chem. Res. **40** (2001) 2335-2339
- [11] Y. Qu, J. Guo, Y. Chu, M. Sun, H. Yin, Appl. Surf. Sci. **282** (2013) 425-431
- [12] Y. Li, J. Zhou, T. Zhu, P. Jing, Waste Biomass Valor. **5** (2014) 125-131
- [13] M.M. Rashad, H.M. Baioumy, E.A. Abdel-Aal, Cryst. Res. Technol. **38** (2003) 433-439
- [14] C. Chen, S. Liu, Y. Gao, Y. Liu, Sci. World J. **2014** (2014) 1-6
- [15] S. Liu, W. Xiao, P. Liu, Z. Ye, Clean: Soil Air Water **36** (2008) 482-487
- [16] L. Akyalcin, S.Kaytakoglu, Chem. Eng. Process. **49** (2010) 199-204
- [17] D.O. Ogenga, M.M. Mbarawa, K.T. Lee, A.R, Fuel **89** (2010) 2549-2555
- [18] Z. Yan, Z. Wang, H. Liu, Y. Tu, W. Yang, H. Zeng, J. Qiu, J. Anal. Appl. Pyrolysis **113** (2015) 491-498
- [19] S. Zhang, J. Yu, A. Zhang, F. Zhang, Ocean Eng. **60** (2013) 1-13
- [20] S. Hou, J. Wang, X. Wang, H. Chen, L. Xiang, Langmuir **30** (2014) 9804-9810
- [21] B.B Hansen, S. Kiil, J.E. Johnsson, Fuel **90** (2011) 2965-2973
- [22] P.K. Mudgal, A.K. Sharma, C.D. Mishra, S.P. Bansal, K.S. Gupta, J. Atmos. Chem. **61** (2008) 31-55
- [23] Y. Dhayal, C.P.S. Chandel, K.S. Gupta, Environ. Sci. Pollut. Res. **21** (2014) 3474-3483
- [24] I. Wilkosz, A. Mainka, J. Atmos. Chem. **60** (2008) 1-17
- [25] J. Berglund, L.I. Elding, Atmos. Environ. **29** (1995) 1379-1391.

LINA LV¹
 JIANBIN YANG²
 ZHIGANG SHEN²
 YANBO ZHOU¹
 JUN LU¹

¹Key Laboratory of Coal Gasification and Energy Chemical Engineering of Ministry of Education, East China University of Science and Technology, Shanghai, People's Republic of China
²R&D Center, Shanghai Oriental Enviro-Industry Co., Ltd., Shanghai, People's Republic of China

NAUČNI RAD

OPTIMIZACIJA KARAKTERISTIKA KALCIJUM-SULFATA DIHIDRATA U PROCESU DESULFURIZACIJE DIMNIH GASOVA: ISTRAŽIVANJE NEČISTOĆA U MULJU - Cl⁻, Fe³⁺ I Mn²⁺

Istraživani su efekti krečnjaka, Cl⁻, Fe³⁺ i Mn²⁺ u suspenziji na karakteristike kalcijum-sulfat dihidrata u procesu desulfurizacije dimnih gasova. Sadržaj vlage, raspodela veličine čestica i morfologija kristala su posmatrane kao krajnje korisne karakteristike kalcijum-sulfata dihidrata. Kao rezultat, povećan je broj igličastih kristala kalcijum-sulfata dihidrata sa povećanjem ukupnog sadržaja MgCO₃, Al₂O₃ i Fe₂O₃ u krečnjaku. Cl⁻ remete strukturu kristala i menjaju ortorombične u nepravilne kristale. Mn²⁺ mogu povećati efikasnost desulfurizacije katalizacijom oksidacije SO₂. Na kraju, Fe³⁺ inhibiraju rast svih ravni kristala, izuzev ravni {011} i {111}.

Ključne reči: kalcijum-sulfat dehidrat, desulfurizacija dimnih gasova, krečnjak, Cl⁻, Fe³⁺, Mn²⁺.

WENYUAN FAN
XIAOHONG YIN

School of Chemistry and Chemical
Engineering, Tianjin University of
Technology, Xiqing District, Tianjin,
China

SCIENTIFIC PAPER

UDC 532/533:66:544:621

BUBBLE FORMATION IN SHEAR-THINNING FLUIDS: LASER IMAGE MEASUREMENT AND A NOVEL CORRELATION FOR DETACHED VOLUME

Article Highlights

- The formation process of a minute bubble was acquired accurately by laser image technique
- A bubble formed in shear-thinning fluid presents slim shape due to the fluid's memory effect
- The detached volume rises with solution mass concentration, gas chamber volume and orifice diameter
- A novel correlation of detached volume was developed and agreed better than previous models

Abstract

A laser image system has been established to quantify the characteristics of growing bubbles in quiescent shear-thinning fluids. Bubble formation mechanism was investigated by comparing the evolutions of bubble instantaneous shape, volume and surface area in two shear-thinning liquids with those in Newtonian liquid. The effects of solution mass concentration, gas chamber volume and orifice diameter on bubble detachment volume are discussed. By dimensional analysis, a single bubble volume detached within a moderate gas flowrate range was developed as a function of Reynolds number, Re , Weber number, We , and gas chamber number, Vc , based on the orifice diameter. The results reveal that the generated bubble presents a slim shape due to the shear-thinning effect of the fluid. Bubble detachment volume increases with the solution mass concentration, gas chamber volume and orifice diameter. The results predicted by the present correlation agree better with the experimental data than the previous ones within the range of this paper.

Keywords: laser image, bubble formation, shear-thinning fluid, empirical correlation.

The phenomenon of bubble formation and motion in non-Newtonian fluids is frequently encountered in chemical, biochemical, environmental, petrochemical processes owing to its advantages of high-efficiency interphase contact [1,2]. In typical applications in bubbly flow, such as bubble columns and bioreactors, single bubble formation has a significant

impact on the mass transfer, heat transfer and chemical reactions between gas and liquid phases, since bubble generation directly determines the bubble characteristics, such as bubble shape, volume, rising trajectory and production frequency. However, the mechanism of bubble formation remains far from fully known due to its inherent complexity. Therefore, an adequate understanding of single bubble formation in non-Newtonian fluids is of great importance to gain insight into bubble swarms dynamics as well as to optimize the design of bubble columns.

Previous research revealed that bubbles in non-Newtonian fluid exhibit various features due to the fluid inherent complexity compared with Newtonian fluid [3]. Earlier investigators mainly focused on the

Correspondence: W. Fan, School of Chemistry and Chemical Engineering, Tianjin University of Technology, No.391 Binshui West Road, Xiqing District, Tianjin 300384, China.

E-mail: wxfan@tjut.edu.cn

Paper received: 19 October, 2015

Paper revised: 30 August, 2016

Paper accepted: 9 September, 2016

<https://doi.org/10.2298/CICEQ151019045F>

experimental measurement of bubble volume [4-6]. Then, Miyahara *et al.* [7] proposed a simple spherical model for bubble formation. Terasaka and Tsuge [8-10] concentrated on the several influence on bubble volume respectively. Li [11] and Li *et al.* [12] predicted the instantaneous size, shape and frequency of generating bubble. Martín *et al.* [13,14] studied further the growing and ascending features of the bubble in both Newtonian and non-Newtonian fluids. Peyghambarzadeh *et al.* [15] explored experimentally bubble departure diameters in pure water and three different electrolyte solutions. Venkatachalam *et al.* [16] developed a new prediction model of gas holdup for a wide range of operating conditions in a homogeneous flow regime. Recently, Vélez-Cordero and Zenit [17] devoted to the bubble cluster formation in power-law shear-thinning fluids. From micro-scale to macro-scale, Dietrich *et al.* [18] revealed the various mechanisms governing the bubble formation. However, most of these investigations are either limited to Newtonian fluids, or insufficient in overall consideration of the essential parameters, which include density, apparent viscosity, surface tension, gas flowrate, orifice diameter and the volume of gas chamber. However, as a crucial parameter in determining bubble formation model, the gas chamber volume is missing in these investigations. Furthermore, the mechanism of bubble growth and detachment remains far from settled.

Despite a large number of studies on bubble formation in non-Newtonian fluids, quantitative measurement of bubbles remains a major challenge to the experimentalists, especially for semi-transparent liquid systems. Two types of experimental means, including mainly intrusive and non-intrusive techniques, are generally employed [19]. However, intrusive techniques, such as conductivity probes [20], optical fiber probes [21], ultrasound probes [22] and hot film anemometry [23], inevitably disturb the flow field and become invalid for the small difference of the measured indexes between the gas-liquid phases. By contrast, non-intrusive techniques overcome the disadvantage of interfering with the flow field and are applied widely in various forms [24-26]. Among these non-intrusive techniques, high-speed cameras are employed extensively owing to their capability of catching instantaneous bubble behavior and continuously recording. Obviously, this method requires transparent liquids and relatively low gas holdup in the near wall region.

In this work, a laser image system was set up for determination of the bubble formation process at a single submerged orifice. Bubble formation process in

shear-thinning fluids was directly visualized and recorded in real-time by CCD camera and computer by means of He-Ne laser as the light source using beam expanding and light amplification technology. Bubble generation mechanism was investigated through comparing bubble shape evolution in aforementioned fluids with that in Newtonian fluid, and the influence factors on detachment volume of the bubble were determined experimentally. Further, by taking both fluid physical properties and all operating conditions into account, a correlation for the detachment volume of single bubbles formed in a stagnant shear-thinning liquid was developed based on the dimensional analysis of various kinds of parameters.

EXPERIMENTAL

Apparatus and conditions

The experiments were conducted in a square Plexiglas tank (inner dimensions: 0.15 m width, 0.5 m high) filled with aqueous phases, as shown in Figure 1. Bubbles were generated by injecting a volumetric flow of nitrogen through a replaceable orifice drilled in the centre of the Plexiglas plate (0.15 m×0.05 m×0.01 m), located inside the tank 0.1 m above the bottom. Gas flow rate could be displayed accurately by the rotameter calibrated through adjusting a regulation valve, and a gas chamber was applied to avoid any fluctuations induced by bubble formation and detachment. Therefore, bubbles were always generated periodically from a submerged orifice.

In the image measurement system, the laser beam emitted by He-Ne laser source passed through a spatial filter and a collimating lens, then became a parallel beam, and subsequently passed through the experimental tank filled with liquids. The tank was carefully adjusted to keeping the bubble at the centre of the beam spot, and the process of bubble growth and detachment was magnified properly and imaged on a frosted glass screen by an amplifying lens. Meanwhile, these images were saved on the hard disk by the CCD camera (resolution 640×480 pixels, sampling frequency 25 fps) and picture collection card. In our experiment, the bubble always grew symmetrically along its vertical axis passing through the orifice center. Thus the solid of revolution with regard to the boundary of the recorded bubble image was obtained, and was then divided into many elements of cone and truncated cone. Consequently, the bubble volume and surface area could be calculated by integrating above the elements based on a reference scale calibrated previously. Especially, bubble characteristics were finally acquired by averaging the

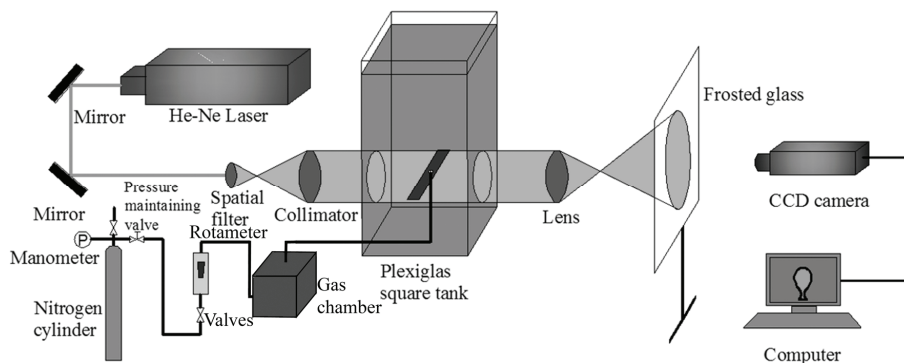


Figure 1. Schematic representation of the experimental apparatus.

results calculated three times using self-developed treatment software. It is noted that assuming a maximum error of ± 1 pixel in the determining of the contour of the bubble yields that the average uncertainty in the diameter calculation ranges from 2.3 to 4.7% for bubble volume and from 1.6 to 3.4% for surface area.

The experiments were implemented under following conditions: orifice diameters (d_0) 1.0, 1.5, 2.0 mm; chamber volume (V_c) 30, 90, 270 mL; gas flowrate (q) 0.1–1.0 mL/s; carboxymethylcellulose (CMC) aqueous solutions 0.8, 0.9, 1.0%; polyacrylamide (PAM) aqueous solutions 0.25, 0.50, 0.75%. Note that q refers to the gas flow rate into the gas chamber. The rheological characteristics, surface tension and density of the solutions involved above were measured by a StressTech Rheometer (Reologica Instruments AB, Sweden), dynamic surface tension apparatus (DCAT21, Dataphysics, Germany) and pycnometer. Moreover, in order to compare the bubble shape evolution in Newtonian fluid, 99.7% glycerol aqueous solution was used and its physical properties were measured. The shear-thinning behaviors of

these solutions could be described adequately by a power law model [11], as shown in Eq. (3), within this experimental range of shear rate. Therefore, the rheological parameters of all solutions were obtained by regression of the measured data and the results are shown in Table 1.

Table 1. Solution physical properties in the experiments

Fluid	Density $\rho / \text{kg m}^{-3}$	Surface tension $\sigma / \text{mN m}^{-1}$	Consistency $K / \text{Pa s}^n$	Flow index, n
0.80% CMC	1002.3	71.20	1.738	0.713
0.90% CMC	1002.6	70.40	2.904	0.664
1.00% CMC	1003.6	69.70	3.629	0.646
0.25% PAM	999.38	72.86	0.092	0.663
0.50% PAM	1001.4	71.98	0.212	0.592
0.75% PAM	1002.8	69.54	0.344	0.555
99.7% GL	1260.2	63.30	1.420	1.000

RESULTS AND DISCUSSIONS

Bubble shape evolution comparison

Figure 2 presents the evolution comparison of the bubble shapes in two shear-thinning fluids and

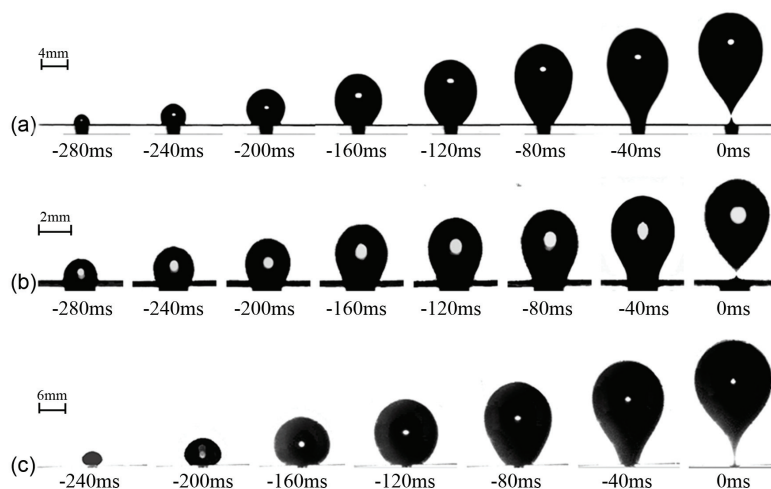


Figure 2. Bubble shapes in shear-thinning and Newtonian fluids at different time: a) 1.0% CMC; b) 0.75% PAM; c) 99.7% GL.

Newtonian fluid under the same condition: $q = 0.15$ mL/s, $d_o = 2.0$ mm and $v_c = 270$ mL. Note that the reference time ($t = 0$) is defined as the moment when a bubble just detaches from the orifice, and that the scale for image sequences is corresponding to the image of the orifice connected with the growing bubble. It is indicated that in both non-Newtonian fluids, bubble formation experiences expansion stage and stretching stage respectively. In the first period, the bubble surface expands spherically in radial direction owing to the dominant role of surface tension. However, the influence of buoyancy on the bubble becomes important gradually with the growth of the bubble. Subsequently, the bubble is elongated vertically to an inverted teardrop-like shape under the combined action of the increasing buoyancy and resistance until its detachment from the orifice.

Furthermore, three main differences between two kinds of shear-thinning fluids and Newtonian fluid are acquired:

1. In contrast with the inverted teardrop-like shape in glycerol solution, the bubble surface located between the maximum horizontal diameter and the tail tip is pulled downward and becomes thin due to the existence of reduced viscosity after the passage of bubbles in non-Newtonian shear-thinning fluid, or so-called the wake behind the previous rising bubble [9]. Further, the above memory effect of the fluid is reinforced with the increase of bubble generation frequency because of the decrease of detached volume under the experimental condition of the same gas flow rate. Consequently, the neck of big bubble is always thinner than that of the small one in shear-thinning fluids.

2. Both instantaneous volume and surface area of the growing bubble in CMC and PAM solutions become smaller than in the glycerol solution, with the same trend as the growth rates corresponding to shear-thinning fluids and Newtonian fluid, as shown in Figure 3. In fact, the overall resistance in glycerol solution, which the bubbling needs to overcome, became larger than that in shear-thinning fluids due to its higher viscosity and density. Thus, in glycerol solution, the gas chamber pressure bubbling needs becomes large and so as the pressure difference between the gas bubble and the chamber, resulting in a large detached volume. Consequently, the bubbling frequency decreases for the same gas flow rate into the chamber. Actually, as the bubble expands further the chamber pressure begins decreasing very quickly as soon as the bubble starts to grow. However, the big overpressure in the chamber causes the bubble to form rapidly, leading to a high instantaneous gas flow

rate through the orifice in Newtonian fluid with high concentration [27].

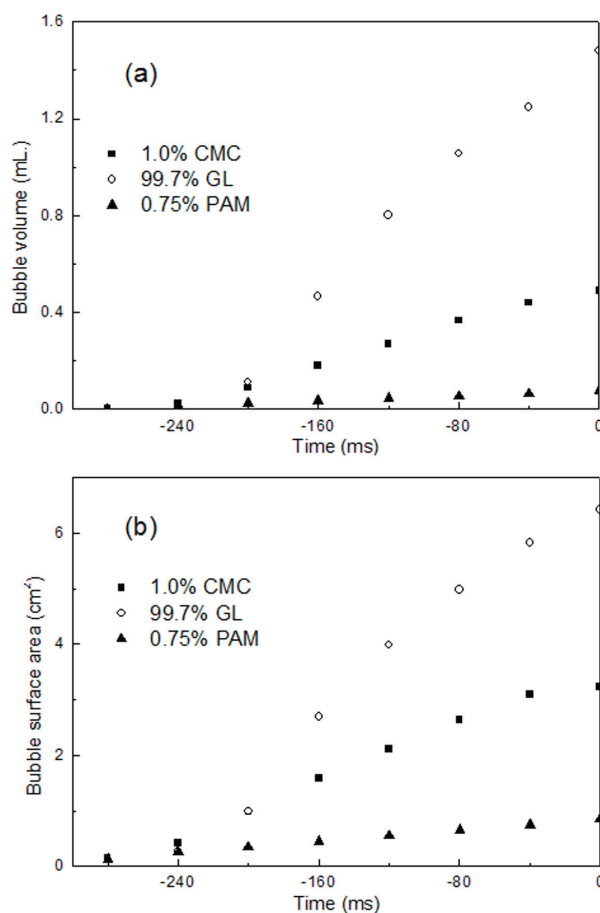


Figure 3. Variation of bubble volume (a) and bubble surface area (b) with time.

Effect of solution mass concentration on bubble detached volume

The effect of solutions mass concentration on bubble detachment volume is illustrated in Figure 4. The results show that the detachment volume formed in both CMC and PAM fluids increases with the solution mass concentration. The main reason lies in three aspects of solution physical properties. First, the apparent viscosity of solutions increases with the mass concentration, and the viscous drag force of the fluid surrounding the bubble blocks the growing and rising of bubble. Second, the density of the solution increases with mass concentration, which also contributes to the increase of the drag force, additionally, the mass of liquid around a bubble increases with its growth. Meanwhile, the buoyancy acted on the bubble increases, which, however, is restrained due to its small magnitude with respect to above two terms. Consequently, the growth time of bubble is prolonged. Third, the surface tension, which tends to hinder the

expansion of bubble surface, reduces slightly with the solution mass concentration, as shown in Table 1. In other words, the high mass concentration of the solution will promote bubble growth. However, Martín *et al.* [13,14] explained the contribution of viscosity from the view point of fluid streamline. According to their reports, there exists a layer of liquid surrounding the bubble, which is directed from the bubble top to the orifice, and while this streamline reaches the gas-liquid-plate point, the dynamic pressure exerted by it will lead to the bubble constriction. As fluid viscosity increases, the velocity of the liquid layer will be lower, allowing the bubble to grow further before the dynamic pressure on the three-phase point is high enough to cut the bubble neck.

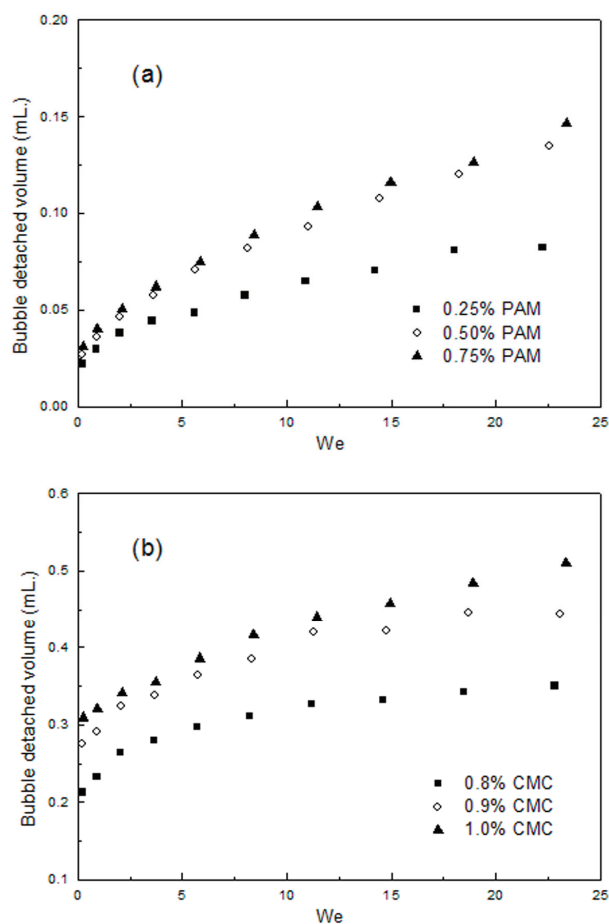


Figure 4. Effect of solutions concentration (a: PAM, b: CMC) on bubble detached volume ($d_o = 1.0 \times 10^{-3} m$, $v_c = 30 \times 10^{-6} m^3$).

Effect of chamber volume and orifice diameter on bubble detached volume

As is well known, the mechanism of bubble formation depends greatly on its intake mode [28], which is closely related to the gas chamber volume. Previously, Satyanarayan *et al.* [29] found that bubble

volume almost increased equivalently with the gas chamber size, however kept constant as the chamber size further added. Besides, Terasaka *et al.* [8] reported that this effect of gas chamber volume on bubble size reduced with the increase of gas flowrate. Particularly, bubble formation mode could be generally classified into three types in terms of a dimensionless number (N_c) [30]. According to Satyanarayan's report, constant gas flowrate mode is drawn in the present investigation whose range of N_c varies from 0.09 to 3.3. Therefore, the pressure in the gas chamber undergoes a periodic change: waiting-bubbling-waiting. There always exists a cyclical fluctuation in the pressure in the gas chamber, but its amplitude goes down with the increase of gas chamber volume. Thus, the greater chamber brings higher average pressure, which leads to the larger driving force for bubble formation, consequently resulting in the bigger bubble, as shown in Figure 5a.

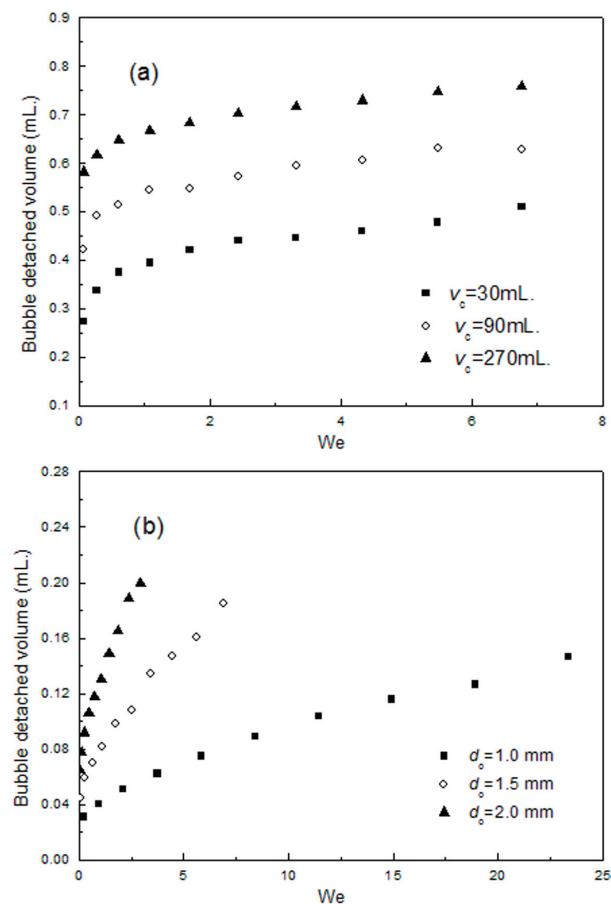


Figure 5. Effect of chamber volume (a: 0.8% CMC, $d_o = 1.5 \times 10^{-3} m$) and orifice diameter (b: 1.0% CMC, $v_c = 30 \times 10^{-6} m^3$) on bubble detached volume.

Bubble detachment volume varies with the gas flowrate under different orifice diameter conditions as

shown in Figure 5b. It is evident that the bubble detached volume gradually increases with the orifice diameter, which is consistent with the reports [31]. However, Terasaka *et al.* [10] reported the same result for relatively high gas flowrate but the contrary result for relatively low gas flowrate. This implies that the influence of orifice diameter becomes more complicated because the rheological behavior of the non-Newtonian fluids is related closely to the gas flowrate.

Dimensional analysis and correction of bubble detached volume

The behavior of bubble formation in non-Newtonian fluids is dominated mainly by such parameters as gas flowrate, gas chamber volume, orifice diameter, as well as density, viscosity and surface tension of gas-liquid systems. The conventional approach for correlating the bubble detached volume is to obtain an equation between the bubble volume and only parts of these parameters in Newtonian fluids.

This work has made an attempt to develop the dimensionless corrections to predict bubble volume V_b in non-Newtonian fluids based upon the Buckingham Pi theorem [32]. Due to $\rho_g \ll \rho_l, \mu_g \ll \mu_l$, a general function of bubble detachment volume V_b can be expressed mathematically as the relevant fluid physical properties and operating condition:

$$V_b = f(\rho_l, \mu_l(K, n), \sigma, q, d_o, v_c) \quad (1)$$

where $\rho_l, \mu_l, \sigma, q, d_o$ and v_c are density, apparent viscosity, surface tension, gas flowrate, orifice diameter and the volume of gas chamber, respectively.

Finally, the application of the Buckingham Pi theorem of dimensional analysis to the present case gives following expression of V_b :

$$\frac{V_b}{d_o^3} = \alpha \left(\frac{\pi \rho_l d_o u_o}{\mu_l} \right)^{\beta_1} \left(\frac{\pi^2 \rho_l u_o^2 d_o}{16 \sigma} \right)^{\beta_2} \left(\frac{v_c}{d_o^3} \right)^{\beta_3} \quad (2)$$

In particular, the average gas flow velocity u_o is calculated by the equation $4q / (\pi d_o^2)$. According to the intermediate region of shear rate, the power law model is used to describe the rheology of fluids, and thus:

$$\mu_l(K, n) = K(\dot{\gamma})^{n-1} \quad (3)$$

Due to the difficulty of experimental measurement for the shear rates of bubble growing in power law fluids, it is obtained through calculating $u_d d_o$ approximatively by referring literature [33], then the viscosity of fluids could be expressed as:

$$\mu_l = K \left(\frac{u_o}{d_o} \right)^{n-1} \quad (4)$$

In fact, Reynolds and Weber numbers in terms of orifice diameter are respectively expressed:

$$Re = \frac{\rho_l d_o^n u_o^{2-n}}{K} \quad (5a)$$

$$We = \frac{\rho_l u_o^2 d_o}{\sigma} \quad (5b)$$

It should be noted that a new dimensionless number V_c related to gas chamber volume has been introduced and written in the form:

$$V_c = \frac{V_c}{d_o^3} \quad (5c)$$

Therefore, Eq. (2) could be rewritten in the form:

$$\frac{V_b}{d_o^3} = \alpha (\pi / 4 Re)^{\beta_1} (\pi^2 / 16 We)^{\beta_2} (V_c)^{\beta_3} \quad (6a)$$

Finally, Eq. (6b) is obtained:

$$\frac{V_b}{d_o^3} = \beta_0 Re^{\beta_1} We^{\beta_2} V_c^{\beta_3} \quad (6b)$$

The constants $\beta_0, \beta_1, \beta_2$ and β_3 in the Eq. (6b) are obtained by fitting the experimental data of various CMC and PAM concentrations solutions under a variety of conditions using the least square method and the result is shown in Table 2.

Table 2. The constants in dimensionless correlations of V_b

Constant	β_0	β_1	β_2	β_3
Value	0.33249	-0.4732	0.4757	0.5815

As a result, a novel correlation for the detachment volume of a bubble formed in shear-thinning fluids in present condition is acquired:

$$\frac{V_b}{d_o^3} = 0.33249 Re^{-0.4732} We^{0.4757} V_c^{0.5815} \quad (7)$$

The validity of Eq. (7) correlation is shown by plotting $V_b d_o^3 / We^{0.4757} V_c^{0.5815}$ of various systems against Re in Figure 6a. The average relative error between the predicted and measured values is below 7%.

To estimate the reliability of the proposed correlation, the following correlations are included. In a wide experimental range of liquid height 0.6–2.1 m, gas flowrate 0–15 mL/s, orifice diameter 0.5–4.0 mm, Jamialahmadi *et al.* [34] made an effort on bubble formation in water as well as the solutions of water with methanol, ethanol, propanol, glycerol and potassium chloride. Then, a nonlinear correlation for bubble diameter in terms of orifice diameter as in Eq. (8) was generated by using radial basis function (RBF) neural

network architecture. Recently, by dividing the bubble formation into the constant volume regime and the growing volume regime, Wang *et al.* [35] proposed an improved correlation for bubble volume in air-water systems as in Eq. (9):

$$\frac{d_b}{d_o} = \left[\frac{5.0}{Bo^{1.08}} + \frac{9.261Fr^{0.36}}{Ga^{0.39}} + 2.147Fr^{0.51} \right]^{1/3} \quad (8)$$

$$V_b = 0.934 \frac{\pi \sigma d_o}{g(\rho_l - \rho_g)} + 1.2 \frac{q^{1.128} d_o^{0.18}}{g^{0.564}} \quad (9)$$

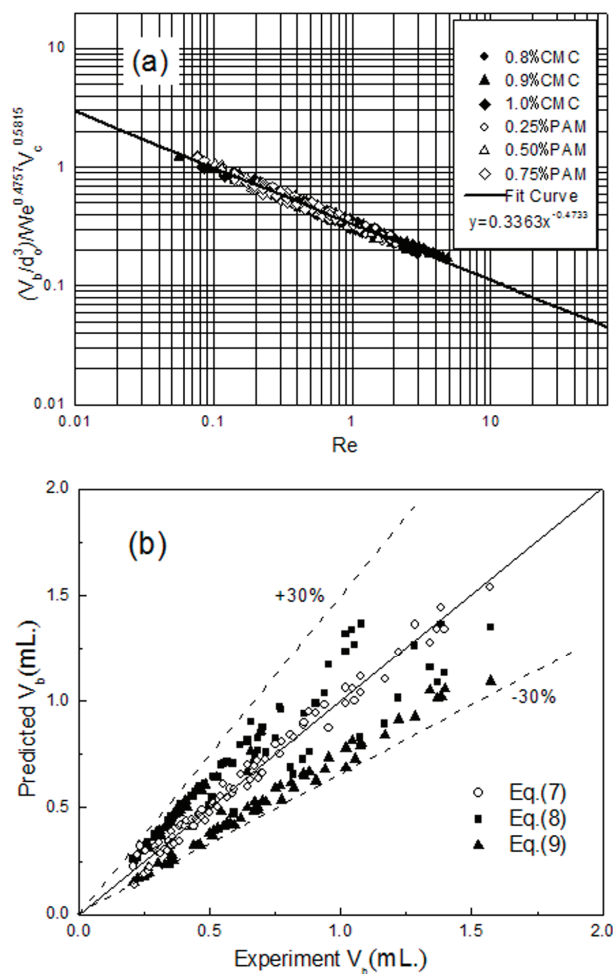


Figure 6. Validity (a) of Eq. (7) and its reliability (b) by comparison with the values calculated from Eqs. (8) and (9).

The comparison between correlations given by Eqs. (7)-(9) is presented in Figure 6b within the range of $0.047 < Re < 5.71$, $0.028 < We < 32.58$, and $3.75 \times 10^3 < V_c < 2.7 \times 10^5$. It should be noted that the experimental volume is taken from our experimental results, and the ranges of three dimensionless variables are based on the whole experimental data in this work. It is clearly seen that the predictions from both Eqs. (8) and (9) are in considerable agreement

with the experimental data within an average error 30%, and the present model is more accurate than Eqs. (8) and (9) with an average error near 10%. Moreover, a further comparison of the present model with experimental data from Jamialahmadi *et al.* [34] and Wang *et al.* [35], also shows a high prediction accuracy of Eq. (7) with error less than 16%, as demonstrated in Figure 7. It has been proved that by applying the proposed correlation, we can predict bubble detachment volume with a reasonable accuracy within the experimental condition.

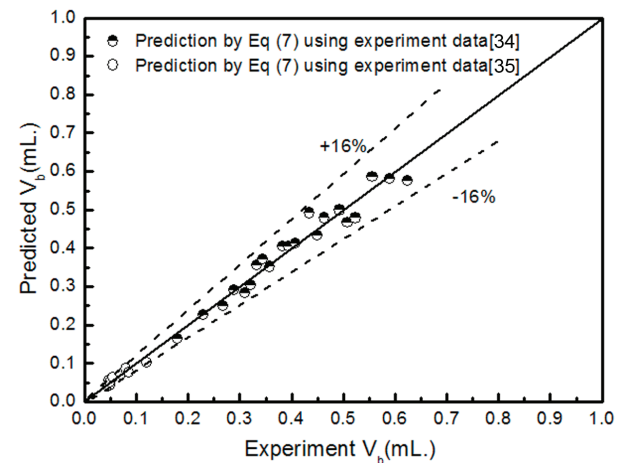


Figure 7. Comparison of the present correlation with the experimental data from Jamialahmadi *et al.* [33] and Wang *et al.* [34].

CONCLUSION

We applied a laser image method combined with computer processing technique to study experimentally single bubble formation in shear-thinning solutions under constant gas flow rate condition. The characteristics of a growing bubble in non-Newtonian fluid have been compared with that in Newtonian fluid, and the effects of solution mass concentration, gas chamber volume and orifice diameter on the bubble detachment volume were discussed. The results indicate that the bubble formation process can be divided into spherical expansion and vertical elongation two stages [36], which are mainly governed by surface tension and buoyancy force, respectively. A bubble formed in non-Newtonian fluid appears slim in shape due to the shear-thinning effect of present solutions compared with that in Newtonian fluid. The bubble detached volume in both studied fluids increases with the mass concentration of solution, chamber volume and orifice diameter. Based on the dimensional analysis on the various comprehensive parameters, a new correlation is developed to predict the detached volume of bubble in shear-thinning

fluids within the range of $.047 < Re < 5.71$, $0.028 < We < 32.58$ and $3.75 \times 10^3 < V_c < 2.7 \times 10^5$. It has a better agreement with the experimental data than the previous ones since an average error decreases from 30% to 10% in the experiments.

Acknowledgements

The authors wish to express their appreciation for the financial support by the National Natural Science Foundation of China (21106106 and 21576214), Tianjin Natural Science Foundation (16JCYBJC20400).

Nomenclature

Bo	Bond number in terms of orifice diameter ($= \rho_l g d_o^2 / \sigma$)
d_b	bubble diameter, mm
d_o	orifice diameter, mm
Fr	Froude number in terms of orifice diameter ($= u_o^2 / d_o g$)
g	gravitational acceleration, m/s^2
Ga	Galileo number in terms of orifice diameter ($= \rho_l d_o^3 g / \mu_l^2$)
K	consistency in Power law model, $Pa \cdot s^n$
n	index in Power law model
N_c	dimensionless number ($= 4v_c \rho_l / (\pi d_o^2 P_h)$)
q	gas volume flowrate, mL/s
Re	Reynolds number in terms of orifice diameter ($= \rho_l u_o d_o / \mu_l$)
u_o	velocity in terms of orifice diameter, m/s
V_c	bubble chamber volume, mL
V_b	bubble detached volume, mL
V_c^*	dimensionless number ($= V_c / d_o^3$)
We	Weber number in terms of orifice diameter ($= \rho_l u_o^2 d_o / \sigma$)

Greek Letters

α	parameter in Eq. (2)
β_0	parameter in Eq. (6b)
β_1	parameter in Eq. (2)
β_2	parameter in Eq. 2
β_3	parameter in Eq. 2
$\dot{\gamma}$	shear rate, $1/s$
μ	gas viscosity, $Pa \cdot s$
ρ	density, Kg/m^3
σ	surface tension, mN/m

Subscripts

g	gas
l	liquid

REFERENCES

[1] Y.T. Shah, B.G. Kelkar, S.P. Godbole, W.D. Deckwer, *AIChE J.* **28** (1982) 353-379

- [2] P.M. Kilonzo, A. Margaritis, *Biochem. Eng. J.* **17** (2004) 27-40
- [3] A.A. Kulkarni, J.B. Joshi, *Ind. Eng. Chem. Res.* **44** (2005) 5873-5931
- [4] N. Rübiger, A. Vogelwohl, in *Encyclopedia of Fluid Mechanics*, N.J. Cheremisinoff Ed., Gulf Pub. Co., Houston, TX, 1986, p. 58
- [5] A. Acharya, R.A. Mashelkar, J.J. Ulbrecht, *Ind. Eng. Chem. Research Fundam.* **17** (1978) 230-232
- [6] A. Acharya, J.J. Ulbrecht, *AIChE J.* **24** (1978) 348-351
- [7] T. Miyahara, W.H. Wang, T. Takahashi, *J. Chem. Eng. Jpn.* **21** (1988) 620-626
- [8] K. Terasaka, H. Tsuge, *Chem. Eng. Sci.* **46** (1991) 85-93
- [9] K. Terasaka, H. Tsuge, *AIChE J.* **43** (1997) 2903-2910
- [10] K. Terasaka, H. Tsuge, *Chem. Eng. Sci.* **56** (2001) 3237-3245
- [11] H.Z. Li, *Chem. Eng. Sci.* **54** (1999) 2247-2254
- [12] H.Z. Li, Y. Mouline, N. Midoux, *Chem. Eng. Sci.* **57** (2002) 339-346
- [13] M. Martín, F.J. Montes, M.A. Galán, *Chem. Eng. Sci.* **61** (2006) 363-369
- [14] M. Martín, F.J. Montes, M.A. Galán, *Chem. Eng. Sci.* **61** (2006) 5196-5203
- [15] S.M. Peyghambarzadeh, A. Hatami, A. Ebrahimi, S.A.A. Fazel, *Chem. Ind. Chem. Eng. Q.* **20** (2014) 143-153
- [16] S. Venkatachalam, A. Palaniappan, S. Kandasamy, K. Kandasamy, *Chem. Ind. Chem. Eng. Q.* **17** (2011) 375-383
- [17] J.R. Vélez-Cordero, R. Zenit, *J. Non-Newton. Fluid Mech.* **166** (2011) 32-41
- [18] N. Dietrich, N. Mayoufi, S. Poncin, N. Midoux, H.Z. Li, *Chem. Eng. Sci.* **92** (2013) 118-125
- [19] C. Boyer, A.M. Duquenne, G. Wild, *Chem. Eng. Sci.* **57** (2002) 3185-3215
- [20] J. Steinemann, R. Buchholz, *Part. Part. Syst. Char.* **1** (1984) 102-107
- [21] S. Saberi, K. Shakourzadeh, D. Bastoul, J. Militzer, *Can. J. Chem. Eng.* **73**(2) (1995) 253-257
- [22] W.A. Al-Masry, E.M. Ali, Y.M. Aqeel, *Chem. Eng. Res. Des.* **83** (2005) 1196-1207
- [23] G. Wang, C.Y. Ching, *Exp. Fluids* **31** (2001) 428-439
- [24] P.N. Rowe, R. Matsuno, *Chem. Eng. Sci.* **26** (1971) 923-935
- [25] Y. Saito, K. Mishima, Y. Tobita, T. Suzuki, M. Matsubayashi, *Appl. Radiat. Isotopes* **61** (2004) 683-691
- [26] H. Braeske, G. Brenn, J. Domnick, F. Durst, A. Melling, M. Ziemann, *Chem. Eng. Technol.* **21** (1998) 415-420
- [27] H.N. Oguz, A. Prosperetti, *J. Fluid Mech.* **257** (1993) 111-145
- [28] J.F. Davidson, B.O.G. Schüler, *Chem. Eng. Res. Des.* **75** (Supplement) (1997) S10-S115
- [29] A. Satyanarayana, R. Kumar, N.R. Kuloor, *Chem. Eng. Sci.* **24** (1969) 749-761

- [30] H. Tsuge, in Encyclopedia of Fluid Mechanics, N.J. Cheremisinoff, Ed., Gulf Pub. Co., Houston, TX, 1986, p. 191
- [31] S.D. Bari, A.J. Robinson, Exp. Therm. Fluid Sci. **44** (2013) 124-137
- [32] E. Buckingham, Phys. Rev. **4** (1914) 354-376
- [33] H.Z. Li, Y. Mouline, L. Choplin, N. Midoux, AIChE J. **43** (1997) 265-267
- [34] M. Jamialahmadi, M.R. Zehtaban, H. Müller-Steinhagen, A. Sarrafi, J.M. Smith, Chem. Eng. Res. Des. **79** (2001) 523-532
- [35] H.Y. Wang, F. Dong, Y.C. Bian, C. Tan, Chinese J. Chem. Eng. **19** (2011) 529-532
- [36] H. Tsuge, S. Hibino, Chem. Eng. Commun. **22** (1983) 63-79.

WENYUAN FAN
XIAOHONG YIN

School of Chemistry and Chemical
Engineering, Tianjin University of
Technology, Xiqing District,
Tianjin, China

NAUČNI RAD

FORMIRANJE MEHURA U PSEUDOPLASTIČNIM FLUIDIMA: ANALIZA LASERSKIH SNIMAKA I NOVA KORELACIJA ZA ZAPREMINU POČETNOG MEHURA

Sistem za lasersko snimanje je korišćen za kvantifikovanje karakteristika rastućeg mehura u mirnim pseudoplastičnim fluidima. Mehanizam formiranja mehura je istraživan poređenjem evolucija trenutnog oblika, zapremine i površine mehura u dve pseudoplastične i jednoj njutnovskoj tečnosti. Diskutovani su uticaji masene koncentracije rastvora, zapremine gasne komore i prečnika otvora na zapreminu početnog mehura. Dimenzionalnom analizom je izvedena korelacija zapremine početnog mehura nastalog pri u umerenom rasponu opsegu protoka gasa sa Reynoldsovom, Veberovim i brojem gasne komore koji uključuju prečnik otvora. Rezultati otkrivaju da početni mehur ima tanan oblik zbog pseudoplastičnosti tečnosti, u poređenju sa njutnovskom tečnošću. Zapremina mehura se povećava sa koncentracijom rastvora, zapreminom gasne komore i prečnikom otvora. Nova korelacija bolje se slaže sa eksperimentalnim podacima od prethodnih u primenjenim uslovima istraživanja.

Ključne reči: laserski snimak, formiranje mehura, pseudoplastični fluid, empirijska korelacija.

R.A.F. OLIVEIRA¹
G.H. JUSTI²
G.C. LOPES¹

¹Graduate Program in Chemical Engineering, Federal University of São Carlos, Rodovia Washington Luís, , São Carlos - São Paulo - Brazil

²Institute of Engineering, Federal University of Mato Grosso, Av. Fernando Corrêa da Costa Cuiabá - Mato Grosso - Brazil

SCIENTIFIC PAPER

UDC 532.5:66:51:633.63:628.3

GRID CONVERGENCE STUDY OF A CYCLONE SEPARATOR USING DIFFERENT MESH STRUCTURES

Article Highlights

- A numerical study of a cyclone separator was carried out using CFD techniques
- A grid independence analysis was carried out to optimize simulation effort and accuracy
- Two mesh structures were used to find out the best numerical mesh for these simulations
- Wall-refined meshes better represent collection efficiency
- Regular element meshes better represent pressure drop

Abstract

In a cyclone design, pressure drop and collection efficiency are two important performance parameters to estimate its implementation viability. The optimum design provides higher efficiencies and lower pressure drops. In this paper, a grid independence study was performed to determine the most appropriate mesh to simulate the two-phase flow in a Stairmand cyclone. Computational fluid dynamic (CFD) tools were used to simulate the flow in an Eulerian-Lagrangian approach. Two different mesh structure, one with wall-refinement and the other with regular elements, and several mesh sizes were tested. The grid convergence index (GCI) method was applied to evaluate the result independence. The CFD model results were compared with empirical correlations from bibliography, showing good agreement. The wall-refined mesh with 287 thousand elements obtained errors of 9.8% for collection efficiency and 14.2% for pressure drop, while the same mesh, with regular elements, obtained errors of 8.7% for collection efficiency and 0.01% for pressure drop.

Keywords: CFD, cyclone separator, bagasse soot, numerical mesh, grid convergence index.

As researchers came into a consensus about all harmful effects of fossil fuels on health and due to the high prices of gasoline, renewable fuels such as ethanol from sugarcane became a solution that is not only cheaper, but also less harmful to health and of lower impact to the environment.

As a secondary product, the bagasse of the milled sugarcane still has energetic value and it is generally combusted, in order to produce electric energy to sustain the whole industry and, sometimes,

sell the exceeding energy. However, its combustion produces sugarcane bagasse soot, a particulate matter also noxious to health and environment that cannot be simply dumped at the environment.

So, in order to control the emission of particulate matter at atmosphere, industries install specific equipment for gas effluent treatment at the outlet of the boiler, such as cyclone separators, electrostatic precipitators or Venturi scrubbers. One of the main used device on air treatment is the cyclone separator, due to its low cost on building, maintenance and capacity of operating at high pressures and temperatures [1,2], and its wide range of gas flow treatment, reaching values between 50 and 50000 m³/h [3].

Even though these advantages, its usage is limited to its collection efficiency of particles with diameter lower than 2 μm, compared to other equipment

Correspondence: R.A.F. Oliveira, Department of Chemical Engineering, Federal University of São Carlos, Rodovia Washington Luís, km 235 - SP-310, P.O. Box: 13565-905, São Carlos - São Paulo - Brazil.

Paper received: 16 May, 2016

Paper revised: 8 July, 2016

Paper accepted: 17 September, 2016

<https://doi.org/10.2298/CICEQ160516044O>

[4], so that cyclone separators are generally used as a pre-collection device, attached to other equipment with higher efficiency.

The usage of computational fluid dynamics (CFD) is a cheap and reliable way to predict the complex flow field and particle trajectories inside a cyclone separator [5,6] in order to optimize the viability of implementation of equipment in a process, saving time and money for the industry. In order to optimize a simulation, improving its accuracy without increasing the simulation time and machine effort, a grid independence study should be performed before running cases.

When studying cyclone separator by CFD methods, researchers emphasize on optimization of the device, by analyzing the effects of the dimensions and operational conditions. Zhao, Su and Zhang [7] compared the effects of a spiral double inlet and a single inlet in the performance, obtaining a better gas flow pattern in a double spiral inlet, while Elsayed and Lacor [8] studied the performance of the device comparing different widths and heights, concluding that the width is more relevant than the height for collection efficiency.

Studies of effects of the height of the cyclone are carried out for different cone and cylinder lengths. It is common to see in the literature studies of the cone effects, comparing the performance of different heights and bottom diameter [9-11], obtaining better collection efficiency as the bottom diameter is reduced. In this research field, Brar, Sharma and Elsayed [12] carried out numerical simulations not only for different cone lengths, but also for different cylinder heights, concluding that increasing the cylinder mainly saves more pressure drop, while the major benefit of increasing the cone is the improvement of the collection efficiency.

It is recurring to see studies that optimize the performance by restructuring the depth and diameter of the vortex finder. Recent researches showed that a smaller pressure drop per flow rate unit can be achieved when a cone-shaped vortex finder is used, although the collection efficiency was insignificant for smaller vortex finder [13,14]. Other vortex finder innovation is seen in the work of Safikhani and Mehrabia [15], whose proposal consists of an outer cylinder and vortex limiter, instead of a conical part, decreasing the pressure drop.

The mesh generation is one of the most important requirements in CFD simulation. Understanding the influence of the mesh size and structure on the flow fields is essential to get reliable results. The analysis of different mesh parameters allows the obtaining of a suitable mesh for a specific problem with acceptable computational effort and numerical accuracy [16].

Barthe and Zhang [17], for example, showed the importance of adapting the fluid mesh when high gradients are present or boundary layer effects are important and proposed a mesh adaptivity procedure using triangular and tetrahedral elements in the mesh.

It is known that great velocity and pressure gradients are observed in cyclone separators, so that wall effects are essential to be analyzed in CFD simulations of these devices. It is common to see meshes with a high quantity of elements, in order to obtain accurate results near walls [8,15,17]. However, few studies are concerned with the influence of the mesh structure on the flow field in cyclones. In this context, the present study aims to propose proper mesh structure and size for a laboratory Stairmand cyclone separator with low quantity of elements without losing accuracy. For this purpose, a grid independence study was performed, using the grid convergence index (*GCI*) method, which consists in quantifying the numerical uncertainty by basing on the Richardson extrapolation method for discretization error estimation, so that a consistent and reliable report of the grid refinement and its accuracy is obtained [18].

METHODOLOGY

Design and meshes generation

The simulated cyclone has a rectangular entry, so, it has seven essential geometry parameters sized in function of its body diameter, D_c , as shown in Figure 1. The inlet has a height, a , and width, b . The outlet of particle matter has a diameter B , while the outlet of air is a cylinder with diameter D_e and a depth of S . The high of the device is divided in h_c , corresponding to the cylindrical part, and H_T , corresponding to its total high.

The cyclone simulated was based on a high efficiency Stairmand model, with ratios and dimensions given in Table 1.

So, the computational domain was generated in software Design Modeler, available on ANSYS 14.5 packages. The complex geometry of this cyclone was subdivided in 33 simple bodies, such as cones and cylinders divided in four parts, in order to match with the rectangle that guides the O-grid generated, as seen in Figure 2.

Using this method, generation of well-structured meshes got simpler when using software Meshing, also available on ANSYS 14.5 packages, with elements exclusively hexahedral, so the simulation could become easier to converge, reducing its process time and machine efforts, was favored.

In order to apply the GCI method, 12 well-structured meshes with a refinement ratio between 1.3 and

1.33 were generated. They were divided in two groups according to the uniformity of the mesh elements - 6 with regular elements and 6 with the same number of elements of the meshes with regular elements, but with wall refinement with a bias ratio of 5. To estimate discretization error, both collection efficiency and pressure drop were used.

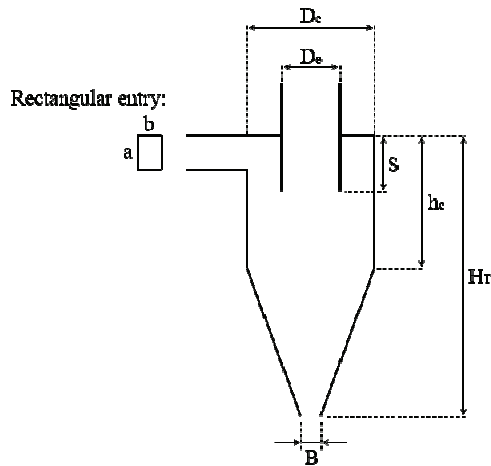


Figure 1. Scheme of a cyclone separator geometry parameters. Source: adapted from Wang (2004).

Table 1. Parameters of the high efficiency stairmand cyclone simulated. Source: Wang (2004)

Parameter	a	b	B	D _c	D _e	h _c	H _r	S
Dimension, m	0.12	0.05	0.09	0.23	0.12	0.35	0.93	0.12
Ratio	0.5	0.2	0.375	1	0.5	1.5	4	0.5

Mathematical model

As a device operating in high velocities, they present complex flow profiles. Two of the main turbulence models suitable to this simulation, also available in commercial software packages are the Reynolds stress model (RSM) and the large Eddy simulation (LES) [19,20]. Due to the complexity of LES model and computational efforts required by it, RSM is a common choice to describe the developed flow. By using the RSM, the exact transport equation is given by [21]:

$$\frac{\partial}{\partial t}(\rho \overline{u_i u_j}) + \frac{\partial}{\partial x_k}(\rho u_k \overline{u_i u_j}) = D_{ij} + P_{ij} + \Pi_{ij} + \varepsilon_{ij} \quad (1)$$

where the first term is the local time derivate of stress, the second term corresponds to the convective transport, the stress diffusion term, D_{ij} is given by:

$$D_{ij} = -\frac{\partial}{\partial x_k}(\rho \overline{u_i u_j u_k} + (\rho \overline{u_i}) \delta_{jk} + (\rho \overline{u_j}) \delta_{ik} - \mu(\frac{\partial}{\partial x_k} \overline{u_i u_j})) \quad (2)$$

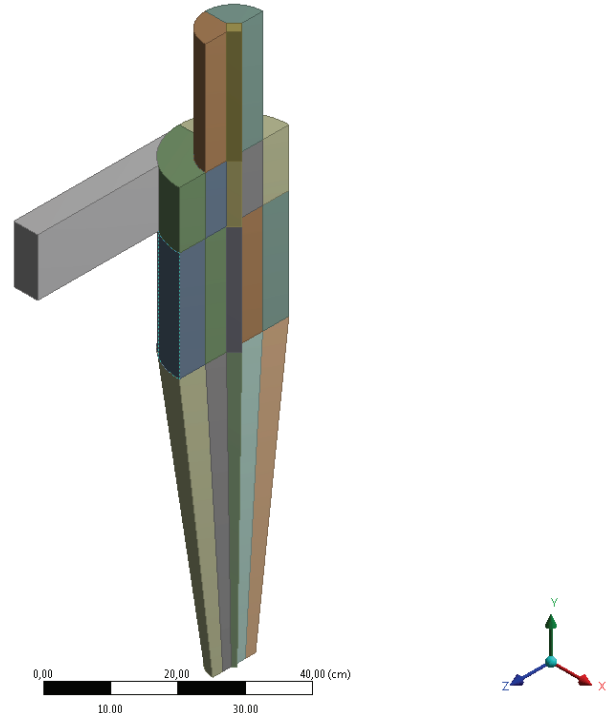


Figure 2. Scheme of a cyclone separator subdivided in simple bodies.

The shear production, P_{ij} is given by:

$$P_{ij} = -\rho \left[\overline{u_i u_k} \frac{\partial u_j}{\partial x_k} + \overline{u_j u_k} \frac{\partial u_i}{\partial x_k} \right] \quad (3)$$

The pressure-strain, Π_{ij} is given by:

$$\Pi_{ij} = \rho \left(\frac{\partial u_i}{\partial x_j} + \frac{\partial u_j}{\partial x_i} \right) \quad (4)$$

The dissipation term, ε_{ij} given by:

$$\varepsilon_{ij} = -2\mu \overline{\frac{\partial u_i}{\partial x_k} \frac{\partial u_j}{\partial x_k}} \quad (5)$$

By using the one-way coupling, the discrete phase follows a fixed continuous phase flow field, in which the effects of the discrete phase on the continuum and the interaction between particles are neglected. The effects of gravity and gas drag force describe the flow, and the momentum equation of a particle is described as:

$$\frac{du_p}{dt} = F_D(\bar{u} + u' - u_p) - g \quad (6)$$

$$\frac{dv_p}{dt} = F_D(\bar{v} + v' - v_p) + \frac{w_p^2}{r_p} \quad (7)$$

$$\frac{dw_p}{dt} = F_D (\bar{w} + w' - w_p) - \frac{v_p w_p}{r_p} \quad (8)$$

where the momentum transport coefficient between fluid and particles, F_D , is given by:

$$F_D = \frac{18\mu C_D Re_p}{\rho_p d_p^2 24} \quad (9)$$

the drag coefficient for particles, C_D , is given by:

$$C_D = \begin{cases} \frac{24}{Re_p} & Re_p \leq 1 \\ \frac{24(1 + 0.15 Re_p^{0.687})}{Re_p} & 1 < Re_p \leq 1000 \\ 0.44 & Re_p > 1000 \end{cases} \quad (10a)$$

$$C_D = \begin{cases} \frac{24(1 + 0.15 Re_p^{0.687})}{Re_p} & 1 < Re_p \leq 1000 \end{cases} \quad (10b)$$

$$C_D = \begin{cases} 0.44 & Re_p > 1000 \end{cases} \quad (10c)$$

and Re_p is the particle Reynolds number, given by:

$$Re_p = \frac{\rho_g d_p |\bar{v}_g - \bar{v}_p|}{\mu} \quad (11)$$

where v assumes velocity components u , v and w .

Case set up

A gas-solid mixture at 20 m/s and 45.5 °C of air, with density of 1.103 kg/m³ and viscosity of 1.8582×10⁻⁵ Pa·s, and sugarcane bagasse soot with average particle diameter of 9 μm and density of 2351.1 kg/m³. As the focus of this paper is to analyze the structure of the meshes, the diameter of the particle was set as constant, in order to simplify the simulations, which were carried out using Fluent Solver 14.5 in an Eulerian-Lagrangian approach, in which the gas was treated as continuum phase, particulate phase was treated as single particles and particle trajectories, representing a stream of particles, are calculated as a result of a balance of forces acting on them, by using a one-way coupling.

Each simulation was set up in a transient state with a time step of 0.0001 second for 10000 time steps, in order to simulate a cyclone operating for 1 s. This was enough to ensure that the inlet static pressure converged to a steady state.

Spatial discretization was carried out in a second order upwind Scheme, adopting the spherical drag law model for drag coefficient and the SIMPLE scheme for pressure-velocity coupling.

The solution was set to converge when the residuals of all the flow variables, such as continuity, turbulent kinetic energy, turbulent dissipation and stress tensors, fell below 1×10⁻⁵ and the monitored total

pressures at the surface of inlet and the surface of the outlet of air became steady. All the numerical simulations were carried out using the default relaxation factor values in the Fluent solver.

As soon as static pressure of air at the inlet converged to a steady value, particles were injected in the domain at 20 m/s using a one-way coupling scheme, in which the effects of interaction between particles and the gas are neglected, and its flow was tracked, using the discrete phase model (DPM). In this model, particles were set up to reflect on wall, escape on air outlet and get trapped when reaches the bottom of the cyclone.

In order to use this coupling scheme, it is necessary to assume that the dispersed phase occupies a low volume fraction, generally lower than 10% [18]. To ensure that this condition was suited, the injection of particles was set up to be proportional to the number of elements in the inlet of the numerical mesh.

Grid independence analysis

In this study, the GCI method was used to optimize the simulation, choosing a numerical mesh which results in higher precision and lower required machine effort.

The procedure for estimation of discretization error suggested [20] is, first of all, defining a representative mesh size h , given by:

$$h = \left[\frac{1}{N} \sum_{i=1}^N \Delta V_i \right]^{1/3} \quad (12)$$

where ΔV_i is the volume of the i^{th} cell and N is the total number of cells used for the computations.

It is desirable a grid refinement factor, given by Eq. (13), greater than 1.3 and constant, based on experimental studies [20]:

$$r = \frac{h_{\text{coarse}}}{h_{\text{fine}}} \quad (13)$$

After selecting the 3 finest meshes and running simulations to determine the values of relevant variables, φ , the apparent order, ρ , is calculated using fixed-point iteration in the equations:

$$\rho = \frac{1}{\ln r_{21}} \ln \left| \frac{\varepsilon_{32}}{\varepsilon_{21}} \right| + q(\rho) \quad (14)$$

$$q(\rho) = \ln \left(\frac{r_{21}^\rho - s}{r_{32}^\rho - s} \right) \quad (15)$$

$$s = 1 \cdot \text{sign} \left(\frac{\varepsilon_{32}}{\varepsilon_{21}} \right) \quad (16)$$

where $h_1 < h_2 < h_3$, $r_{21} = h_2/h_1$, $r_{32} = h_3/h_2$, $\varepsilon_{32} = \varphi_3 - \varphi_2$, $\varepsilon_{21} = \varphi_2 - \varphi_1$ and φ_k is the solution on the k^{th} mesh.

So, extrapolated values can be calculated by the Eq. (16), and similarly it can be done for ϕ_{ext}^{32} . By calculating the extrapolated values, approximate relative error and extrapolated relative error can be estimated by Eqs. (17) and (18), respectively:

$$\phi_{\text{ext}}^{21} = \frac{r_{21}^p \phi_1 - \phi_2}{r_{21}^p - 1} \quad (17)$$

$$e_a^{21} = \left| \frac{\phi_1 - \phi_2}{\phi_1} \right| \quad (18)$$

$$e_{\text{ext}}^{21} = \left| \frac{\phi_{\text{ext}}^{21} - \phi_1}{\phi_{\text{ext}}^{21}} \right| \quad (19)$$

At last, the grid convergence index can be calculated by the Eq. (19) as follows:

$$GCI_{\text{fine}}^{21} = \frac{1.25 e_a^{21}}{r_{21}^p - 1} \quad (20)$$

RESULTS AND DISCUSSION

Following *GCI* criteria and based on an initial coarse mesh with 10590 elements, the 6 different sizes of numerical meshes and the grid refinement factor were obtained, as shown in Table 2. As the sizes of the numerical meshes were established, two different kinds of meshes were generated for each size. The first one had only regular elements, while the other had wall-refined elements. The meshes quality statistics, shown in Table 3, in order to analyze its structures, shows that none of the 12 meshes had average aspect ratio over 6.1, average orthogonality below 0.97 or

average skewness over 0.125.

In order to analyze the tangential and axial velocities of air and total pressure according to their radial position, an *X*-axis based line was set up in the middle of the cylindrical section of the device, obtaining profiles shown in Figure 3. The profiles were not only developed according to expectations, but also got better defined as meshes were refined.

Analyzing the figures above, each one has a trend line well developed at meshes with at least 129 thousand elements for wall-refined meshes and 287 thousand elements for regular element meshes. This difference can be easily explained due to the fact walls in a cyclone separator are the critical region. Thus, in order to obtain more accurate results with less computational efforts, a better refinement on walls is recommended.

In both situations, the ideal would be using meshes with 683 thousand elements, in which results got more precise. However, one of the objectives of this study was optimizing both accuracy and computational effort, so it was more viable to use the mesh with 287 thousand wall-refined elements.

The chosen mesh has around 287 thousand elements, all of them hexahedral, which 95.6% of them has orthogonal quality over 0.96 and 99.99% of them has an aspect ratio below 20. Thus, this mesh is considered well-structured, as seen in Figure 4, and has reliable results.

As soon as pressures at inlet, P_{in} , and outlet, P_{out} , converged to a steady value, pressure drop, ΔP , can be estimated by the equation:

$$\Delta P_{\text{CFD}} = |P_{\text{in}} - P_{\text{out}}| \quad (21)$$

while collection efficiency, in a CFD approach, can be

Table 2. Comparison between CFD results in wall-refined and regular elements meshes and correlations expectations

Mesh	Number of elements	<i>r</i>	$\Delta P_{\text{CFD}} / \text{Pa}$	$\Delta P_{\text{correlation}} / \text{Pa}$	$\delta / \%$	$\eta_{\text{CFD}} / \%$	$\eta_{\text{correlation}} / \%$	$\delta / \%$
Wall-refined meshes								
1	10590	-	533.73	1104.14	51.66	80		13.57
2	24864	1.3291	817.54		25.96	66.67		5.35
3	58230	1.328	1007.75		8.73	75	70.44	6.47
4	129312	1.3047	1162.47		5.28	73.75		4.70
5	287232	1.3048	1261.14		14.22	77.35		9.81
6	683312	1.3349	1389.63		25.86	76.68		8.72
Regular elements meshes								
1	10590	-	270.81	1104.14	75.47	100		41.96
2	24864	1.3291	440.84		60.08	83.33		18.30
3	58230	1.328	667.95		39.51	75	70.44	6.47
4	129312	1.3047	830.31		24.80	75		6.47
5	287232	1.3048	1104.07		0.01	76.56		8.69
6	683312	1.3349	1194.17		8.15	76.98		9.28

Table 3. Mesh quality parameters

Mesh quality coefficient		Regular element meshes						Wall-refined meshes					
		10k	24k	58k	129k	287k	683k	10k	24k	58k	129k	287k	683k
Aspect Ratio	Minimum	1.302	1.359	1.246	1.513	1.438	1.381	1.157	1.151	1.053	1.045	1.033	1.146
	Maximum	15.00	16.75	12.96	33.37	12.77	19.54	15.00	17.17	17.44	33.37	14.90	19.54
	Mean	4.211	4.619	3.968	5.316	3.745	5.110	4.983	5.688	4.951	6.084	4.528	5.800
	σ	2.744	2.828	1.832	4.372	1.886	3.229	2.829	3.212	2.554	4.421	2.304	3.299
Orthogonality	Minimum	0.345	0.309	0.300	0.263	0.265	0.233	0.345	0.310	0.300	0.263	0.264	0.233
	Maximum	1.00	1.00	1.00	1.00	1.00	1.00	1.00	1.00	1.00	1.00	1.00	1.00
	Mean	0.976	0.981	0.983	0.984	0.986	0.987	0.971	0.978	0.983	0.981	0.987	0.987
	σ	0.054	0.048	0.045	0.045	4.165	0.043	0.058	0.052	0.046	0.056	4.322	0.046
Skewness	Minimum	0.00	0.00	0.00	0.00	0.00	0.00	0.00	0.00	0.00	0.00	0.00	0.00
	Maximum	0.789	0.810	0.815	0.836	0.834	0.853	0.789	0.810	0.815	0.836	0.835	0.853
	Mean	0.121	0.099	0.094	0.071	0.074	0.064	0.112	0.089	0.084	0.061	0.063	0.054
	σ	0.112	0.099	0.092	0.088	0.083	0.083	0.108	0.093	0.085	0.080	0.076	0.075

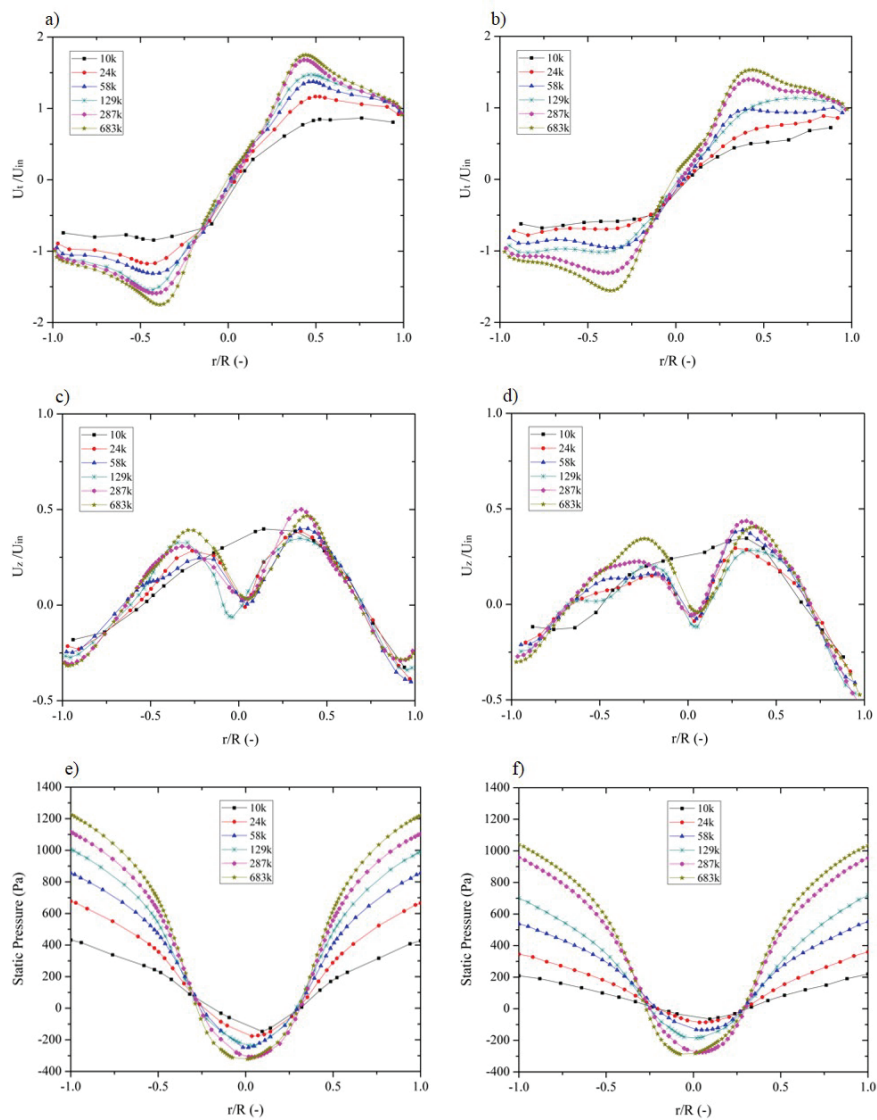


Figure 3. Flow profiles; dimensionless tangential velocity (U_t/U_{in}) for: a) wall-refined and b) regular element meshes; dimensionless axial velocity (U_z/U_{in}) for: c) wall-refined and d) regular element meshes; static pressure in a dimensionless radial position for: e) wall-refined and f) regular element meshes.

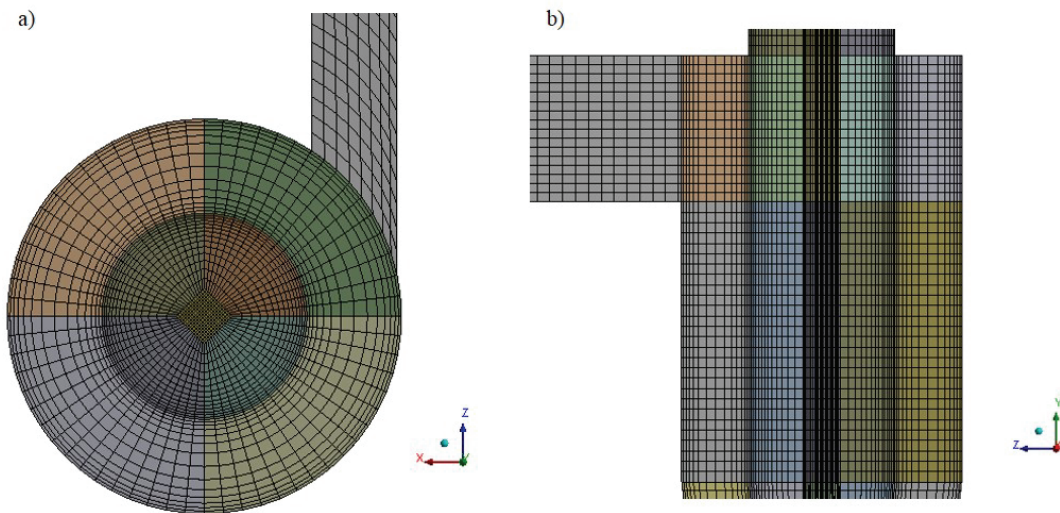


Figure 4. Views of the 287 thousand wall-refined elements mesh: a) superior view of the o-grid; b) interior view of the mesh.

estimated by the equation:

$$\eta_{\text{CFD}} = \frac{n_{\text{trap}}}{n_{\text{inj}}} \quad (22)$$

where n_{trap} is the number of tracked particles trapped in the bottom of the cyclone and n_{inj} is the number of tracked particles injected in the inlet of the cyclone separator.

To compare with CFD results, the following empirical correlations were used to estimate pressure drop:

$$\Delta P_{\text{correlation}} = \frac{\rho V_i^2}{2} \Delta H \quad (23)$$

where ΔH is a dimensionless parameter that depends on the cyclone dimensions. One of the proposed a correlation to estimate ΔH is given by [22]:

$$\Delta H = 20 \left(\frac{ab}{D_e^2} \right) \left[\frac{S/D_c}{\left(H/D_c \right) \left(h_c/D_c \right) \left(B/D_c \right)} \right]^{1/3} \quad (24)$$

For collection efficiency, the empirical correlations used to compare with CFD results are given by [4]:

$$\eta_i = 1 - e^{-2 \left[\frac{G \tau_i Q}{D_c^3} (n+1) \right]^{1/2n+2}} \quad (25)$$

where Q is the flow rate given in m^3/h , G is a dimensionless geometry parameter, given by the equation:

$$G = \frac{8K_c}{K_a^2 K_b^2} \quad (26)$$

with:

$$K_a = \frac{a}{D_c} \quad (27)$$

$$K_b = \frac{b}{D_c} \quad (28)$$

$$K_c = \frac{2V_s + V_{nl}}{D_c^3} \quad (29)$$

where V_s is the annular volume between the central plane of the inlet duct and the bottom of the exit duct, S , given by the equation:

$$V_s = \pi \left(S - \frac{a}{2} \right) \frac{(D_c^2 - D_e^2)}{4} \quad (30)$$

and V_{nl} is an annular volume related to the vortex penetration inside the cyclone and can be calculated by the equation:

$$V_{nl} = \frac{\pi D_c^2}{4} (h_c - S) + \left(\frac{\pi D_c^2}{4} \right) \left(\frac{Z_c + S - h_c}{3} \right) \left(1 + \frac{d_c}{D_c} + \frac{d_c^2}{D_c^2} \right) - \frac{\pi D_e^2 Z_c}{4} \quad (31)$$

where d_c is the diameter of the cyclone central axis, given by:

$$d_c = D_c - (D_c - B) \left(\frac{S + Z_c - h_c}{H - h_c} \right) \quad (32)$$

being Z_c the vortex natural length, given by:

$$Z_c = 2.3 D_e \left(\frac{D_c^2}{ab} \right)^{1/3} \quad (33)$$

and n is the vortex exponent, given by:

$$n = 1 - \left[1 - 0.67 \left(D_c^{0.14} \right) \right] \left(\frac{T}{283} \right)^{0.3} \quad (34)$$

with D_c given in meters and the gas temperature T in Kelvin. Finally, the relaxation time, τ_i , given by:

$$\tau_i = \frac{\rho_p D_i^2}{18\mu} \quad (35)$$

After calculating pressure drop and efficiency by CFD and empirical correlations, relative errors can be estimated by the equation:

$$\delta = 100 \left| \frac{\phi_{\text{CFD}} - \phi_{\text{correlation}}}{\phi_{\text{correlation}}} \right| \quad (36)$$

where ϕ is the analyzed variable.

Another consequence of the results obtained on CFD model is the estimation of the apparent order and GCI for both collection efficiency and pressure drop for each mesh refinement, as shown in Table 4, where p_i is the apparent order for the i^{th} parameter ϕ_i , being 1 the collection efficiency and 2 the pressure drop.

Table 4. Apparent order and GCI for collection efficiency and pressure drop for different kinds of meshes

Grid Step	Wall-refined meshes				Regular elements meshes			
	p_1	ϕ_1 %	p_2	ϕ_2 %	p_1	ϕ_1 %	p_2	ϕ_2 %
GCI ₂₁	5.753	6.04	0.6044	229.66	5.0741	7.73	4.3378	19.80
GCI ₃₂		3.38		128.14		4.31		17.54
GCI ₄₃		0.59		95.40		0.00		11.27
GCI ₅₄		1.60		56.06		0.89		14.28
GCI ₆₅		0.29		60.58		0.20		3.77

As seen in flow profiles on Figure 3, meshes with 683 thousand elements, for both regular elements and wall-refined meshes, better represented the trend of the expected flow, which could be confirmed by the GCI method.

Although the wall-refined mesh of 683 thousand elements developed a discretization error of 0.34% for pressure drop, a very low and good value, its discretization error for collection efficiency was 37.69%. So that, the better option was to simulate this device using the 287 thousand elements with wall refinement, which GCI for collection efficiency and pressure drop were, respectively, 3.08%, still a low and good value, and 17.40%, still a high value, but the lower obtained for the variable.

Now, comparing results between the two types of meshes with 287 thousand elements and expectations

from empirical correlations, results were coherent to predictions of CFD. Collection efficiency is affected by wall effects, such as drag and friction, so it was expected a more reliable result of collection efficiency at the wall-refined mesh, as shown. As a variable equally distributed in the domain, a better accuracy for pressure is expected in meshes with regularly sized elements, as observed on results of pressure drop.

CONCLUSION

After analyzing the obtained results of the 12 simulated meshes it is conclusive that the proposed model correctly represents the expected flow profiles. Due to the critical region of the cyclone separator being located at walls and at vortex region, wall-refined meshes developed the expected trend needing fewer elements than regular element meshes. This caused less simulation time and machine effort, which was one of the objectives of this paper.

Even though the chosen mesh had a higher discretization error for collection efficiency, it was not a significant issue. Gains on accuracy obtained in a more refined mesh did not compensate the necessary time to simulate the device.

Nomenclature

a	Height of the cyclone inlet
b	Width of the cyclone inlet
B	Diameter of the particle matter outlet
d_c	Diameter of the cyclone central axis
D_c	Diameter of the cyclone body
D_e	Diameter of air outlet
D_i	Particle diameter
e_a	Approximated relative error
e_{ext}	Extrapolated relative error
DPM	Discrete phase model
G	Geometric parameter in Eq. (26)
GCI	Grid convergence index
h	Representative mesh size
h_c	Height of the cylindrical part of the cyclone
H_T	Cyclone total height
K_a	Dimensionless parameter in Eq.(27)
K_b	Dimensionless parameter in Eq.(28)
K_c	Dimensionless parameter in Eq. (29)
LES	Large Eddy simulation
N	Vortex exponent
n_{inj}	Number of injected particles in the inlet
n_{trap}	Number of trapped particles in particle outlet
N	Total number of elements in the mesh
p_i	Apparent order of the i^{th} analyzed parameter
P_{in}	Pressure in the inlet of the cyclone
P_{out}	Pressure in the air outlet of the cyclone
Q	Gas volumetric flow rate

r	Grid refinement ratio
RSM	Reynolds stress model
s	Signal function
S	Internal height of the air outlet
SIMPLE	Semi-implicit method for pressure linked equations
T	Temperature in K
u	Fluctuation velocity
v_i	Gas velocity at the cyclone entry
V_{nl}	Annular volume between S and Z_c
Z_c	Vortex natural length
<i>Greek</i>	
δ	Relative error
ε	Aggregated error
ΔH	Dimensionless parameter
$\Delta P_{\text{correlation}}$	Pressure drop by empirical correlation
ΔP_{CFD}	Pressure drop by CFD correlation
ΔV	Volume of the i^{th} element of the mesh
$\eta_{\text{correlation}}$	Collection efficiency by empirical correlation
η_{CFD}	Collection efficiency by CFD correlation
μ	Gas viscosity
ρ	Gas density
ρ_p	Particle density
σ	Standard deviation
τ_i	Relaxation time
φ	Discrete solution
φ_{ext}	Extrapolated discrete solution
<i>Subscript</i>	
i	Cartesian coordinate
j	Cartesian coordinate
k	Cartesian coordinate
in	Inlet
t	Tangential
z	Z axis
21	refers to GCI between meshes 2 and 1
32	refers to GCI between meshes 3 and 2
43	refers to GCI between meshes 4 and 3
54	refers to GCI between meshes 5 and 4
65	refers to GCI between meshes 6 and 5

REFERENCES

- [1] K. Elsayed, C. Lacor, *Comput. Fluids* **68** (2012) 134-147
- [2] A. Keça, *Sep. Purif. Technol.* **75** (2010) 127-131
- [3] L.K. Wang, N.C. Pereira, Y. Hung (Eds.), *Air Pollution Control Engineering*, Humana Press Inc., New Jersey, 2004, pp. 97-105
- [4] W.L. Heumann (Eds.), *Industrial Air Pollution Control Systems*, McGraw-Hill, New York, 1997, pp. 514-519
- [5] W.D. Griffiths, F. Boysan, *J. Aerosol Sci.* **27** (1996) 281-304
- [6] A.C. Hoffmann, L.E. Stein (Eds.), *Gas Cyclones and Swirl Tubes: Principles, Design and Operation*, Springer, New York, 2002, pp. 123-135
- [7] B. Zhao, Y. Su, J. Zhang, *Chem. Eng. Res. Des.* **84** (2006) 1158-1165
- [8] K. Elsayed, C. Lacor, *Appl. Math. Model.* **35** (2011) 1952-1968
- [9] T.G. Chuah, J. Gimbut, T.S.Y. Choong, *Powder Technol.* **162** (2006) 126-132
- [10] R. Xiang, S.H. Park, K.W. Lee, *J. Aerosol Sci.* **32** (2011) 549-561
- [11] R.B. Xiang, K.W. Lee, *Sci. Technol.* **19** (2001) 327-338
- [12] L.S. Brar, R.P. Sharma, K. Elsayed, *Powder Technol.* **286** (2015) 668-677
- [13] K.S. Lim, H.S. Kim, K.W. Lee, *J. Aerosol Sci.* **35** (2004) 743-754
- [14] A. Raoufi, M. Shams, M. Farzaneh, R. Ebrahimi, *Chem. Eng. Process.* **47** (2008) 128-137
- [15] H. Safikhani, P. Mehrabian, *Adv. Powder Technol.* **27** (2016) 379-387
- [16] N.M.C. Marting, N.J.G. Carriço, H.M. Ramos, D.I.C. Covas, *Comput. Fluids* **105** (2014) 218-230
- [17] K. Bathe, H. Zhang, *Comput. Struct.* **87** (2009) 604-617
- [18] K. Elsayed, C. Lacor, *Chem. Eng. Sci.* **65** (2010) 6048-6058
- [19] A.Y.T. Leung, S.G. Bogodage, *Powder Technol.* **286** (2015) 488-506
- [20] P.J. Roache, *J. Fluids Eng.* **116** (1994) 405-413
- [21] B.E. Launder, *Int. J. Heat Fluid Flow* **10** (1989) 282-300
- [22] G. Ramachandran, D. Leith, J. Dirgo, H. Feldman, *Aerosol Sci. Technol.* **15** (1991) 135-148.

R.A.F. OLIVEIRA¹
G.H. JUSTI²
G.C. LOPES¹

¹Graduate Program in Chemical Engineering, Federal University of São Carlos, Rodovia Washington Luís, São Carlos - São Paulo - Brazil

²Institute of Engineering, Federal University of Mato Grosso, Av. Fernando Corrêa da Costa Cuiabá - Mato Grosso - Brazil

NAUČNI RAD

PROUČAVANJE SEPARATORA CIKLONA KORIŠĆENJEM KONVERGENCIJE KOORDINATNE MREŽE RAZLIČITIH STRUKTURA

U projektovanju ciklona, dva značajna parametra za ocenu njegove praktične primenljivosti su smanjenje pritiska i efikasnost separacije. Optimalni dizajn pruža veću efikasnost i manji pad pritiska. U ovom radu, primenjene su nezavisne mreže kako bi se odredila najprijkladnija mreža za simulaciju dvofaznog toka u Stairmand ciklonu. Alati proračunske dinamike fluide (CFD) sa Eulerian-Lagrangian pristupom korišćeni su za simulaciju protoka. Istražene su dve različite strukture mreže, sa nekoliko veličina okaca: jedna sa uticajem zida i druga sa regularnim elementima. Metoda indeksa konvergencije mreže (GCI) je primenjena za procenu nezavisnosti rezultata. Rezultati CFD modela upoređeni su sa empirijskim korelacijama iz literature i utvrđeno je dobars slaganje. Prva mreža sa 287 hiljada elemenata dala je grešku od 9,8% za efikasnost separacije i 14,2% za pad pritiska, dok je ista mreža, sa regularnim elementima, dala grešku od 8,7% za efikasnost separacije i 0,01% za pad pritiska.

Ključne reči: CFD, ciklon, čađ otpadaka prerade šećerne repe, numerička mreža, indeks konvergencije mreže.

SHAOBAI LI
JUNGENG FAN
SHUANG XU
RUNDONG LI
JINGDE LUAN

College of Energy and
Environment and Liaoning Key
Laboratory of Clean Energy,
Shenyang Aerospace University,
Shenyang, China

SCIENTIFIC PAPER

UDC 66.021.3:532.516:544

THE INFLUENCE OF pH ON GAS-LIQUID MASS TRANSFER IN NON-NEWTONIAN FLUIDS

Article Highlights

- The mass transfer process of bubble swarms in non-Newtonian fluids was studied experimentally
- The $k_L a$ increased with the gas flow rate and decreased with the apparent viscosity of the liquid
- The pH value exhibited a marginal effect on the gas-liquid mass transfer for $\text{pH} < 7$
- The gas-liquid mass transfer rate increased with increasing pH for $\text{pH} > 7$

Abstract

In this study, the effect of pH on the mass transfer of oxygen bubble swarms in non-Newtonian fluids was experimentally studied. The volumetric liquid side mass transfer coefficient ($k_L a$), liquid side mass transfer coefficient (k_L), and specific interfacial area (a) were investigated. The pH was regulated by the addition of hydrochloric acid and sodium hydroxide (NaOH). It was found that the $k_L a$ increased with the gas flow rate increasing and decreased with the apparent viscosity of the liquid increasing. In the case of $\text{pH} < 7$, a marginal effect of pH on the gas-liquid mass transfer was observed, but when pH value was higher than 7, mass transfer was promoted with the increase of pH value. Via investigating the impact of pH on k_L and a , the variation of mass transfer at $\text{pH} > 7$ was attributed to the decomposition of the Xanthan molecular structure by the hydroxyl of NaOH.

Keywords: bubble swarms, xanthan gum solution, non-Newtonian fluids, pH, mass transfer.

Mass transfer between dispersed bubble swarms and continuous liquid phase is widely encountered in various biotechnological processes, such as food fermentation, sludge anaerobic digestion, and biological wastewater treatment [1]. Mass-transfer efficiency is decisive to those biological processes mentioned above [2]. Hence, in recent years, considerable research efforts have been devoted to the mass transfer of bubble swarms in Newtonian fluids. These studies mainly focus on the effect of different parameters on mass transfer, including gas flow rate

[3], temperature [4], bubble column diameter [5], density and loading [6], liquid properties [7-8], and geometrical characteristics of sparger design [9].

However, notably, the vast majority of the materials encountered in biological processes exhibit non-Newtonian characteristics [10]. Owing to complex rheological properties, the mass transfer of bubble swarms in those fluids is more intricate, which attracts the interest of many researchers. Gómez-Díaz *et al.* [11,12] have investigated gas-liquid mass transfer in shear-thinning fluids and analyzed the effect of the gas flow rate and solution concentration on mass transfer. They also proposed a correlation for predicting the interface area and gas hold up of bubble swarms rising in non-Newtonian fluids. Garcia-Ochoa [13] has investigated the mass transfer phenomenon of rising oxygen bubbles in xanthan gum solutions and proposed a mass-transfer correlation by introducing shear viscosity. Li *et al.* [14] have investigated the mass transfer of

Correspondence: S. Li, College of Energy and Environment and Liaoning Key Laboratory of Clean Energy, Shenyang Aerospace University, Shenyang, 110136, China.

E-mail: lishaobai1982@163.com

Paper received: 5 July, 2016

Paper revised: 12 September, 2016

Paper accepted: 26 September, 2016

<https://doi.org/10.2298/CICEQ160705046L>

carbon dioxide bubble swarms in three rheological fluids (Newtonian fluids, shear thinning fluids and viscoelastic fluids) and further developed a semi-theoretical model based on Higbie's penetration theory and Kolmogorov's theory of isotropic turbulence.

Despite all these studies, the available information about the gas liquid mass transfer in non-Newtonian fluids is still insufficient, especially, in more complex biological processes in which the liquid phase exhibits non-Newtonian behavior. pH is well known to be one of the most important parameters, which should be optimized to promote the product yield. Thus, HCl or NaOH aqueous solutions are usually added to the bioreactors and fermentors for neutralizing the generated bases or acids, by which the pH is maintained to an optimum biological value [15]. Although, the effect of pH on the gas liquid mass transfer is imperative in biological processes, marginal experimental data is observed in past studies.

Xanthan is a typical non-Newtonian fluid, and its apparent viscosity exhibits shear thinning behavior. Xanthan is utilized in many practical fields, for example being added into foods as thickener and employed as polymer-flooding agent for enhancing oil recovery [16]. In this study, the effect of pH on the gas-liquid mass transfer in a xanthan solution was experimentally investigated. The volumetric mass transfer coefficient and interfacial area were respectively determined using an oxygen probe and by the photographic method. The effects of pH, liquid concentration, and gas flow rate on the volumetric mass-transfer coefficient, interfacial area, and mass-transfer coefficient were systematically analyzed.

EXPERIMENTAL

Experimental apparatus and procedure

The experimental set-up (Figure 1) consisted of cylindrical Plexiglas tanks (with an internal diameter of 0.08 m and a height of 1 m) surrounded by a square duct (0.1 m×0.1 m×1 m). The square duct serves to eliminate optical distortions for visualization. Two orifices with a diameter of 2 mm were submerged in the liquid in the bottom section of the tanks: an oxygen inlet and a nitrogen inlet. Before the beginning of the experiment, the cylindrical plexiglas bubble column and its external rectangular plexiglas sink were first filled with Xanthan solution to 750 mm under the specific condition. Next, nitrogen was added into the bubble column for desorption of oxygen from the liquid phase. Meanwhile, the concentration of oxygen in liquids was measured using a calibrated oxygen sensor (FC-100: ASR Co., Ltd.), which was located at 500 mm above

the nozzle. Because of the disturbance of bubbles, the distribution of oxygen concentration becomes homogeneous within a few seconds, *i.e.*, the readings from the oxygen sensor can be considered as the actual oxygen concentration in the bulk liquids. The ventilated process of nitrogen was stopped when the readings of the oxygen sensor goes to zero. After standing for 30 min, the nitrogen inlet valve was switched off, and the oxygen inlet valve was opened and controlled by a calibrated rotameter. The dissolved oxygen concentration was recorded at 1 min intervals. The bubbles were determined using a high-speed camera with a resolution of 500×1728 pixels. On these obtained images, at least 60 well-defined bubbles were used to calculate the Sauter mean diameter of bubbles and specific interfacial area at different conditions. A self-written program was operated on Matlab 6.0 to obtain the necessary geometric characteristics of the bubbles. In this experiment, the selected gas flow rate was 10, 15, 20 and 25 L/h, and the selected pH values were 3, 4, 5, 6, 7, 8, 9, 10 and 11. All experiments were conducted at room temperature under constant pressure.

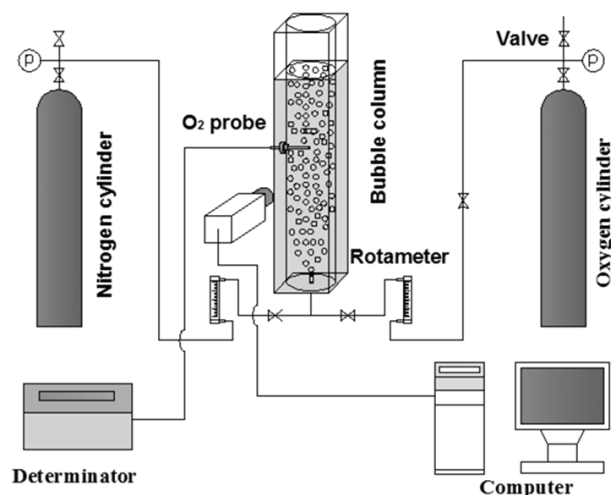


Figure 1. Schematic representation of experimental apparatus.

Materials

In this study, different concentrations of xanthan solutions (0.2, 0.4, 0.6, 0.8 and 1.0 wt.%) were used as experimental liquids. Analytical-purity xanthan (analytical purity, type KX-F supplied by Tianjin Kermel Chemical Reagent Co. (Tianjin, China)) and double-distilled deionized water were used in the experiments. The experimental liquid density was measured using a balance hydrometer. Rheology properties were measured using a Brookfield viscometer (Brookfield, DV-III, USA) with a shear rate ranging from 0.1 to 1000 s⁻¹. As can be seen in Figure 2, all of the xanthan solutions exhibit shear thinning behavior. The variation of the

apparent viscosity of xanthan solutions is well represented by the power-law model [17]:

$$\mu = K\gamma^{n-1} \quad (1)$$

where K is the consistency index, and n is the flow index.

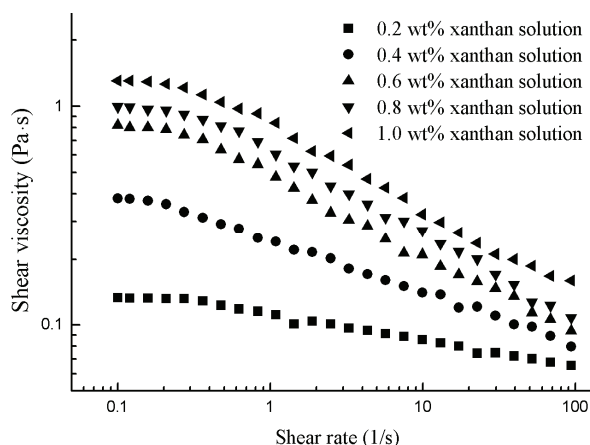


Figure 2. Variation of the viscosity of the different fluids used in the present study.

Table 1 summarizes the liquid physical properties.

Table 1. Rheological and physical properties of experimental fluids

Fluid, xanthan content, wt. %	$K / \text{Pa}\cdot\text{s}^n$	n	$\rho / \text{kg m}^{-3}$
0.2	0.13	0.88	996.32
0.4	0.25	0.77	997.65
0.6	0.51	0.67	1006.44
0.8	0.64	0.63	1008.24
1.0	0.85	0.59	1010.43

RESULTS AND DISCUSSION

In the mass-transfer process, the experimental data of oxygen concentration obtained in the bulk of the liquid phase increases with time increasing until the liquid phase is saturated. Based on mass balance, the liquid phase volumetric mass transfer coefficient ($k_L a$) can be defined as follows:

$$\frac{dC}{dt} = k_L a (C^* - C) \quad (2)$$

here, $k_L a$ represents the volumetric liquid-side mass transfer coefficient, and C^* and C represent the solubility and instantaneous oxygen concentration, respectively. Integrating Eq. (2), Eq. (3) is obtained:

$$\ln\left(\frac{C^*}{C^* - C}\right) = k_L a t \quad (3)$$

Using the experimental data of instantaneous oxygen concentration at different times, $k_L a$ is calculated by linear regressions. Figure 3 shows the effect of the gas flow rate and xanthan concentration upon the mass transfer of oxygen to the liquid phase at pH 7, representing the effect based on $k_L a$. As can be observed from Figure 3, $k_L a$ increases with the increase of flow rate and the decrease the xanthan concentration. Similar results have been obtained using different non-Newtonian fluids in the liquid phase in previous studies [14,18,19]. The effect of the gas flow rate could be attributed to the enhancement of the liquid turbulence and enlargement of the interfacial area. Figure 2 shows the rheological curve of Xanthan solutions, where the apparent viscosity of Xanthan solutions increases with increasing concentration. The study of Alvarez *et al.* [20] has revealed that viscosity increases the resistance of mass transfer and decreases the turbulence of liquids. Thus, $k_L a$ decreases with increasing concentration of the xanthan solution, as shown in Figure 3. Accordingly, $k_L a$ is not sensitive to the gas flow rate in highly viscous liquids, which may be attributed to the coalescence of bubbles in highly viscous liquid at high gas flow rate. The coalescence of bubbles increases the size of the bubbles, which results in the decrease of the residence time, the gas holdup and $k_L a$, and ultimately offsets the increase of mass transfer by increasing the gas flow rate [12].

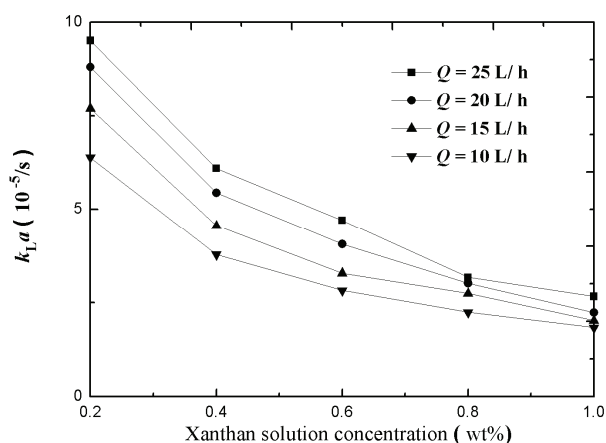


Figure 3. Influence of xanthan solution concentration and gas flow rate on $k_L a$.

Figure 4 shows the variation of $k_L a$ with pH at $Q = 20 \text{ L/h}$. At $\text{pH} < 7$, it can be seen from Figure 4 that no apparent change of $k_L a$ can be found with the regulation of pH. Thus, it seems that HCl exerts almost no effect on the gas-liquid mass transfer in xanthan solutions. On the other hand, $k_L a$ clearly increases with increasing pH value at $\text{pH} > 7$ as shown in Figure 4, and the increasing trend is further enhanced as the

concentration increases, indicating that addition of NaOH solution can promote the gas-liquid mass transfer in Xanthan solutions and this effect increases with solution concentration.

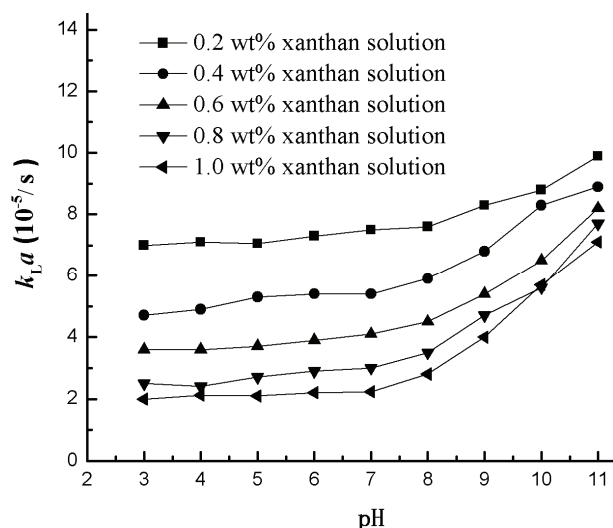


Figure 4. Influence of pH on $k_L a$ at $Q = 20$ L/h for different concentration xanthan solution.

Although $k_L a$ is more general for dealing with the mass transfer of bubble swarms in a two-phase flow, it only reflects the effect of operation conditions upon the gas-liquid mass transfer and cannot explain the related influence mechanism. $k_L a$ is the combination of the mass transfer coefficient (k_L) and interfacial area (a). Thus, it is necessary to separately consider the values of k_L and a to obtain more information about the effect of pH on global mass transfer. However, it is very difficult to acquire the value of a in industry. In this study, the bubble column is fabricated with Plexiglas, and the liquid phase is transparent. Hence, information of the bubble size could be obtained from the methodology developed by Ferreira *et al.* [21].

The bubbles rising in the Xanthan solution are ellipsoidal. Hence, major (d_h) and minor (d_v) axes of the projected ellipsoid (in two dimensions) were determined. The diameter of the equivalent sphere was taken as the representative bubble dimension:

$$d = \sqrt[3]{d_h^2 d_v} \quad (4)$$

As the bubble swarms freely rise through liquids, the distribution of the bubble size is well represented by the Sauter mean diameter (d_{32}), expressed as follows:

$$d_{32} = \frac{\sum_i (n_i d_i^3)}{\sum_i (n_i d_i^2)} \quad (5)$$

here, n_i is the number of bubbles, which have the same equivalent diameter (d_i).

The gas hold up values was obtained by visual observation [22]. In this case, the total gas holdup, ϕ is defined as follows:

$$\phi = \frac{H - H_L}{H} \quad (6)$$

where H_L is the clear liquid height, and H is the liquid dispersion height attributed to the presence of bubble swarms. The results represent the average values of five repeated experiments under same conditions, and experimental data were reproducible to within $\pm 5\%$.

The specific interfacial area, a , can be obtained from ϕ and d_{32} as follows [23]:

$$a = \frac{6\phi}{d_{32}(1-\phi)} \quad (7)$$

Figure 5 shows the bubbles size distribution under different gas flow rate at pH 7, based on the diameter of the equivalent sphere. It can be observed from Figure 5 that the bubble size has a normal distribution, and the degree of bubble size dispersion increases with the gas flow rate elevated due to the increase of bubble-coalescing frequency at high gas flow rate.

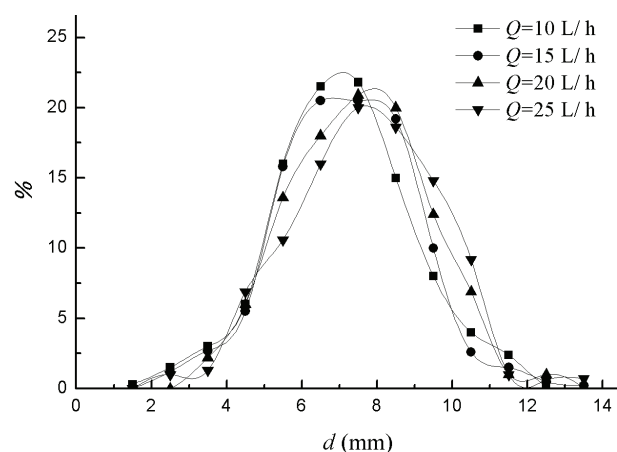


Figure 5. The bubbles size distribution under different gas flow rate for pH 7.

Figure 6 shows the effect of pH and the xanthan solution concentration on the specific interfacial area (a) at $Q = 20$ L/h. As shown in Figure 6 the specific interfacial increases with the decreased concentration of xanthan solution. Similar results were reported in the studies conducted by Gómez-Díaz *et al.* [12] and Li *et al.* [14]. Gómez-Díaz *et al.* [12] have attributed the decrease to the difficulty for the bubble to ascend in the high-viscosity liquid phase and produce the increment

of bubble size, followed by a clear decrease of the specific interfacial area. Li *et al.* [14] have proposed that the rheological property of liquid phase significantly affects the specific interfacial area. According to Li *et al.* [24], when bubbles rise in shear-thinning fluids, even two bubbles with a specifically long distance, the shear-thinning effect caused by the passage of the leading bubble can provide a reduced local viscosity, resulting in the decrease in the drag force opposing the trailing bubble. Namely, two bubbles coalescing in non-Newtonian fluids is an accelerating process as compared to that in Newtonian fluids. Typically, large bubbles have a short residence time and small specific surface area, which consequently causes decrease on the specific interfacial area with the increased concentration of xanthan solution. From Figure 6, a increases with increasing pH at pH > 7 but remains constant at pH < 7. The variation is assumed to be related to the change on the xanthan molecular structure. In fact, bases react with the acetyl group of xanthan molecules and decrease the viscosity of xanthan solution [25]. The rheological property of 0.6 wt.% xanthan solution at different pH was measured in order to evidence the hypothesis above, and the results are shown in Table 2. Notably, K decreases and n increases with increasing pH at pH > 7 but both K and n remain approximately constant at pH ≤ 7. According to the study by Weissenborn *et al.* [26], there is no difference expected between acid and alkali on a , as no significant differences on liquid properties are observed. Their results are consistent with those in our study at pH < 7, in which the xanthan molecular structure is not destroyed by HCl. This is consistent with the variation of bubble size distributions with three different pH values in 0.6 wt.% xanthan solution and at $Q = 20$ L/h (Figure 7). The experimental data plotted in Figure 7 indicate that there is not a clear influence of the pH values upon the bubbles size distribution for pH 3 and 7, but smaller bubbles are observed for pH 10.

$k_L a$ is composed of the mass transfer coefficient (k_L) and the interfacial area (a). Once the information of the specific interfacial area (a) could be calculated, the mass-transfer coefficient (k_L) can be obtained from the production of $k_L a$ divided by a . Figure 8 shows the effect of pH on the mass-transfer coefficient (k_L) for xanthan solutions of different concentrations. From Figure 8, the variation of k_L is basically the same as that of $k_L a$. At pH < 7, no significant change of k_L can be noticed in the range of experiments. Nevertheless, k_L increases with the increased pH at pH > 7, and the higher concentration of xanthan solutions, the larger of the increase trend, which could be attributed to the variation of the xan-

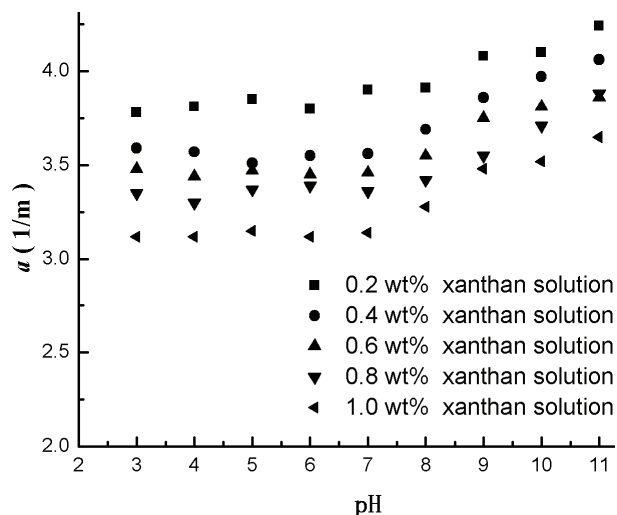


Figure 6. Influence of pH upon gas-liquid specific interfacial area ($Q = 20$ L/h).

Table 2. Rheological property of 0.6 wt.% xanthan solution at different pH

pH	K / Pa·s ^{<i>n</i>}	n
3	0.51	0.65
5	0.52	0.69
7	0.51	0.68
9	0.38	0.74
11	0.24	0.88

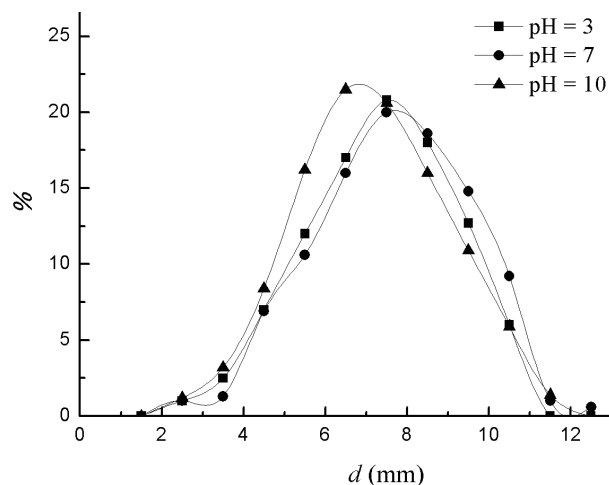


Figure 7. The bubble size distributions with three different pH values in 0.6 wt.% xanthan solution and at $Q = 20$ L/h.

than solution caused by the addition of acids and bases. According to the result in Table 2, HCl marginally affects the rheological property of Xanthan solutions, which indicates that HCl will not destroy the molecular structure of xanthan. However, the rheological property of the xanthan solutions decreases because of the destruction of the Xanthan molecular structure by NaOH, resulting in the decrease of appa-

rent viscosity. Xanthan monomer is a molecule consisting of D-glucose, D-mannose, D-glucuronic acid, pyruvic acid and acetyl. Therefore, acetyl has a significant effect on the spatial conformation of xanthan molecule, thus affecting the xanthan solution rheology [27]. Abundant studies have demonstrated that sodium hydroxide could remove the acetyl group of xanthan molecules. The reaction mechanism is as follows [28]:

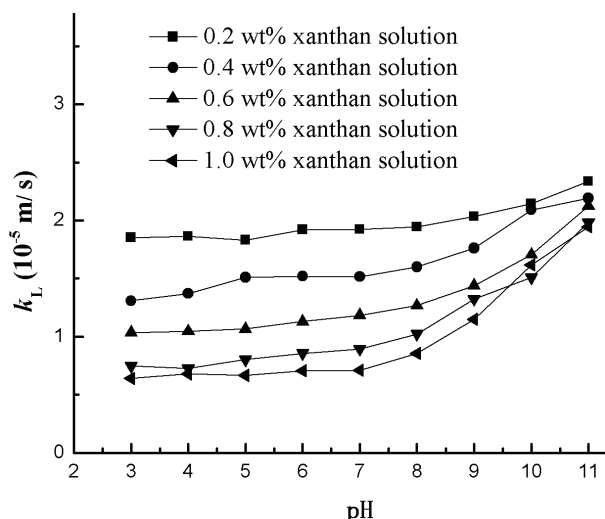
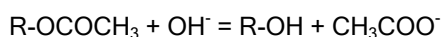


Figure 8. Influence of pH on the gas-liquid mass transfer coefficient.

As the amount of sodium hydroxide increasing, the acetyl group content on xanthan molecules decreased, which lead to the decrease of rheological property and apparent viscosity. As reported by Alvarez *et al.* [20], the decrease of apparent viscosity is able to cause the increase of k_L . Ferreira *et al.* [29] have investigated the effect of pH on the oxygen mass-transfer coefficient in distilled water and found that k_L exhibits higher values in solutions with $\text{pH} < 7$ and $\text{pH} > 7$ as compared with those in distilled water, which is different from the result obtained herein. According to the study of Ferreira, the variation of k_L in different pH systems is attributed to the bubble surface contamination. However, in our study, the high-viscosity Xanthan solution was used as the liquid phase. Similar to the work of Tzounakos [30], a competition between the molecules of carboxymethyl cellulose (CMC) and surfactant molecules exists on the bubble surface: CMC allows less surfactant molecules to reach the bubble surface. Thus, no discernible effect by the acid is revealed on k_L and a without breaking xanthan molecular structure, the phenomenon can be attributed to the preventing electrolyte molecule from accumulating on the bubble

surface by xanthan molecules. Thus, the variation of k_L in the system used by Ferreira *et al.* does not exist in the xanthan solution.

CONCLUSIONS

The mass transfer from oxygen bubble swarms in the xanthan solutions was investigated at different pH values, in order to analyze the effect of pH on the gas-liquid mass transfer in non-Newtonian fluids. The results obtained show that HCl has a marginal effect on mass transfer, but NaOH has a significant influence, which can be related to the increase of k_L and a . The variation of the liquid-phase mass transfer coefficient (k_L) and a are possibly related to the viscosity of the liquid phase. At $\text{pH} < 7$, no significant change on the rheological property was observed, indicating that HCl does not destroy the structure of the Xanthan molecule. Nevertheless, at $\text{pH} > 7$, the rheological property of the xanthan solutions changed because of the destruction of the xanthan molecular structure by base, resulting in the decrease of apparent viscosity. The study of the effect of pH on the gas-liquid mass transfer could provide essential information to the optimization of biological processes.

Acknowledgements

The Project supported by the National Natural Science Foundation of China (Grant No. 21406141), the Scientific Research Starting Foundation for Doctors of Liaoning Province, China (Grant No. 20141078), the Research Foundation of Education Bureau of Liaoning Province, China (Grant No. L2014060)

Nomenclature

a	specific interfacial area (m^2/m^3)
C	concentration of oxygen in liquid (mol/L)
C^*	saturation concentration of oxygen in liquid (mol/L)
a_{32}	Sauter mean diameter (m)
H	height of gas-free liquid (m)
H_L	height of the gas-liquid dispersion (m)
K	consistency index in a power-law model ($\text{Pa}\cdot\text{s}^n$)
k_L	liquid-side mass transfer coefficient (m/s)
n	flow index in a power-law model
Q	volumetric gas flow rate (L/h)
t	Time (s)
ϕ	gas hold up
γ	shear rate (1/s)
μ	viscosity of liquid phase ($\text{Pa}\cdot\text{s}$)
ρ	liquid phase density (kg/m^3)

REFERENCES

- [1] R.P. Chhabra, Bubbles, drops, and particles in non-Newtonian fluids, CRC, Taylor & Francis, New York, 2007, p. 2
- [2] J.Y. Jing, J. Feng, W.Y. Li, *Asia-Pac. J. Chem. Eng.* **4** (2009) 618-623
- [3] L.K. Ishkintana, C.P.J. Bennington, *Can. J. Chem. Eng.* **88** (2010) 322-328
- [4] A. Ferreira, C. Ferreira, J.A. Teixeira, F. Rocha, *Chem. Eng. J.* **162** (2010) 743-752
- [5] X. Su, P.D. Hol, S.M. Talcott, A.K. Staudt, T.J. Heindel, *Chem. Eng. Sci.* **61** (2006) 3098-3104
- [6] P. Mena, A. Ferreira, J. A. Teixeira, F. Rocha, *Chem. Eng. Process.* **50** (2011) 181-188
- [7] X. Li, C. Zhu, *Chem. Ind. Chem. Eng. Q.* **22** (2015) 85-93
- [8] V. Sivasubramanian, *Asia-Pac. J. Chem. Eng.* **5** (2010) 361-368
- [9] N.A. Kazakis, A.A. Mouza, S.V. Paras, *Chem. Eng. J.* **137** (2008) 265-281
- [10] R.P. Chhabra, J.F. Richardson, *Fluid Dyn. Res.* **5** (1999) 147-158
- [11] D. Gómez-Díaz, J. M. Navaza, *Chem. Eng. Technol.* **26** (2003) 1068-1073
- [12] D. Gómez-Díaz, J.M. Navaza, L.C. Quintáns-Riveiro, *Chem. Eng. J.* **146** (2009) 16-21
- [13] F. Garcia-Ochoa, E. Gomez, *Chem. Eng. Sci.* **59** (2004) 2489-2501
- [14] S. Li, C. Zhu, T. Fu, Y. Ma, *Int. J. Heat Mass Transfer.* **55** (2012) 6010-6016
- [15] S.Y. Lee, Y.P. Tsui, *Chem. Eng. Prog.* **95** (1999) 23-49
- [16] B. Katzbauer, *Polym. Degrad. Stab.* **59** (1998) 81-84
- [17] W.R. Schowalter, *AIChE J.* **6** (1960) 24-28
- [18] A. Tecante, L. Choplin, *Can. J. Chem. Eng.* **71** (1993) 859-865
- [19] G. Diego, J.M. Navaza, *J. Chem. Technol. Biotechnol.* **79** (2004) 1105-1112
- [20] E. Álvarez, B. Sanjurjo, A. Cancela, J.M. Navaza, *Chem. Eng. Res. Des.* **78** (2000) 889-893
- [21] A. Ferreira, G. Pereira, J.A. Teixeira, F. Rocha, *Chem. Eng. J.* **180** (2012) 216-228
- [22] A.D. Anastasiou, A.D. Passos, A.A. Mouza, *Chem. Eng. Sci.* **98** (2013) 331-338
- [23] P.H. Calderbank, M.B. Moo-Young, *Chem. Eng. Sci.* **16** (1961) 39-54
- [24] H.Z. Li, *Chem. Eng. Sci.* **54** (1999) 2247-2254
- [25] F. García-Ochoa, V.E. Santos, J.A. Casas, E. Gómez, *Biotechnol. Adv.* **18** (2000) 549-57
- [26] P.K. Weissenborn, R.J. Pugh, *J. Colloid Interface Sci.* **184** (1996) 550-563
- [27] F. García-Ochoa, V.E. Santos, J.A. Casas, E. Gómez, *Biotechnol. Adv.* **18** (2000) 549-579
- [28] F. Callet, M. Milas, M. Rinaudo, *Int. J. Biol. Macromol.* **9** (1987) 291-293
- [29] A. Ferreira, P. Cardoso, J.A. Teixeira, F. Rocha, *Chem. Eng. Sci.* **100** (2013) 145-152
- [30] A. Tzounakos, D.G. Karamanev, A. Argyrios Margaritis, M.A. Bergougnou, *Ind. Eng. Chem. Res.* **43** (2004) 5790-5795.

SHAOBAI LI
JUNGENG FAN
SHUANG XU
RUNDONG LI
JINGDE LUAN

College of Energy and Environment
and Liaoning Key Laboratory of Clean
Energy, Shenyang Aerospace
University, Shenyang, China

NAUČNI RAD

UTICAJ pH NA PRENOS MASE GAS-TEČNOST U NENJUTNOVSKIM FLUIDIMA

U ovom radu je eksperimentalno istraživana uticaj pH na prenos mase kiseonika u disperziji gasnih mehurova u nenjutnovskim fluidima. Istraživani su zapreminski koeficijent prenosa mase u tečnoj fazi ($k_L a$), koeficijent prenosa mase u tečnoj fazi (k_L) i specifična međufazna površina (a). pH je podešavana dodatkom hlorovodonične kiseline ili natrijum hidroksida. Utvrđeno je da se $k_L a$ povećava sa povećanjem protoka gasa a smanjuje sa povećanjem prividne viskoznosti tečnosti. Za $pH < 7$, uticaj pH na prenos mase gas-tečnost je zanemarljiv. A kada je $pH > 7$, prenos mase se ubrzava sa povećanjem pH vrednosti. Istraživanje uticaja pH na k_L i a utvrđeno je da je promena prenosa mase pri $pH > 7$ uzrokovana razgradnji molekulske strukture ksantana hidroksilnim jonima.

Ključne reči: barbotaza mehura, rastvor ksantana, nenjutnovski fluidi, pH, prenos mase.

BOJANA Ž. BAJIĆ
DAMJAN G. VUČUROVIĆ
SINIŠA N. DODIĆ
ZORANA Z. RONČEVIĆ
JOVANA A. GRAHOVAC
JELENA M. DODIĆ

University of Novi Sad, Faculty of
Technology, Department of
Biotechnology and Pharmaceutical
Engineering, Bulevar cara Lazara
1, Novi Sad 21000, Serbia

SCIENTIFIC PAPER

UDC 664.3:628.3.034.2:547.815:60:66

THE BIOTECHNOLOGICAL PRODUCTION OF XANTHAN ON VEGETABLE OIL INDUSTRY WASTEWATERS. PART I: MODELLING AND OPTIMIZATION

Article Highlights

- Optimization of xanthan production media based on the vegetable oil industry wastewaters
- The response surface method was used for the optimization of xanthan production
- The experimental values are in excellent agreement with the predicted values for modelled responses

Abstract

*The aim of this research was to examine the possibility of using the vegetable oil industry wastewater as the basis of the cultivation media for xanthan production, using *Xanthomonas campestris* ATCC 13951, in order to reuse the wastewater obtained in one industry as a raw material in another. Furthermore, the aim was to optimize the composition of wastewater based media in terms of carbon, nitrogen, and phosphorus content. Experiments were carried out in accordance with the Box-Behnken design with three factors on three levels (glucose: 10.00–30.00 g/L; nitrogen: 0.02–0.20 g/L; phosphorus: 0.0045–0.045 g/L) and three repetitions at the central point. The success of biosynthesis was assessed by analysing broths to determine xanthan yield, cultivation broth apparent viscosity, residual carbon, nitrogen, and phosphorus content. Graphical and numerical optimization using response surface methodology was performed to determine the optimal content values of the carbon source, nitrogen, and phosphorus content. The results of graphical optimization suggest that for the defined response interval values, the defined model predicts that the xanthan production is possible when 15.00–16.00 g/L of the carbon source, 0.02–0.09 g/L of nitrogen and 0.01–0.02 g/L of phosphorus are added to the media that as a basis contains vegetable oil industry wastewater.*

Keywords: biotechnological production, cultivation media, wastewaters, RSM, xanthan biosynthesis.

Xanthan is a complex exopolysaccharide produced by the plant-pathogenic bacterium *Xanthomonas campestris* pv. *campestris* [1]. It has a wide range of applications, especially in the food industry due to its various beneficial properties, including

emulsion stabilization, temperature stability, compatibility with food ingredients, and its pseudoplasticity. Additionally, it is widely used in the pharmaceutical, cosmetic, agricultural, and petroleum industry [2]. Due to its increasing use in the aforementioned industries, the world market of xanthan is expected to rise significantly in the next decade and reach the value of 987.7 million US dollars by the year 2020, according to the report of the Grand View Research Inc.

Polysaccharides derived from plants or synthetic polymers are used instead of xanthan in various industrial branches due to its relatively high price. Therefore, using cheaper raw materials instead of glucose or

Correspondence: B.Ž. Bajić, Department of Biotechnology and Pharmaceutical Engineering, Faculty of Technology, University of Novi Sad, Bulevar cara Lazara 1, 21000 Novi Sad, Serbia.

E-mail: baj@uns.ac.rs

Paper received: 30 April, 2016

Paper revised: 22 September, 2016

Paper accepted: 29 September, 2016

<https://doi.org/10.2298/CICEQ160430048B>

sucrose, which are common carbon sources, can reduce the price of the final product [3,4]. Based on various scientific papers published in the current literature it can be observed that xanthan production is possible using food industry and agricultural waste effluents as a basis for cultivation media, and several bacterial strains that belong to the genus *Xanthomonas*, in most cases the species of *Xanthomonas campestris*. Several waste effluents, such as molasses [4-6], date fruit waste [7,8], cheese whey [9,10], tapioca pulp [11], potato residues [12,13], sugar beet pulp [3], citrus waste [14], acid-hydrolyzed wastes from melon, watermelon, cucumber and tomato [15], chestnut flour [16], ram horns [17], sugar cane broth [18], cassava starch [19,20] were successfully used for its production. Additionally, wastewaters of the food industry are used instead of expensive synthetic cultivation media [21]. Potential raw material sources for xanthan production come from all food industries, which produce large amounts of wastewaters rich in compounds necessary for microorganism growth and multiplication. Furthermore, our previous research showed that, among others, vegetable oil industry wastewaters can be used as a substrate for biotechnological xanthan production [22,23].

Most of these studies confirmed the possibility of using various wastewaters and emphasized the need for optimizing the composition of the media based on them. This is particularly important considering the fact that wastewaters obtained from different food processing industries will necessarily have different characteristics and compositions. Defining the appropriate composition of cultivation media is one of the crucial factors for the growth of the microorganism and the production of xanthan. The optimized cultivation media, which is based on food processing industry wastewater, will ensure an uninterrupted metabolism of the production microorganism and consequently the highest yield and quality of the obtained biopolymer. Therefore, choosing an appropriate experimental design in order to optimize cultivation media composition would be a step towards obtaining a higher product yield. In a large number of experimental design methods, response surface methodology (RSM) has been comprehensively applied for its minimal amount of experiments required and effective process optimization. Additionally, this statistical method utilizes quantitative data in order to determine and simultaneously resolve multivariate equations. RSM is a statistical technique based on the essential principles of statistics, which aim to execute experimental planning, to build empirical models, and to evaluate the effect of independent variables on the desired variable response [24-26]. This method has been

applied in the optimization of medium composition and other critical variables which have an influence on the production of biopolymers such as curdlan gum, xanthan gum, gellan gum, welan gum, pullulan, dextran, levan etc. [27].

Therefore, the aim of this study is the numerical and graphical optimization of the macronutrients in the cultivation media based on vegetable oil industry for the xanthan production, by using the RSM approach. Mathematical relationships were used to describe the obtained responses and the developed models were applied to find an optimal cultivation media composition. The obtained optimization results will represent a basis for increasing the scale and efficiency of this biotechnological process.

EXPERIMENTAL

Production microorganism

As a production microorganism, the referent culture *Xanthomonas campestris* ATCC 13951, was used for experiments. The inoculum was prepared in two steps - first, by refreshing the culture by incubation for 24 h, at 26 °C, on yeast maltose (YM[®], Difco) agar slants, and second, by double passaging of the microorganism on the synthetic YM[®] (Difco) media for 36 h, at 26 °C. Samples were spontaneously aerated and externally stirred (laboratory shaker, 150 rpm).

Cultivation media

In accordance with the defined aim of the research and applied experimental plan, 15 cultivation media based on vegetable oil industry wastewater were prepared. Wastewater obtained from vegetable oil industry located in Vojvodina were first analysed to determine its composition significant for the biotechnological production. Initial total nitrogen content was 0.018 g/L, total phosphorus was 0.0037 g/L, COD value was 7240 mg/L, BOD value was 3200 mg/L and the obtained wastewater did not contain any digestible sugars. Based on the obtained results, all cultivation media were enriched with glucose as the carbon source, yeast extract and (NH₄)₂SO₄ as the nitrogen source (in 2:1 ratio), while K₂HPO₄ was added as the phosphorus source. The amounts of aforementioned nutrients are defined by the experimental plan. All cultivation media were additionally enriched with 0.05% of MgSO₄·7H₂O. The pH value of the cultivation media was set to 7.0 and sterilized in an autoclave at 121 °C and overpressure of 1.1 bar during 20 min.

Cultivation

The biotechnological process of xanthan production was carried out under the same experimental con-

ditions in 15 erlenmeyer flasks, containing one-third of the volume, of the wastewater based media. The inoculation was performed with 10 vol.% of the inoculum. A rotational laboratory shaker at 150 rpm was used for aeration and stirring of cultivation media. Cultivation was performed at a temperature of 26 °C for the first 48 h, after which it was increased to 30 °C and kept at this value until the end of the process, which lasted for 96 h [32].

Analytical methods

At the end of the process, samples of the cultivation broths were analysed. Rheological properties of the cultivation broth samples were determined using a rotational viscometer (REOTEST 2 VEB MLV Prüfgeräte-Verk, Mendingen, SitzFreitel), with a double gap coaxial cylinder sensor system, spindle N. Rheological parameters were calculated according to the Ostwald de Vaele equation.

The samples of the cultivation broth were centrifuged at 10,000 rpm for 30 min (Hettich Rotina 380R, Germany) and the obtained supernatants were used to determine residual carbon content. The supernatants were filtered through a 0.45 µm nylon membrane (Agilent Technologies, Germany) and then analyzed by HPLC (Thermo Scientific Dionex UltiMate 3000series). The HPLC instrument was equipped with a HPG-3200SD/RS pump, WPS-3000(T)SL autosampler (10 µL injection loop), ZORBAX NH2 column (250 mm×4.6 mm, 5 µm) and a RefractoMax520 detector. 75 vol.% acetonitrile was used as the eluent at a flow rate of 1.2 mL/min and an elution time of 20 min at a column temperature of 25 °C.

In order to determine residual nitrogen and phosphorus content, prior to centrifugation (10,000 rpm, 30 min) the obtained cultivation broths were diluted with 4 volumes of the distilled water. From the obtained supernatants the residual nitrogen content was determined by the Kjeldahl method [28], and a standard method was used to determine the residual phosphorus content [29].

Product separation

Xanthan was recovered by precipitation with 96 vol.% ethanol in the presence of KCl as the electrolyte. Ethanol was gradually added to the supernatant at 15 °C until the alcohol content in the mixture was 60%, at constant stirring. A saturated solution of KCl was added when half of the necessary ethanol amount was poured into the supernatant in a quantity to obtain a final content of 1 vol.%. After precipitation, the mixture of xanthan was kept at 4 °C, for 24 h and then centrifuged (4000 rpm, 15 min). The precipitate was dried

to a constant mass at 60 °C and this data was used to calculate the xanthan yield.

Statistics and data analysis

Response surface methodology (RSM) is a collection of mathematical and statistical techniques for empirical model building. By careful design of experiments, the objective is to optimize responses (output variables: Y_1, Y_2, \dots, Y_n) which are influenced by several experimental factors or independent variables (input variables: X_1, X_2, \dots, X_k). Optimization by Box-Behnken design under RSM vividly underscores interactions between variables and their effects. Box-Behnken design is rotatable second-order designs based on three-level incomplete factorial designs, and has been used for the optimization of several processes by a significant number of researchers. A total of 15 experiments is needed for the three-level three-factorial Box-Behnken experimental design [30,31]. The experimental factors and their values (g/L) are: X_1 - carbon source content (10.00-30.00), X_2 - nitrogen content (0.02-0.20); and X_3 - phosphorus content (0.0045-0.045). For the description of the responses a second-degree polynomial model was fitted to data:

$$Y_i = b_0 + b_1X_1 + b_2X_2 + b_3X_3 + b_{11}X_1^2 + b_{22}X_2^2 + b_{33}X_3^2 + b_{12}X_1X_2 + b_{13}X_1X_3 + b_{23}X_2X_3$$

where b_0 represents the intercept, b_i represents the linear, b_{ii} the quadratic and b_{ij} represents the interaction effect of the examined factors. Selected responses are xanthan yield (Y_1), cultivation media apparent viscosity (Y_2), residual carbon content (Y_3), residual nitrogen content (Y_4) and residual phosphorus content (Y_5).

Experimental data were subjected to statistical analysis using software Statistica 9.0 (StatSoft, USA). Response surface curves were plotted with a constant value of one of the parameters, while remaining two parameters were varied. The obtained data was analyzed using the software package Design Expert 8.1 (StatEase, Inc., USA) and the method of desirability function was applied for numerical and graphical optimization and determination of optimal values of examined parameters.

RESULTS AND DISCUSSION

In accordance with the defined aim and experimental plan of this research, the media for xanthan biosynthesis were defined with vegetable oil industry wastewater as the basis. The values of varied experimental factors and their responses as well as the calculated value of the xanthan conversion are shown in Table 1. Carbon source, nitrogen, and phosphorus

Table 1. Combinations of experimental factors and obtained response values after completed biosynthesis of xanthan

Experimental factors			Responses					Conversion ^a %
X ₁	X ₂	X ₃	Y ₁	Y ₂	Y ₃	Y ₄	Y ₅	
C source content, g/L	N content g/L	P content g/L	Xanthan yield g/L	Apparent viscosity, mPa s	Residual C g/L	Residual N g/L	Residual P g/L	
10.00	0.02	0.025	8.26	34.41	0.852	0.007	0.009	82.59
30.00	0.02	0.025	15.25	64.04	14.060	0.009	0.011	50.83
10.00	0.20	0.025	8.81	25.18	0.775	0.011	0.008	88.14
30.00	0.20	0.025	16.17	65.87	15.865	0.017	0.010	53.90
10.00	0.11	0.0045	8.19	29.12	0.801	0.014	0.001	81.88
30.00	0.11	0.0045	15.63	64.20	14.962	0.014	0.002	52.10
10.00	0.11	0.045	9.51	23.87	0.870	0.008	0.015	95.10
30.00	0.11	0.045	14.94	59.92	15.865	0.013	0.017	49.80
20.00	0.02	0.0045	14.81	46.77	6.514	0.014	0.002	74.07
20.00	0.20	0.0045	11.08	49.22	7.030	0.025	0.002	55.39
20.00	0.02	0.045	12.33	48.16	6.901	0.008	0.015	61.63
20.00	0.20	0.045	13.12	41.34	6.385	0.022	0.014	65.59
20.00	0.11	0.025	13.93	43.00	8.314	0.010	0.010	69.66
20.00	0.11	0.025	14.59	42.56	8.903	0.009	0.011	72.97
20.00	0.11	0.025	14.85	42.65	9.124	0.010	0.011	74.23

^aConversion [%] = 100(P/S₀); P - xanthan yield (g/L); S₀ - initial C source content (g/L)

contents were chosen as experimental factors because they represent macronutrients that are essential for the biosynthesis of xanthan as well as for the metabolism of production microorganism. The success of the performed biosynthesis was determined by the xanthan yield and the apparent viscosity of the cultivation media, while the residual carbon, nitrogen, and phosphorus contents indicate the economic and ecological efficiency of the process.

The obtained values of xanthan yield ranges from 8.19 to 16.17 g/L and the highest values are achieved with 30.00 g/L of initial glucose content. Moreover, when using the highest examined initial amount of glucose, the xanthan conversion is the lowest and ranges between 49.80-53.90%, but according to the available literature data [32] the xanthan conversion is between 50-85%, and the obtained values are in this range. When using 10.00 g/L of carbon source, conversion is between 81.88-95.10%, while when using 20.00 g/L of glucose, conversion values are lower (54.38-68.85%). Additionally, based on the obtained results it can be seen that the conversion value decreases with increasing of the initial carbon content. It is evident that no matter how much carbon source is added to the cultivation media, xanthan yield approximately reaches the maximal value of 15 g/l. It is evident that when using this experimental conditions and cultivation media composition, the aforementioned amount of produced xanthan changes the rheology of the system and decreases the rate of oxygen mass

transfer that is necessary for xanthan biosynthesis as well as for metabolism of the production strain. The absence of sufficient amount of dissolved oxygen inhibits further biosynthesis as well as consumption of carbon source in the media, which affects high residual carbon content in media and consequently decrease of the conversion value [40]. The obtained results indicate that vegetable oil industry wastewaters can be used as a basis for cultivation media for xanthan production, due to the absence of inhibitory substances that would endanger *Xanthomonas campestris* metabolism.

All the obtained cultivation broths showed a pseudoplastic type of flow, which is characteristic of the xanthan solutions [2] and the rheological parameters (data not shown), consistency factor (obtained values are in the range between 0.2008 and 0.8452 Pa·sⁿ) and flow behaviour index (obtained values are in the range between 0.4878 and 0.5725) were used for calculating the apparent viscosity of cultivation media.

In industrial systems, when the amount of residual carbon content is lower than 5 g/L xanthan biosynthesis is considered as finished. Based on these results, it can be concluded that when using the highest examined glucose content (30.00 g/L), the process is economically and ecologically inefficient. Based on the obtained results it can be concluded that, compared to initial media nitrogen contents, nitrogen content was significantly reduced in all experiments (50.00-94-50%), while the amount of residual nitrogen is slightly higher than the nitrogen content of the util-

ized wastewater only in the experiments in which the amount of added nitrogen was highest. Phosphorus content is also significantly reduced compared to the initial content in the cultivation media (46.68–68.10%). In addition to producing a high-value product, significant environmental benefits can be achieved throughout the minimization of the residual nutrients, especially nitrogen and phosphorus, which increase the organic load of the process effluents and must be treated before being discharged into the environment. Additionally, the unutilized nutrients that remain in the cultivation broth represent an economical wastage and a problem during product separation and purification.

Statistical analysis of experimental results

By applying RSM, it is possible to design experiments, build models, search for optimal conditions for desirable responses and evaluate the interaction of factors that may influence process efficiency with a reduced number of experiments [33]. The response surface method was selected for the optimization and fitting of results of xanthan production using vegetable

oil industry wastewater as a basis of the cultivation media. For responses obtained after experiments, a second degree polynomial model was established to evaluate and quantify the influence of the variables. Table 2 shows the results of the statistical analyses, while Table 3 shows the ANOVA results for selected responses.

The results were statistically processed by analysing the variance at the significance level of $\alpha = 0.05$ (confidence interval 95%). The coefficient of determination (R^2) and the model p -value were used to estimate the adequacy of the model. The significance of each coefficient in the obtained second-degree polynomial model is determined by the p -value and statistically significant coefficients ($p < 0.05$) are marked in Table 2.

For the xanthan yield response, the coefficient of determination was 0.972 which points to a high correlation between observed and predicted values. The most significant effects are the linear and squared effect for the initial carbon source content as well as the interaction effect of nitrogen and phosphorus

Table 2. Regression equation coefficients for selected responses; C - coefficient; * - effect significant at $p < 0.05$ confidence level

Coefficient	Response									
	Y_1		Y_2		Y_3		Y_4		Y_5	
	Xanthan yield, g/L		Apparent viscosity, mPa s		Residual C, g/L		Residual N, g/L		Residual P, g/L	
	C	p -value	C	p -value	C	p -value	C	p -value	C	p -value
Intercept										
b_0	-0.076	0.976	25.999*	0.0001	-6.726*	0.0038	0.0138	0.0815	-0.0263	0.1860
Linear										
b_1	1.011*	0.003	0.891*	0.0025	0.530*	0.0036	0.0006	0.2658	0.0018	0.2303
b_2	1.670	0.920	-137.6*	0.0002	26.782*	0.0290	-0.0668	0.1772	0.1961	0.1491
b_3	8.322	0.289	-1.185	0.8524	11.007*	0.0376	-0.079*	0.008	0.4675*	0.0003
Quadratic										
b_{11}	-0.016*	0.014	0.013*	0.0168	0.003	0.3134	-0.0000	0.1650	-0.0000	0.2190
b_{22}	-96.724	0.121	415.87*	0.0002	-142.5*	0.0044	0.3909*	0.0377	-0.8963	0.0633
b_{33}	-20.475	0.102	5.903	0.5329	-22.36*	0.0113	0.1071*	0.0115	-0.331*	0.0067
Interaction										
b_{12}	0.101	0.830	3.072*	0.0005	0.523	0.0908	0.0011	0.3985	0.0004	0.9008
b_{13}	-0.247	0.269	0.120	0.5150	0.102	0.4001	0.0006	0.2993	0.0024	0.1571
b_{23}	62.482*	0.037	-127.5*	0.0011	-14.000	0.3083	0.0401	0.5305	-0.1970	0.2754

Table 3. Analysis of variance (ANOVA) of the modelled responses; DF - degrees of freedom; SS - sum of squares; MS - mean square

Response	Residual			Model			F	p -value	R^2
	DF	SS	MS	DF	SS	MS			
Y_1	5	3.253	0.6506	10	2555.42	255.54	392.8060	0.000001	0.972
Y_2	5	2.41	0.483	10	33501.32	3350.132	6940.800	0.000000001	0.999
Y_3	5	1.013	0.2026	10	1338.540	133.8540	660.7866	0.0000004	0.998
Y_4	5	0.000023	0.000005	10	0.002792	0.000279	59.41991	0.000146	0.939
Y_5	5	0.000172	0.000034	10	0.169177	0.016918	491.7948	0.000001	0.995

(Table 2). These effects will be described in more details later on.

Viscosity, including apparent viscosity, depends on the amount of xanthan in the cultivation broth, molecular weight and structures formed between the biopolymer molecules, which all are influenced by the basic nutrient contents, among other parameters [34]. The most significant effects on apparent viscosity of cultivation media are the linear and squared effect for the initial carbon source and nitrogen content, as well as the effects of interaction between the carbon source and nitrogen and between nitrogen and phosphorus content.

During xanthan biosynthesis, the carbon source is used both for the cell growth and for the production of xanthan, for which the presence of suitable phosphorus and nitrogen sources are necessary and is of great importance [35]. Therefore, it is expected that residual carbon content response is affected by initial contents of these nutrients (linear effects of carbon source, nitrogen and phosphorus and squared effect of initial nitrogen and phosphorus). This very clearly indicates that carbon source consumption can be managed by limiting nitrogen and phosphorus contents, or the ratio of these nutrients.

The significant effects on the response for residual nitrogen content is the linear and squared effect of initial phosphorus and the squared effect of initial nitrogen content, while for residual phosphorus response the most significant is the linear and squared effect of initial phosphorus content, which indicates that these nutrients are important for the production microorganism metabolism in the initial phases of cultivation.

Values of the coefficient of determination, for all the obtained responses, are high and have a value close to 1.00 and indicate a good fit of experimental data to the second degree polynomial equation. Only for the value of the response for residual nitrogen content is somewhat lower (0.939). The model F -values for xanthan yield (Y_1), cultivation media apparent viscosity (Y_2), residual carbon content (Y_3), residual nitrogen content (Y_4) and residual phosphorus content (Y_5) imply that models for selected responses are significant. Additionally, comparisons between experimental and predicted values for the obtained responses are graphically showed in Figure 1.

Mathematical model for xanthan yield

Statistical analysis and graphical analysis of the data were performed using Statistica 9.0 software (StatSoft, USA). Plotting responses for xanthan yield as a function of two factors drew response surface plots, while the third factor had the mean value from the

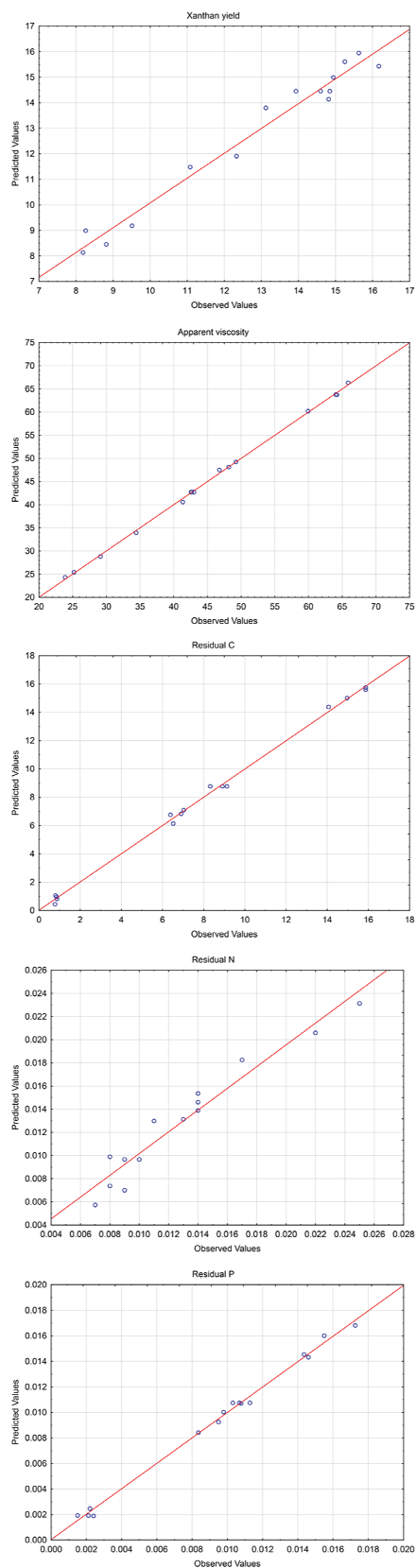


Figure 1. Comparison of experimentally obtained data for selected responses (xanthan yield, apparent viscosity of cultivation broths, residual carbon, residual nitrogen and residual phosphorus) and the values predicted by the models.

selected range. Figure 2 presents the effect of initial carbon source, nitrogen and phosphorus content on xanthan yield.

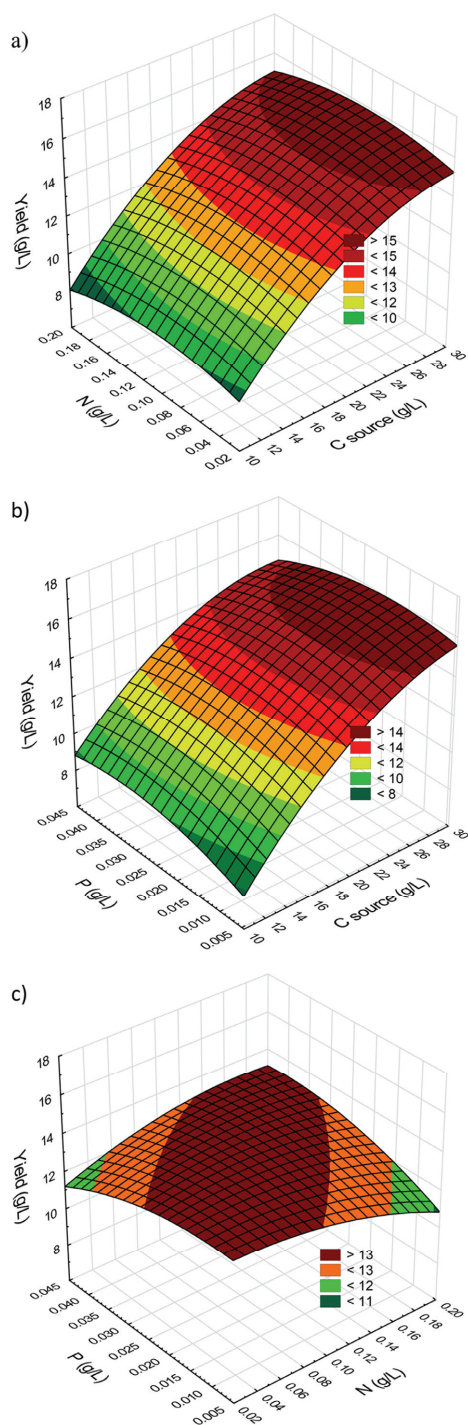


Figure 2. Xanthan yield value as a function of two variables at constant value of third: a - phosphorus content (0.025 g/L) b - nitrogen content (0.11 g/L); c - carbon source content (20.00 g/L).

The response surface shown in Figure 2a undoubtedly shows that at the phosphorus content of

0.025 g/L, the initial nitrogen content in examined range has very low effect on xanthan yield, while the effect of the carbon source content (10.00-30.00 g/L) is clear, and increasing the carbon source content in the xanthan production media increases the yield of the desired product. Additionally, the most significant effects are the linear ($p=0.003$) and squared ($p=0.014$) effect for the initial carbon source content, confirming that the concentration of carbon source affects the xanthan yield [36]. These results are in agreement with previously reported findings in the literature [37] showing that the carbon source had a more positive effect on xanthan yield than the nitrogen source. The response surface shows that the maximum yield of xanthan (15.00-16.00 g/L) is obtained at a carbon source concentration above 26.00 g/L, for all applied initial nitrogen content. Therefore, a high concentration ratio of carbon source to the limiting nutrient, which can be nitrogen, phosphorus, or sulphur positively influence xanthan biosynthesis and when the nitrogen is used as the limiting nutrient, a high C/N ratio is required to stimulate xanthan production [38].

Figure 2b shows that the effect on xanthan yield of initial carbon source and phosphorus contents at a constant value of nitrogen content (0.11 g/L) is similar to the effect of initial carbon source and nitrogen content at a constant value of phosphorus content (Figure 2a). From the response surface, it can be seen that maximum xanthan yield (15.00-16.00 g/L) is obtained at carbon concentrations higher than 26.00 g/L, in the entire range of applied phosphorus concentration, but somewhat higher yield values (about 16.00 g/L) can be observed when using lower amounts of initial phosphorus (0.01-0.03 g/L). The graph shows that at constant nitrogen content, changing phosphorus content does not significantly affect xanthan yield. Moreover, at constant phosphorus content, changing carbon source content significantly affects xanthan yield in the entire examined range.

The effect of initial nitrogen and phosphorus contents on the obtained xanthan yield during biosynthesis at carbon source content of 20.00 g/L is shown on Figure 2c, as predicted by the model. The interaction effect of nitrogen and phosphorus contents has a statistically significant effect ($p=0.036$) on xanthan yield and their positive interaction (Table 2) indicates their synergistic effect. The lower values of xanthan yield (about 10.00 g/L) were obtained at the highest used phosphorus content (about 0.040-0.045 g/L) and the lowest used nitrogen content (<0.04 g/L), as well as at the lowest used phosphorus content (<0.015 g/L) and the highest used nitrogen content (about 0.18-0.20 g/L). Figure 2c also shows that the maximum xanthan

yield (about 13 g/L) was obtained when the cultivation media contained the uniform ratio of nitrogen and phosphorus in the entire examined ranges. Based on the obtained results and in the applied experimental conditions it can be concluded that ratio of the nitrogen and phosphorus content in the cultivation media containing wastewater from vegetable oil industry, in order to achieve highest possible xanthan yield, needs to be approximately 4 to 1 (N:P = 4:1).

Optimization of cultivation medium for xanthan production

This research used the desirability function method in order to obtain the optimum composition of cultivation media that is based on vegetable oil industry wastewater for the production of the biopolymer xanthan. The final goal of the application of the response surface method is process optimization, so the developed models are used for simulation and optimization. This method consists of converting individual responses into individual desirability functions whose values range from 0 to 1. The overall desirability function is equal to the geometric average of individual desirability functions, and its validity is assessed using the aforementioned method. The desirability method is recommended due to its simplicity, availability in the software and provides flexibility in weighting and giving importance for individual response [39].

In order to determine the optimal content of carbon, nitrogen and phosphorus in media based on vegetable oil industry wastewater that is necessary for unimpeded xanthan production, the specific intervals for requested response values were set. The defined interval for xanthan yield ranged between 12.00 and 16.17 g/L, considering that all the values that are lower than these are not justified for downstream processing. The defined interval for cultivation media apparent viscosity is 23.87–65.87 mPa·s, which represents the entire obtained range. The residual carbon interval

values were set to 0.78–5.00 g/L, because 5.00 g/L is the amount that represents the critical amount for xanthan biosynthesis in industrial systems. Also, the defined ranges for residual nitrogen and residual phosphorus ranged between 0.0070–0.01 g/L and 0.0015–0.01 g/L, respectively, in order to decrease the initial amounts of nitrogen and phosphorus used for the experiments.

The usual numerical optimization method produced a large number of combinations of varied parameters for which the total desirability function was 1.000, and Table 4 shows 10 selected solutions.

For the requested optimization conditions, using the applied method, the software assesses correct values for all factors/responses relevant to optimization (Table 4). Based on the obtained results it can be seen that the optimized amount of carbon source content is between 14.31 and 14.99 g/L, except for one value of 16.27 g/L, the optimized amount of initial phosphorus content is equal in all optimization combinations, and is 0.02 g/L, and the optimized amounts of initial nitrogen contents are very different and ranges between 0.02–0.14 g/L. In production conditions on the industrial scale it is impossible to achieve experimental factor values (contents of carbon source, nitrogen and phosphorus) exactly as assessed by the optimization process which would, together with the maximum total desirability function value, enable an ideal prediction of response values (xanthan yield, apparent viscosity of cultivation media, residual carbon, residual nitrogen and residual phosphorus). Thereby it is necessary to assess intervals of experimental factor values for which the assessed response values will be acceptable. These intervals of experimental factor values, which represent the optimal condition, can be visualized graphically by superimposing the contours for the various response surfaces in an overlay plot [33]. Therefore, Figure 3 shows overlay plots of the selected responses

Table 4. Selected optimization results: estimated values; desirability function, $D = 1$; P content = 0.02 g/L

Solution	C source content, g/L	N content, g/L	Xanthan yield, g/L	Apparent viscosity mPa s	Residual C, g/L	Residual N, g/L	Residual P, g/L
1	14.73	0.04	12.05	37.83	4.40	0.0077	0.0089
2	14.78	0.03	12.03	38.72	4.17	0.0086	0.0078
3	16.27	0.02	12.52	42.11	4.90	0.0082	0.0091
4	14.80	0.14	12.11	33.38	5.00	0.0100	0.0099
5	14.99	0.03	12.06	39.32	4.30	0.0079	0.0088
6	14.48	0.12	12.00	33.34	4.87	0.0091	0.0094
7	14.31	0.10	12.00	33.67	4.76	0.0081	0.0095
8	14.68	0.13	12.03	33.46	4.95	0.0098	0.0094
9	14.74	0.13	12.06	33.52	4.99	0.0099	0.0094
10	14.39	0.11	12.01	33.52	4.82	0.0086	0.0093

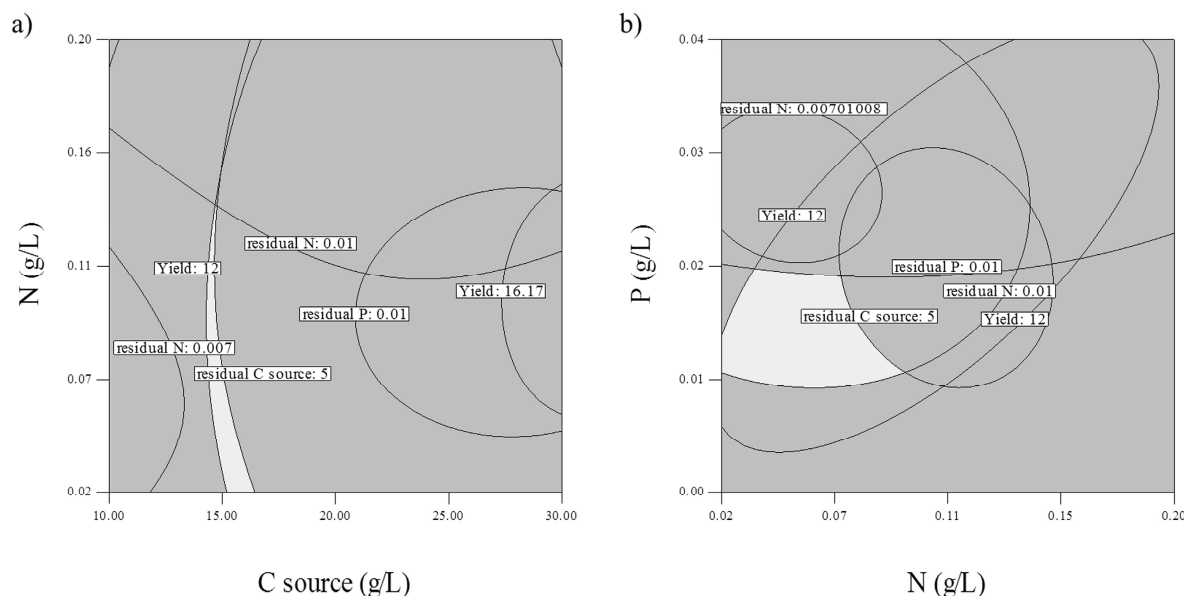


Figure 3. Overlay plots for selected responses as a function of: (a) carbon source and nitrogen content with constant value of initial phosphorus content (0.02 g/L); (b) nitrogen and phosphorus contents with constant value of initial carbon source content (15.00 g/L).

(xanthan yield, apparent viscosity of cultivation media, residual carbon, residual nitrogen and residual phosphorus content) as a function of carbon source and nitrogen content in the examined ranges and with constant initial phosphorus content value of 0.02 g/L (a), as well as nitrogen and phosphorus contents in the examined ranges, and with constant initial carbon source content value of 15.00 g/L (b).

The light grey fields represent the ranges of varied parameters (experimental factors) in which all the requested conditions were satisfied. Dark grey fields on the other hand, represent the ranges of parameters where one or more of the requested conditions weren't satisfied.

Overlay plot presented in Figure 3a shows that at initial phosphorus content of 0.02 g/L, xanthan production is possible when 15.00–16.00 g/L of carbon and 0.02–0.11 g/L of nitrogen were added to the cultivation media based on vegetable oil industry wastewater. Then it is possible to obtain yields of around 12.00 g/L of xanthan with residual carbon and nitrogen of 5.00 and 0.01 g/L, respectively. The obtained results are in accordance with previously published data [7, 17] which showed that low nitrogen content has a positive effect on xanthan production. If the cultivation media based on vegetable oil industry wastewater is initially enriched with 15.00 g/L, according to the overlay plot shown on Figure 3b it can be seen that nitrogen and phosphorus which are necessary to be added range from 0.02–0.09 g/L and 0.01–0.02 g/L, respectively. In this case, maximum xanthan yield is obtained (12.00

g/L) with residual carbon, nitrogen and phosphorus values of around 5.00, 0.01 and 0.01 g/L, respectively.

Validation of the model

In order to validate the developed models, three confirmation experiments were carried out using the average experimental factor values (carbon source 15.5 g/L, nitrogen content 0.065 g/L and phosphorus content 0.0145 g/L) of the obtained optimal cultivation media composition range. For the actual responses, the calculated average results of three measurements, for xanthan yield, apparent viscosity of cultivation media, residual carbon, residual nitrogen and residual phosphorus were 12.06 ± 0.19 g/L, 38.32 ± 2.08 mPa·s, 3.87 ± 0.27 g/L, 0.015 ± 0.002 g/L and 0.009 ± 0.001 g/L, respectively. The values predicted with developed models for xanthan yield, apparent viscosity of cultivation media, residual carbon, residual nitrogen and residual phosphorus were 11.79 g/L, 38.67 mPa·s, 3.953 g/L, 0.016 g/L and 0.008 g/L, respectively. Based on the obtained results, it can be seen that experimental values are in excellent agreement with the predicted values for all modelled responses.

CONCLUSION

The obtained results proved that the Box-Behnken experimental design and response surface methodology represent an efficient approach for optimization of cultivation media based on vegetable oil industry wastewater, in terms of carbon source, nitrogen and phosphorus content, for the production of xanthan. The

values predicted by the developed models for xanthan yield, apparent viscosity of cultivation media, residual carbon, residual nitrogen and residual phosphorus were 11.79 g/L, 38.67 mPa·s, 3.953 g/L, 0.016 g/L and 0.008 g/L, respectively, when using the initial values of the carbon source (15.5 g/L), nitrogen (0.065 g/L) and phosphorus (0.0145 g/L) contents. Using the same initial values of experimental factors, experimentally obtained values for xanthan yield, apparent viscosity of cultivation media, residual carbon, residual nitrogen and residual phosphorus were 12.06 ± 0.19 g/L, 38.32 ± 2.08 mPa·s, 3.87 ± 0.27 g/L, 0.015 ± 0.002 /L and 0.009 ± 0.001 g/L, respectively, which validates the developed models. Additionally, the obtained results indicate that vegetable oil industry wastewaters have a lot of potential for the efficient production of cost-effective xanthan. Further research should consist of optimizing process parameters in order to increase yield and quality of xanthan, as well as defining the kinetics and kinetic parameters as an important step towards industrializing this biotechnological process.

REFERENCES

- [1] A. Becker, F. Katzen, A. Puhler, L. Ielpi, *Appl. Microbiol. Biotechnol.* **50** (1998) 145-152
- [2] F. Garcia-Ochoa, V.E. Santos, J.A. Casas, E. Gomez, *Biotechnol. Adv.* **18** (2000) 549-579
- [3] S.D. Yoo, S.W. Harcum, *Bioresour. Technol.* **70** (1999) 105-109
- [4] S.L. Gilani, G.D. Najafpour, H.D. Heydarzadeh, H. Zare, *Chem. Ind. Chem. Eng. Q.* **17** (2011) 179-187
- [5] S. Kalogiannis, G. Iakovidou, M. Liakopoulou-Kyriakides, D.A. Kyriakidis, G.N. Skaracis, *Process Biochem.* **39** (2003) 249-256
- [6] M. Moosavi-Nasab, S. Pashangeh, M. Rafsanjani, *World Acad Sci Eng Technol.* **68** (2010) 1234-1237
- [7] S. Moshaf, Z. Hamidi-Esfahani, M.H. Azizi, *World Acad. Sci. Eng. Technol.* **5** (2011) 471-474
- [8] M. Moosavi-Nasab, F. Shekaripour, M. Alipoor, *Iran Agric. Res.* **27** (2008) 89-98
- [9] M.F. Silva, R.C.G. Fornari, M.A. Mazutti, D. Oliveira, F.F. Padilha, A.J. Cichoski, R.L. Cansian, M.D. Luccio, H. Treichel, *J. Food Eng.* **90** (2009) 119-112
- [10] S.L. Gilani, H.D. Heydarzadeh, N. Mokhtarian, A. Alemian, M. Kolaei, *Aust. J. Basic Appl. Sci.* **5** (2011) 855-859
- [11] V. Gunasekar, K.R. Reshma, G. Treesa, D. Gowdhaman, V. Ponnusami, *Carbohydr. Polym.* **102** (2014) 669-673
- [12] R. Vidhyalakshmi, C. Vallinachiyar, R. Radhika, *Waste. J. Adv. Sci. Res.* **3** (2012) 56-59
- [13] D. Bilanovic, F.H. Chang, P. Isobaev, P. Welle, *Biomass Bioenergy* **35** (2011) 2683-2689
- [14] M. Green, G. Shelef, D. Bilanovic, *Chem. Eng. J.* **56** (1994) B37-B41
- [15] J. Moreno, M.J. Lopez, C. Vargas-Garcia, R. Vazquez, *J. Ind. Microbiol. Biotechnol.* **21** (1998) 242-246
- [16] M. Liakopoulou-Kyriakides, S.K. Psomas, D.A. Kyriakidis, *Appl. Biochem. Biotechnol.* **82** (1999) 175-183
- [17] E.B. Kurbanoglu, N.I. Kurbanoglu, *Process Biochem.* **42** (2007) 1146-1149
- [18] S.Faria, C.L.O. Petkowicz, S.A.L. Morais, M.G.H. Terrores, M.M. Resende, F.P. Franca, V.L. Cardoso, *Carbohydr. Polym.* **86** (2011) 469-476
- [19] P. Kerdsup, S. Tantratian, R. Sanguandeeikul, C. Imjongjirak, *Food Bioprocess Technol.* **4** (2011) 1459-1462
- [20] Q. Li, W. Yan, K. Yang, Y. Wen, J. Tang, *Afr. J. Biotechnol.* **11** (2012) 13809-13813
- [21] M.J. Lopez, J. Moreno, A. Ramos-Cormenzana, *J. Appl. Microbiol.* **90** (2001) 829-835
- [22] J. Dodić, J. Grahovac, A. Jokić, B. Bajić, S. Dodić, D. Vučurović, S. Popov, *Analecta Technica Szegediensia* (2012) 41-46.
- [23] B. Bajić, J. Dodić, Z. Rončević, J. Grahovac, S. Dodić, D. Vučurović, I. Tadijan, *Anal. Tech. Szegediensia* **8** (2014) 13-17
- [24] G.E.P. Box, K.B. Wilson, *J. R. Stat. Soc., B* **13** (1951) 1-45
- [25] D.B. Goncalves, J.A. Teixeira, D.M.S. Bazzolli, M.V. De Queiroz, E.F. de Araujo, *Biocatal. Agric. Biotechnol.* **1** (2012) 140-146
- [26] M. Esfahanian, M. Nikzad, G. Najafpour, A.A. Ghoreyshi, *Chem. Ind. Chem. Eng. Q.* **19** (2013) 241-252
- [27] S.M. Rafigha, A.V. Yazdia, M. Vossoughib, A.A. Safekordia, M. Ardjmand, *Int. J. Biol. Macromol.* **70** (2014) 463-473
- [28] K. Herlich, *Official Methods of Analysis of the Association of Official Analytical Chemists*, fifth ed., Association of Official Analytical Chemists, Arlington, 1990, p 758
- [29] M.E.J. Gales, E.C. Julian, R.C. Kroner, *J. Am. Water Works Assess.* **58** (1966) 1363-1368
- [30] S.L.C. Ferreira, R.E. Bruns, H.S. Ferreira, G.D. Matos, J.M. David, J.M. Brandao, E.G.P. da Silva, L.A. Portugal, P.S. Reis, A.S. Souza, W.N.L. Santos, *Anal. Chim. Acta* **597** (2007) 179-186
- [31] V.K. Sangal, V. Kumar, I.M. Mishra, *Chem. Ind. Chem. Eng. Q.* **19** (2013) 107-119
- [32] S. Rosalam, R. England, *Enzyme Microb. Technol.* **39** (2006) 197-207
- [33] A.L. Ahmad, S.S. Wong, T.T. Teng, A. Zuhairi, *J. Hazard. Mater.* **145** (2007) 162-168
- [34] M.I. Tait, I.W. Sutherland, C. Sturman, *J. Gen. Microbiol.* **132** (1986) 1483-1492
- [35] P. Souw, A.L. Demain, *Appl. Environ. Microbiol.* **37** (1979) 1186-1192
- [36] A. Palaniraj, V. Jayaraman, *J. Food Eng.* **106** (2011) 1-12
- [37] R. B. Salah, K. Chaari, S. Besbes, N. Ktari, C. Blecker, C. Deroanne, H. Attia, *Food Chem.* **121** (2010) 627-633.
- [38] Y.M. Lo, S.T. Yang, D.B. Min, *Appl. Microbiol. Biotechnol.* **47** (1997) 689-694
- [39] R.H. Myers, D.C. Montgomery, *Response surface methodology- process and product optimization using designed experiment*, John Wiley & Sons, New York, 1995
- [40] F. Garcia-Ochoa, E. Gomez Castro, V.E. Santos, *Enzyme Microb. Technol.* **27** (2000) 680-690.

BOJANA Ž. BAJIĆ
DAMJAN G. VUČUROVIĆ
SINIŠA N. DODIĆ
ZORANA Z. RONČEVIĆ
JOVANA A. GRAHOVAC
JELENA M. DODIĆ

Univerzitet u Novom Sadu,
Tehnološki fakultet Novi Sad,
Katedra za biotehnologiju i
farmaceutsko inženjerstvo, Bulevar
cara Lazara 1, 21000 Novi Sad,
Srbija

NAUČNI RAD

BIOTEHNOLOŠKA PROIZVODNJA KSANTANA NA OTPADNOJ VODI IZ PROIZVODNJE JESTIVOG ULJA. DEO I: MODELOVANJE I OPTIMIZACIJA

*Cilj ovog rada je utvrđivanje mogućnosti primene otpadne vode iz proizvodnje jestivog ulja kao osnove kultivacionog medijuma za proizvodnju ksantana, primenom *Xanthomonas campestris* ATCC 13951, kako bi se otpadna voda iz jedne grane industrije upotrebila kao sirovina u drugoj. Takođe, cilj je i optimizacija sastava medijuma čija je osnova otpadna voda u pogledu sadržaja ugljenika, azota i fosfora. Eksperimenti su izvedeni u skladu sa Box-Behnken eksperimentalnim planom sa tri faktora na tri nivoa (glukoza: 10,00-30,00 g/L; azot: 0,02-0,20 g/L; fosfor: 0,0045-0,045 g/L) i tri ponavljanja u centralnoj tački. Uspešnost biosinteze je procenjena na osnovu analize dobijenih kultivacionih tečnosti i određivanja količine ksantana, prividnog viskoziteta kultivacione tečnosti, kao i sadržaja rezidualnog ugljenika, azota i fosfora. Postupak odzivne površine je primenjen za određivanje vrednosti optimalnog sadržaja izvora ugljenika, azota i fosfora. Na osnovu rezultata grafičke optimizacije, za intervale zahtevanih vrednosti odziva, definisani model predviđa da je proizvodnja ksantana moguća kada se u kultivacioni medijum čija je osnova otpadna voda iz proizvodnje jestivog ulja doda 15,00-16,00 g/L izvora ugljenika, 0,02-0,09 g/L azota i 0,01-0,02 g/L fosfora.*

Ključne reči: biosinteza ksantana, biotehnoška proizvodnja, kultivacioni medijum, otpadne vode, RSM.

NILGÜN ERTAŞ

Department of Food Engineering,
Engineering & Architecture Faculty,
Necmettin Erbakan University,
Konya, 42060, Turkey

PROFESSIONAL PAPER

UDC 664.696.3(560):54:66

A COMPARISON OF INDUSTRIAL AND HOMEMADE BULGUR IN TURKEY IN TERMS OF PHYSICAL, CHEMICAL AND NUTRITIONAL PROPERTIES

Article Highlights

- Bulgur is a perfect food in terms of high nutritional value, keeping quality, healthy and low cost
- Bulgur is produced industrially and homemade in villages by farmers who grow durum wheat, in Turkey
- Depending on the applied process, physical, chemical and nutritional properties of bulgur can vary
- Dehulling process in industrial production causes the mineral elements to be thrown with the shell
- All bulgur samples contained lower amount of heavy metals as cadmium and lead than JECFA limits

Abstract

Determination of functional and nutritional properties of bulgur is of paramount importance for the growth of healthy generations. In this study, physical, chemical, nutritional and sensorial qualities of bulgur produced at the industrial, homemade and laboratory scale in Turkey were determined and the results were compared. The ash content of bulgur samples was determined between 1.04 and 1.81%, the total protein contents of the samples were found between 11.90 and 14.47%. Evaluation of nutritional status of bulgur; the total phenolic contents value varied 449.82 to 1047.09 µg/g, the phytic acid values were found between 422.14 and 1173.56 mg/100 g. The mineral contents of the samples were analyzed, and all the bulgur samples contained lower amounts of cadmium and lead than JECFA limits. Homemade bulgur samples had a more aromatic taste and smell than industrially produced bulgur samples, and also industrially produced bulgur samples had lighter color than homemade bulgur.

Keywords: bulgur, industrial producing, homemade, mineral, phytic acid, Turkey.

Bulgur is a semi-finished food product that is usually obtained by cleaning, cooking and drying under sunlight or in high drying towers, then pearling by friction, grinding and then sifting according to size of durum wheat (*Triticum durum*) [1,2]. It has been one of the most important food products of Turkish

people in Anatolia for over 3000 years. Mostly hard wheat, especially durum wheat, is preferred for bulgur production. Durum wheat is the hardest of all wheat varieties and used in making products such as pasta and bulgur due to its high protein, high gluten strength and uniform golden color.

The general composition of bulgur includes: 9-12% water, 10-16% protein, 1.2-1.5% fat, 76-78% carbohydrates, 1.2-1.4% ash and 1.1-1.3% fiber. Protein, calcium, iron, B1 vitamin and niacin contents of bulgur are higher from the cereal products like bread and pasta, and also protein, calcium and iron contents of bulgur are higher than wheat. Many nutrients leach out of wheat, but nutrients are absorbed back

Correspondence: Department of Food Engineering, Engineering and Architecture Faculty, Necmettin Erbakan University, Konya, 42060, Turkey.

E-mail: nilgunertas@gmail.com

Paper received: 12 January, 2016

Paper revised: 11 August, 2016

Paper accepted: 30 September, 2016

<https://doi.org/10.2298/CICEQ160112047E>

into the grain during the bulgur production. Losses of water-soluble nutrients like vitamins are prevented. Bulgur digestibility increases due to coagulated protein and gelatinized starch. The excess nitrogenous substances are caused by the hard structure of starch fused with protein. This is a desirable feature in bulgur because of resistance to insect, mites and microorganisms, and long shelf life [3-5]. Also, bulgur is a natural food because no chemicals or additives are used in processing.

Differences in the processing of bulgur and properties of wheat used in bulgur production are among factors that can affect the quality. Today, two types of bulgur production systems are used in Turkey: Antep type and Karaman (Mut) type production [6]. The Antep type bulgur production involves cleaning, cooking, drying, tempering, debranning and cracking in disc mill or hammer mill. The Karaman type bulgur production involves cleaning, cooking, drying, longer tempering of dried wheat, debranning, re-drying and milling process by stone mill. In Karaman, cooking and milling processes of bulgur vary from plant to plant. The most important difference is that the cooking process is done with steam and not with water. The main advantages of steam are higher degradation of phytic acid and higher absorption of nutrients. Due to the steam cooking process, more water absorption of bulgur occurs during cooking. In some companies, stone millers are used instead of metal millers, and companies argue that bulgur produced with stone mills is better tasting. In bulgur production, a modified color sorting system line is used due to the fact that color is an important visual quality parameter for bulgur [7]. In recent years, it has accelerated efforts to achieve yellow colored bulgur according to consumer demand [8]. Mechanical yellowing process (pearling of the wheat) is peeled more bran content than normal process and color materials are removed from bulgur. Pearling step is used in industrial production, while homemade production not contains this step. There are advantages like attractive bulgur color, as well as disadvantages like falling bulgur yields from 80-85% to 70-72%, increased labor cost, increased additionally machinery and building costs. But also this process has disadvantages for consumer like reduced nutrient absorption due to decrease the amount of cellulose and minerals that useful for the health of human body [9].

There are about 500 bulgur factories in Turkey and the current annual production capacity is 1,125,000 t in terms of production volume. Turkey took the top spot with 1,125,000 tons bulgur production and 500 bulgur factories in the year of 2005.

Today that number is expressed as 278 factories with 630,000 t capacity. But the decline in the number of factories has not led to the production decline. Despite the decline in the number of factories, findings also show increased production capacity in existing factories. With 300,000 tons of annual production and 20 bulgur factories, USA and Canada were in the second place while Middle East countries were in third place with 120,000 tons and 15 bulgur factories [10]. The main bulgur producers are in Gaziantep, Karaman, Çorum, Mardin and Urfa in Turkey. Although it is made from the same material (durum wheat), bulgur production is 2.5 times higher than production of pasta. The average annual consumption of bulgur is 12 kg per person [4,11].

In this study, industrially and homemade produced bulgur products in Turkey are collected from the market, and physical, chemical, nutritional and sensorial properties are compared to each other and with laboratory scale bulgur.

EXPERIMENTAL

Materials

In order to perform this study, fifteen samples of bulgur were analyzed, twelve bulgur samples from an industrial and four from homemade sources in Turkey. For comparison, laboratory scale bulgur sample was produced and investigated in this study as well. The total number of samples of this study was 34 with 2 replications. The wheat used to produce the laboratory bulgur sample was obtained from Selva Inc. All the collected samples were stored in a cool and dry place until they were analyzed.

Homemade bulgur samples were collected from villages. During the production of homemade bulgur, wheat was washed in cool water for removing the dust and soil particles and water was discarded, wheat was cooked with water (2 or 3 times the amount of wheat) until there is not any white area on cooked wheat, and spread on sheets for sun-drying in open air, bran of the wheat was removed by wooden hammers called dibek, after which the wheat was cracked in stone mills and stored in a cool and dry place.

According to industrial and homemade bulgur production in Turkey, the region of Central Anatolia, the cultivar of *Triticum durum L. cvs. C1252* and *Triticum durum Desf. cv. Kızıltan-91* are used, in the region of Southeast Anatolia, the varieties of Svevo (*Triticum durum Desf.*), burgos (*Triticum durum Desf.*) and zenit (*Triticum durum Desf.*) are mostly used in bulgur production.

Laboratory bulgur production

Laboratory bulgur samples were produced using Antep type bulgur method with some modifications. Wheat samples (2 kg, *Triticum durum L. cvs. C1252*) free from cracks, dust and other foreign materials were soaked in distilled water (1:5) for 5 h, and then cooked in the autoclave (Hirayama HV-50, Saitama, Japan) at 121 °C for 20 min with distilled water (1:2). Cooked wheat samples were dried at 50±5 °C to 10% moisture content in the oven (Nüve FN-500, Ankara, Turkey). The dried wheat seeds were tempered with 2% additional water by mixing for 10 min, and then milled into course grist with disk mill (Inovamer, Mersin, Turkey). All the cracked material was passed through a 3.55 mm sieve and over 1.6 mm sieve, and aspirated to remove bran material.

Physical attributes

Thousand kernel weights were obtained by weighting in grams of 1000 seeds, using an electronic balance weighting to 0.001 g accuracy. 1000 kernel volume values were determined using the water displacement method. Length, width and thickness values of wheat were measured using a digital caliper (0.01 mm precision, Mitutoyo 0.001mm, Japan). The sphericity $((\text{length} \times \text{width} \times \text{thickness})^{1/3} / \text{height})$ and diameter ratio (length/width) of wheat kernels were calculated. The color of the wheat kernels and bulgur samples were evaluated by measuring the L^* , a^* and b^* values using a Hunter Lab Color QUEST II Minolta CR-400 (Minolta Camera, Co., Ltd, Osaka, Japan). The hue angle ($\tan^{-1} b^* / a^*$) was calculated from a^* and b^* values.

Chemical and nutritional properties

Wheat and bulgur samples were analyzed in triplicate for their moisture (method 44-19), crude ash (method 08-01), crude protein (method 46-12), crude fat (method 30-25) using standard methods [12]. The mineral element contents of the samples were determined by inductively coupled plasma spectroscopy, ICP-AES (Vista series, Varian International AG, Switzerland) according to method by [13]. Total phenolic content (*TPC*) was determined using the Folin-Ciocalteu method [14] as modified by [15]. Total phenolic results were expressed as µg gallic acid equivalents per g sample. Phytic acid was determined by the method described by [16].

Sensory properties

Bulgur samples were boiled in water (1:2) at 100±2 °C. After all the boiling water was absorbed, 25 g bulgur sample was served to the panelists at approximately 40 °C in identical glass containers. Sensory

analyses of bulgur samples were conducted by twelve panelists. The attributes selected were: hardness, taste, chewiness, color and smell. Bulgur characteristics were rated on a 1-5 scale: 1 - dislike extremely; 3 - acceptable and 5 - like extremely.

Statistical analysis

JMP statistical package software program (version 5.0.1.a, SAS Institute. Inc. Cary, NC, USA) was used to perform statistical analyses. Tukey honestly significant difference test were performed to establish the significance of differences among samples. Significance was accepted at $p < 0.01$ throughout the analysis.

RESULTS AND DISCUSSION

Analytical results

The mean length, width and thickness values of wheat used in bulgur production on a laboratory scale were measured as 7.43, 3.15 and 2.81 mm. Sphericity and diameter ratio of wheat sample (*T. durum L. cvs. C1252*) were 4.04 and 2.37, respectively. 1000 kernel weight and 1000 kernel volume values of wheat which determine the marketing price were measured as 45.44 g and 70.0 ml, respectively. Similar results have been reported by some researchers [17,18]. L^* , a^* , b^* and hue angle values of wheat were 54.04, 5.26, 18.57, and 74.17, respectively. Some researchers reported that color values of durum wheat ranged between 45.55 to 49.15 in terms of L^* values, between 7.47 to 8.67 in terms of a^* values, between 16.34 to 17.50 in terms of b^* values [19].

Chemical bulgur properties

Table 1 shows the chemical and nutritional results obtained in this study. Those average values that resulted in significant differences at $p < 0.01$ as revealed by ANOVA analysis have been marked with an asterisk. Table 1 also shows the minimum and maximum values of chemical and nutritional components of bulgur produced at the industrial, homemade and laboratory scale. The mean moisture content of the industrial bulgur samples (11.5%) was higher than homemade bulgur (9.7%). The mean moisture content of the laboratory bulgur sample was 9.2%. The moisture content in bulgur is an important parameter for trade and storage. The amount of water in grain depends on the relative humidity and temperature of the storage place. According to the Turkish Food Codex Communiqué of bulgur, the maximum moisture content of bulgur should be as 13%. But moisture content of two bulgur samples (13.15 and 14.07%) produced industrially were higher than this

Table 1. Chemical and nutritional composition of industrially, homemade and laboratory scale manufactured bulgur samples; mean values were significantly different ($P < 0.01$) between homemade and industrial samples; LMB: laboratory made bulgur

Component	Industrial (I)				Homemade (H)				LMB	Contrast (I-H) diff.
	Mean	SD	Max	Min	Mean	SD	Max	Min		
Moisture (%)	11.5	1.51	14.1	9.2	9.7	2.82	11.9	5.9	9.2	1.77
Crude Ash (%)	1.25	0.19	1.60	1.04	1.49	0.21	1.81	1.33	1.69	-0.24
Crude Protein (%)	12.6	0.49	13.3	11.9	13.7	0.74	14.5	12.8	13.9	-1.10
Crude Fat (%)	1.01	0.26	1.76	0.78	1.02	0.07	1.12	0.96	1.75	0.01
Energy (kcal)	354.1	5.4	361.9	345.0	360.2	11.8	375.8	350.1	364.8	-6.15
Phytic acid (mg/100 g)	712.3	233.6	1153.9	422.1	994.9	132.7	1173.6	852.7	1533.8	-282.6
Total Phenolic Content ($\mu\text{g}/\text{kg}$)	662.9	173.1	968.0	449.8	828.1	173.8	1047.1	632.6	986.64	-165.2
Ca (mg/100 g)	24.7	3.64	30.9	20.1	40.9	6.4	49.5	34.6	56.8	-16.2
Fe (mg/100 g)	1.89	0.40	2.68	1.51	2.99	1.07	4.36	2.05	5.85	-1.11
K (mg/100 g)	363	24.7	400	328	378	25.2	406	346	473	-14.9
Mg (mg/100 g)	75.7	15.0	102.4	60.2	111.9	9.6	126.3	106.5	127	-36.3
Mn (mg/100 g)	1.36	0.45	2.51	0.89	1.98	0.52	2.29	1.20	5.7	-0.62
Na (mg/100 g)	52.2	6.65	59.6	40.7	48.9	2.41	51.4	46.7	65.83	3.23
P (mg/100 g)	284	40.5	382	250.9	345.6	48.7	412.2	295.1	407.2	-61.6
Zn (mg/100 g)	2.02	0.58	3.21	1.20	3.21	1.68	4.74	1.34	4.15	-1.19
Cu (mg/kg)	4.08	0.24	4.41	3.57	5.08	0.63	5.69	4.45	5.37	-1.00
Cd (mg/kg)	0.05	0.02	0.09	0.01	0.04	0.03	0.08	0.02	0.08	0.00
Pb (mg/kg)	0.09	0.11	0.31	0.00	0.00	0.00	0.00	0.00	0.02	0.09

level (13%). In Karaman type production, due to the tempering process of the cooked and dried wheat, and at the later stages without additional drying process, moisture problems can occur, which is the likely reason for the high moisture content. In a previous study, bulgur from five different companies was investigated and the total moisture contents of the bulgur samples were determined in the range of 11.1 to 13.4%, and the average moisture content of the bulgur was 12.4% [20]. The mean ash content in the analyzed bulgur samples produced industrially, homemade and laboratory scale was found as 1.25, 1.49 and 1.69%, respectively. The average ash contents found in bulgur were within the range of 0.86 to 1.80% described by some researchers [20-22]. The average values of ash contents were lower in the industrial bulgur samples than in homemade samples, because of the better separation of wheat bran from bulgur during bulgur production. The pearling step in industrial production allows more bran separation from the wheat compared to the homemade, because the de-branning step is not adequately performed in homemade bulgur production. Also, de-branning or pearling of wheat could not be adequately performed by laboratory scale bulgur production. Therefore, laboratory scale bulgur had high ash content. Protein content is expressed as a percentage of dry matter. Bulgur samples produced by industrial producers,

homemade and laboratory scale ranged between 11.9-13.3%, 12.8-14.5% and 13.9%, respectively. Similar results (14.72%) have been observed previously [21]. Homemade bulgur samples gave the highest protein content. Homemade bulgur is made with hard durum wheat with high protein content. Bulgur produced from different wheat varieties showed significant differences in the amount of protein in previous study [22]. These differences can result from factors such as areas where wheat is grown, the amount of fertilizer in the soil, and annual rainfall [23]. Furthermore, the average amount of protein content of bulgur samples produced by any method in Turkey gave higher values than the minimum level of protein in bulgur described by Communiqué of Bulgur (11%) [24]. The protein content of bulgur samples increased course granulation to fine, peeled shell to unpeeled shell, and also stated that removal of the aleurone layer by peeling reduces the amount of protein in other study [25]. Similar results were observed by previous researchers and they found that the protein content of barley ranged between 9.8-11.4%, in barley bulgur, protein content was constant throughout the bulgur process [26]. The fat contents showed levels in the order of 0.78-1.76%, 0.96-1.12% and 1.75% in those manufactured using industrial procedures, homemade and laboratory scale, respectively. The energy values, expressed as a kcal of dry matter,

were statistically similar, with values of around 345.0–361.9 kcal, 350.1–375.8 kcal and 364.8 kcal respectively, in the industrial, homemade and laboratory scale bulgur. The highest mean energy value was determined with bulgur produced as homemade.

Nutritional properties

According to ANOVA results, bulgur varieties as a variation source significantly affected the phytic acid values ($p < 0.01$). The phytic acid contents found in the bulgur were within the range of 422.1–1153.9 mg/100 g for the industrial bulgur samples, within the range of 852.7–1173.6 mg/100 g for homemade bulgur. The average content in phytic acid was higher in the samples of laboratory produced bulgur (1533.8 mg/100 g). This fact may be justified, probably, by high fiber content of un-separated wheat bran in laboratory and homemade bulgur production. In bulgur produced industrially, separation of wheat bran was efficient, which was proven with lower ash content. Some investigators studied bulgur samples and determined the phytic acid content of raw, cooked wheat and bulgur samples ranged between 872–1124 mg/100 g; 845–1126 mg/100 g; and 681–941 mg/100 g [27]. Phytic acid content decreased in the range of 18.9–33.9% during the bulgur production in another study [28]. In literature, decreases of phytic acid were explained by the phytic acid change in the aleurone layer, as well as the contamination of germ layer [26]. The 0.5 mm sieve material (düğürçük) of bulgur represents nutritional riches with significant ash, fat, cellulose and phytic acid content. When phytic acid and phytate breaks down, it indicates a significant mineral usefulness. On the other hand, phytic acid is an important functional food with its anticancer and antioxidant properties [29]. The mean values of total phenolic content (449.8–968.0 µg/g in the industrially produced and 632.6–1047.1 µg/g in homemade) were the same as those determined in bulgur samples [20]. These values were higher than those previously observed with wheat samples (50.1 to 56.2 mg gallic acid/100 g) by other authors [30]. From the results obtained in this study and from those previously reported, it can be deduced that compared to the wheat samples, bulgur samples gave high values of total phenolic content. As a result of thermal processes, cellulosic compounds and cell walls broken and thus bound form phenolic will remain free [31]. Some researchers stated that thermal effects lead to an increase in phenolic compounds [32]. Also, the color was highly significant for bran phenolic contents. In literature, the hue angle values and phenolic contents were negatively correlated [33]. In this study, similar negative

correlation was found with hue angle and total phenolic content. Therefore, homemade bulgur samples had lower hue angle values and gave higher total phenolic content than industrially produced bulgur. The calcium content of industrially produced, homemade and laboratory scale bulgur samples were varied between 20.1 to 30.9 mg/100 g, 34.6 to 49.5 mg/100 g and 56.8 mg/100 g, respectively. The mean iron values of industrial, homemade and laboratory scale bulgur were 1.89, 2.99 and 5.85 mg/100 g, respectively. The mean potassium content of industrially produced and homemade bulgur samples were determined as 363 and 378 mg/100 g, respectively. The content of magnesium of bulgur produced industrially, homemade and laboratory scale ranged between 60.2 and 102.4 mg/100 g, 106.5 and 126.3 mg/100 g and 127 mg/100 g, respectively. In another study, the amount of magnesium of bulgur was determined as 211.6 mg/100g [21]. Magnesium levels in wheat significantly ($p < 0.05$) reduced with bulgur processing was observed by some researchers [34]. The average manganese content was 1.36 mg/100 g in the bulgur sample produced industrially in Turkey. Average manganese values of homemade produced bulgur sample were higher than industrially produced (1.98 mg/100 g) and the highest values obtained with laboratory scale bulgur samples (5.70 mg/100 g). Similar calcium and iron contents of 360 and 31 ppm of dry matter have been described for bulgur samples [35]. Homemade and laboratory produced bulgur samples were investigated in terms of chemical properties that homemade bulgur samples contain 612 ppm calcium and 24.8 ppm iron, 17.6 ppm zinc, 1084 ppm magnesium, and also bulgur samples produced laboratory condition contain 604 ppm calcium and 24.6 ppm iron, 18.4 ppm zinc, 1100 ppm magnesium were determined by some researchers [34]. The average sodium content of industrially produced and homemade bulgur samples were 52.2 and 48.9 mg/100 g, respectively. Laboratory scale produced bulgur sample gave the highest sodium (65.83 mg/100 g) content. Phosphorus content ranged from 250.9–382.0 mg/100 g in bulgur samples that produced industrially in Turkey. Phosphorus content of homemade bulgur was found between 295.1–412.2 mg/100 g. Homemade and laboratory scale bulgur samples (407.27 mg/100 g) gave higher phosphorus content than industrially produced bulgur. It was previously determined that the changes of phosphorus and magnesium content between 338 and 380 mg/100 g; between 84 and 107 mg/100 g, in barley respectively [26]. When barley processed to bulgur, phosphorus and magnesium content reduced to 294–342 mg/100 g to 90–100

mg/100 g, respectively [26]. Zinc content changed between 1.20-3.21 mg/100 g in industrially bulgur, between 1.34-4.74 mg/100g in homemade bulgur, laboratory scale produced bulgur sample gave 4.15 mg/100 g zinc content. The higher portion of mineral elements found in a kernel of wheat is contained in the wheat germ, husk or bran and the least amount in endosperm. For this reason, high mineral content consisting of homemade wheat gave higher amount of mineral content than industrially produced bulgur. According to the World Health Organization, heavy metals like Pb, Cd and Ni accumulated by plants in toxic forms should be controlled in food systems [36]. Heavy metals will finally damage the health of living organism by food [37]. Therefore, the determination of heavy metal contents in foods systems becomes important. The content of copper of industrially produced, homemade and laboratory scale bulgur, expressed as mg/kg with values of around 4.08, 5.08 and 5.37, respectively. The cadmium content of bulgur produced of industrially produced, homemade and laboratory scale ranged between 0.01 and 0.09 mg/kg, 0.02 and 0.08 mg/kg and 0.08 mg/kg, respectively. Whereas JECFA [38], permit levels up to 0.1 mg/kg, the recommended limit for Cd in cereal grains including wheat and rice, bran and germ. It was clear that there was no risk with respect to the concentrations of cadmium in bulgur. The average lead content of industrially produced, homemade and laboratory scale bulgur samples were 0.09, 0.00 and 0.02 mg/kg, respectively. The maximum lead level permitted for cereal grains is 0.2 mg/kg [38]. Lead content of homemade produced bulgur sample was not determined. It was clear from the results that there was no risk with respect to the concentrations of lead in bulgur.

Color properties

Lightness (L^*), redness (a^*), yellowness (b^*) and hue angle values are given in Table 2. The average L^* value of industrially produced and homemade bulgur samples ranged between 52.48-75.16 and 45.52-80.44, respectively. Laboratory scale produced bulgur sample gave the lowest L^* value (45.52). Lightness values of industrially produced bulgur samples showed wide range, this is maybe due to the effective pearling processes or wheat varieties of using in bulgur production. In general, homemade produced bulgur samples have been found to lighter than industrially produced bulgur in Turkey. The highest redness values were determined in laboratory scale bulgur samples, but the highest yellowness values were obtained with industrially produced bulgur samples. In Southeast Anatolia, durum wheat cultivars as svevo, burgos and zenit are major dominating varieties and used in bulgur production and this cultivars possessing high yellow pigmentation. Therefore, industrial bulgur samples gave highest yellowness values due to the wheat cultivar used in production. Also, the pearling step in industrial production allows more bran separation from the wheat. The average hue angle values of industrially produced, homemade and laboratory scale bulgur samples were 86.51, 82.79 and 79.03, respectively. Bulgur was produced from siyez and durum wheat, and found the average values of L^* , a^* and b^* as 38.02, 7.30, 15.02 in uncooked siyez bulgur and as 46.54, 5.60, 19.25 in durum bulgur, respectively [39].

In the villages, homemade bulgur is produced by traditional cooking, but in industrial production autoclaving is used. High pressure and temperature applied in autoclave cooking results in darkening of bulgur color, which are undesirable. Also, cooking in autoclave resulted in a more significant decrease on

Table 2. Color and sensorial properties of industrially, homemade and laboratory scale manufactured bulgur samples; mean values were significantly different ($P < 0.01$) between homemade and industrial samples; LMB: laboratory made bulgur

Parameter	Industrial (I)				Homemade (H)				LMB	Contrast (I-H) diff.
	Mean	SD	Max	Min	Mean	SD	Max	Min		
L^*	58.04	5.72	75.16	52.48	69.32	16.37	80.44	45.52	54.50	-11.27
a^*	1.48	1.29	4.59	-0.52	2.23	1.72	4.33	0.68	4.19	-0.75
b^*	25.84	2.48	29.97	21.81	20.43	4.38	23.18	13.89	21.63	5.41
Hue angle	86.51	3.18	90.99	78.78	82.79	7.11	88.33	72.84	79.03	3.73
Hardness	4.44	0.35	4.90	3.85	4.59	0.42	4.95	4.20	4.50	-0.15
Cohesiveness	4.43	0.36	4.85	3.75	4.79	0.14	4.95	4.65	4.25	-0.35
Taste	4.03	0.63	5.00	3.10	4.61	0.31	4.85	4.15	4.00	-0.59
Color	4.32	0.63	4.95	3.35	4.29	0.74	4.95	3.55	4.25	0.03
Odor	4.23	0.70	4.95	3.30	4.91	0.08	5.00	4.85	3.75	-0.68
Overall acceptability	4.29	0.29	4.87	3.86	4.64	0.29	4.90	4.33	4.00	-0.35

vitamins as thiamin, niacin, pantothenic acid, pyridoxine, and riboflavin, when compared with traditional cooking. It is well known that autoclaving is the best method to reduce the antinutritional factor in the cooking methods. Despite this, autoclaving gave non-clumped and non-deformed grains. Drying temperature is the factor that affects the bulgur quality. In homemade production, it is dried under the sun, but it in industrial production drying is carried out in hot air flow. Higher temperatures cause irreversible darkening and opaqueness of bulgur color.

Sensorial properties

According to the variance analysis results, bulgur samples were statistically significant in hardness, cohesiveness and taste values ($p < 0.01$). When hardness values assessing by panelists, samples crushed between the teeth in the mouth and perceived feeling of hardness was scored. A lower hardness scores represent the perceived of hardness, and higher scores represent desirable hardness feelings. Industrially produced bulgur samples gave lower hardness values than homemade bulgur samples. Homemade bulgur samples represent desirable hardness values; it may be due to the wheat properties used in bulgur making. Lower scores in terms of cohesiveness in industrially produced bulgur were observed. This might be due to the showing tendency of adhesion between the teeth in mouth. All bulgur samples (industrially, homemade and laboratory scale) were preferred for taste, showing mean scores of 4.03; 4.61 and 4.00, respectively. Yellow color of bulgur produced industrially positively affected the panelists. Industrially produced bulgur samples gave higher color scores than homemade and laboratory scale. The best odor scores of bulgur were observed with homemade bulgur. Panelists emphasized that darker bulgur samples were harder but better tasting than lighter samples. In terms of general acceptability, homemade produced bulgur samples showed higher odor and taste scores than industrially produced samples.

CONCLUSION

Industrially produced bulgur samples gave an attractive brighter yellow color than homemade bulgur samples. Homemade bulgur samples showed higher energy values than industrially produced bulgur. In terms of nutritional properties, industrially produced bulgur contained lower phytic acid content than homemade bulgur due to the effective pearling step of wheat. The total phenolic content reached maximum level in laboratory scale bulgur samples; this was fol-

lowed by homemade bulgur. Higher nutritional mineral content and also lower heavy metal were observed with homemade bulgur samples. In terms of sensory characteristics, homemade bulgur samples showed more pleasant fragrance and taste than industrially produced bulgur. Homemade bulgur samples got more appreciation than industrially produced bulgur in terms of general acceptability by panelists.

Acknowledgement

We are grateful to the Commission for the Scientific Research Projects (BAP:131219003) at Necmettin Erbakan University for supporting and funding this research study.

REFERENCES

- [1] M. Certel, S. Mahnke, P. Gerstenkorn, Muhle Mischfüttertechnik **126** (1989) 414
- [2] A. Elgün, S. Türker, Agricultural Faculty Press, Konya, 2005, p. 188
- [3] M. Certel, Ataturk University of Science Ins. Food Science and Tech. Department. Phd thesis, Erzurum, 1990, p. 131
- [4] M. Bayram, A. Tiryakioğlu, S. Kayabaş, I. Duru, H., Arslan, E. Koçak, S. Altınbaş, M. Baharoğlu, A. Dağyutan, I. Kılınç, F. Balcı, Dünyada ve Türkiyede bulgur sanayinin durumu, üretim teknolojisindeki gelişmeler ve sorunları-çözüm önerileri. Makarnalık buğday ve mamulları Konferansı. Urfa, Turkey, 2010, p. 33-41
- [5] M. Bayram, World Grain **6** (2005) 72-75
- [6] M. Bayram, M.D. Öner, J. Cereal Sci. **41** (2005) 291-296
- [7] M. Bayram, M.D. Öner, J. Food Eng. **74** (2006) 232-239
- [8] M.D. Öner, Bulgur Sanayi, Sorunları ve Çözüm Önerileri. Hububat 2002, Gaziantep, Turkey, 2002, p. 39-48
- [9] A. Elgün, Z. Ertugay, M. Certel, Cereal Chem. **67** (1990) 1-6
- [10] Market research of bulgur. Karacadağ Development Agency, Trc2-10-Dfd Foreign Trade Market Research Project Turkey, 2011, p.127
- [11] M. Bayram, M.D. Öner, World Grain **11** (2002) 51-53
- [12] AACC, Approved Methods of The American Association of Cereal Chemists. 8th ed. St. Paul, MN, USA, 1990
- [13] H. Bubert, W.D. Hagenah, Detection and measurement. P.W.J.M. Boumans, Ed., Wiley, New York, 1987 pp. 536-567
- [14] K. Slinkard, V.L. Singelton, Am. J. Enol. Vitic. **28** (1977) 49-55
- [15] T. Beta, S. Nam, J.E. Dexter, H.D. Sapirstein, Cereal Chem. **82** (2005) 390-393
- [16] W. Haugh, H.J. Lantzsch, J. Sci. Food Agric. **34** (1983) 1423-1426
- [17] O. Bilgin, K.Z. Korkut, I. Başer, O. Dağlıoğlu, I. Öztürk, T. Kahraman, J. Tekirdag Agric.Faculty **5** (2008) 101-109
- [18] N. Yürür, Z.M. Turan, S. Çakmakçı, A research on the effects of some bread and durum wheat varieties on

- efficiency and adaptability in Bursa condition, Turkey Grain Symposium, Bursa, 1987, pp. 59-68
- [19] M. Şahin, M. Akçura, A.A. Göçmen, S. Aydoğan, *Bitkisel Araştırma Dergisi* **2** (2008) 17-21
- [20] Z. Tacer, İstanbul Teknik University, Institute of Science Department of Food Eng, Master's Thesis, 2008, p. 79
- [21] I. Toufeili, C. Melki, S. Shadarevian, R.K. Robinson, *Food Qual. Pref.* **10** (1999) 9-15
- [22] S. Singh, S. Sharma, H.P.S. Nagi, *J Sci Technol.* **44** (2007) 310-314
- [23] K.H. Tipples, R.H. Kilborn, K.R. Preston, in: *Bread-wheat quality defined*, in *Wheat Production, Properties and Quality*, W. Bushuk, V.F. Rasper, Eds., Blackie academic and Professional, London, 1996, p. 27
- [24] Turkish Food Codex, Comminique of bulgur, <http://www.resmigazete.gov.tr/eskiler/2009/02/20090216-7.htm> (accessed 3.January 2016)
- [25] A.D. Ünüvar, Selcuk University, The Department Of Food Engineering, Master's Thesis, Konya, 2009, p. 64
- [26] H. Köksel, M.J. Edney, B. Özkaya, *J Cereal Sci.* **29** (1999) 185-190
- [27] B. Özkaya, H. Özkaya, H. Köksel, *Getreide Mehl Brot.* **52** (1998) 182-184
- [28] H. Özkaya, B. Özkaya, H. Bayrak, F. Gökpinar, The effect of process on phytic acid content of bulgur. Traditional Food Symposium, Van, Turkey, 2004, pp. 54-55
- [29] M. Jenab, L.U. Thompson, *Carcinogenesis* **19** (1998) 1087-1092
- [30] S. Ragaei, E.M. Abdel-aal, M. Noaman, *Food Chem.* **98** (2006) 32-38
- [31] Q. Cheng, S. Wang, D. Zhou, T. Rials, Y. Zhang, *J. Nanjing Forestry Univ.* **4** (2006) 21-26
- [32] S. Fanasca, Y. Rouphael, E. Venneria, E. Azzini, A. Durazzo, G. Maiani, *Int. J Food Sci. Technol.* **44** (2009) 1017-1023
- [33] Y. Shen, L. Jin, P. Xiao, Y. Lu, J. Bao, *J. Cereal Sci.* **49** (1) (2009) 106-111
- [34] B. Özkaya, H. Özkaya, E. Köksel, *J Field Crops Res Inst.* **2** (1993) 36-56
- [35] A. Baysal, S. Keçecioglu, P. Arslan, S. Yücecan, G. Pekcan, U. Güneyli, S. Birer, F. Sağlam, M. Yurttagül, R. Çehrelî, *Dieticians Association of Turkey*, 1991
- [36] M. Heidarieh, M.G. Maragheh, M.A. Shamami, M. Behgar, F. Ziaei, Z. Akbari, *Springerplus* **2** (2013) 72
- [37] A. Ene, I.V. Popescu, C. Stihî, *Ovidius Univ. Ann. Chem.* **20** (2009) 35
- [38] JECFA ftp://ftp.fao.org/codex/meetings/cccf/cccf5/cf05_14e.pdf (accessed 3.January 2016)
- [39] V.A. Yılmaz, Ondokuz Mayıs University Institute of Science Department of Food Eng, Master's Thesis, 2012.

NILGÜN ERTAŞ

Department of Food Engineering,
Engineering & Architecture Faculty,
Necmettin Erbakan University, Konya,
42060, Turkey

STRUČNI RAD

POREĐENJE FIZIČKIH, HEMIJSKIH I NUTRITIVNIH SVOJSTAVA INDUSTRIJSKOG I DOMAĆEG BULGURA U TURSKOJ

Određivanje funkcionalnih i nutritivnih svojstava bulgura (pilav) je od najveće važnosti za zdrave generacije. U ovom radu, određen je fizički, hemijski, nutritivni i senzorni kvalitet bulgura proizvedenih industrijski, u domaćinstvu i laboratoriji u Turskoj, a zatim je poređen njihov kvalitet. Sadržaj pepela u uzorcima bulgura je bio između 1,04 i 1,81%, a ukupni sadržaj proteina između 11,90 i 14,47%. Evaluacija nutritivnog statusa bulgura je ukazala na sadržaj ukupnih fenola 449.82 do 1047.09 mg/g i sadržaj fitinske kiseline pronađene između 422.14 i 1173.56 mg/100 g. Sadržaj minerala (kadmijum i olovo) u uzorcima bulgura je bio i manji propisanog maksimuma. Uzorci domaćeg bulgura imali su bolji aromatični ukus i miris nego industrijski proizvedeni uzorci bulgura. Industrijski proizvedeni uzorci bulgura su imali svetliju boju od domaćeg bulgura.

Ključne reči: bulgur, industrijski proizveden bulgur, domaći bulgur, minerali, fitinska kiselina, Turska.

JELENA FILIPOVIĆ¹
SHAHIN AHMETXHEKAJ²
VLADIMIR FILIPOVIĆ³
MILENKO KOŠUTIĆ¹

¹Institute of Food Technology,
University of Novi Sad, Novi Sad,
Serbia

²High School "Ali Hadri", Peć,
Serbia

³Faculty of Technology, University
of Novi Sad, Novi Sad, Serbia

SCIENTIFIC PAPER

UDC 664.69/761:544:66

SPELT PASTA WITH INCREASED CONTENT OF FUNCTIONAL COMPONENTS

Article Highlights

- Addition of flax seed flour in spelt pasta increases the share of ω -3 fatty acids and improves ω -6/ ω -3 ratio
- Pasta with 20 g sesame flour/100 g spelt flour has the best content of essential mineral elements
- New functional product with enriched mineral content, a source of monounsaturated fatty acids

Abstract

This paper investigates the effects of addition of flax seed, sesame seed, or eggs (10 g/100 g of sample and 20 g/100 g of sample) in spelt flour to obtain new pasta products with improved ω -3/ ω -6 ratio and minerals profile. Gas chromatography with mass spectrometry was used for carrying out a quantitative analysis of the liposoluble pasta extract. Post-hoc Tukey's HSD test at 95% confidence limit showed significant differences between observed samples. Daily average consumption of 75 g of spelt pasta containing 20 g flax seed/100 g of sample contributes to essential fatty acids intake of 3.8 g and improved ω -6/ ω -3 ratio (1:2.4). The obtained results indicate that the investigated spelt pasta samples are new products with improved nutritional properties due to higher level of ω -3 fatty acids and minerals content (Ca, Zn, Cu and Fe). Pasta (PS 7) with 20 g/100 g of eggs has the best sensory quality (maximum scores for odor, texture, flavor and overall acceptability were 8.8, 8.9, 8.9 and 8.9, respectively).

Keywords: ω -6/ ω -3 ratio, fatty acid, mineral content, GC-MS analysis, functional properties.

Nutritional and functional properties of pasta can be improved by using spelt as basic raw material for the production of pasta and some additional raw material such as fatty acids, flax seed or eggs for improving functional properties [1,2]. Spelt is a suitable raw material for pasta production, breakfast cereals, bread and other products of altered nutritional characteristics compared to conventional wheat products. Some spelt cultivars have very high protein content and even 30 to 60% higher concentration of mineral elements (Fe, Zn, Cu, Mg and P) compared to *Triticum aestivum* [1,3,4]. Pasta is also suitable for correcting nutrition plans because it is quick and easy

to prepare, easily digestible food and it is one of the widespread foods in many countries around the world [1,2].

Eggs added to pasta contribute to better mechanical properties and quality of the product and also increase the nutritive and biological value of the product, which is reflected in the increase of lysine, ω -3 fatty acids and lecithin. By consumption of products enriched with eggs human meets recommended needs ω -3 fatty acids [5-7]. Flax seed (*Linum usitatissimum*) contains important substances in its composition such as vitamins A, B and E, magnesium, calcium, zinc, selenium, phosphorus, and it is also an excellent source of fibres and one of the best sources of ω -3 fatty acid and lignan (phytoestrogens with antioxidant effects) [8]. The intake of long-chain ω -3 PUFA in many developed countries (average 0.15 g per day) is below the recommended level [9]. The ratio of ω -6 to ω -3 in the diet should be 4 to 1 [10]. For

Correspondence: J. Filipović, Institute of Food Technology, Blvd. cara Lazara 1, 21000 Novi Sad, Serbia.

E-mail: jelena.filipovic@fins.uns.ac.rs

Paper received: 8 February, 2016

Paper revised: 7 September, 2016

Paper accepted: 3 October, 2016

<https://doi.org/10.2298/CICEQ160208049F>

this reason, food products enriched with ω -3 fatty acids can improve the ratio of ω -3/ ω -6 in the diet in order to decrease the level of risk of the diseases caused by "lifestyle", especially cardiovascular disease [11,12]. Sesame (*Sesamum indicum L.*) plays an important role in human nutrition. The chemical composition of sesame shows that the seed is an important source of oil (44-58%), protein (18-25%), carbohydrate (13.5%) and ash (5%) [13]. Sesame seed provides additional medical and nutritional enrichment by contributing high levels of polyphenol antioxidant rich dietary lignins that also have anti-mutagenic properties [14]. New studies are identifying potential benefits for a wide range of conditions including cancer, inflammatory bowel disease and other autoimmune diseases such as lupus and rheumatoid arthritis. The main challenges of food producers are to produce food enriched with ω -3 fatty acids in the way that it does not reduce their current quality despite the added active ingredient [15].

The aim of this study was to produce spelt pasta with addition of flax seed, sesame seed or eggs with improved nutritional properties: improved ratio ω -6/ ω -3 fatty acids and minerals content.

MATERIAL AND METHODS

Materials

The following materials were used for pasta production: whole meal organic spelt flour, (Serbia, 2015) characterized by starch, protein, lipids and cellulose content of 56.6, 17.6, 2.5 and 2.4% d.m., respectively, and nutritive components:

- flax seed from organic production, purchased in an organic food store in Novi Sad,

- sesame seed from organic production, purchased in an organic food store in Novi Sad,
- eggs, purchased from a local food market.

The nutritive components and mineral profile of different flours are presented in Table 1.

Methods

Preparation of pasta

Pasta was made using the device "La Parmigiana D45" MAC 60 (Fidenza, Italy). The raw material was placed in a paddle mixer - a constituent part of the device (capacity 4 kg/h), equipped with 6 paddles (rotating speed of 60 rpm). The moisture content of raw material was adjusted to 31.5% by adding tap water preheated at 40 °C. During mixing (15 min), 6 paddles help to distribute added water evenly over the surface of flour particles [16]. Immediately after mixing, the hydrated mass entered the extrusion screw (length 300 mm, diameter 55 mm) which moved the loose dough forward (speed of feeding 250 g/min, screw speed 60 rpm, extruded temperature 40 °C) and simultaneously compressed it into a homogeneous plastic mass prior to extrusion through a die with 1.4 mm diameter used for spaghetti. The extrusion temperature was around 40 °C. Constant temperature during pasta forming was ensured by tap water circulating through the barrel.

Raw pasta was dried in a chamber drier EC25GE (Italgy S.r.l., Pasiano di Pordenone, Italy) about 12 h at controlled temperature that did not exceed 45 °C. Humidity was adjusted to 70% and controlled until pasta reached the moisture around 12.5%, followed by cooling to 25 °C, for 4 h and then stored at room temperature in sealed containers. Drying conditions and air flow were stringently controlled to avoid the creation of a discontinuity in the moisture

Table 1. Fatty acids and mineral profile of different samples; the results are presented as mean \pm SD; C16:0 palmitic acid, C18:0 stearic acid, C1:18 oleic acid, C18:2N linoleic acid ω -6, C18:3 N-linolenic acid ω -3

Property	Component	Sample			
		Spelt flour	Flaxseed flour	Sesame seed flour	Eggs
Fatty acids ($\bar{X}\pm SD$, g/100 g of sample)	C 16:0	0.40 \pm 0.05	2.8 \pm 2.06	5.61 \pm 1.09	1.84 \pm 1.4
	C 18:0	0.11 \pm 0.09	2.72 \pm 1.94	0.54 \pm 0.77	0.70 \pm 0.05
	C 1:18	0.79 \pm 0.12	9.40 \pm 2.37	22.45 \pm 3.5	0.27 \pm 0.04
	C 18:2N, ω -6	0.89 \pm 0.25	6.84 \pm 1.15	3.58 \pm 1.6	3.93 \pm 0.07
	C 18:3N, ω -3	0.04 \pm 0.01	25.75 \pm 5.08	0.08 \pm 0.7	0.05 \pm 0.09
	ω -6/ ω -3	22:1	1:3.8	44:1	78.6:1
Mineral content ($\bar{X}\pm SD$, mg/100 g of sample)	Ca	247.55 \pm 9.15	1824.5 \pm 21.10	19065 \pm 17.45	0.05
	Zn	18.93 \pm 2.03	39.5 \pm 1.54	48.5 \pm 5.21	Trace
	Cu	3.37 \pm 0.74	11.89 \pm 2.04	13.82 \pm 1.6	Trace
	Mn	39.59 \pm 1.89	2143.5 \pm 33.12	16.36 \pm 3.54	Trace
	Fe	27.38 \pm 3.51	108.51 \pm 41.56	85.22 \pm 6.58	0.0027

gradient between the interior and exterior of spaghetti.

Seven formulations of pastas were tested. Table 2 describes pasta formulations enriched with different quantities of nutritive components: PS 1 (control sample), PS 2 (10% flax seed and 90% spelt flour), PS 3 (20% flax seed and 80% spelt flour), PS 4 (10% sesame seed and 90% spelt flour), PS 5 (20% sesame seed and 80% spelt flour), PS 6 (10% of liquid eggs and 90% spelt flour), PS 7 (20% of liquid eggs and 80% spelt flour). For each formulation, pastas were prepared in batches of 2 kg, with two replicates.

Table 2. Pasta formulation with different quantities of nutritive components

Sample	Raw material (g/100 g of sample)			
	Spelt flour	Flax seed	Sesame seed	Liquid eggs
PS 1	100	0	0	0
PS 2	90	10	0	0
PS 3	80	20	0	0
PS 4	90	0	10	0
PS 5	80	0	20	0
PS 6	90	0	0	10
PS 7	80	0	0	20

Fatty acid analysis - GC-MS analysis

The fat phase for fatty acid (FA) analysis was extracted from the samples by the Folch method as recommended for isolation of total lipids [17]. FA methyl esters were prepared from the extracted lipids by transesterification using 14 wt.% boron trifluoride/methanol solution [18]. Obtained samples were analyzed by an Agilent 7890A gas chromatographer (Agilent Technologies, CA, USA) with a flame ionization detector (GC-FID), autoinjection module for liquid, equipped with a fused silica capillary column (Supelco SP-2560 Capillary GC Column 100 m×0.25 mm, $d = 0.20 \mu\text{m}$) and helium as a carrier gas (purity = 99.9997 vol.%, flow rate = 1.5 ml/min and pressure of 1.092 bar). The samples were injected in volumes of 1 μl in split regime with a ratio of 30:1. Following temperature regime was applied: initial temperature 140 °C, initial temperature hold time 5 min, heating rate 3 °C/min, final temperature 240 °C and final temperature hold time 10 min. Nitrogen was used as a makeup gas. The FAs peaks were identified by comparison of retention times with retention times of standards from "Supelco 37 component FA methyl ester mix" (Sigma-Aldrich) and with data from internal data library, based on previous experiments and FA methyl ester determination on GC-MS. The results were expressed as mass of individual fatty acid or fatty acid

group (g) in 100 g of fatty acids, or as relative mass contents.

Mineral profile of pasta with nutritive components

Mineral contents of calcium, zinc, copper, magnesium and iron were determined using an Atomic Absorption Spectrophotometer, AOAC [19].

Sensory analysis

The test to assess the quality and acceptability was performed by 60 inexperienced tasters. The tasters were asked to evaluate the following sensory properties of seven formulations of pastas with different quantities of nutritive components: odor, texture, flavor, and overall acceptability using a 9 point hedonic scale (1 = dislike extremely, 2 = dislike very much, 3 = dislike moderately, 4 = dislike slightly, 5 = neither like nor dislike, 6 = like slightly, 7 = like moderately, 8 = like very much, 9 = like extremely) [20].

Statistical analyses

Descriptive statistical analyses for all the obtained technological parameters were expressed as the mean \pm standard deviation (SD). The evaluation of one-way ANOVA analyses of the obtained results were performed using StatSoft Statistica 10.0 software. Collected data were subjected to one-way analysis of variance (ANOVA) for the comparison of means, and significant differences are calculated according to post-hoc Tukey's HSD (honestly significant differences) test at $p < 0.05$ significance level, 95% confidence. The pattern recognition technique was applied within assay descriptors to characterize and differentiate various pasta samples, and the classification and discrimination of analyzed samples was done by principal component analysis (PCA) using presented fatty acid and mineral data.

The score analysis uses min-max normalisation of pasta samples fatty acids and mineral profile parameter responses and transfers them from their unit system in new dimensionless system which allows further mathematical calculation of different types of responses [21]. The maximum value of normalised score presents the optimum value of all analysed responses and indicates on optimal pasta formulation:

$$S_{ki} = 1 - \frac{x_{ki} - x_{k\min}}{x_{k\max} - x_{k\min}}, \quad k=1-3 \quad (1)$$

where x_k represents: palmitic acid, stearic acid and ω -6/ ω -3 ratio.

$$S_{ni} = \frac{y_{ni} - y_{n\min}}{y_{n\max} - y_{n\min}}, \quad n=1-3 \quad (2)$$

where y_n represents: oleic acid, linoleic acid and linolenic acid.

$$S_{mi} = \frac{z_{mi} - z_{mmin}}{z_{mmax} - z_{mmin}}, m = 1-5 \quad (3)$$

where z_m represents: Ca, Zn, Cu, Mn and Fe.

$$S_{ME_i} = \frac{\sum_{i=1}^m S_{mi}}{5} \quad (4)$$

$$S_{T_i} = \frac{\sum_{i=1}^k S_{ki} + \sum_{i=1}^n S_{ni} + S_{ME_i}}{k + n + 1} \quad (5)$$

$$\max[S_{T_i}] = \text{optimum}$$

RESULTS AND DISCUSSION

Fatty acids composition of the pasta with different shares of nutritive components

The distribution of saturated, monounsaturated and polyunsaturated fatty acids in spelt pasta, pasta with flax seed, sesame seed or eggs are given in Table 3. The spelt pasta (PS 1) contains 2.31 g/100 g of total fatty acids with the shares of linoleic acid (0.91 g/100 g) and linolenic acid (0.05 g/100 g, Table 3). In pasta PS 1, ω -6 fatty acids make a share of 39.2% while the ω -3 fatty acids make a share of only 2.1%, which is similar to findings of Abdel *et al.* [22], and the essential fatty acids ratio of ω -6/ ω -3 was 18.2:1. The addition of flax seed (Table 2) in spelt pasta significantly ($p < 0.05$ level) increases the share of linolenic acid (Table 3). This resulted in improvement of ω -6/ ω -3 ratio, which was 1:1.7 and 1:2.4, for the samples PS 2 and PS 3, respectively (Table 3). Pastas PS 4 and PS 5 have significant ($p < 0.05$ level) higher content of palmitic acid than other samples (PS 1, PS 2, PS 3,

PS 6, and PS 7). The addition of eggs (20 g/100 g) (Table 2) in spelt pasta significantly increases the share of linoleic acids (Table 3) compared to PS1 and also significantly improved technological quality of the pasta as stated by Filipović *et al.* [1,6]. Despite conflicting evidence about the role of cholesterol intake in cardiovascular disease risk, according to Exler [7] the level of cholesterol in pastas PS 6 and PS 7 was low, around 11.5 and 23 mg/100 g, respectively. While obtaining pasta with eggs, it is also worth considering using eggs with low amount of cholesterol [7]. By consuming 75 g of pasta with 20 g/100 g of sample flax seed intake ω -3 fatty acids is about the 3.8 g, which contributes to the improvement of ω -6/ ω -3 ratio (1:2.1) in the daily diet (Table 3). Consumption of 75 g pasta with 20 g/100 g of sample flax seed is also satisfying daily needs of ω -3 fatty acid intake recommended by the Food and Drug Administration (FDA) [23,24].

Mineral composition of the pasta with different shares of nutritive components

The mineral composition properties of pasta with different shares of nutritive components are presented in Table 4. Due to sesame seed mineral composition (Table 1), these tests show statistically significant differences in calcium and copper content between the values of pastas without sesame seed: PS 1, PS 2, PS 3, PS 6, PS 7 and pastas with sesame seed content in formulation: PS 4 and PS 5 (Table 3). The manganese content of different pastas ranged between 32.26 mg/100 g in PS 3 and 39.72 mg/100 g in PS 7. Tukey's HSD test indicates the significantly ($p < 0.05$ level) higher iron contents of pasta PS 5 (Table 3), which confirms that sesame seed (Table 1) is rich sources of essential minerals and its addition to pasta significantly improves mineral content intake. Highest values of Ca, Zn, Cu and

Table 3. Fatty acids composition of the pasta with different shares of nutritive components; the results are presented as mean \pm SD (g/100g of sample); different letter within the same column indicates significant differences ($p < 0.05$), according to Tukey's test, number of repetitions: $n = 3$; SFA-saturated fatty acids, MUFA-monounsaturated fatty acids, PUFA-polyunsaturated fatty acids, C16:0 palmitic acid, C18:0 stearic acid, C1:18 oleic acid, C18:2N linoleic acid ω -6, C18:3 N-linolenic acid ω -3

Sample/pasta	Fatty acid					ω -6/ ω -3 Ratio
	SFA		MUFA	PUFA		
	C16:0	C18:0	C1:18	C18:2N, ω -6	C18:3N, ω -3	
PS 1	0.43 \pm 0.03 ^a	0.10 \pm 0.01 ^a	0.82 \pm 0.07 ^a	0.91 \pm 0.07 ^a	0.05 \pm 0.03 ^a	18.2:1
PS 2	0.50 \pm 0.06 ^a	0.26 \pm 0.03 ^c	1.64 \pm 0.10 ^b	1.51 \pm 0.08 ^{ab}	2.51 \pm 0.04 ^b	1:1.7
PS 3	0.99 \pm 0.04 ^c	0.52 \pm 0.04 ^d	2.57 \pm 0.24 ^c	2.09 \pm 0.11 ^b	5.10 \pm 0.27 ^c	1:2.4
PS 4	0.95 \pm 0.11 ^c	0.14 \pm 0.01 ^{ab}	0.82 \pm 0.19 ^a	2.94 \pm 0.23 ^c	0.06 \pm 0.01 ^a	49:1
PS 5	1.49 \pm 0.09 ^d	0.19 \pm 0.08 ^{abc}	0.8 \pm 0.44 ^a	5.19 \pm 0.59 ^d	0.07 \pm 0.02 ^a	74:1
PS 6	0.57 \pm 0.07 ^{ab}	0.16 \pm 0.03 ^{abc}	0.77 \pm 0.10 ^a	0.86 \pm 0.10 ^a	0.05 \pm 0.03 ^a	17.2:1
PS 7	0.71 \pm 0.02 ^b	0.22 \pm 0.04 ^{bc}	0.71 \pm 0.07 ^a	1.51 \pm 0.13 ^{ab}	0.05 \pm 0.01 ^a	30.2:1

Table 4. Mineral composition of the pasta with different shares of nutritive components; the results are presented as mean±SD (mg/100 g of sample); different letter within the same column indicates significant differences ($p < 0.05$), according to Tukey's test, number of repetitions: $n = 3$

Sample/pasta	Element				
	Ca	Zn	Cu	Mn	Fe
PS 1	251.92±6.98 ^a	18.77±1.01 ^{ab}	3.37±0.18 ^a	39.37±2.00 ^a	27.22±1.08 ^{ab}
PS 2	250.33±7.48 ^a	17.33±0.99 ^a	3.18±0.20 ^a	35.81±1.73 ^{ab}	29.4±1.94 ^{abc}
PS 3	257.74±11.97 ^a	15.88±1.10 ^a	3.0±0.31 ^a	32.26±1.70 ^b	31.58±1.75 ^{bc}
PS 4	417.38±25.78 ^b	21.76±1.24 ^{bc}	4.41±0.27 ^b	37.07±0.99 ^{ab}	33.02±2.03 ^c
PS 5	591.84±8.89 ^c	24.76±1.41 ^c	5.46±0.39 ^c	34.77±1.84 ^{ab}	38.82±1.69 ^d
PS 6	251.20±4.78 ^a	18.36±1.09 ^a	3.28±0.17 ^a	39.55±2.09 ^a	26.58±2.03 ^{ab}
PS 7	250.29±5.17 ^a	17.91±0.98 ^a	3.18±0.20 ^a	39.72±2.41 ^a	25.98±2.01 ^a

Fe (591.84; 24.76; 5.46 and 38.82 mg/100 g, respectively) were founded in pasta with 20 g/100 g sesame seed (PS 5). These minerals are positively contributing to recommended daily intakes. As these minerals have a vital role in bone mineralization, red blood cell production, enzyme synthesis, hormone production, as well as regulation of cardiac and skeletal muscle activities [25,26], pasta with sesame seed can be beneficial.

The optimal mineral status is essential for maintaining health and ensuring optimal body function. The nutritional status can be understood as the body condition that results from the process of using the nutrients contained in food, leading to an equilibrium between supply and assimilation of the nutrients and the nutrients consumption of the organism which is influenced by sex and age of the individual [27]. The recommended daily intakes according to FAO/WHO [24] for Ca, Zn, Cu, Mn and Fe are 100,15, 0.9, 5 and 15 mg/day, respectively.

The sensory parameters of pasta with different shares of nutritive components are presented in Table 5. Sensory values for odor, texture, flavor and overall acceptability statistically insignificantly decreased with addition of flax seed (10 g/100 g of sample and 20 g/100 g of sample). On the hedonic scale they were

rated as "like moderately" (7), which indicates that flax seed had minor negative influence on pastas sensor quality. These products are designed for consumers interested in functional food and those who are willing to improve the ω -6/ ω -3 ratio in their diet. The results of the present study show that the addition of sesame seed to pastas (PS 4 and PS 5) caused statistically significant changes in taste, odor, texture and overall acceptability of the product compared to the control (PS 1). The present study points that pastas with sesame seed (PS 4 and PS 5) were scored above 6.0 ("like slightly"). Adding eggs to pastas is highly scored from the sensory standpoint (scores above 8.0 - "like very much"). Addition of eggs in pasta is beneficial both the sensory quality (taste, odor, texture and overall acceptability). As the aim of this study was not to consider what is happening with the functional components during pasta cooking, these pasta products are recommended for soups or dishes where the pasta is not separately cooked. According Verado *et al.* [28], spaghetti enriched with long chain n-3 polyunsaturated fatty acids had a shelf life comparable to the control pasta.

The PCA allows a considerable reduction in a number of variables and the detection of structure in the relationship between measuring parameters and

Table 5. Sensory analysis of pasta with different shares of nutritive components; the results are presented as mean±SD; different letter within the same column indicates the significant difference in mean values ($p < 0.05$), according to Tukey's test. Number of repetitions: $n = 60$

Sample/pasta	Sensory parameter			
	Odor	Texture	Flavor	Overall acceptability
PS 1	8.1±0.91 ^{ab}	8.2±0.80 ^{abc}	8.1±0.82 ^{ac}	8.1±0.83 ^{abc}
PS 2	7.7±1.09 ^{ab}	7.1±1.07 ^{abcd}	7.8±0.28 ^{abc}	7.5±0.62 ^{abc}
PS 3	7.4±0.10 ^{ab}	6.6±0.70 ^{abd}	7.3±1.17 ^{abc}	7.1±1.45 ^{abc}
PS 4	6.8±1.24 ^{ab}	6.1±0.99 ^{ad}	6.6±0.78 ^{bc}	6.7±0.56 ^{ab}
PS 5	5.9±1.31 ^b	5.9±0.86 ^d	6.0±0.49 ^b	6.2±0.45 ^a
PS 6	8.5±0.50 ^a	8.7±0.27 ^{bc}	8.8±0.18 ^a	8.7±0.31 ^{bc}
PS 7	8.8±0.15 ^a	8.9±0.05 ^c	8.9±0.07 ^a	8.9±0.09 ^c

Table 6. Score values of pasta samples with different shares of nutritive components

Sample/pasta	PS 1	PS 2	PS 3	PS 4	PS 5	PS 6	PS 7
Partial score values for mineral composition	0.31	0.20	0.09	0.58	0.87	0.281	0.26
Total score values	0.40	0.46	0.50	0.34	0.41	0.43	0.42

CONCLUSIONS

Based on the results of the investigation of the effects of the addition of flax seed, sesame seed or eggs, it can be concluded:

- The addition of flax seed flour in spelt pasta in the quantities of 10 or 20 g/100 g significantly increases the share of ω -3 fatty acids, which results in improved ratio of ω -6/ ω -3, 1:1.7 and 1:2.4.

- Daily intake of 75 g pasta with 20 g flax seed /100 g of sample (PS 3) completely satisfies minimum daily needs of ω -3 essential fatty acids (3.8 g/100 g) recommended by FDA.

- The best content of essential minerals elements (maximum of Ca, Zn, Cu and Fe 591.84, 24.76, 5.46 and 38.82 mg/100 g; respectively) was experienced with pasta PS 5 (20 g sesame seed /100 g sample and 80 g/100 g of spelt flour).

- The best sensory quality (maximum scores for odor, texture, flavor and overall acceptability 8.8, 8.9, 8.9 and 8.9, respectively) was with pasta containing 20 g/100 g sample eggs (PS 7). Pasta with 20 g/100 g flax seed has good quality and it is recommended to consumers who are willing to improve ω -6/ ω -3 ratio in their diet.

PCA is a useful tool for pointing at neat separation of samples according to different shares of nutritive components, while Score analysis was used to calculate the best quality of tested samples regarding fatty acid and mineral composition with sample PS 3 as the optimal.

Acknowledgements

These results are part of the project supported by the Ministry of Education, Science and Technological Development of the Republic of Serbia, III 46005 and TR 31029.

REFERENCES

- [1] J. Filipović, L. Pezo, N. Filipović, V. Filipović, M. Bodroža-Solarov, M. Plančak, *J. Food Sci. Technol.* **48** (2013)195-203
- [2] J. Filipović, L. Pezo, V. Filipović, J. Brkljača, J. Krulj, *LWT* **63** (2015) 43-51
- [3] G. Bonafaccia, V. Galli, R. Francisci, V. Mair, V. Skrabanja, I. Kreft, *Food Chem.* **68** (2000) 437-441
- [4] J. Filipović, L. Pezo, N. Filipović, V. Filipović, *APTEFF* **45** (2014) 23-30
- [5] V. Jurić, I. Jajić, V. Bursić, J. Jurić, *Letopis naučnih radova* **1** (2005) 138-145
- [6] J. Filipović, Z. Miladinović, L. Pezo, N. Filipović, V. Filipović, A. Jevtić-Vukmirović, *Hem. Ind.* **69** (2015) 59-69
- [7] J. Exler, K.M. Phillips, K.Y. Patterson, J.M. Holden, *J. Food Compos. Anal.* **29** (2013) 110-116
- [8] E.C. Lowcock, M. Cotterchio, B.A. Boucher, *Cancer Causes Control* **24** (2013) 813-816
- [9] W. Kolanowski Polish, *J. Food Nutr. Sci.* **4** (2005) 335-340
- [10] A.P. Simopoulos, A. Leaf, N. Salem, *Ann. Nutr. Metab.*, **43** (1999) 127
- [11] A.P. Simopoulos, *Biomed. Pharmacother.* **56** (2002)365-379
- [12] S.U. Kadam, P.J. Prabhasankar, *Cereal Sci.* **43** (2010) 1975-1980
- [13] M. Elleuch, S. Besbes, O. Roiseux, C. Blecker, H. Attia, *Food Chem.* **103** (2007) 641-650
- [14] M. Eleuch, D. Bedigian, B.Maazoun, S. Besbes, C. Blecker, H. Attia, *Food Chem.* **145** (2014) 765
- [15] S. Drusch, S. Mannino, *Trends Food Sci. Technol.* **20** (2009) 237-244
- [16] G. Kaluđski, N. Filipović, *Methods for the investigation of cereals, flour and finalproduct quality*, Faculty of Technology, Novi Sad, 1998, p. 71
- [17] J. Folch, M. Lees, G.H. Sloane-Stanley, *J. Biol. Chem.* **226** (1957) 497-509
- [18] Đ. Karlović, N. Andrić, *Quality control of oilseeds*, Faculty of Technology, Novi Sad, Federal Bureau of Standards, Belgrade, 1996, pp. 35-46
- [19] AOAC. *Official methods of analysis* (17th ed.), Association of Official Analytical Chemists, Arlington, VA, 1990
- [20] H. Lawless, H. Heymann, *Sensory Evaluation of Food: Principles and Practices*, Springer, New York, 2009
- [21] T. Jayalakshmi, A. Santhakumaran, *Int. J. Comp. Theory Eng.* **3** (2011) 89-93
- [22] E.-S.M. Abdel-Aal, P. Hucl, F.W. Sosulski, *Cereal Chem.* **72** (1995) 621-624
- [23] Food and Drug Administration (FDA), *Letters regarding dietary supplement health claim for omega-3 fatty acids and coronary heart disease*, 2000 (<http://www.fda.gov>)
- [24] <http://www.eufic.org/article/en/artid/The-importance-of-omega-3-and-omega-6-fatty-acids/>
- [25] *Human Vitamin and Mineral Requirements*, Report of a joint FAO/WHO expert consultation, Bangkok, 2001
- [26] E.E. Santos, D.C. Lauria, C.L. Porto da Silveira, *Sci. Total Environ.* **327** (2004) 69-79

- [27] M. de la Guardia, A. Garrigues, Handbook of Mineral element in Food, Diagnosis of mineral status, Wiley Blackwell, Valencia 2015, p. 7
- [28] V. Verado, F. Feroli, Y. Riciputi., G. Lafelice, Food Chem. **114** (2009) 472-477
- [29] M. Otto, Chemometrics Statistics and Computer Application in Analytical Chemistry, Wiley-VCH, Weinheim, 1999
- [30] L. Fongaro, K. Kvaal, Food Res. Int. **51** (2013) 693-705.

JELENA FILIPOVIĆ¹
SHAHIN AHMETXHEKAJ²
VLADIMIR FILIPOVIĆ³
MILENKO KOŠUTIĆ¹

¹Naučni institut za prehrambene tehnologije, Univerzitet u Novom Sad, Bulevar cara Lazara 1, 21000 Novi Sad, Srbija

²Viša škola "Ali Hadri", Kraljica Teuta, 59, 30000 Peć, Srbija

³Tehnološki fakultet, Univerzitet u Novom Sad, Bulevar cara Lazara 1, 21000 Novi Sad, Srbija

NAUČNI RAD

TESTENINA OD SPELTE SA DODATKOM FUNKCIONALNIH KOMPONENTI

Ovaj rad istražuje uticaj dodavanja lanenog semena, semena susama ili jaja (10 g / 100 g uzorka i 20 g / 100 g uzorka) u brašno za dobijanje nove vrste testenine sa poboljšanim odnosom ω -3/ ω -6 masnih kiselina i minerali sastava. Gasna hromatografija sa masenom spektrometrijom je korišćena za kvantitativno određivanje liposolubilnog ekstrakta testenine. Post-hoc Tukey HSD test sa 95% pouzdanosti pokazuje da postoje statistički značajne razlike između posmatranih uzoraka. Dnevnom unosom 75 g testenine sa 20 g lanenog semena/100 g uzorka doprinosi unosu esencijalnih masnih kiselina (3,8 g) i poboljšanim odnosu ω -6/ ω -3 (1: 2,4). Dobijeni rezultati ukazuju da je kreiran nov proizvod sa poboljšanim nutritivnim sastavom zbog višeg sadržaja ω -3 masnih kiselina i sadržaja mineralnih materija (Ca, Zn, Cu i Fe). Testenina (PS 7) sa 20 g / 100 g jaja ima najbolji senzorni kvalitet (najbolji rezultati za miris, teksturu, ukus i ukupnu prihvatljivost 8,8, 8,9, 8,9 i 8,9).

Ključne reči: odnos ω -6/ ω -3, masne kiseline, mineralni sastav, GC-MS analysis, funkcionalna svojstva.

A. SUDHA¹
V. SIVAKUMAR²
V. SANGEETHA¹
K.S. PRIYENKA DEVI¹

¹Department of Food Technology,
Kongu Engineering College,
Perundurai, Erode, TN, India
²Department of Chemical
Engineering, Alagappa College of
Technology Campus, Anna
University, Chennai, India

SCIENTIFIC PAPER

UDC 635.23:66.: 543:664.27

IMPROVING ENZYMATIC SACCHARIFICATION OF CASSAVA STEM USING PEROXIDE AND MICROWAVE ASSISTED PRE-TREATMENT TECHNIQUES

Article Highlights

- Impact of peroxide and microwave pre-treatment on enzymatic saccharification of cassava stem was evaluated
- Microwave assisted pre-treatment was found to be effective in enhancing enzymatic saccharification of cassava stem
- Optimal factors were 1.5% NaOH, 31 min and 132 W microwave power
- Spectral and SEM studies give the information of physicochemical structural changes in the stem after pre-treatment

Abstract

The effectiveness of microwave assisted alkali (MAA) and alkaline hydrogen peroxide (AHP) pre-treatment methods in improving the enzymatic saccharification of cassava stem was investigated. Ground cassava stems were by MAA method by varying microwave power, NaOH concentration and pre-treatment time. AHP method was performed at various H₂O₂ concentrations, pre-treatment temperatures and times. The results showed that reducing sugar yield was higher from MAA pretreated stem when compared with AHP pre-treatment, which demonstrated that MAA pre-treatment was effective in releasing sugars. SEM studies on the pre-treated samples revealed extensive distortion of fibres in MAA pre-treated than AHP pre-treated samples, which showed pores and cracks in the fibrous structure. Spectral studies showed the change in the chemical structure of pre-treated samples. The work revealed that the studied pre-treatment methods were effective in improving the enzymatic saccharification of cassava stem.

Keywords: cassava stem, pre-treatment, microwave, hydrogen peroxide.

There is an increasing worldwide interest in using fuels from renewable resources, for instance ethanol, due to a rising alarm about the depletion of our world's fossil fuel reserves and its greenhouse effect [1]. The production of value added fuels and chemicals from biomass through bioconversion offers potential, economic, environmental and planned advantages over products from fossils [2]. Lignocellulosic

biomass, such as agro-industrial residues, which are cheap and abundant in nature, seems to be potential feedstock for the production of second generation bio-fuels [3]. Conversion of lignocellulosic biomass to fermentable sugars can be accomplished by dilute acid or cellulase [4]. As enzymatic hydrolysis is milder and more specific and does not produce byproducts [5], it seems to be the most promising approach for ethanol production. However, the hydrolytic process is affected by two categories of factors such as structural substrate factors (degree of crystallinity, degree of polymerization, structural composition and available surface area) and mechanical factors (thermal inactivation, cellulase adsorption, and synergism) [6,7]. Consequently, prior to enzymatic hydrolysis, lignocel-

Correspondence: V. Sivakumar, Department of Chemical Engineering, Alagappa College of Technology Campus, Anna University, Chennai, India.

E-mail: drvsivakumar@yahoo.com

Paper received: 13 November, 2015

Paper revised: 9 August, 2016

Paper accepted: 10 October, 2016

<https://doi.org/10.2298/CICEQ151113050S>

lulosic biomass require pre-treatment to increase their digestibility and accessibility by cellulolytic enzymes to cellulosic fibres [8].

Cassava (*Manihot esculenta* Crantz.) crop is cultivated in an area of 20 million ha, with a total production of 256.53 million t in approximately 102 countries of the world and it meets approximately 6% of the world's dietary energy. In India, with a total production of 9.62 million t, it is cultivated in 0.28 million ha. The mature cassava plant contains 50% roots, 44% stems and 6% leaves. The primary agricultural residues from cassava include leaves and stems and the secondary processing waste comprises the cassava peels. The annual yield of dry primary and secondary processing waste in India come to 2.24 and 0.48 million t, respectively [9]. Cassava stem, after harvesting of the starchy roots, is mostly abandoned or burned in the wild. Only 10-20% of the stems are used as mushroom substrates and for propagation, or recycled to maintain soil fertility. As cassava stem is lignocellulosic in nature and to fully utilize it as a potential feedstock for bioethanol production, pre-treatment is required in order to render the cellulosic fibers more accessible to enzymatic hydrolysis. The studies on pre-treatment of cassava stem by hydrothermal treatments [9], dilute acid hydrolysis at high temperatures [10] and wet oxidation [11] makes the process expensive because of the use of steam and there arises a need for the use of corrosion resistant reactors [12].

Microwave irradiation has been widely used for process operations because of the shorter processing time and higher heating efficiency [13]. Microwave (MW) pre-treatment of rice straw and bagasse slurry has been found to improve enzymatic hydrolysis [14]. It has been reported that microwave irradiation could modify the ultra-structure of cellulose, degrade lignin and hemicellulose and thereby increase its enzymatic degradability [15,16]. Alkaline pre-treatments at low temperatures have been reported to be effective although most of the pre-treatment studies have focused on acidic conditions and temperatures greater than 150 °C. AHP pre-treatment have been applied to a number of lignocellulosic biomass and conditions. Following SO₂ steam pre-treatment of softwood or dilute acid pre-treatment of corn stover, AHP has also been studied as a post-treatment for delignification [17]. Hydrogen peroxide has the advantages of not leaving residues in the biomass, as it degrades into oxygen and water and practically there is no formation of secondary products [8].

In this work, the efficacy of microwave assisted alkali pre-treatment (MAA) and alkaline hydrogen

peroxide (AHP) pre-treatment technologies were studied in improving the release of reducing sugars from cassava stem after enzymatic saccharification. These two processes were selected because both are alkaline processes, and are predicted to cause less sugar loss than acid processes [18]. The ultra-structural changes occurring during pre-treatment are also studied.

MATERIALS AND METHODS

Substrate

Cassava stems were collected from a farm in Chennimalai, Tamilnadu, India, and washed manually using tap water to remove dirt, dried at 50 °C in a hot air oven for 5 days, milled, screened to select the fraction of particles with a size of 800 µm, homogenized in a single lot and stored at 4 °C until needed.

Pre-treatment

The pre-treatment methods evaluated were AHP and MAA. The effect of hydrogen peroxide concentration (0.9-6%), pre-treatment time (9.54-110.4 min) and temperature (23.1-56.8 °C) were evaluated during AHP method. The pre-treatment solution of alkaline peroxide was prepared by dissolving H₂O₂ in distilled water and adjusting the pH to 11 with sodium hydroxide. Cassava stem (5 g) was treated with 100 ml of the pre-treatment solution in 250 ml flasks in an orbital shaker (REMI CIS-24BL) agitated at 100 rpm. In MAA pre-treatment method, the effect of sodium hydroxide concentration (0.6-2.3%), microwave power (106-173 W) and pre-treatment time (13-46 min) were evaluated under atmospheric pressure. Cassava stem (5 g) was treated with 100 ml sodium hydroxide solution with solid liquid ratio of 1:5 (g/ml) and placed in microwave (ENERZI Microwave Systems Pvt. Ltd, 2.45 GHz, max. output 800 W). After pre-treatment, the contents were filtered through Whatman No. 1 filter paper and the supernatant was subjected to sugar, furfural and acetic acid analyses. The alkali in the solid residue was removed by washing with distilled water repeatedly. The residues were dried at 100 °C until constant weight was observed and used to calculate the mass loss during pre-treatment. The wet residue was further subjected to enzymatic hydrolysis. The effect of variables on reducing sugar yield was evaluated using central composite design (CCD) using 20 experimental runs.

Enzymatic hydrolysis

The pre-treated cassava stem was suspended in 100 ml of 50 mM sodium citrate buffer (pH 4.8) containing amylase, amyloglucosidase, cellulase and β-glucosidase supplemented with 0.02% sodium

azide under aseptic conditions. As cassava stem contains considerable amount of starch, it was treated with amylase (Himedia[®] Laboratories, 200U/g biomass) and amyloglucosidase from *Aspergillus niger* (70 U/mg, Sigma-Aldrich Co, St. Louis, MO). Cellulases (SRL, India) loading was 20 FPU/g biomass. β -Glucosidase (SRL, India) was added to completely convert cellobiose to glucose, loading 1.00 IU/g biomass. The reaction mixture was incubated in a shaking incubator at 50 °C and 120 rpm [19]. Aliquots were taken regularly at intervals and analyzed for reducing sugars after deactivating the enzymes by boiling. The value of reducing sugar yields used for the statistical analysis was picked at the reaction time after which no significant changes in the variable was noticed. Experiments were conducted in triplicate and the mean values were used in the analyses.

Analytical methods

The biomass under study was analysed for the biochemical composition. The total starch content in cassava stem was determined by using the hydrolytic enzymes such as amylase and amyloglucosidase. Cassava stem slurry (5%) was treated with amylase (50.0 mg) at 90 °C for 45 min at pH 5.5. After 45 min, the slurry was brought to room temperature (30±1 °C) and its pH was lowered to 4.6. Amyloglucosidase (70 U) was then added to it and kept for incubation at room temperature for 24 h and the glucose released was assayed by anthrone method of Sadasivam and Manickam [20]. Since glucose was originally present in the samples, enzyme blank was also kept to nullify the values. Starch content was calculated from the glucose value using the Morris factor, 0.9. The crude protein content of the cassava stem was determined by Kjeldahl method using automatic Nitrogen digestion and distillation system (Biokjel, TechnoReach). The percentage of protein was calculated by multiplying nitrogen content with 6.25.

Ash content was determined by igniting the sample in muffle furnace at 550 °C for 7 h. The ash percentage was calculated from the weight of ash. Cellulose was estimated by the method of Sadasivam and Manickam [20] using acetic/nitric reagent. Cassava stem (0.5 g) was boiled with 3 ml acetic/nitric reagent for 20 min and cooled. The suspension was centrifuged at 4000 rpm for 20 min and the supernatant was discarded. The residue was washed with distilled water and suspended in 10 ml of 67% H₂SO₄ for 1 h during which hydrolysis takes place. The hydrolysate was appropriately diluted and was added to the diluted aliquot 10 ml anthrone reagent. The colour developed was read spectrophotometrically at 630 nm. The cellulose content was calculated from the optical density of pure cellulose.

metrically at 630 nm. The cellulose content was calculated from the optical density of pure cellulose.

Hemicellulose content was determined by detergent extraction method of Goering and Van Soest [21] by taking the difference of neutral detergent fibre (NDF) and acid detergent fibre (ADF). NDF was determined by boiling 1 g of cassava stem with 10 ml of cold neutral detergent solution, 2 ml decahydronaphthalene and 0.5 g sodium sulphite for 1 h. After 1 h, the mixture was filtered, washed with acetone and dried at 100 °C for 8 h. The weight of the dry residue is noted as NDF. ADF was determined by heating 1 g cassava stem with 100 ml acid detergent solution for 1 h. After 1 h, the mixture was filtered, washed and dried at 100 °C for 8 h. The weight of the dry residue was noted as ADF. Lignin content was determined by subtracting cellulose and ash content (%) from ADF(%).

The reducing sugar concentration was determined using 3,5-dinitrosalicylic acid (DNS) method [22]. Glucose, xylose, arabinose and acetic acid were determined using high performance liquid chromatography (HPLC) coupled with UV and refractive index detector (Shimadzu, Japan) and C18 column (Enable C18G, 5 μ m, 250 mm×4.6 mm) using acetonitrile and water as mobile phase at a flow rate of 0.6ml/min. Furfural was detected at 280 nm [23]. The morphological differences of untreated and pre-treated cassava stem were examined using scanning electron microscopy (JEOL Ltd., Tokyo, Japan). The changes in the functional groups of cassava stem before and after pre-treatment were analyzed by Fourier-transform infrared spectroscopy (FTIR) (Bruker ALPHA, Germany). The spectra were recorded between 4000 and 600 cm⁻¹.

Statistical analysis

ANOVA and regression analyses were executed to study the direct and interactive effects of variables. Coefficients of the model developed were analyzed for their significance and the insignificant ones were eliminated from the model. The optimal levels of the variables and predicted response were obtained by solving second-order polynomial model for maximization of response using Design Expert software (version 8.0.7.1, Stat-Ease, Inc., USA).

RESULTS AND DISCUSSION

Pre-treatment of lignocellulosic resources are regularly studied to enhance the hydrolysis of cellulose by reducing the crystallinity of cellulose fibre and, lignin and hemicellulose contents, and increasing the porosity of cellulose [24]. The type of pre-treatment method adopted influences the structural

modifications, based on which the extent of enzymatic hydrolysis of the biomass depends [25]. CCD with five replicates in the central point was performed for each pre-treatment considered to study the influence of process parameters.

Composition of cassava stem

Characterization of the lignocellulosic biomass is the key step in designing appropriate pre-treatment techniques and the production of bioethanol depends on biomass quality. Raw cassava stem contained 18.4% starch, 23.3% cellulose, 27.6% hemicelluloses, 21.8% lignin, 3.8% protein and 3.5% ash (% dry weight). The results indicated that cassava stem could be a potential feedstock as the major constituents are carbohydrates.

Effect of pre-treatment on composition of liquor

It is necessary to analyze the sugars and the degradation products in order to identify the mechanism by which the pre-treatment methods influence the process. It has been established that furfural is the direct degradation product of xylose. Moreover, acetic acid is produced from the decomposition of O-acetyl groups in the branched chain of hemicellulose [26]. The more the acetic acid recovered, the more the hemicellulose decomposed. Xylose was the major product in all experiments (Table 1). Furfural concen-

trations ranged from 0.26 to 0.63 g/L in MAA method and it was negligible in AHP method. Acetic acid release was below the inhibitory concentration (6 g/L) which ranges from 1.10 to 5.56 g/L in AHP method and from 1.42 to 6.43 g/L in MAA method, above this level may affect the activity of cellulase and production of ethanol [27].

Effect of pre-treatment on mass loss

Table 2 shows the solid loss during AHP and MAA pre-treatment of cassava stem. In AHP method, H₂O₂ concentration and pre-treatment time had a significant effect on mass loss. The mass loss ranged from 14.37 mass% at low concentration of H₂O₂ to 41.87% at high concentration of H₂O₂. Although both H₂O₂ concentration and pre-treatment time contributed to the mass loss, H₂O₂ concentration was found to have the greatest impact on mass loss. Banerjee [17] observed a 35% decrease in total insoluble biomass after AHP pre-treatment of corn stover. In MAA method, NaOH concentration was found to have significant effect on mass loss, which ranged from 21.47 to 45.33 mass%. The mass loss increased as the concentration of NaOH was increased. McIntosh and Vancov [28] have found loss of hemicelluloses following exposure to alkaline substances during the pre-treatment process. Alkali is effective at solubilizing grass xylans although much of the solubilised

Table 1. Composition (g/L) of liquor obtained after the pre-treatment of cassava stem

Run	AHP				MAA				
	Glucose	Arabinose	Xylose	Acetic acid	Glucose	Arabinose	Xylose	Acetic acid	Furfural
1	0.24	0.82	4.15	3.75	0.32	0.98	4.56	5.42	0.54
2	0.31	0.92	4.24	4.45	0.41	1.26	6.54	5.42	0.62
3	0.26	1.23	6.45	4.21	0.24	1.34	6.89	5.32	0.42
4	0.26	0.87	4.24	3.54	0.42	0.96	4.36	4.34	0.34
5	0.28	0.94	5.67	3.23	0.45	1.06	6.01	4.32	0.58
6	0.25	1.02	6.34	3.56	0.38	1.24	6.52	5.67	0.32
7	0.32	0.84	4.27	1.27	0.41	1.56	6.32	5.83	0.46
8	0.26	0.78	3.45	1.43	0.37	0.86	3.89	4.45	0.42
9	0.24	1.12	6.24	2.67	0.34	0.98	5.28	4.76	0.54
10	0.38	1.34	5.45	3.74	0.4	0.89	4.63	6.43	0.48
11	0.35	0.87	3.43	2.45	0.29	1.24	5.41	5.42	0.36
12	0.32	0.96	5.67	2.32	0.39	0.92	5.26	6.41	0.41
13	0.31	1.32	7.24	5.56	0.38	1.22	4.92	5.62	0.5
14	0.24	0.86	4.01	1.1	0.32	0.74	3.21	6.43	0.63
15	0.21	0.94	4.21	3.54	0.45	0.82	5.01	5.42	0.52
16	0.25	0.96	5.32	1.62	0.35	0.78	3.46	3.21	0.26
17	0.27	0.92	5.32	2.48	0.25	0.98	5.43	6.34	0.32
18	0.24	1.02	6.83	4.65	0.21	0.92	6.28	2.85	0.54
19	0.31	1.23	6.1	3.21	0.46	1.13	5.89	5.43	0.64
20	0.26	0.92	5.31	2.83	0.18	0.86	3.23	1.42	0.21

Table 2. Design matrix presenting reducing sugar yield after hydrolysis and percentage of mass loss for the pre-treated cassava stem with alkaline hydrogen peroxide (AHP) and microwave assisted alkali (MAA)

Run	AHP Experimental factors			MAA Experimental factors			Reducing sugar yield, mg/g pulp		Mass loss, %	
	H ₂ O ₂ conc., %	Temperature, °C	Pre-treatment time, min	NaOH conc., %	Microwave power, W	Pre-treatment time, min	AHP	MAA	AHP	MAA
1	3.5	40	60	2.3	140	30	409.0	397.7	38.54	38.23
2	3.5	40	60	1	160	40	412.7	321.7	34.63	25.36
3	2	50	30	1.5	140	30	286.3	456.0	25.32	44.24
4	6.0	40	60	1.5	140	30	442.7	451.7	41.87	43.97
5	2	50	90	1.5	140	30	297.3	457.3	21.54	45.14
6	2	30	90	2	120	20	286.0	431.0	20.32	35.36
7	0.9	40	60	1.5	140	30	243.7	457.3	14.37	36.22
8	3.5	40	60	2	120	40	421.7	431.3	36.49	38.28
9	3.5	40	60	2	160	20	417.7	289.0	37.25	32.34
10	5	30	90	1	160	20	447.7	263.7	39.43	31.23
11	3.5	40	60	1.5	140	30	415.7	459.0	36.14	44.55
12	2	30	30	1.5	140	46.8	274.3	416.7	24.59	44.24
13	5	50	90	1.5	140	13.1	416.0	331.3	36.22	31.22
14	3.5	40	9.54	1.5	173.6	30	254.7	318.0	18.31	41.37
15	5	30	30	1.5	140	30	367.0	453.0	30.95	45.33
16	3.5	23.1	60	1	120	40	367.3	354.0	30.23	35.39
17	3.5	40	60	2	160	40	396.3	378.0	36.88	38.42
18	3.5	56.8	60	1.5	106.3	30	413.7	420.7	35.77	33.24
19	5	50	30	1	120	20	387.3	361.3	31.24	35.32
20	3.5	40	110.4	0.6	140	30	347.3	274.7	35.39	21.47

xylan may reprecipitate when pH is decreased for hydrolysis [17].

Effect of alkaline hydrogen peroxide pre-treatment

Alkali pre-treatment incorporates the use of alkaline solutions to remove various uronic acid substitutions on hemicellulose and lignin that reduces the enzyme accessibility to cellulose and hemicellulose. Generally, alkaline pre-treatment is found to be more effective on herbaceous crops and agricultural residues than on wood materials. Peroxide pre-treatment reduces cellulose crystallinity by oxidative delignification and enhances enzymatic conversion. Increased cellulose availability and lignin solubilisation were observed during the peroxide pre-treatment of wheat straw, Douglas fir and oak [29].

Table 2 shows the design matrix, reducing sugar yield after hydrolysis and percentage of mass loss for the pre-treated cassava stem with AHP. An analysis of variance was performed and the results are shown in Table 3. The results specified that the fitting model ($p < 0.0001$) was highly significant. The coefficient of determination (R^2) was 0.959, which indicated that the model could explain 95.9% variability of the response variable. The adjusted value of coefficient of deter-

mination ($R^2 = 0.944$) was also satisfactory, indicating the significance of the model.

Analysis of the response trend showed that the model could explain the effect of hydrogen peroxide concentration, temperature and pre-treatment time on reducing sugar yield satisfactorily. The coefficients calculated for each variable by regression analysis are presented in Table 3. The regression coefficients of linear and squared terms for the variables such as, H₂O₂ concentration and pre-treatment time were highly significant ($p < 0.05$). The interactive effect of H₂O₂ concentration and pre-treatment time was significant for reducing sugar yield at the 90% confidence level ($p < 0.1$). The temperature had no significant effect on reducing sugar yield. The positive coefficients of H₂O₂ concentration and pre-treatment time suggest that these factors had a positive influence on reducing sugar yield. Alkaline peroxide pre-treatment of wheat straw has been studied and found to remove 65.97% lignin and 20.10% hemicelluloses of raw materials. AHP pre-treated wheat straw (1.5% NaOH, 50 °C, 6h and 0.3% H₂O₂, 6 h) showed 97.01% enzymatic hydrolysis rate [4]. Rabelo *et al.* [8] have obtained 494.7 mg/g reducing sugar on enzymatic hydrolysis from sugarcane bagasse pre-treated at 20

Table 3. ANOVA for quadratic model^f and regression coefficients of the model for reducing sugar yield after hydrolysis of AHP pre-treated cassava stem; coefficient of determination, $R^2 = 0.959$; adjusted $R^2 = 0.944$; coefficient of variation (CV): 4.28%; SS, sum of squares; DF, degree of freedom; MS, mean square; A: H_2O_2 concentration (%), B: temperature ($^{\circ}C$), C: pre-treatment time (min); p value less than 0.05 indicates model terms are significant

Source	SS	DF	MS	Coefficient estimate	Standard error	F value	probability (P) > F
Intercept	-	-	-	406.5295	5.422901	66.11762	< 0.0001
A	-	-	-	59.22131	4.238588	195.2151	< 0.0001
C	-	-	-	21.07616	4.238588	24.72523	0.0002
AC	-	-	-	10.8375	5.537983	3.829614	0.0706
A^2	-	-	-	-22.7882	4.10576	30.80575	< 0.0001
C^2	-	-	-	-37.7081	4.10576	84.34954	< 0.0001
Model	81111.12	5	16222.22	-	-	66.11762	< 0.0001
Residual (error)	3434.956	14	245.354	-	-	-	-
Lack of fit	3038.908	9	337.6564	-	-	4.262818	0.0624
Pure error	396.0483	5	79.20967	-	-	-	-
Total	84546.07	19	-	-	-	-	-

$^{\circ}C$ with 5% H_2O_2 for 24 h. Cotton stalk pre-treated with 2% H_2O_2 for 60 min at 121 $^{\circ}C$ and 15 psi showed 49.8% of cellulose conversion [29].

The optimal pre-treatment conditions for maximum reducing sugar yield considering efficiency were H_2O_2 concentration of 4.91%, temperature of 40.3 $^{\circ}C$ and pre-treatment time of 76.7 min, which would result in a predicted reducing sugar yield of 447.71 mg/g cassava stem. To confirm the result of the predicted value, experiments were performed at the optimal condition which was suggested as 5% H_2O_2 /77 min at 40 $^{\circ}C$. Another trial was conducted at room temperature, since the temperature was found to be an insignificant factor. The reducing sugar yield from the experiment conducted at 40 $^{\circ}C$ and room temperature were found to be 445.6 ± 2.5 and 441.3 ± 1.5 mg/g cassava stem respectively, which does not have a significant difference. The optimized condition was found to be 5% H_2O_2 and 77 min.

Effect of microwave assisted alkali pre-treatment

Some studies have reported that microwave irradiation could degenerate lignin and hemicelluloses in lignocellulosic biomass and change the ultra-structure of cellulose, thereby augmenting the enzymatic susceptibility of lignocellulosic biomass [13]. MAA pre-treatment of wheat straw was found to lower sugar losses and enhance hydrolysis rates than conventional alkali pre-treatment methods [30]. A significant increase in the conversion of starch materials to glucose, on pre-treating with microwave irradiation has been reported [15,30]. Combination of microwave treatment with either acid or alkali or combined acid/alkali, an option for pre-treatment of lignocellulosic biomass, has been recently explored [12,30,31].

Table 2 shows the design matrix, reducing sugar yield after hydrolysis and percentage of mass loss for the pre-treated cassava stem with MAA method. An analysis of variance was performed and the results are shown in Table 4. The results specified that the fitting model ($p < 0.0001$) was highly significant. The coefficient of determination (R^2) was 0.987, which indicated that the model could explain 98.7% variability of the response variable. The model was considered as significant, as the adjusted value of coefficient of determination ($R^2 = 0.978$) was satisfactory. Analysis of the response trend was rational and the model explained the effect of NaOH concentration, microwave power and pre-treatment time, on reducing sugar yield satisfactorily. Model coefficients were determined by regression analysis and their significance was tested. The values for linear, square and interaction effects are presented in Table 4. The regression coefficients of linear and squared terms were highly significant ($p < 0.0001$) and the interactive effects of NaOH concentration and microwave power, and microwave power and pre-treatment time were significant ($p < 0.05$). Positive coefficients indicate a linear increase in reducing sugar yield while negative coefficients indicate a linear decrease in reducing sugar yield. Among the various factors, microwave power had a negative effect on reducing sugar yield during MAA pre-treatment. It supports previous studies that hemicellulose removal and cellulose digestibility has been enhanced by increasing severity (pre-treatment time and temperature) of pre-treatment process [32]. An extended pre-treatment time with a higher microwave power could also lead to a decrease in reducing sugar yield, because increase in pre-treatment time and microwave power increases

Table 4. ANOVA for quadratic model and regression coefficients of the model for reducing sugar yield after hydrolysis of MAA pre-treated cassava stem; coefficient of determination (R^2) = 0.987; adjusted R^2 = 0.978; coefficient of variation (CV): 2.5%; SS, sum of squares; DF, degree of freedom; MS, mean square; A: NaOH concentration (%), B: microwave power (W), C: pre-treatment time (min); p value less than 0.05 indicates model terms are significant

Source	SS	DF	MS	Coefficient estimate	Standard error	F value	probability (P) > F
Intercept				455.7259	3.987539	110.7765	< 0.0001
A				31.88586	2.645641	145.2561	< 0.0001
B				-36.4594	2.645641	189.9136	< 0.0001
C				20.76797	2.645641	61.62062	< 0.0001
AB				-8.175	3.456697	5.593104	0.0375
BC				19.25	3.456697	31.01265	0.0002
A ²				-42.3156	2.57546	269.955	< 0.0001
B ²				-30.5953	2.57546	141.1237	< 0.0001
C ²				-28.9513	2.57546	126.3648	< 0.0001
Model	84899.26	9	9433.251			109.024	< 0.0001
Residual (error)	865.2453	10	86.52453				
Lack of fit	825.857	5	165.1714			20.96705	0.0023
Pure error	39.38833	5	7.877667				
Total	85764.5	19					

the pre-treatment temperature, which could activate degradation of sugars in the pre-treatment process [32,33]. Alkali cause less degradation of sugars as it do not favour dehydration [34]; however, alkali release acetyl and other acidic groups on hemicelluloses and produce organic acids that lower the pH [35]. For example, at high temperature, furfural, an undesirable end-product of xylose decomposition is formed, resulting in a much lower total xylose yield [36].

The optimal pre-treatment conditions for highest reducing sugar yield considering efficiency were NaOH concentration of 1.48%, microwave power of

131.37 W and pre-treatment time of 30.96 min, which would result in a predicted reducing sugar yield of 464.9 mg/g cassava stem. To confirm the result of the predicted value, experiments were conducted at the optimal conditions (1.5% NaOH, 132 W and 31 min), displaying the reducing sugar yield of 463.3±1.5 mg/g cassava stem.

Spectral characterization

The FTIR spectra of native and treated cassava stem at optimized conditions of AHP method and MAA method are shown in Figure 1. The most rep-

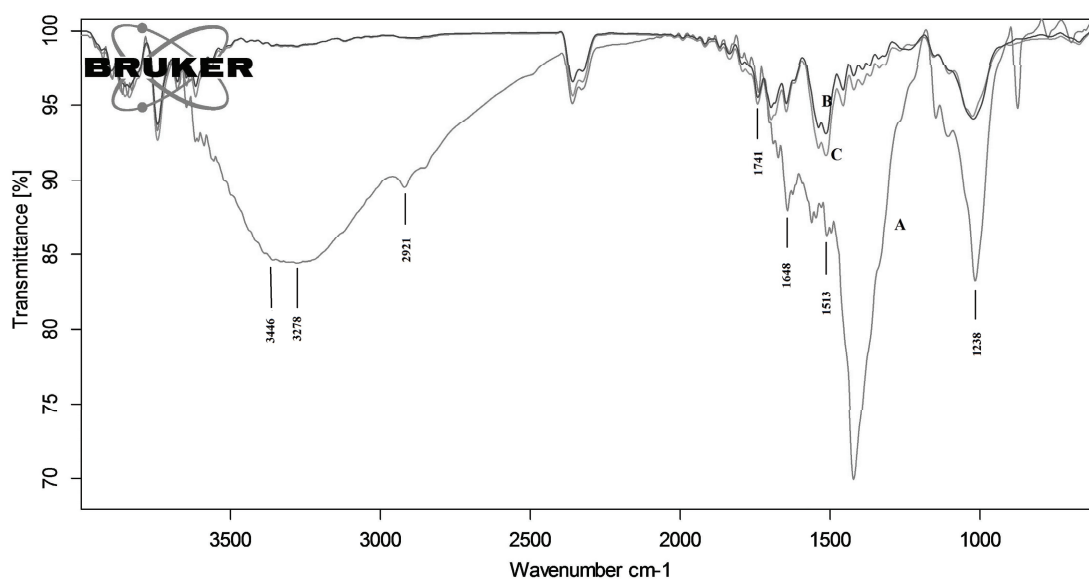


Figure 1. FTIR spectra of native cassava stem (A), MAA pre-treated (B), 1.5% NaOH, 132 W, 31 min, and AHP pre-treated cassava stem (C), 5% H₂O₂, 40 °C, 77 min.

representative bands can be briefed as follows. The broad absorption at $3278\text{--}3446\text{ cm}^{-1}$ related to the stretching of H-bonded OH groups, and one at 2921 cm^{-1} to the C-H stretching [37,38]. The absorption peak at 1741 cm^{-1} could be attributed to the acetyl groups of hemicelluloses or to the ester linkage of carboxylic stretching group of ferulic acid [39]. The occurrence of peak at 1513 cm^{-1} was attributed to the aromatic skeletal vibrations of the associated lignin in the hemicelluloses [40]. The band region between 1650 and 1410 cm^{-1} indicates the stretching of the aromatic phenyl ring of lignin. Absorption at $1000\text{--}1200\text{ cm}^{-1}$ was related to the structural features of cellulose and hemicelluloses. The peak between 1019 and 1028 cm^{-1} interprets the C-O(H) stretching, which was found with cellulose containing higher C=O compounds. The peak at 1238 cm^{-1} indicates C-O-C stretching at $\beta(1\text{--}4)$ glycosidic linkages of cellulose [23]. The profile of FTIR spectra of native AHP and MAA pre-treated cassava stem were different. This illustrated that there were structural changes in the cassava stem and partial removal of lignin and hemicellulose. The low signal intensity at 1744 cm^{-1} in AHP and MAA pre-treated cassava stem imply that alkali have cleaved the ester bond of hemicelluloses. The absorption peak at 1513 cm^{-1} was found to be smaller in MAA pre-treatment than in AHP pre-treatment. This implies that MAA pre-treatment was effective in solubilizing lignin. The MAA pre-treatment gave maximum reducing sugar yield on enzymatic hydrolysis compared to AHP pre-treatment. The pore size

of the substrate compared to the size of enzyme is one of the major factors restricting the enzymatic hydrolysis of lignocelluloses. There are reports that removal of hemicelluloses could increase the pore size thereby, permitting accessibility for the degrading enzymes to reach cellulose [9]. The broadness of the peak at 3280 cm^{-1} was reduced in pre-treated cassava stem compared to native cassava stem. It might be due to microwave irradiation and alkali which enhances the saponification of intermolecular ester bonds cross-linking xylan hemicelluloses and lignin or other hemicelluloses, and hence O-H absorption band intensity lowers due to its involvement in this reaction [13].

Scanning electron microscopy analysis

Scanning electron microscopy (SEM) analysis was performed to establish the structural changes and surface characteristics of cassava stem after pre-treatment. The cassava stem pre-treated at optimized conditions of AHP method and MAA method were imaged by SEM. As shown in Figure 2, the pre-treatment resulted in significant physical changes. The SEM images of native cassava stem showed the presence of starch granules along with fibrous materials. The native stem appears to have an even and smooth flat surface, revealing a rigid surface structure (Figure 2a), while the pre-treated samples had a rugged, rough, and broken surface (Figure 2b and c). The images clearly demonstrate that the pre-treatment could change the lignocellulosic structure and distorted the fibers of cassava stem. These alterations of

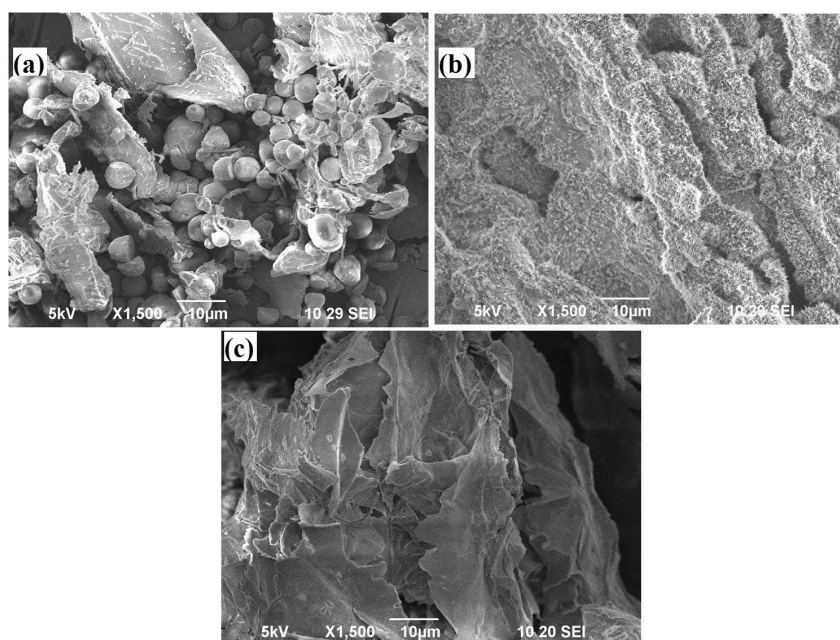


Figure 2. Scanning electron micrographs. a) native cassava stem, b) MAA pre-treated cassava stem (1.5% NaOH, 132 W, 31 min) and c) AHP pre-treated cassava stem (5% H_2O_2 , 40 °C, 77 min).

structure and reduction in crystallinity could be expected to increase the enzyme accessibility to cellulosic fibres by increasing surface area. Cassava stem pre-treated by MAA method was found to show extensive distortion of the structure and increase in surface area when compared with AHP pre-treated biomass. The pre-treatment of cassava stem by microwave irradiation together with alkali seems to be disintegrating the fibers completely.

Comparative analysis of pre-treatment effect on reducing sugar yield

Untreated cassava stem yielded 123 mg/g of reducing sugar after enzymatic saccharification whereas after AHP and MAA pre-treatment the yield was 445.6 and 463.3 mg/g, respectively. The results indicated that pre-treatment methods have improved the hydrolysis yield fourfold when compared to native cassava stem. MAA pre-treatment method has enhanced the performance of saccharification considerably than AHP pre-treatment of cassava stem. The reducing sugar yield after AHP pre-treatment was found to be slightly lower than reducing sugar yield after MAA pre-treatment. SEM analysis has indicated extensive disintegration of fibres in MAA pre-treated stem than AHP pre-treated stem. A degradation byproduct (acetic acid) was formed in MAA pre-treatment but its concentration was less than the inhibitory limit (6 g/L) for cellulase activity and fermentation. The profile of FTIR spectra of native, AHP and MAA pre-treated cassava stem were different. This indicates that there were structural changes of cellulose and partial removal of lignin and hemicelluloses. The spectra of MAA pre-treated cassava pulp have shown low intensity of absorption peaks at 1516 indicating the removal of lignin effectively compared to AHP method. There is a statistically significant difference in the reducing sugar yield from cassava stem pre-treated by MAA and AHP methods. Hence, pre-treatment with microwave assisted alkali can be preferred as it takes less time and is efficient in enhancing the reducing sugar yield.

CONCLUSION

The effectiveness of AHP and MAA pre-treatment in improving cassava stem amenability to enzymatic hydrolysis was evaluated. The processing conditions for the pre-treatment methods were optimized and their influence on the reducing sugar yield was studied using CCD. Good correlations between the experimental and predicted reducing sugar yields were found. Pre-treatment of cassava stem resulted in an improved reducing sugar yield (four fold) on

enzymatic hydrolysis when compared to native cassava stem. The changes in chemical structure as well as physical characteristics made the pre-treated cassava stem more susceptible to enzymatic saccharification. Both AHP and MAA pre-treatment methods were found to be effective in enhancing saccharification of cassava stem, however, the latter was significantly superior in improving the reducing sugar yield than the former.

REFERENCES

- [1] G. Ramadoss, K. Muthukumar, *Chem. Ind. Eng. J.* **260** (2015) 178-187
- [2] R.P. Anex, L.R. Lynd, M.S. Laser, A.H. Heggenstaller, M. Liebman, *Crop Sci.* **47** (2007) 1327-1335
- [3] T. Dalgaard, U. Jorgensen, J.E. Olesen, E.S. Jensen, E.S. Kristensen, *Science* **312** (2006) 1743-1744
- [4] B. Qi, X. Chen, F. Shen, Y. Su, Y. Wan, *Ind. Eng. Chem. Res.* **48** (2009) 7346-7353
- [5] Z. Wen, W. Liao, S. Chen, *Bioresour. Technol.* **91** (2004) 31-39
- [6] L.R. Lynd, P.J. Weimer, W.H. van Zyl, I.S. Pretorius, *Microbiol. Mol. Biol. Rev.* **66** (2002) 506-577
- [7] S.D. Mansfield, C. Mooney, J.N. Saddler, *Biotechnol. Prog.* **15** (1999) 804-816
- [8] S.C. Rabelo, R. Maciel Filho, A.C. Costa, *Appl. Biochem. Biotechnol.* **148** (2008) 45-58
- [9] N.S. Pooja, G. Padmaja, *Waste Biomass Valorization* **6** (2015) 303-315
- [10] C. Martin, B. Alriksson, A. Sjöde, N.O. Nilvebrant, L.J. Jönsson, *Appl. Biochem. Biotechnol.* **137** (2007) 339-352
- [11] C. Martin, A.B. Thomsen, *J. Chem. Technol. Biotechnol.* **82** (2007) 174-181
- [12] P. Binod, K. Satyanagalakshmi, R. Sindhu, K.U. Janu, R.K. Sukumaran, A. Pandey, *Renew. Energy* **37** (2012) 109-116
- [13] S.M. Nomanbhay, R. Hussain, K. Palanisamy, *J. Sustain. Bioenergy Syst.* **3** (2013) 7-17
- [14] H. Ooshima, K. Aso, Y. Harono, T. Yamamoto, *Biotechnol. Lett.* **6** (1984) 289-294
- [15] T. Palav, K. Seetharaman, *Carbohydr. Polym.* **67** (2007) 596-604
- [16] A.T.W.M. Hendriks, G. Zeeman, *Bioresour. Technol.* **100** (2009) 10-18
- [17] G. Banerjee, S. Car, T. Liu, D. L. Williams, S. L. Meza, J. D. Walton, D. B. Hodge, *Biotechnol. Bioeng.* **109** (2012) 922-931
- [18] W.E. Kaar, M.T. Holtzaple, *Biomass Bioeng.* **18** (2000) 189-199
- [19] R. Velmurugan, K. Muthukumar, *Bioresour. Technol.* **112** (2012) 293-299
- [20] S. Sadasivam, A. Manickam, *Biochemical Methods*, New Age International Publishers, New Delhi, 1996

- [21] H.K. Goering, P.J. Van soest, Forage fibre analysis, in: Agriculture Handbook, Agricultural Research Services, United States Department of Agriculture, 1970
- [22] G.L. Miller, Anal. Chem. **31** (1959) 426-428
- [23] G. Ramadoss, K. Muthukumar, Biochem. Eng. J. **83** (2014) 33-41
- [24] Y. Sun, J. Cheng, Bioresour. Technol. **83** (2002) 1-11
- [25] P. Kumar, D.M. Barrett, M.J. Delwiche, P. Stroeve, Ind. Eng. Chem. Res. **48** (2009) 3713-3729
- [26] Q. Yu, X. Zhuang, Z. Yuan, W. Qi, Q. Wang, X. Tan, Bioresour. Technol. **102** (2011) 3445-3450
- [27] S. Larsson, E. Palmqvist, B. Hahn-Hagerdal, C. Tengborg, K. Stenberg, G. Zacchi, N. Nilvebrant, Enzyme Microb. Technol. **24** (1999) 151-159
- [28] S. McIntosh, T. Vancov, Bioresour. Technol. **101** (2010) 6718-6727
- [29] R.A. Silverstein, Y. Chen, R.R. Sharma-Shivappa, M.D. Boyette, J. Osborne, Bioresour. Technol. **98** (2007) 3000-3011
- [30] S. Zhu, Y. Wu, Z. Yu, Q. Chen, G. Wu, F. Yu, C. Wang, S. Jin, Process Biochem. **94** (2006) 437-442
- [31] Z. H. Hu, Z.Y. Wen, Biochem. Eng. J. **38** (2008) 369-378
- [32] M.A. Kabel, G. Bos, J. Zeevalking, A.G.J. Voragen, H.A. Schols, Bioresour. Technol. **98** (2007) 2034-2042
- [33] C.G. Liu, C.E. Wyman, Bioresour. Technol. **96** (2005) 1978-1985
- [34] V.S. Chang, M.T. Holtzapfel, Fundamental factors affecting biomass enzymatic reactivity, in Proceedings of Twenty-First Symposium on Biotechnology for Fuels and Chemicals, Humana Press, 2000, pp. 5-37
- [35] M. Nikzad, K. Movagharnejad, F. Talebnia, G. Najafpour, F.G.A. Hosein, Chem. Ind. Chem. Eng. Q. **20** (2014) 261-271
- [36] T. Eggeman, R.T. Elander, Bioresour. Technol. **96** (2005) 2019-2025
- [37] L. Wang, G. Han, Y. Zhang, Carbohydr. Polym. **69** (2007) 391-397
- [38] K.K. Pandey, Polym. Degrad. Stabil. **90** (2005) 9-20
- [39] F. Peng, J. Bian, P. Peng, Y. Guan, F. Xu, R.C. Sun, Bioresources **7** (2012) 4744-4759
- [40] K.K. Pandey, J. Appl. Polym. Sci. **71** (1999) 1969-1975.

A. SUDHA¹
 V. SIVAKUMAR²
 V. SANGEETHA¹
 K.S. PRIYENKA DEVI¹

¹Department of Food Technology,
 Kongu Engineering College,
 Perundurai, Erode, TN, India

²Department of Chemical Engineering,
 Alagappa College of Technology
 Campus, Anna University, Chennai,
 India

NAUČNI RAD

POBOLJŠANJE ENZIMSKE SAHARIZACIJE STABLJIKI KASAVE PRETHODNOM OBRADOM PEROKISODOM I MIKROTALASIMA

Ispitivana je efikasnost prethodne obrade mikrotalasima (MAA) i vodonik-peroksidom (AHP) u poboljšanju alkalne enzimske saharizacije stabiljki kasave. Kod MAA metode, nadzemni delovi kasave su tretirani različitim intenzitetima energije mikrotalasnog zračenja, koncentracijama NaOH i vremenima trajanja predtretmana. AHP metoda je izvedena pri različitim koncentracijama H₂O₂, temperaturama i vremenima trajanja predtretmana. Rezultati su pokazali da je smanjenje prinosa šećera bilo veće kod stabiljki tretiranih MAA nego AHP metodom, što je pokazalo da je MAA metodom bio efikasan u oslobađanju šećera. SEM fotografije prethodno tretiranih uzoraka otkrile su veće izobličjenje vlakana u uzorcima prethodno tretiranih MAA metodom, dok uzorci tretirani AHP metodom imaju pore i pukotine u fibroznoj strukturi. Spektroskopska proučavanja pokazale su promenu hemijske strukture prethodno tretiranog uzorka. Rad je otkrio da su metode predhodnog tretmana bile efikasne u poboljšanju enzimske saharizacije stabiljki kasave.

Ključne reči: stabiljke kasave, prethodni tretman, mikrotalasi, vodonik-peroksid.

DIDEM ÖZÇİMEN
M. ÖMER GÜLYURT
BENAN İNAN

Department of Bioengineering,
Faculty of Chemical and
Metallurgical Engineering, Yıldız
Technical University, Davutpasa
Campus, Istanbul, Turkey

SCIENTIFIC PAPER

UDC 662.756.3:582.26:66.095.13:54

OPTIMIZATION OF BIODIESEL PRODUCTION FROM *Chlorella protothecoides* OIL VIA ULTRASOUND ASSISTED TRANSESTERIFICATION

Article Highlights

- Ultrasound-assisted transesterification of *C. protothecoides* oil was proposed
- The optimum conditions were determined using factorial design method
- The catalyst/oil ratio was found as the most effective parameter on methyl ester yield
- This method is an alternative way to produce biodiesel efficiently and cost effective
- The highest FAME was obtained with 40 min, 9:1 methanol/oil mole ratio and 1.5% catalyst in oil

Abstract

There is a growing interest in biodiesel as an alternative fuel for diesel engines because of the high oil prices and environmental issues related to massive greenhouse gas emissions. Nowadays, microalgal biomass has become a promising biodiesel feedstock. However, traditional biodiesel production from microalgae consumes a lot of energy and solvents. It is necessary to use an alternative method that can reduce the energy and alcohol consumption and save time. In this study, biodiesel production from Chlorella protothecoides oil by ultrasound assisted transesterification was conducted and effects of reaction parameters such as methanol:oil ratio, catalyst:oil ratio and reaction time on fatty acid methyl ester yields were investigated. The transesterification reactions were carried out by using methanol as alcohol and potassium hydroxide as the catalyst. The highest methyl ester production was obtained under the conditions of 9:1 methanol/oil mole ratio, 1.5% potassium hydroxide catalyst in oil, and for reaction time of 40 min. It was also found that catalyst/oil molar ratio was the most effective parameter on methyl ester yield according to statistical data. The results showed that ultrasound-assisted transesterification may be an alternative and cost effective way to produce biodiesel efficiently.

Keywords: algal biodiesel, Chlorella protothecoides, methyl ester, transesterification, ultrasound.

Today, substitution of non-conventional sources such as biodiesel over traditional ones is inevitable due to the depletion of petroleum based sources, high oil prices, and air pollution caused by the combustion of conventional petroleum-based diesel. Development of industrial growth, transportation, and many other

basic human needs are met with petroleum based fuels. Worldwide average demand of oil and liquid fuels is nearly 96 million barrels of per day according to the agencies and oil companies for 2016 [1-3]. In addition to this, emissions of many greenhouse gases (GHG) and pollutants such as particulate matter (PM), carbon monoxide (CO), carbon dioxide (CO₂), nitrogen oxides (NO_x) and unburnt hydrocarbon (UBHC) have significant effects on global warming and human health. Biodiesel is defined as a renewable fuel for diesel, which can be produced from various feedstocks such as vegetable oils, waste oils and microbial oils. Studies show that using biodiesel improves

Correspondence: D. Özçimen, Department of Bioengineering, Faculty of Chemical and Metallurgical Engineering, Yıldız Technical University, Davutpasa Campus, 34220, Istanbul, Turkey.

E-mail: didem.ozcimen@gmail.com

Paper received: 6 March, 2016

Paper revised: 26 September, 2016

Paper accepted: 12 October, 2016

<https://doi.org/10.2298/CICEQ1603060510>

the combustion in the engine due to its high cetane number and oxygen content. This efficient combustion also significantly reduces the emissions of PM, HC, and CO [1]. As mentioned before, many feedstocks can be utilized for biodiesel production. As the first generation biodiesel feedstock, vegetable oil is the most common raw material for biodiesel production. However, cultivation of vegetable plants is also contributing to GHG emissions because of the fertilizer used for their growth. Besides that, there is a debate on cultivating them for food or use in biodiesel production. Storage of these feedstocks is another issue due to decomposition over time. To overcome these problems, waste oils are considered to be utilized in biodiesel production instead of vegetable oils. However, there is a purification requirement for waste oil, due to different waste particles in the oil can affect the combustion and reduce the performance of engine. Microalgae have come into prominence in the last decade due to the productivity of microalgae and being an alternative for vegetable feedstock. It is known that there are more than 30,000 algal species which have been defined [4]. As photosynthetic microorganisms, they can perform photosynthesis by utilizing sunlight and carbon dioxide in the atmosphere. In addition to having 30% lipid content in microalgae cells, lipid production of microalgae is about 4.5–7.5 metric t ha⁻¹ year⁻¹ without optimizing the growth conditions. When these data compared with other feedstocks, lipid production of microalgae is higher than the production from other sources such as soybeans (0.4 metric t ha⁻¹ year⁻¹), palm oil (3.62 metric t ha⁻¹ year⁻¹), and jatropha (4.14 metric t ha⁻¹ year⁻¹) [5]. Microalgae produce different amounts of fatty acids with different compositions. These fatty acids contain medium-chain (C10–C14), long chain (C16–C18) and very long chain (>C20) fatty acids and their derivatives. However, most microalgae species accumulate neutral lipids in the form of triacylglycerol under stress conditions by changing their biosynthetic pathways. Microalgal fatty acids range from 12 to 22 carbons in length and can be either saturated or unsaturated. Fatty acid composition of microalgal oil basically consists of mixture of unsaturated fatty acids. This mixture includes palmitoleic (C16:1), oleic (C18:1), linoleic (C18:2) and linolenic acid (C18:3). In addition to these fatty acids, saturated fatty acids, palmitic and stearic acid are available in a small proportion [6]. The number of double bonds in the fatty acid chains never exceeds 6 and almost all of the unsaturated fatty acids are cis isomers [7]. The quality of microalgal biodiesel meets American Society for Testing and Materials (ASTM) Biodiesel Standard

D6751, thus can substitute for petroleum diesel [8]. Fuel properties such as oxidation stability and cold filter plugging point are affected from fatty acid composition of the oil. Methyl ester of oleic acid provides a better balance between these properties. Conversely, linoleic acid has very high oxidation instability, which means it can be easily oxidized. For this reason, microalgae with high oleic acid and low linoleic acid content are suitable for high quality biodiesel production [9]. Microalgal lipid content varies from species in a range of 5 to 77 wt.% dry biomass according to cultivation conditions and genetic engineering applications. Microalgae accumulate lipid under nitrogen limitation, yet excess carbon is assimilated and converted to TAG by microalgal cells when lipid synthesis is carried out in phase of balance cell growth. Important parameters such as nutrient starvation, salinity, pH, temperature and light intensity can change the fatty acid composition by altering the unsaturation and formation of polar lipids. In this study, *Chlorella protothecoides* oil was evaluated for biodiesel production. *Chlorella protothecoides* is a green microalgae species belonged to *Chlorella* genus. *Chlorella protothecoides* is presented as promising microalgal feedstock due to its capability to achieve a relative high biomass and lipid accumulation using different carbon sources under various environmental conditions [10]. Microalgae are currently not economically viable because of the expensive operation and capital costs in the process steps such as algae growth, harvesting, dewatering, and conversion to a fuel. For fuel production, transesterification of oil is the most common technique applied in today. However, high amount of energy input, solvent usage and undesired by-product formation lead the researchers to evaluate novel methods in biodiesel production. As a novel method, ultrasound assisted process meets green chemistry principals and has a wide application area in chemical processes including biodiesel production. Mixing is a significant parameter that affects biodiesel yield in transesterification reactions. Smaller droplets are created by powerful mixing, which increases the contact areas between the oil phases. The required activation energy is also provided by this effective mixing for initiating transesterification reactions. Ultrasonication is an effective mixing method that provides needed activation energy and better liquid-liquid mass transfer [11,12]. Ultrasonic baths and ultrasonic probes are usually operated at a fixed frequency. Ultrasound assisted transesterification of oil has significant advantages compared to conventional stirring methods such as: reduced reaction time, higher rate of chemical reaction, and lower mole

ratio of alcohol requirement, increasing the yield and conversion. Production of biodiesel *via* ultrasound is an effective and economically functional method due to its time and energy savings [13]. The effect of ultrasound is clearly explained by Gryglewicz who found that the transesterification reaction rate can be enhanced by ultrasound as well as by introducing an appropriate reagent into a reactor to promote methanol solubility in the rapeseed oil. In this study, calcium compounds were examined to produce methyl esters of rapeseed oil. It was reported that the transesterification of rapeseed oil by methyl alcohol can be catalysed effectively by basic alkaline-earth metal compounds: calcium oxide, calcium methoxide and barium hydroxide. It is known that, ultrasonic waves resulted an increase of reaction rate if the catalyst is soluble or well dispersed in the liquid phase of the reagents. In the considered case, sodium and barium hydroxides are well soluble in solvents such as methanol [14]. Stavarahe *et al.* also indicated that the reaction time is much shorter (10–40 min) than for mechanical stirring, the quantity of required catalyst is 2 or 3 times lower, and the alcohol/oil mole ratio used is only 6:1 *via* ultrasound process [15].

As it was mentioned before, due to algal biofuel production is expensive, in this respect, cost effective methods such as ultrasound assisted biodiesel production should be considered. Although there are lots of studies about ultrasound assisted biodiesel production from various vegetable or waste oils, there is a just few studies on microalgal biodiesel production *via* ultrasound assisted process. In the study of Ehimen *et al.*, *in situ* transesterification of microalgae by ultrasound technique was carried out in 1 h with the use of methanol/oil ratio of 315:1. At the end of the reaction, it was found that 0.295 ± 0.003 g biodiesel/g dry *Chlorella* was obtained and it was showed that this was higher than mechanically stirred *in situ* technique [16]. Most of the studies that used algae as feedstock for biodiesel production *via* ultrasound assisted process were carried out with *in-situ* transesterification. Even though there are studies on biodiesel production from algal sources, to our knowledge, there have been no investigations of ultrasound assisted biodiesel production from *C. protothecoides* and the transesterification parameters on biodiesel yield [17–21]. The aims of this work are to conduct transesterification of *C. protothecoides* oil by using ultrasound assisted method and observe the effect of reaction parameters that affect the purity of the ester product. In addition, parameters which include the mole ratio of methanol and microalgal oil, alkaline catalyst/oil ratio, and the reaction time were

also analyzed statistically by using factorial design technique to provide accuracy and reproducibility for further studies. Determination of methyl ester properties of algal product was also performed.

EXPERIMENTAL

Materials

Methanol (99.5%), and potassium hydroxide were purchased from Merck (Darmstadt, Germany). All the chemicals used for transesterification experiments and characterization tests were carried out with these analytical reagent grade chemicals. As raw material, *C. protothecoides* oil was obtained from Soley Biotechnology Institute (CA, USA). Characteristics of *C. protothecoides* oil are presented in the Table 1 [22].

Table 1. Properties of *C. protothecoides* oil

Property	Unit	Result
Density at 15 °C	kg/m ³	867
Viscosity at 40 °C	mm ² /s	3.8
Flash point	°C	124
Carbon residue (on 10% distillation residue)	mass%	0.2
Total contamination	mg/kg	2
Oxidation stability, 110 °C	h	12
Calorific value	MJ/kg	37.49
Acid value	mg KOH/g	0.3
Iodine value	mg KOH/g	47
Water content	mg/kg	80
Sulfur content	mg/kg	2
Phosphorus content	mg/kg	3
Monoglyceride content	mass%	0.31
Diglyceride content	mass%	1.22
Triglyceride content	mass%	97.26

Experimental procedure

Transesterification reactions were carried out under the conditions of different methanol: microalgal oil mole ratios (3:1, 6:1 and 9:1) in the presence of varying KOH catalyst in oil content (0.5, 1 and 1.5 wt.%) at different reaction times (20, 30 and 40 min). A Bandelin Sonopuls ultrasonic probe (20 kHz frequency and 200 W power) was used to conduct transesterification reactions, which were carried out in a 250 mL round bottom flask at autogenous temperature (60–65 °C). An ice bath was used to cool the product that composed of methyl ester-glycerine mixture obtained at the end of the reaction. After the cooling, centrifugation was performed at 5000 rpm for 5 min and created two phases as bottom and super-

nant. Glycerin, soap, methanol and impurities were separated from the product as bottom phase and methyl ester product was separated as supernatant. The obtained methyl ester was analyzed by gas chromatography to determine its fatty acid methyl ester (FAME) yield and profile. Experiments were repeated two times and the results obtained from each experiment were the average of these data.

Analysis of FAME content

Analyzing fatty acid methyl ester (FAME) and the determination of FAME content were carried out with FID gas chromatography (YL Instruments 6100 GC). ZB-FFAP (30 m×0.32 mm×0.25 μm) column was used for GC analysis. Analyses were carried out according to our previous study. The temperature program of the column was started with the temperature of 75 °C, and heated to 140 °C with heating rate of 16 °C/min, and then it was heated to 300 °C with heating rate of 15 °C/min, respectively. Hydrogen gas was used as carrier gas and gas flow was adjusted to 2 ml/min. The injection of the samples volume was 1 μl. In order to identify the peaks, methyl margarate (C17:0) was used as an internal standard and the samples were prepared with mixing methyl margarate and *n*-heptane for GC analysis. Peak identification of fatty acids was carried out according to comparison of the retention times [22].

RESULTS AND DISCUSSION

Statistical evaluation of the experimental results

In this study, 2³ factorial design was used to provide information regarding the interior of the experiment region and it was utilized to observe the effects and interactions of the amounts of methanol and KOH, and reaction time on the yield of FAME. In Table 2, experimental results of transesterification of *C. protothecoides* oil are presented. The experimental variables consisting of methanol/oil mole ratio (X_1),

catalyst/oil ratio (X_2), reaction time (X_3) and their levels were given as:

X_1 : 9:1 (superior level), 6:1 (central level), 3:1 (inferior level);

X_2 : 1.5 (superior level), 1 (central level), 0.5% (inferior level);

X_3 : 20 (superior level), 30 (central level), 40 min (inferior level).

X_1 , X_2 and X_3 are the normalized values of the experimental variables in the regression equation. Regression equation was obtained to evaluate the methyl ester yield and to understand the effects of experimental variables on the yield. The design matrix was examined statistically to define and measure the main effects quantitatively by using the analysis of variance (ANOVA) technique. For an approximate calculation of the methyl ester yield values of microalgal oil with this statistical analysis, regression Eq. (1) was developed:

$$Y_{(\text{FAME}(\%))} = 0.709 + 0.0427X_1 + 0.134X_2 + 0.0705X_3 \quad (1)$$

The coefficient of determination for regression Eq. (1) was found as 0.95.

According to the regression equation, it was found that the coefficient of catalyst/oil molar ratio was the highest among all the variables, and therefore effect of catalyst/oil mole ratio on the methyl ester yield is the strongest. The reaction time and the methanol/oil ratio also affected the methyl ester yield, positively. The interactive effect of X_1X_2 (methanol/oil mole ratio and catalyst/oil ratio), X_2X_3 (catalyst/oil ratio and time) and X_1X_3 (methanol/oil mole ratio and time) has very small coefficient values, this interactional effects were not presented in equation of regression model.

The ANOVA method compares the variances within and between the groups. The reliability of the model is confirmed with this technique. ANOVA parameters for the model equation are presented in Table 3. In order to observe these parameters, Mini-

Table 2. The methyl ester yields and design matrix obtained at different reaction conditions

Experiment No.	Methanol:oil mole ratio	Catalyst to oil share, wt. %	Time, min	X_1	X_2	X_3	Total area (uV.Min)	Total area, %
1	3:1	0.5	20	-1	-1	-1	217.41	47.34
2			40	-1	-1	1	265.82	57.88
3		1.5	20	-1	1	-1	349.30	76.06
4			40	-1	1	1	381.23	83.01
5	9:1	0.5	20	1	-1	-1	246.02	53.57
6			40	1	-1	1	317.36	69.10
7		1.5	20	1	1	-1	349.73	76.15
8			40	1	1	1	457.26	99.56
9	6:1	1	30	0	0	0	345.05	75.13

tab statistical software (Minitab 14) was used. The F -value of 34.14 with a very low probability value ($p < 0.01\%$) implies that the model is significant. Moreover, a high value of correlation coefficient shows a close agreement between predicted value and actual value of response. The determination coefficient (R^2) controls the suitability of the model. As the value of R approaches 1, it demonstrates better correlation between observed and predicted values [23]. The determination coefficient value was determined as $R^2 = 0.95$ and it represented that only about 5% of the total variation was not explained by the respective model. Besides that, the value of the adjusted determination coefficient was found very high as $\text{adj. } R^2 = 0.928$. When the normalized values (-1, 0, 1) of experimental variables were converted to real values, the real regression Eq. (2) was obtained. The equation developed with real values helps determining methyl ester yield value without doing any experiments in the investigated parameter range:

$$Y_{\text{real}} = 14.5 + 1.42X_1 + 26.7X_2 + 0.705X_3 \quad (2)$$

The optimum conditions for maximum FAME yield were determined as: catalyst content = 1.5 wt.%, methanol/oil mole ratio = 9 and time = 40 min, according to these results.

Table 3. ANOVA results of statistical evaluation for the methyl ester yield; $R^2 = 0.95$, $R = 0.974$, $R^2(\text{adj}) = 0.926$

Sources of variations	Degree of freedom	Sum of squares	Mean square	F-value	Probability
Regression model	3	0.197495	0.065832	34.14	0.001
Error	5	0.009641	0.001928		
Corrected total	8	0.207136			

Four main fatty acids - palmitic (C16:0), oleic (C18:1), linoleic (C18:2) and linolenic acid (C18:3) - were determined with noticeable quantities. As can be

seen in Table 4, the highest FAME yields were belonged to oleic and linoleic acids. In order to see the effects of the reaction parameters on FAME yield of these fatty acids, oleic and linoleic acids were selected for the analysis. In Table 4, methyl ester yields of these fatty acids and design matrix obtained at different reaction conditions are presented.

Regression equation and ANOVA results were obtained as Eqs. (3) and (4) and Table 5 by using Minitab 14 software:

$$Y_{(\text{C18:1})} = 0.504 + 0.00395X_1 + 0.0144X_2 + 0.00165X_3, R^2 = 0.924 \quad (3)$$

$$Y_{(\text{C18:2})} = 0.176 + 0.00173X_1 + 0.00612X_2 + 0.00128X_3, R^2 = 0.913 \quad (4)$$

In the same way, it can be seen from the Eqs. (3) and (4) that the highest coefficient belonged to the catalyst/oil molar ratio among all the variables. It can also be indicated that C18:1 and C18:2 methyl ester yields were influenced positively from the reaction time and the methanol/oil ratio. The value of the determination coefficients were determined as $R^2 = 0.92$ and 0.91. These results showed that only about 8 and 9% of the total variation was not explained by the respective model. In conclusion, the optimum conditions for maximum FAME yield of C18:1 and C18:2 were found as catalyst content = 1.5 wt.%, methanol/oil mole ratio = 9 and time = 40 min, similar to previous results.

The effect of methanol/oil mole ratio

Transesterification reaction is an equilibrium reaction, larger amounts of alcohol can enhance the reaction to result in the equilibrium favorable to the FAME formation. Even though methyl ester production from any oil requires three moles of methanol for each mole of oil in theory, stoichiometrically, an excess amount of methanol is desirable for the completion of the reaction in practice [24]. In the ultrasound assisted process, alcohol reacts quite rapidly

Table 4. Methyl ester yields of fatty acids and design matrix obtained at different reaction conditions

Experiment No.	Methanol:oil mole ratio	Catalyst in oil share, wt. %	Time, min	X_1	X_2	X_3	C16=0	C18=1	C18=2	C18=3
1	3:1	0.5	20	-1	-1	-1	3.99	48.41	16.73	5.03
2			40	-1	-1	1	4.14	48.89	16.9	4.85
3		1.5	20	-1	1	-1	4.19	51.33	17.92	5.08
4			40	-1	1	1	4.31	51.79	18.08	5.22
5	9:1	0.5	20	1	-1	-1	4.22	49.92	17.21	5.02
6			40	1	-1	1	4.13	49.02	17.03	4.90
7		1.5	20	1	1	-1	4.14	51.68	17.95	5.05
8			40	1	1	1	4.27	52.96	18.82	5.32
9	6:1	1	30	0	0	0	4.16	49.96	17.41	4.97

Table 5. ANOVA results of statistical evaluation for the C18:1 and C18:2 methyl ester yield

Fatty acid	Sources of variations	Degree of freedom	Sum of squares	Mean square	F-value	Probability	R^2	R	R^2 (adj)
C18:1	Regression model	3	0.00180548	0.00060183	20.22	0.003	0.92	0.959	0.878
	Error	5	0.00014884	0.00002977					
	Corrected total	8	0.00195432						
C18:2	Regression model	3	0.00033693	0.0001123	17.51	0.004	0.91	0.955	0.861
	Error	5	0.00003207	0.00000641					
	Corrected total	8	0.00036901						

due to an increased mass transfer in the presence of ultrasound. Ultrasound causes methanol to cavitate and disperse as nano-droplets into the oil, form a fine emulsion of methanol in oil, so the contact surface between reagents increases dramatically and consequently accelerates the reaction rate [15,25]. In order to investigate the effect of methanol/oil ratio on transesterification of microalgal oil in the presence of 0.5, 1 and 1.5 wt.% KOH catalyst in oil at different reaction times (20, 30 and 40 min), 3:1, 6:1 and 9:1 methanol/oil mole ratios were used, in this study. According to the results, it was found that, when methanol/oil ratio increased from 3:1 to 9:1, methyl ester yield increased. The highest methyl ester production was obtained with 9:1 methanol/oil mole ratio at the reaction time of 40 min and 1.5 wt.% KOH in oil. Similar results have been reported from various transesterification studies. Tamilarasan and Sahadevan have investigated ultrasonic assisted acid base transesterification of *Caulerpa peltata* oil. It was observed that an increase in the methanol to oil molar ratio concluded with an increase in methyl ester yield [21]. Tamilarasan *et al.* have studied ultrasound-enhanced rapid in situ transesterification of *Enteromorpha compressa*, marine macroalgae. Various quantity of methanol to algal biomass as 4:1, 4.5:1, 5:1, 5.5:1, 6:1 and 6.5:1) were applied to observe the effect of the methanol quantity on in situ transesterification process. It was reported that, 5.5:1 methanol to biomass ratio was suggested to be a suitable ratio for *in situ* transesterification process. For further increase of methanol ratio up to 6:1, no significant difference on the biodiesel yield was observed, and excess usage of methanol to biomass ratio above 6:1 decreased methyl ester yields [17]. Thanh *et al.* also carried out transesterification of canola oil by use of ultrasonic probe in the presence of KOH at the reaction time of 50 min. The highest methyl ester yield was obtained at methanol:oil mole ratio of 5:1 in their study [26]. Chuah *et al.* investigated empty fruit bunch doped with potassium hydroxide as a heterogeneous solid base catalyst for transesterification of rubber seed oil with methanol in ultrasonic batch system. It was found

that up to 15:1 methanol:oil mole ratio, free fatty acid amount decreased with increasing amounts of the methanol:oil ratio. On the other hand, 15:1 methanol:oil ratio caused a reduction of methyl ester conversion and yield due to creating interference with the phase separation of glycerol which made an equilibrium of the reaction shift to reactants leading to difficulty of the separation process [27].

The effect of catalyst content

The effect of KOH in microalgal oil share was also studied, with various concentrations ranging from 0.5 to 1.5 wt.%. In comparison with sodium-based catalyst and methoxide catalyst, KOH was chosen due to its effectiveness on methyl ester conversion. The highest methyl ester yield was obtained with 1.5 wt.% KOH under the conditions of 9:1 methanol/oil mole ratio and reaction time of 40 min. As can be seen with the results, it was concluded that high yields of methyl ester were obtained with increasing catalyst/oil ratio when methanol/oil ratio was not varied. Stavarache *et al.* reported that, the yield of methyl ester increased with increasing catalyst quantity up to 1.0 wt.% NaOH. In the case of using 1.5 wt.% NaOH, methyl ester yield was very low due to the soap production in high quantity led to formation of gels in high quantity, and a high amount of esters remains trapped in the glycerin layer. However, when KOH was used, high yields were obtained even for 1.5% catalyst concentration. Potassium soap is softer, more soluble in water and does not make as much foam as sodium soap. The washing of esters when using KOH is easier and the yields of isolated product are higher. It was also reported that, in comparison between mechanical stirring and ultrasonic irradiation, ultrasonic irradiation showed higher efficiency than mechanical stirring [15].

Thanh *et al.* [24] studied the ultrasound assisted transesterification of triglycerides with methanol in the presence of KOH catalyst. It was reported that, the highest yield of FAME was achieved more than 98% after 20 and 25 min reaction time at the concentration of 1.5 and 1.0 wt.% KOH, respectively. Tamilarasan

and Sahadevan investigated the effect of catalyst concentration on methyl ester conversion with different catalyst concentrations of 0.25, 0.5, 0.75, 1, 1.25 and 1.5 wt.% NaOH. It was reported that, as the NaOH catalyst concentration increased, methyl ester conversion was found to be increased [21]. Chuah *et al.* also reported that, as catalyst, empty fruit bunch (EFB) embedded with KOH whose amount ranging from 0.5 to 2.5 wt.%, indicated the maximum FFA reduction was achieved when the catalyst concentration increased above 1.5 wt.% [27].

The effect of reaction time

The duration of the reaction has been established as one of the critical parameters for biodiesel production [17]. Reaction time is a crucial factor, which can not only determine the efficiency of biodiesel formation but also the quality of final products [19]. For this reason, choosing an optimum reaction time is required for both the completion of the reaction and produce high yields of methyl esters. Transesterification reactions were performed at 20, 30 and 40 min with different methanol:microalgal oil mole ratios and KOH catalyst/oil ratios to observe the effect of reaction time on methyl ester yield. An increase in reaction time resulted with higher methyl ester yields. It was observed that the highest methyl ester yield was obtained with the reaction time of 40 min under the conditions of 1.5% KOH and 9:1 methanol/oil mole ratio. The findings obtained from this experiment showed that the effect of reaction time on methyl ester yield were similar with the results of other studies in the literature. Kesgin *et al.* found that the highest formation of methyl ester was observed within 20 min at 4:1 and 5:1 mole ratios of alcohol:oil and indicated the ultrasound assisted transesterification reduces the processing time to 10-20 min when it was compared with the conventional transesterification [28]. In another study, transesterification of different vegetable oils with methanol, in the presence of potassium hydroxide as catalyst with low frequency ultrasound (40 kHz) was performed. In the experiments, effect of various reaction time (3-6-10-20-30-40-60 min) on conversion of vegetable oil to methyl ester was investigated and results showed that, increasing reaction time caused a decrease in the concentration of mono-, di- and triglycerides and increase in FAME concentration [25]. Avramovic *et al.* studied the ultrasound-assisted KOH catalyzed sunflower oil methanolysis kinetics, and results showed that FAME production increased fast up to 30 min reaction time, on the other hand, it was observed that after 30 min, FAME production increased slowly up to 60 min. As

expected, the initial rate of the reaction was slow due to mass transfer limitation. As the transesterification proceeded, the drops of methanol were disintegrated by the effect of the ultrasound waves and they were stabilized by monoglycerides, diglycerides and soaps. This was resulted in an increase of the interfacial area available for mass transfer [29]. Suganya *et al.* have studied ultrasound-enhanced rapid *in situ* transesterification of *E. compressa* and investigate the effect of time on the process, the reaction time ranging from 10 to 120 min which was maintained with the optimized parameters of 10% H₂SO₄ concentration, 30 vol.% of tetrahydrofuran and 5.5:1 methanol to biomass ratio. Under these conditions, they have achieved the highest yield of 98.89% in 90 min of reaction time [17]. In the study of Hindryawati and Maniam, transesterification experiments were carried out with different reaction times varying 0-80 min. It was found that the highest methyl ester yield was obtained at the reaction time of 30 min under the conditions of 3 wt.% catalyst and methanol to oil molar ratio of 9:1 at 55 °C. It was reported that any further time increase caused no remarkable variations in the content due to equilibrium [30].

Fatty acid profile in FAME samples

According to the GC results, it was found that there were four main fatty acids as palmitic (C16:0), oleic (C18:1), linoleic (C18:2) and linolenic acid (C18:3). In all samples, oleic acid was determined as the highest amount of fatty acid methyl ester found in biodiesel. It constituted more than 50% of the FAME. Palmitic, linoleic and linolenic acid content were approximately determined as 4, 17 and 5%, respectively. Trace amounts of other fatty acids such as C16:1, C18:0, C20:0 and C20:1 were also determined, however they could not be calculated with these results. Fatty acid profile of biodiesel is a very important measure for determining the quality of the product that will be used as fuel. Therefore, achieving high quality biodiesel depends on suitable fatty acid composition [31]. In order to decrease oxidative stability and cold flow problems, it is required to have low levels of polyunsaturated and low levels of saturated FAs. Studies showed that, monounsaturated fatty acids of palmitoleic acid (16:1) and oleic acid (18:1) can provide an appropriate balance between oxidative stability and cold flow. Besides that, the five most common C16-C18 fatty acids, as palmitic (16:0), stearic (18:0), oleic (18:1), linoleic (18:2), and linolenic (18:3) acids are necessary for a good quality biodiesel product. Also, it has been indicated that C16:1 and C18:1 fatty acids (palmitoleic acid and

oleic acid, respectively) are the most favorable fatty acids for biodiesel production [32]. According to this, it can be said that the obtained biodiesel possessed suitable fatty acids convenient for biodiesel production. In literature, it was indicated that high linolenic acid content has negative effects on oxidative stability and cold flow properties of biodiesel. In this study, linolenic acid content was found to be only around 5% of total FAME.

Properties of methyl esters

Important properties that affect biodiesel usage as a fuel should be determined in order to evaluate its potential as a substitute for diesel fuel. Determination of these properties was carried out with characterizing the obtained product with its acid value, iodine value, density, methyl ester content, water content and viscosity. Experimental procedures were applied in according to biodiesel standards. Methyl ester which was obtained under the conditions of methanol-oil mole ratio: 9:1; 1.5% KOH; and $t = 40$ min used to perform characterization experiments. Ester, mono-glyceride, diglyceride and triglyceride contents of the obtained product were determined as 99.56, 0.119, 0.021 and 0.031%, respectively. Characterization of methyl ester was carried out according to experimental procedures of EN 14104, EN 14111, EN ISO 3679, EN ISO 12937 and EN ISO 3104. Acid value, iodine value and density of algal biodiesel were found as 0.36 mg KOH/g, 86.40 g I₂/100 g and 0.868 g/cm³, respectively. Water content and viscosity of biodiesel were measured as 0.014% and 4.7 mm²/s, respectively. According to the commercial biodiesel standards, values of the properties of algal biodiesel were in the range of acceptance criteria as compared with commercial biodiesel standards. As a result, this product can be evaluated as a fuel.

CONCLUSIONS

In this study, *C. protothecoides* oil was transesterified by using ultrasound assisted method, and transesterification parameters on methyl ester production were investigated. Experimental and statistical results showed that the catalyst/oil ratio is the most effective parameter on methyl ester yield. Similarly, statistical results showed that effect of catalyst/oil ratio on methyl ester yield of oleic and linoleic acid is the highest in comparison with methanol/oil ratio and reaction time. Oleic acid methyl ester was found as more than 50% of the FAME, which was the highest amount of FAME in algal biodiesel in all samples. Although ultrasound assisted transesterification is a very promising way for biodiesel production,

there are only a few studies on biodiesel production from microalgal oils by using this method. Besides that, ultrasound assisted transesterification does not presently seem economically viable for large scale production of algal biodiesel. Therefore, there is still need for innovations for both high productivity and green productions.

ACKNOWLEDGMENTS

The authors acknowledge financial support from the Yıldız Technical University Scientific Research project (2013-07-04-KAP08) provided for this work.

REFERENCES

- [1] W.N.M.W. Ghazali, R. Mamat, H.H. Masjuki, G. Najafi, *Renewable Sustainable Energy Rev.* **51** (2015) 585-602
- [2] BP, BP Statistical Review of World Energy June 2015 64th ed., <https://www.bp.com/content/dam/bp/pdf/energy-economics/statistical-review-2015/bp-statistical-review-of-world-energy-2015-full-report.pdf> (accessed 30 July 2016)
- [3] International Energy Agency, Oil, <https://www.iea.org/aboutus/faqs/oil/> (accessed 30 July 2016)
- [4] M. Koberg, M. Cohen, A. Ben-Amotz, A. Gedanken, *Bioresour. Technol.* **102**(5) (2011) 4265-4269.
- [5] D.C. Kligerman, E.J. Bouwer, *Renewable Sustainable Energy Rev.* **52** (2015) 1834-1846
- [6] A. Singh, P.S. Nigam, J.D. Murphy, *Bioresour. Technol.* **102**(1) (2011) 26-34
- [7] R. Halim, M.K. Danquah, P.A. Webley, *Biotechnol. Adv.* **30**(3) (2012) 709-732
- [8] K. Soratana, W.F. Harper Jr., A.E. Landis, *Energy Policy* **46** (2012) 498-510
- [9] S. Goto, M. Oguma, N. Chollacoop, in *EAS-ERIA Biodiesel Fuel Trade Handbook*, S. Goto, M. Oguma, N. Chollacoop, Eds., ERIA, Jakarta, 2010, pp. 27-62
- [10] X. Feng, T.H. Walker, W.C. Bridges, C. Thornton, K. Gopalakrishnan, *Bioresour. Technol.* **166** (2014)17-23
- [11] D. Özçimen, M.Ö. Gülyurt, B. İnan, in *Biodiesel - Feedstocks, Production and Applications*, Z. Fang, Ed., InTech, Rijeka, 2012, pp. 25-57
- [12] A.P. Vyas, J.L. Verma, N. Subrahmanyam, *Fuel* **89**(1) (2010) 1-9
- [13] D. Özçimen S. Yücel, in *Biofuel's Engineering Process Technology*, M.A. Bernardes, Ed., InTech, Rijeka 2011, pp. 353-384
- [14] S. Gryglewicz, *Bioresour. Technol.* **70**(3) (1999) 249-253
- [15] C. Stavarache, M. Vinatoru, R. Nishimura, Y. Maeda, *Ultrason. Sonochem.* **12**(5) (2005) 367-372
- [16] E.A. Ehimen, Z. Sun, G.C. Carrington, *Procedia Environ. Sci.* **15** (2012) 47-55
- [17] T. Suganya, R. Kasirajan, S. Renganathan, *Bioresour. Technol.* **156** (2014) 283-290
- [18] A. Guldhe, B. Singh, I. Rawat, F. Bux, *Chem. Eng. Res. Des.* **92**(8) (2014) 1503-1511

- [19] G. Ma, W. Hu, H. Pei, L. Jiang, M. Song, R. Mu, *Energy Convers. Manage.* **90** (2015) 41-46
- [20] E. Martinez-Guerra, V. G. Gude, A. Mondala, W. Holmes, R. Hernandez, *Appl. Energy*, **129** (2014) 354-363
- [21] S. Tamilarasan, R. Sahadevan, *Fuel* **128** (2014) 347-355
- [22] M.Ö. Gülyurt, D. Özçimen, B. İnan, *Int. J. Mol. Sci.* **17**(4) (2016) 579
- [23] D. Özçimen, *J. Biobased Mater. Bioenergy* **7**(4) (2013) 449-456
- [24] L.T. Thanh, K. Okitsu, Y. Maeda, H. Bandow, *Ultrason. Sonochem.* **21**(2) (2014) 467-471
- [25] C. Stavarache, M. Vinatoru, Y. Maeda, *Ultrason. Sonochem.* **14**(3) (2007) 380-386
- [26] L.T. Thanh, K. Okitsu, Y. Sadanaga, N. Takenaka, Y. Maeda, H. Bandow, *Bioresour. Technol.* **101**(14) (2010) 5394-5401
- [27] L.F. Chuah, M.M. Amin, S. Yusup, A. Bokhari, J.J. Klemeš, M.S. Alnarabiji, *J. Cleaner Prod.* (2016) (in press)
- [28] C. Kesgin, S. Yücel, D. Özçimen, P. Terzioğlu, A. Attar, *Int. J. Green Energy*, (2014) in press.
- [29] [J. M. Avramović, O. S. Stamenković, Z. B. Todorović, M. L. Lazić, V. B. Veljković, *Chem. Ind. Chem. Eng. Q.* **18**(1) (2012) 115-127
- [30] N. Hindryawati, G.P. Maniam, *Ultrason. Sonochem.* **22** (2015) 454-462
- [31] A.F. Talebi, S.K. Mohtashami, M. Tabatabaei, M. Tohidfar, A. Bagheri, M. Zeinalabedini, H. H. Mirzaei, M. Mirzajanzadeh, S. M. Shafaroudi, S. Bakhtiari, *Algal Res.* **2**(3) (2013) 258-267
- [32] M. Song, H. Pei, W. Hu, G. Ma, *Bioresour. Technol.* **141** (2013) 245-251.

DIDEM ÖZÇİMEN
M. ÖMER GÜLYURT
BENAN İNAN

Department of Bioengineering,
Faculty of Chemical and
Metallurgical Engineering, Yıldız
Technical University, Davutpasa
Campus, Istanbul, Turkey

NAUČNI RAD

OPTIMIZACIJA PROIZVODNJE BIODIZELA IZ ULJA *Chlorella protothecoides* ULTRAZVUKOM POTPOMOGNUTOM TRANSESTERIFIKACIJOM

*Sve je veći interes za biodizelom kao alternativnim gorivom za dizel motore zbog visokih cena nafte i ekoloških problema uzrokovanih na masivvelikom emisijom gasova sa efektom staklene bašte. Danas je mikroalgalna biomasa postala obećavajuća sirovina za dobijanje biodizela. Međutim, tradicionalna proizvodnja biodizela iz mikroalgi troši mnogo energije i rastvarača. Neophodno je koristiti alternativnu metodu koja može smanjiti potrošnju energije i alkohola i uštedeti vreme. U ovom radu, istraživana je uticaj odnosa metanol:ulje i vremena trajanja reakcije na prinos metil estara masnih kiselina (MEMK) u proizvodnji biodizela iz ulja *Chlorella protothecoides* pomoću ultrazvukom-potpomognute transesterifikacije metanola i kalijum-hidroksida kao katalizatora. Najveća prinos metil-estra dobijen je pod uslovima molskog odnosa metanol:ulje od 9:1, odnosa katalizator:ulje od 1,5% kalijum-hidroksida i reakcionog vremena od 40 min. Takođe, utvrđeno je da je molski odnos katalizator:ulje statistički najvažniji faktor. Rezultati pokazuju da ultrazvukom-potpomognuta transesterifikacija može biti efikasna i isplativ alternativni način za proizvodnju biodizela.*

*Ključne reči: biodizel dobijen iz algi, *Chlorella protothecoides*, metil-estar, transesterifikacija, ultrazvuk.*

LIANGCHAO LI
BIN XU

Key Laboratory of Testing
Technology for Manufacturing
Process of Ministry of Education,
School of Manufacturing Science
and Engineering, Southwest
University of Science and
Technology, Mianyang, Sichuan,
China

SCIENTIFIC PAPER

UDC 532:519.87:66.063.8:66

CFD SIMULATION OF GAS-LIQUID FLOATING PARTICLES MIXING IN AN AGITATED VESSEL

Article Highlights

- Gas-liquid floating particles mixing in an agitated vessel were studied by using CFD simulation
- The increasing of gas inlet rates is in favor of floating particles off-surface suspension
- Gas dispersion becomes worse, while solid dispersion changes little with increasing solid loading

Abstract

Gas dispersion and floating particles suspension in an agitated vessel were studied numerically by using computational fluid dynamics (CFD). The Eulerian multi-fluid model along with standard $k-\epsilon$ turbulence model was used in the simulation. A multiple reference frame (MRF) approach was used to solve the impeller rotation. The velocity field, gas and floating particles holdup distributions in the vessel were first obtained, and then, the effects of operating conditions on gas dispersion and solid suspension were investigated. The simulation results show that velocity field of solid phase and gas phase are quite different in the agitated vessel. Floating particles are easy to accumulate in the center of the surface region and the increasing of superficial gas velocity is in favor of floating particles off-surface suspension. With increasing solids loading, the gas dispersion becomes worse, while relative solid holdup distribution changes little. The limitations of the present modeling are discussed and further research in the future is proposed.

Keywords: three-phase flow, computational fluid dynamics (CFD), floating particle, agitated vessel, numerical simulation, multiple reference frame (MRF).

The most common gas-liquid-solid three-phase agitated vessel involves mixing of gas-liquid sinking particles. However, some of the gas-liquid floating particle mixing is also often encountered in polymerization, petrochemical, wet metallurgy, food and fermentation industries. Unlike sinking particles, suspensions of floating particles need the drawdown of the particles from liquid surface to bulk fluid in order to disperse. For gas-liquid floating particles three-phase

systems, effective gas dispersion is required. Therefore, research on the flow field characteristics in the gas-liquid floating particles agitated vessel is needed.

So far, a number of studies has focused on gas-liquid [1-4] or solid-liquid [5-7] systems and the studies on gas-liquid-solid mixing in agitated vessels are sparse. Compared to two-phase flow, the flow field in three-phase systems is more complex and more difficult to investigate. In the literature, some researchers have studied the mixing of gas-liquid sinking particles in agitated vessels [8-11], which have been covered in a detailed review [12]. Xu [13] pointed out that the suspension of floating particles is greatly different from that of sinking particles. The challenge of floating particles suspensions is the drawdown of particles into the fluid. Hence, the research results of the gas-liquid sinking particles mixing may not be suitable for that of gas-liquid floating particles systems. As for the suspension of floating particles in solid-liquid sys-

Correspondence: L. Li, Key Laboratory of Testing Technology for Manufacturing Process of Ministry of Education, School of Manufacturing Science and Engineering, Southwest University of Science and Technology, Mianyang, Sichuan 621010, P.R. China.

E-mail: tchllc@126.com

Paper received: 29 January, 2016

Paper revised: 19 June, 2016

Paper accepted: 17 October, 2016

<https://doi.org/10.2298/CICEQ160129052L>

tems, Edwards *et al.* [14] first studied on the suspension of the floating particles and found a strong effect of stirrer types on critical speed of off-surface suspension. Bakker *et al.* [15] also studied floating particles suspended stirred with different impellers and found that upward pumping pitched blade impeller was more energy-efficient than disc turbines in aerated and unaerated agitated vessels. Furthermore, Karcz *et al.* [16] found that the up-pumping pitched blade had the highest efficiency of drawing down floating particles in a fully baffled vessel when it is mounted at a height of $0.67H$. Taşkin *et al.* [17,18] investigated the effect of impeller-tank diameter and scale of tank on the drawdown of floating particles. In addition, other scholars such as Wójtowicz [19] and Takahashi [20] have also studied the suspension characteristics of floating particles in an agitated vessel. Nevertheless, only very few studies have focused on suspensions of floating particles in gas-liquid-solid three-phase systems. Xu *et al.* [21,22] investigated the gas-liquid-floating particles mixing in an agitated vessel with different multiple-impellers. They obtained the optimal combinations of impellers, baffles and spargers, and found that the effect of the upper impeller on critical speed was the highest. Bao *et al.* [23] studied the suspension of floating particles in a three-phase multiple-impeller agitated vessel and found that gas holdup decreases with increasing of solid concentration, and the downward pumping top impeller has significant higher critical speed and power consumption, which is not suitable for the drawdown of floating particles.

Over the past several decades, computational fluid dynamics (CFD) has become a powerful and useful tool for investigating the flow field in agitated vessels. It has been shown that CFD models can predict flow field successfully and accurately in single-phase agitated vessel [24-26]. For multiphase flows, many researchers [27-30] have used CFD to study flow fields in gas-liquid or solid-liquid systems. These simulation studies are very helpful for understanding the flow field characteristics of two-phase flow systems. The Eulerian-Eulerian method and Eulerian-Lagrange method are the two main approaches to predict the flow field in two-phase systems [31]. The Eulerian-Lagrange method treats bubbles or particles as dispersed phase and liquid as the continuous phase. This method is not suitable for modeling of the high holdup of dispersed phase for large calculations. The Eulerian-Eulerian method treats all the phases as interpenetrating continua, which has been used by many authors for its obvious advantages of small calculations and wide range of operating conditions.

Sattar [32,33], Sardeshpande [34] and Jahoda [35] used the Eulerian-Eulerian method to study on the two-phase flow field characteristics in the two-phase systems. Furthermore, some scholars applied the Eulerian-Eulerian method to model the flow field in gas-liquid-solid three-phase systems. Murthy *et al.* [36], for example, predicted the critical impeller speeds for solid suspension in a gas-liquid sinking particles stirred reactor with CFD method. They investigated the effects of particle size, solid loading and superficial gas velocity on critical impeller speeds and flow field, etc. Panneerselvam *et al.* [37] numerically studied solid suspension in a gas-liquid sinking particle with a mechanically agitated contactor using an Eulerian-Eulerian multi-fluid approach along with the standard $k-\varepsilon$ turbulence model. The obtained the critical impeller speeds were in good agreement with experimental data under various operating conditions. In addition, Feng *et al.* [38] numerically modeled local hydrodynamics in a gas-liquid-nanoparticles three-phase fluidization with Eulerian-Eulerian multifluid approach. Sarhan *et al.* [39] investigated the effects of solid particles on bubbles breakage and coalescence rates in a flotation cell using the Eulerian-Eulerian multiphase model. By reviewing these studies, it can be found that more CFD simulations are about gas-liquid-sinking particles systems, while the CFD modeling of flow field in gas-liquid-floating particles agitated vessel is rarely reported.

Hence, in the present work, the flow field characteristics in a gas-liquid-floating particles agitated vessel with multiple impellers are numerically simulated by using the commercial CFD software package Fluent 6.2. The Eulerian-Eulerian multifluid approach along with standard $k-\varepsilon$ turbulence model is used in the simulation. The flow pattern, gas and solid holdup distributions in the agitated vessel are predicted firstly. Furthermore, the effects of operating conditions such as superficial gas velocity and solid loading on flow field characteristics are investigated.

NUMERICAL MODELS AND SIMULATION METHODS

Simulation domain

As shown in Figure 1, a cylindrical vessel of $T = 0.386$ m diameter with a dished base was used in this study, which was similar to the experimental agitated vessel from the literature [22]. The media of gas, liquid and floating particles are air, water and polypropylene beads, respectively. The densities are 1.225, 998 and 900 kg/m³ for the working media, respectively. Gas dispersion and floating particles sus-

pension are driven by three conventional Rushton turbines with diameter $D = 0.77T$. The clearance of lower impeller from the vessel bottom equals to $0.37T$. The spacing between the lower and middle impeller, and spacing between middle and upper impeller are $0.66T$ and $0.67T$, respectively. The rotational speed of the impellers is 500 rpm, which corresponds to Reynolds number larger than 10^4 according to the definition of Reynolds number in agitated vessel as $Re = \rho ND^2/\mu$. Gas was introduced from a $0.8D$ diameter ring gas distributor with 8 holes of 2.0 mm diameter. The gas distributor is mounted underneath the lower impeller with spacing of 81 mm. Four full-length baffles of $0.1T$ width are used in the study. To avoid flow stagnant zones, the baffles are mounted at distance of 19.6 mm from the vessel wall. The solid loading ranges from 3.2 to 6.4% for average solid holdup under un-aerated operating condition, and the range of the superficial gas velocity is $0\text{--}6.44 \times 10^{-3}$ m/s. Since the superficial gas velocity is very low, the breakage and coalescence of the bubbles are neglected. It is assumed that the bubbles are spheres with diameter of 3.0 mm. In the same way, a mean diameter of 1.0 mm is set for polypropylene beads.

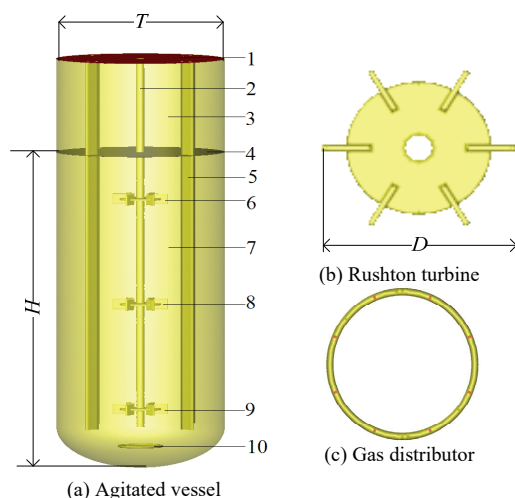


Figure 1. Schematic diagram of the agitated vessel: 1) gas outlet, 2) shaft, 3) air zone, 4) liquid level, 5) baffles, 6) upper impeller, 7) liquid zone, 8) middle impeller, 9) lower impeller, 10) gas distributor.

Grid division

The geometry and grids of the agitated vessel were prepared by the pre-processor Gambit 2.4 (Fluent Inc.). A multiple reference frame approach is employed to model the impeller-baffle interaction. To meet the approach, the simulation domain is divided into two fluid regions, *i.e.*, impeller region and stationary region as shown in Figure 2. The impeller region

contains three parts, including lower ($-0.5 < r/R < 0.5$, $0.14 < z/H < 0.22$), middle ($-0.5 < r/R < 0.5$, $0.45 < z/H < 0.58$) and upper impeller ($-0.5 < r/R < 0.5$, $0.70 < z/H < 0.83$). The hybrid unstructured meshes are generated for the two regions. To accurately model the flow field in the agitated vessel, the meshes for some important surfaces, such as impellers blades, the holes of gas distributor and interfaces, etc. are refined. The grid independence study has been carried out. Three numbers of grids have been tested, and found that the present mesh and the finer mesh have the same values of impeller power number and pumping number. Then, the present mesh that consists of 858,064 cells was used for our simulation. Similar grid independence analysis method can be found elsewhere [40,41].

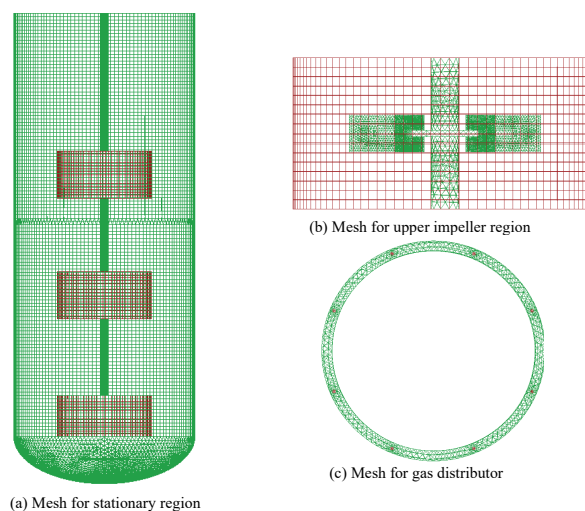


Figure 2. Mesh for the agitated vessel.

Governing equations

In this work, the hydrodynamics of gas-liquid-solid flow in the agitated vessel was simulated by using Eulerian multiphase flow model. The Eulerian multiphase model is a very complex model in which each phase is treated as different interpenetrating continua. The conservation equations of mass and momentum for each phase have similar structure and are shown as follows.

The mass conservation equation for phase i ($i = l$ for liquid phase, g for gas phase and s for solid phase) is given as:

$$\frac{\partial}{\partial t}(\rho_i \alpha_i) + \nabla \cdot (\rho_i \alpha_i \vec{U}_i) = 0 \quad (1)$$

where t is flow time. ρ , α and \vec{U} represent density, volume fraction and velocity vector of phase i , respectively. For the conservation of the equation, the

volume fraction of the phases should meet the compatibility conditions as :

$$\alpha_g + \alpha_l + \alpha_s = 1.0 \quad (2)$$

The momentum conservation equations for each phase are given as follows.

Gas phase (dispersed fluid phase):

$$\begin{aligned} \frac{\partial}{\partial t}(\alpha_g \rho_g \bar{U}_g) + \nabla(\alpha_g \rho_g \bar{U}_g \bar{U}_g) = \\ = -\alpha_g \nabla p + \nabla \tau_{eff,g} + \alpha_g \rho_g g - F_{lg} \end{aligned} \quad (3)$$

Liquid phase (continuous phase):

$$\begin{aligned} \frac{\partial}{\partial t}(\alpha_l \rho_l \bar{U}_l) + \nabla(\alpha_l \rho_l \bar{U}_l \bar{U}_l) = \\ -\alpha_l \nabla p + \nabla \tau_{eff,l} + \alpha_l \rho_l g + F_{lg} + F_{ls} \end{aligned} \quad (4)$$

Solid phase (dispersed solid phase):

$$\begin{aligned} \frac{\partial}{\partial t}(\alpha_s \rho_s \bar{U}_s) + \nabla(\alpha_s \rho_s \bar{U}_s \bar{U}_s) = \\ = -\alpha_s \nabla p + \nabla \tau_{eff,s} + \alpha_s \rho_s g - F_{ls} \end{aligned} \quad (5)$$

where p is the static pressure and g is gravitational force. $\tau_{eff,i}$ is the Reynolds stress tensor of phase i . F_{lg} and F_{ls} represent the interphase forces between liquid and gas phase, liquid and solid phase, respectively. The interphase forces between phases are composed of a series of different forces, such as drag force, lift force, virtual mass force and turbulence dispersed force, etc. It is reported [42] that the contribution of drag force is the largest and the other forces have no considerable effects on the flow field characteristics in gas-liquid or solid-liquid agitated vessel. So in this study, the drag forces between continuous phase and dispersed phase are considered while the other forces are ignored.

The drag forces between continuous phase and dispersed phase, *i.e.*, F_{lg} and F_{ls} can be calculated as:

$$F_{lg} = \frac{3}{4} \frac{C_{D,lg}}{d_g} \rho_l \alpha_l \alpha_g |\bar{U}_g - \bar{U}_l| (\bar{U}_g - \bar{U}_l) \quad (6)$$

$$F_{ls} = \frac{3}{4} \frac{C_{D,ls}}{d_s} \rho_l \alpha_l \alpha_s |\bar{U}_s - \bar{U}_l| (\bar{U}_s - \bar{U}_l) \quad (7)$$

where d is the diameter of dispersed phase (d_g for bubble, d_s for polypropylene beads) and C_D is drag coefficient. In this work, the drag coefficients of $C_{D,lg}$ and $C_{D,ls}$ are calculated according to the model proposed by Schiller and Naumann [43]. The Schiller and Naumann model for drag coefficient $C_{D,ls}$ can be written as:

$$C_{D,ls} = \begin{cases} \frac{24}{Re} (1 + 0.15 Re^{0.687}) & Re \leq 1000 \\ 0.44 & Re > 1000 \end{cases} \quad (8)$$

$$Re = \frac{\rho_l d_s |\bar{U}_s - \bar{U}_l|}{\mu_l} \quad (9)$$

The modeling of multiphase turbulent flow in an agitated vessel is very complex and computationally expensive for the effects among the phases. To simplify the calculation, the turbulence in the three-phase agitated vessel is restricted within continuous phase in our CFD simulations for the relatively low holdup of dispersed phases. The standard k - ε model is used to describe the turbulent flow in the agitated vessel. The equations for continuous phase turbulent kinetic energy (k_i) and its dissipation rate (ε_i) are given by:

$$\begin{aligned} \frac{\partial}{\partial t}(\rho_l \alpha_l k_l) + \nabla(\rho_l \alpha_l \bar{U}_l k_l) = \\ = \nabla \left(\alpha_l \left(\mu_l + \frac{\mu_{t,l}}{\sigma_k} \right) \nabla k_l \right) + \alpha_l \rho_l (P_{k,l} - \varepsilon_l) + \alpha_l \rho_l \Pi_{k,l} \end{aligned} \quad (10)$$

$$\begin{aligned} \frac{\partial}{\partial t}(\rho_l \alpha_l \varepsilon_l) + \nabla(\rho_l \alpha_l \bar{U}_l \varepsilon_l) = \\ = \nabla \left(\alpha_l \left(\mu_l + \frac{\mu_{t,l}}{\sigma_\varepsilon} \right) \nabla \varepsilon_l \right) + \alpha_l \frac{\varepsilon_l}{k_l} (C_{1\varepsilon} P_{k,l} - C_{2\varepsilon} \rho_l \varepsilon_l) + \\ + \alpha_l \rho_l \Pi_{\varepsilon,l} \end{aligned} \quad (11)$$

$$\mu_{t,l} = \rho_l C_\mu \frac{k_l^2}{\varepsilon_l} \quad (12)$$

where the model constants are $C_{1\varepsilon}=1.44$, $C_{2\varepsilon}=1.92$, $C_\mu=0.09$, $\sigma_k=1.0$ and $\sigma_\varepsilon=1.3$. $P_{k,l}$ is the production of turbulent kinetic energy. $\Pi_{k,l}$ and $\Pi_{\varepsilon,l}$ are the effects of the dispersed phase on the continuous phase. The term $\Pi_{k,l}$ is derived from the instantaneous equation of the continuous phase and takes the form:

$$\Pi_{k,l} = \sum_{p=1}^M \frac{K_{pl}}{\alpha_l \rho_l} (k_{pl} - 2k_l + \bar{v}_{pl} \bar{v}_{dr}) \quad (13)$$

where M is the number of the dispersed phase, K_{pl} represents the momentum exchange coefficient of the continuous phase l and the dispersed phase p , k_{pl} is the covariance of the velocities of the two phases. v_{pl} is the relative velocity and v_{dr} is the drift velocity. The drift velocity is caused by turbulent fluctuations in the volume fraction. For our simulation, the drift velocity is not considered.

$\Pi_{\varepsilon,i}$ can be modeled according to Elgobashi *et al.* [44]:

$$\Pi_{\varepsilon,i} = C_{3\varepsilon} \frac{\varepsilon_i}{K_1} \Pi_{k,i} \quad (14)$$

where the model constant $C_{3\varepsilon} = 1.2$.

In Eqs. (3)-(5), the Reynolds stress tensor $\tau_{eff,i}$ is related to the mean velocity gradients and can be written as:

$$\tau_{eff,i} = \alpha_i \mu_{eff,i} (\nabla \bar{U}_i + \nabla \bar{U}_i^T) - \frac{2}{3} \alpha_i (\rho_i k_i + \mu_{eff,i} \nabla \bar{U}_i) I \quad (15)$$

where μ_{eff} is the effective viscosity, which contains the molecular viscosity and turbulent viscosity. The effective viscosity of phase i can be written as:

$$\mu_{eff,i} = \mu_i + \mu_{t,i} \quad (16)$$

where μ_i is molecular viscosity and $\mu_{t,i}$ is turbulent viscosity of phase i . The turbulent viscosity of the continuous phase is obtained by using the standard $k-\varepsilon$ model as mentioned above. The turbulent viscosity of the dispersed phase (gas and solid) is calculated by using a model proposed by Simonin *et al.* [45].

Initial and boundary conditions

The commercial CFD software Fluent 6.2 was used to perform all the simulations. Under the initial conditions, the impeller speed and gas inlet rate are assumed to be zero, and liquid is still at the height of $H = 0.772$ m. The zone above liquid level is filled with air. The floating particles suspend uniformly in liquid within the zone of $1.5 < z/T < 2.0$. Then, gas was introduced from the holes of the gas distributor with volume fraction of 1.0, and the impeller agitation was started. Gas flows out from the gas outlet port where gauge pressure is zero. As mentioned earlier, the fluid domain was divided into impeller region and stationary region to apply the MRF approach. Then, the faces between the two regions are defined as the "interface" through which the mass, momentum and energy are exchanged. The solid walls, such as the vessel internal wall, the surfaces of shaft, baffles and blades are defined as no-slip boundaries for liquid phase with standard wall functions while free slip boundaries for dispersed phases. The unsteady calculation was carried out and the time step was 0.005 s with 20 iterations. To solve the partial differential equations, the SIMPLE algorithm was applied to couple the pressure and velocity. The first order upwind scheme was used for all the spatial terms.

RESULTS AND DISCUSSION

Two-phase flow in agitated vessels

The experimental data about gas-liquid-solid agitated vessels are scarce and cannot be used to verify our CFD simulation results directly. Hence, two extreme cases of gas-liquid and solid-liquid simulated results are compared with the experimental data in the literature. The reliability and accuracy of the simulation are discussed. Although the structures of the two-phase agitated vessels are different from that of the three-phase agitated vessel, the multiphase models for the simulation are almost the same. The details of the geometry for gas-liquid and solid-liquid agitated vessels in the present work are consistent with that in the literature [2,46]. For the gas-liquid system, the flow field in a dual-impeller stirred tank is predicted and the local gas holdup are compared with experimental results of Alves *et al.* [2] as shown in Figure 3a. For the solid-liquid system, the flow field characteristics in a solid-liquid tank agitated by PBTD45 impeller are investigated. The simulated local solid holdup distribution is compared with the experimental data of Spidla *et al.* [46] as shown in Figure 3b (under conditions of $N = 159$ r/min, $d_s = 0.14$ mm, $\rho_s = 2470$ kg/m³). It can be observed that the trends of simulated results for solid holdup distributions are in good agreement with the experiments reported elsewhere [46]. The values of simulated local solid holdup are relatively close to the experimental data reported elsewhere [46]. For the gas-liquid system, the simulated results are in good agreement with the experimental data [2] at radial location of $r = 0.024$ m, while the comparison is not very good at radial location of $r = 0.07775$ m. Indeed, it is difficult to simulate multiphase flow accurately in agitated vessels for the complexity of the flow field. For the simulations of the present study, some of the discrepancies between the simulation results and experimental data in the literature maybe caused by the following aspects. i) Some of the interphase forces are ignored in the simulation as mentioned earlier. ii) The breakage and coalescence of bubbles are not considered in the simulation of gas-liquid system. iii) The $k-\varepsilon$ turbulence model is not accurate enough, since the $k-\varepsilon$ turbulence model governs the transport equations of averaged flow quantities with the whole range of the turbulence scales being modeled. To solve the problem, some scholars adopted the large eddy simulation (LES) method to describe the turbulence flow in the agitated vessel. Zhang [47], for example, compared the large eddy simulation results with experimental data and the simulation results by

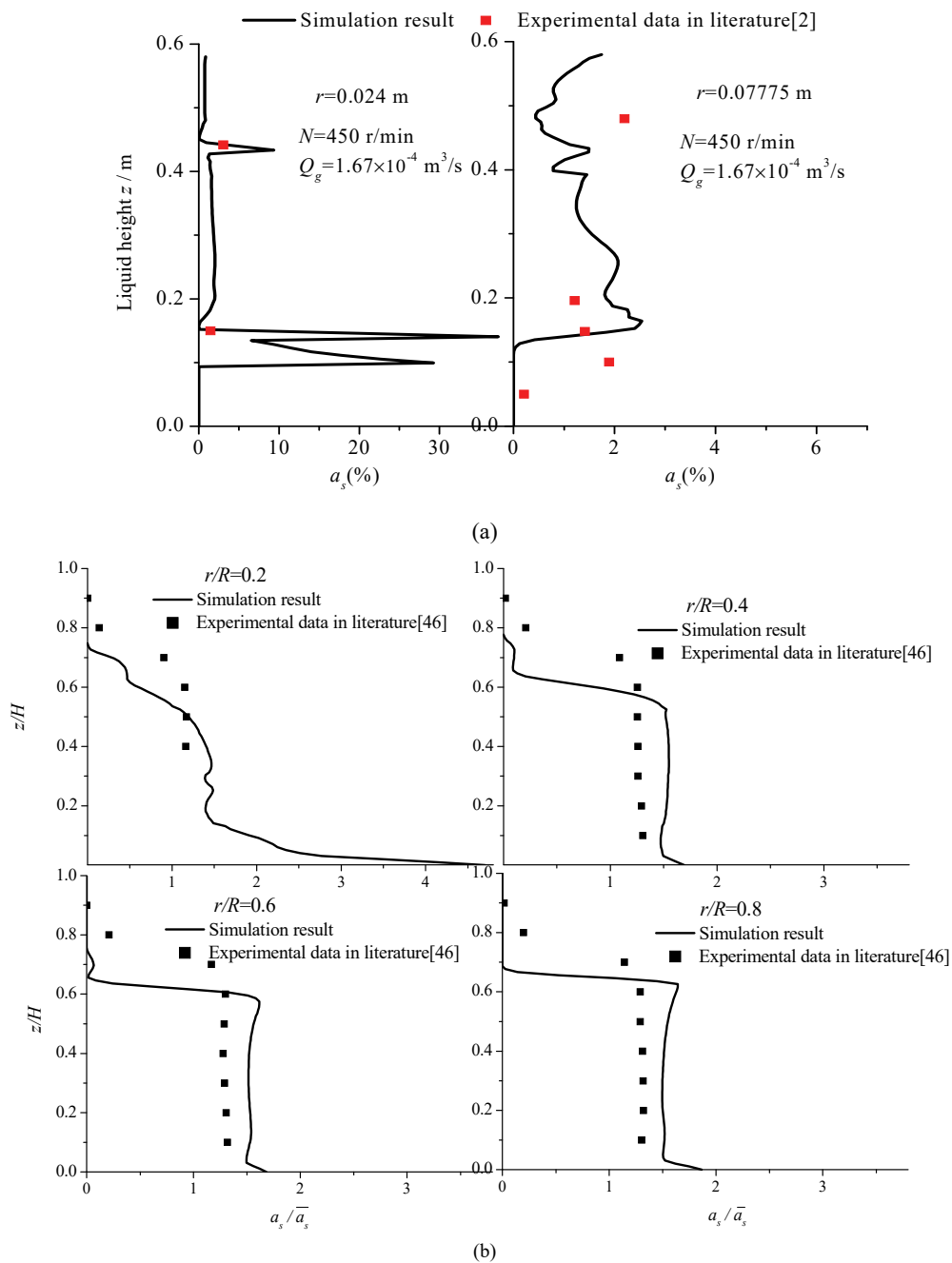


Figure 3. Comparison of simulated gas and solid holdup distributions with experimental data in the literature (a) for gas holdup distribution, b) for solid holdup distribution).

the $k-\varepsilon$ model, and found that the LES has much better accuracy than the $k-\varepsilon$ model. Derksen [48] used the large eddy simulation to investigate the solid suspension in agitated vessels. However, the LES method requires very fine meshes and a significant amount of CPU time. *iv)* The particle size distributions in the experiments are not considered in the simulation of solid-liquid system.

Gas dispersion and solid suspension in the three-phase agitated vessel

Figure 4 shows the solid and gas holdup distributions in a vertical plane in the three-phase agitated vessel. As can be seen from Figure 4a, solid particles are mainly suspended in the liquid surface region, especially in the center of the liquid surface region since the particles density is lower than that of liquid. On the whole, particles concentration increases with increasing of the axial height. For the gas

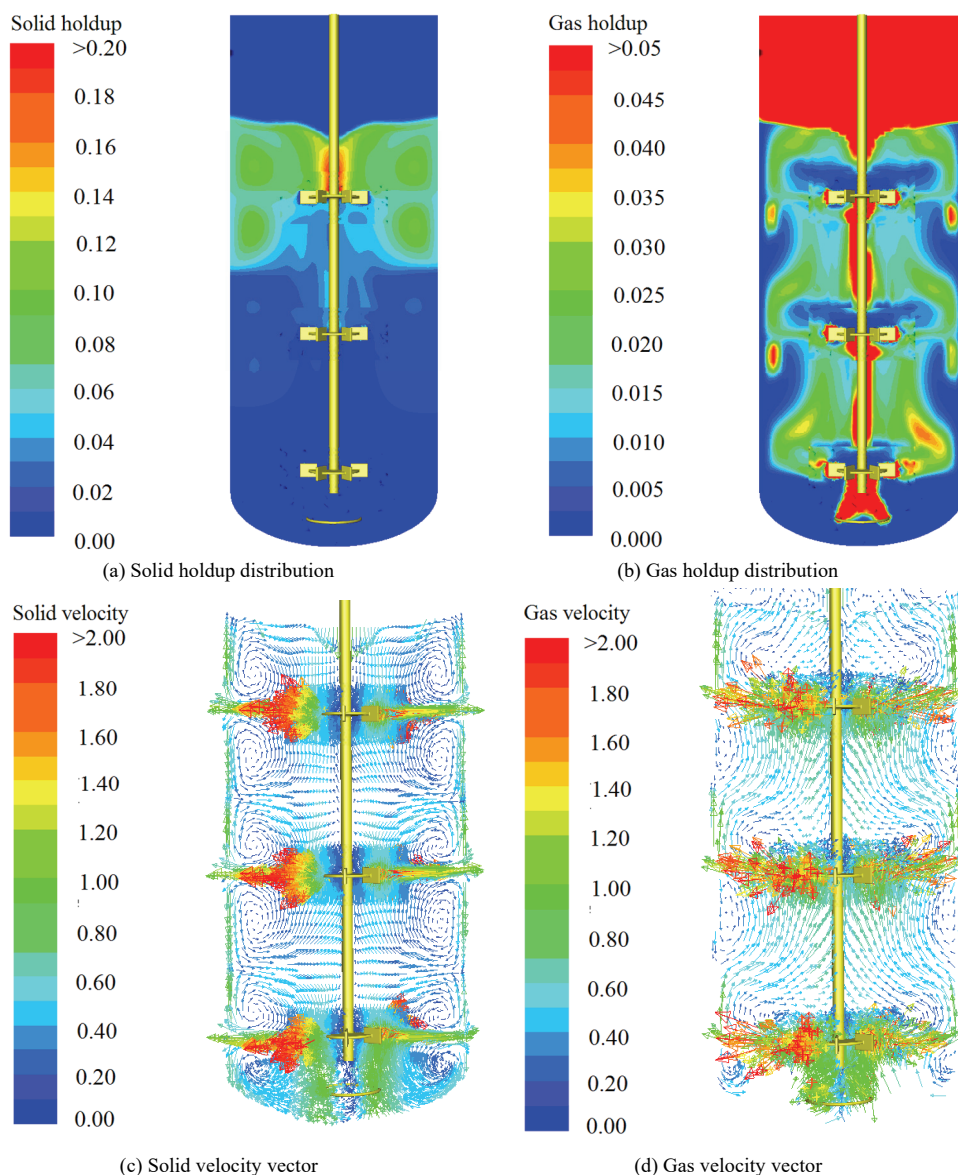


Figure 4. Solid and gas holdup distributions in a vertical plane mid-way between two adjacent baffles ($v_G = 4.3 \times 10^3$ m/s, $\bar{\alpha}_s = 3.2\%$).

holdup distribution, gas was dispersed by three impellers in turn after introduced from the gas distributor and eventually escaped from the liquid surface as shown in Figure 4b. The characteristics of solid suspension and gas dispersion are closely related to the velocity field. It can be seen from Figure 4c and d that, velocity fields of solid phase and gas phase are quite different. For the velocity field of solid phase, since the solid phase density is close to that of liquid phase, double-circulation flow pattern is formed for each of the disc turbine. The velocity in the center of the circular vortex is low, which leads to high floating particles concentration there. For the velocity field of gas phase, gas mainly flows upward after discharged from the impeller region. Gas circular vortex in the vessel is not obvious. Gas holdup in the path of gas

flow is relatively high while relatively low directly above the impellers for the blocking effect of the disc on the air flow.

Effect of superficial gas velocity on solid holdup distribution

Figure 5 presents the floating particles holdup distributions at radial location of $r/R = 0.5$ under different superficial gas velocities. It should be noted that the local particles holdup in Figure 5 is the mean value of four radial locations mid-way between two adjacent baffles at $r/R = 0.5$. Accordingly, the local particles (or gas) holdup in other figures is also the mean value of four radial locations. It can be seen from Figure 5 that the influence of superficial gas velocity on floating particles suspension is great.

Local solid holdup in upper of the vessel decreases gradually with increasing of superficial gas velocity. When superficial gas velocity increases from 0 to 6.44×10^{-3} m/s, the highest float particles holdup in the center of the surface region decreases from 0.22 to 0.18. The simulation results show that increasing of superficial gas velocity is in favor of floating particles off-surface suspension. In the literature, Xu [13] experimentally measured the critical just drawdown impeller speed for floating particles off-surface suspension and found that the critical just drawdown impeller speed decreases with increasing of superficial gas velocity. It indicates that the reduction of critical just drawdown impeller speed is that the increase of superficial gas velocity can help partly the floating particles off-surface suspension. Thus, the simulation results of the present study are in agreement with the experimental findings in the literature [13]. It can also be seen from Figure 5 that, for the upper impeller region, with increasing of superficial gas velocity, floating particles holdup decreases obviously in the upper part of the upper impeller. For the lower impeller region, the floating particles holdup is very low and floating particles holdup decreases under aerated conditions.

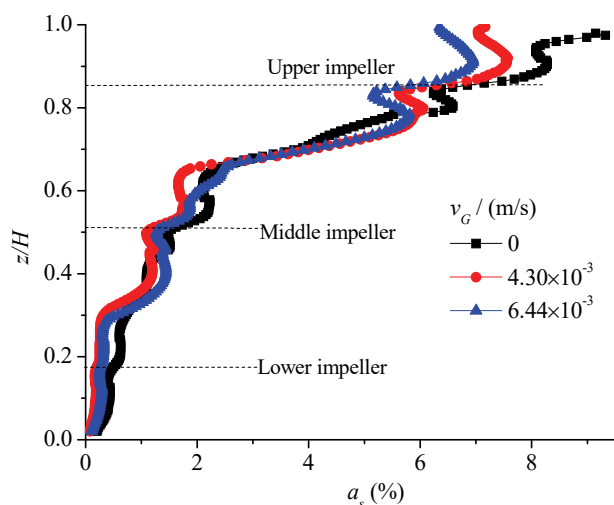


Figure 5. Effect of superficial gas velocity on axial distribution of solid holdup ($\bar{\alpha}_s = 3.2\%$, $r/R = 0.5$).

Effect of superficial gas velocity on gas holdup distribution

Figure 6 gives the gas holdup distributions under different superficial gas velocities. It is easy to understand that global gas holdup rises in the agitated vessel with increasing of superficial gas velocity. Furthermore, it can be found that the influence of superficial gas velocity on local gas holdup varies with regions. As shown in Figure 6a, with increasing of

superficial gas velocity, local gas holdup in the bubbles rising channel and surface region increases obviously, while staying almost unchanged in the bottom region. For the bottom region, owing to the buoyancy of the bubbles, very few bubbles can be entrained to the bottom region, which leads to a gas holdup of almost zero. For the surface region, liquid level fluctuation increases with increasing of superficial gas velocity and more bubbles are easy to be suctioned to the liquid, which leads to obvious increasing of gas holdup there. Figure 6b shows the axial distribution of gas holdup in the agitated vessel. It can be seen that the highest local gas holdup is not found at the axial height of each impeller. For the upper and middle impeller regions, there are two gas holdup peaks just above and below the planes of each impeller. For the lower impeller, there is only one gas holdup peak above the plane of the impeller.

Effect of solid loading on gas holdup distribution

Figure 7a shows the gas holdup distributions in the agitated vessel for two different solid loadings. It can be observed that, with increasing of floating particles loading, local gas holdup in the lower circular vortex of upper and middle impellers decreases significantly, while increases slightly in the gas rising channel. Figure 7b gives the quantitative analysis of gas holdup axial distribution at radial location of $r/R = 0.85$. Local gas holdup changes mainly in the lower part of upper and middle impellers for different solid loadings. At this radial location, average gas holdup falls from 1.34 to 1.22% when solid loading rises from 3.2 to 6.4%. It suggests that, in general, adding solid loading makes gas-liquid dispersion worse in the vessel. In the literature, Bao [23] also found that gas holdup decreases as the solid loading is increased through experimental investigation. The reason may be that the floating particles could accelerate the ascending gas bubbles and make the ability of fluid flow in the lower part of the upper and middle impellers weakened. Moreover, since particle density is slightly lower than that of liquid, the power consumption reduces with increasing of solid loading. For the CFD simulation results of this study, the power consumption reduces slightly from 133 W to 131 W when the solid loading rises from 3.2 to 6.4%.

Effect of solid loading on solid holdup distribution

As shown in Figure 8a, it is certain that local solid holdup in most regions increases with increasing of solid loading. For further analyzing the influence of solid loadings on the uniformity of floating particles distribution in the agitated vessel, the axial distri-

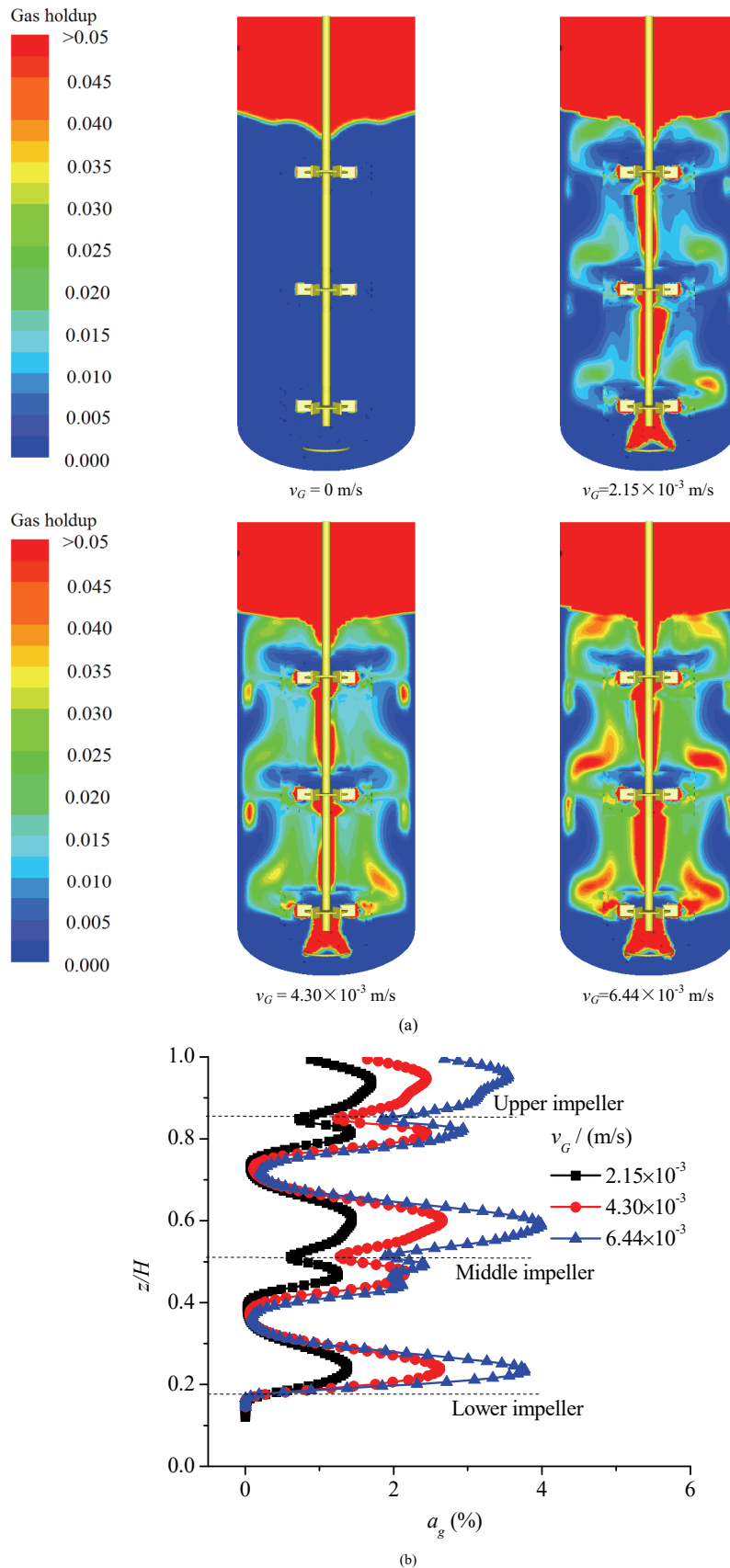


Figure 6. Effect of superficial gas velocity on gas dispersion in the agitated vessel ($\bar{\alpha}_s = 3.2\%$, a) gas holdup distributions in a vertical plane mid-way between baffles, b) axial distribution of gas holdup at $r/R = 0.85$).

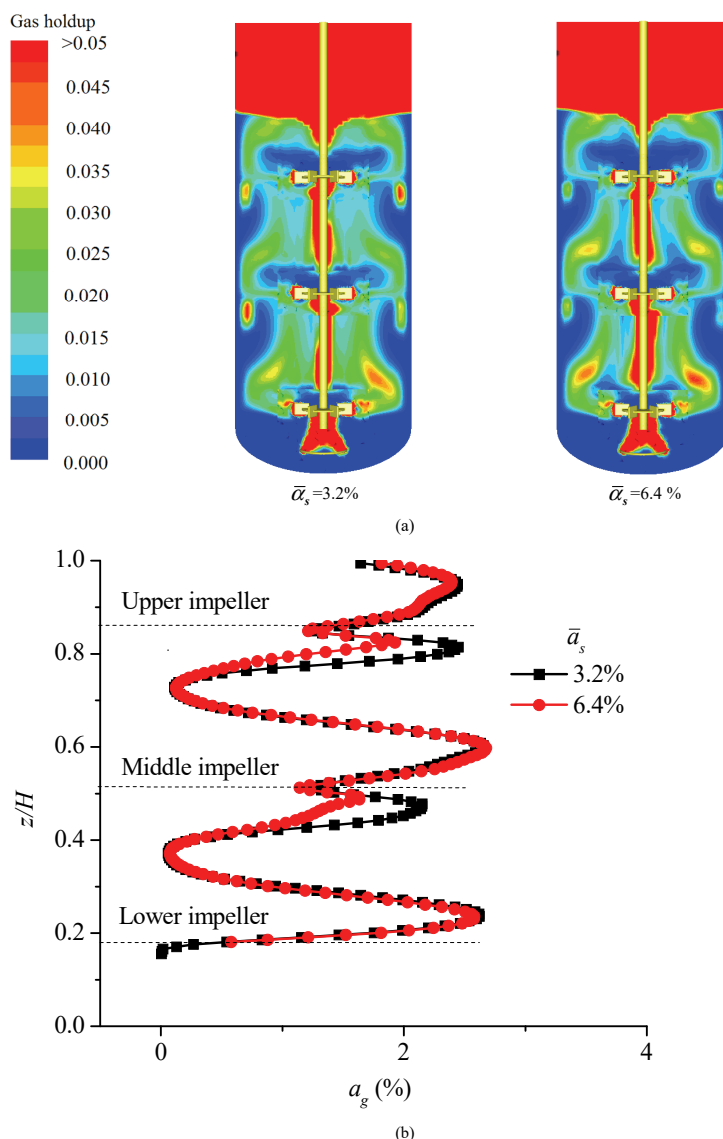


Figure 7. Effect of solid loading on gas dispersion in the agitated vessel ($v_G = 4.30 \times 10^{-3}$ m/s, a) gas holdup distributions in a vertical plane mid-way between baffles, b) axial distribution of gas holdup at $r/R = 0.85$).

bution of relative solid holdup (a_s / \bar{a}_s) at radial location of $r/R = 0.5$ was investigated. It can be seen from Figure 8b that the relative solid holdup in the upper part of the vessel is higher slightly for high solid loading than that for low solid loading. On the whole, the solid loading has little effect on the relative solid holdup distribution. However, since local absolute solid holdup increases with increasing of solid loading, some of the floating particles will accumulate in the surface region and not flow in the agitated vessel for very high solid loading.

CONCLUSIONS

In the present work, CFD simulation was carried out to investigate gas dispersion and floating particles

suspension in a gas-liquid-solid agitated vessel. The Eulerian multi-fluid model along with the standard $k-\epsilon$ turbulence model was applied in the simulation. It is found that flow patterns in the agitated vessel vary with phases. Double-circulation flow pattern is formed for each of the disc turbine for the velocity field of solid phase, while the double-circulation flow pattern is not obvious for the velocity field of the gas phase. Floating particles are easy to accumulate in the center of the surface region. Increasing superficial gas velocity results in solid holdup decrease in surface region and is in favor of floating particles off-surface suspension. Adding solid loading causes gas-liquid dispersion becoming worse in the agitated vessel, while has little effect on relative solid holdup distribution. The simulated results of two extreme cases of

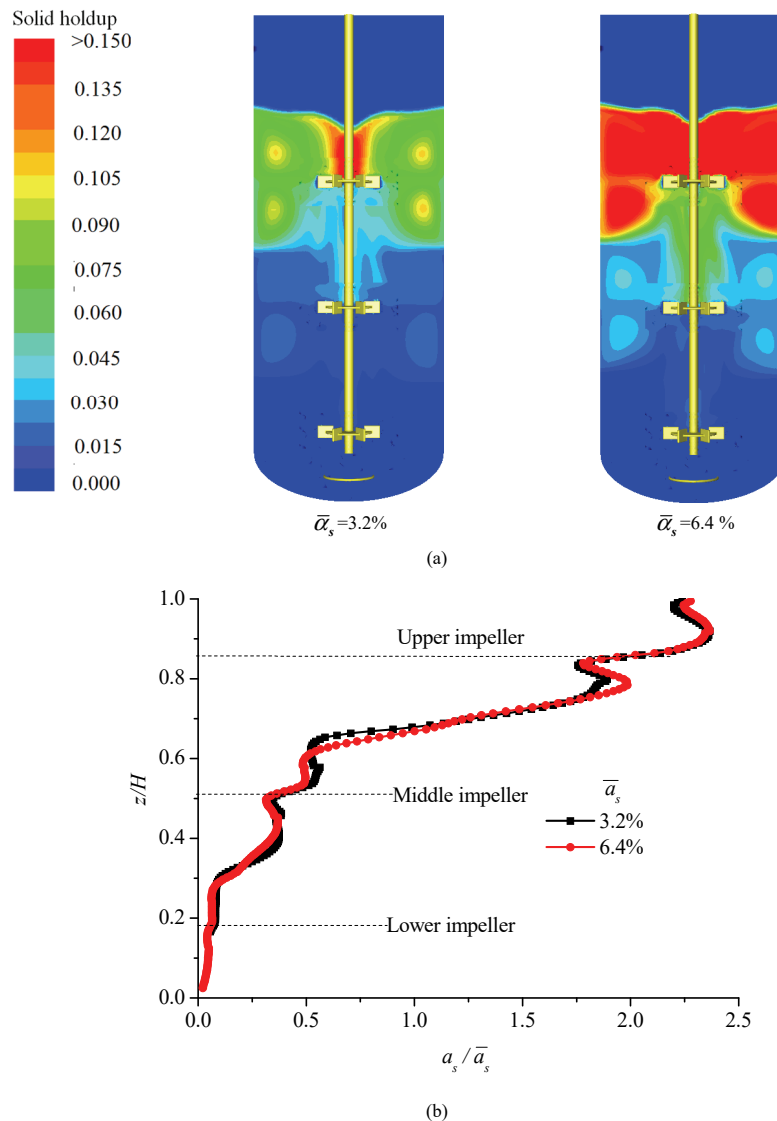


Figure 8. Effect of solid loadings on solid suspension in the agitated vessel ($v_G = 4.30 \times 10^{-3}$ m/s, a) solid holdup distributions in a vertical plane mid-way between baffles, b) axial distribution of solid holdup at $r/R = 0.5$).

gas-liquid and solid-liquid are compared with the experimental data in the literature. Some discrepancies in comparison with experimental data in the literature are discussed. The present modeling can be improved by employing more reliable turbulence model such as LES method, and considering the coalescence and breakage of bubbles, etc. These topics thus will be the main focus of our further work in the field of three-phase CFD simulations. Overall, the prediction of gas dispersion and floating particles suspension in the present work would be helpful for better understanding of the flow field characteristics in the three-phase agitated vessel and the subsequent further studies.

Nomenclature

$C_{1\epsilon}, C_{2\epsilon}, C_{3\epsilon}, C_\mu$ turbulence model constants

C_D drag coefficient
 d diameter of the dispersed phase particles, m
 D diameter of the impeller, m
 F interphase forces, N/m^3
 g gravitational force, m/s^2
 H unaerated liquid height, m
 k turbulent kinetic energy, m^2/s^2
 k_{pl} covariance of the velocities of the two phases, m^2/s^2
 K_{pl} momentum exchange coefficient
 M number of the dispersed phase
 N impeller rotation speed, r/min
 p static pressure, Pa
 $P_{k,l}$ production of turbulent kinetic energy, $\text{kg/m}^3 \text{s}^3$
 Q_g gas volume flux, m^3/s
 r radial location in the vessel, m

R radius of the vessel, m
 t time, s
 T diameter of the vessel, m
 \vec{U} velocity vector, m/s
 v_{dr} drift velocity, m/s
 V_{pl} relative velocity, m/s
 V_G superficial gas velocity, m/s
 z axial coordinate in the vessel, m

Greek Letters

α phase hold up
 ε turbulent energy dissipation, m^2/s^3
 μ_{eff} effective viscosity, kg/m s
 μ_t molecular viscosity of continuous phase, kg/m s
 $\mu_{t,l}$ turbulent viscosity of continuous phase, kg/m s
 $\Pi_{k,l}$ effects of the dispersed phase on the continuous phase in equation(10), m^2/s^3
 $\Pi_{\varepsilon,l}$ effects of the dispersed phase on the continuous phase in equation(11), m^2/s^4
 ρ density, kg/m^3
 $\sigma_k, \sigma_\varepsilon$ turbulent model constants

Subscripts

i – number of phase
g – gas phase
l – liquid phase
s – solid phase

Acknowledgements

The authors would like to acknowledge the support by Key Scientific Research Project of Sichuan Provincial Education Department (15ZA0107), Doctor Foundation of Southwest University of Science and Technology (11zx7162).

REFERENCES

- [1] B.W. Lee, M.P. Dudukovic, Chem. Eng. Sci. **109** (2014) 264-275
- [2] S.S. Alves, C.J. Maid, J.M.T. Vasconcelos, Chem. Eng. Sci. **57** (2002) 487-496
- [3] F. Cabaret, L. Fradette, T. Tanguy, Chem. Eng. Sci. **63** (2008) 1636-1647
- [4] G. Montante, A. Paglianti, Chem. Eng. J. **279** (2015) 648-658
- [5] R. Angst, M. Kraume, Chem. Eng. Sci. **61** (2006) 2864-2870
- [6] H. Unadkat, C.D. Rielly, G.K. Hargrave, Z.K. Nagy, Chem. Eng. Res. Des. **87** (2009) 573-586
- [7] J.C. Godfrey, Z.M. Zhu, AIChE Symp. Ser. **299** (1994) 181-185
- [8] D. Dohi, T. Takahashi, K. Minekawa, Y. Kawase, Chem. Eng. J. **97** (2004) 103-114
- [9] Y. Zhu, J. Wu, Can. J. Chem. Eng. **80** (2002) 1-6
- [10] V.B. Rewatkar, R. Raghava, J.B. Joshi, Ind. Eng. Chem. Res. **30** (1991) 1770-1784
- [11] C.W. Wong, J.P. Wang, S.T. Huang, Can. J. Chem. Eng. **65** (1987) 412-419
- [12] G.R. Kasat, A.B. Pandit, Can. J. Chem. Eng. **83** (2005) 618-642
- [13] S. Xu, Research on gas-liquid-solid three phase mixing equipment [D]. Hangzhou: Zhejiang University, 2001
- [14] M.F. Edwards, D.I. Ellis, Inst. Chem. Eng. Symp. Ser. **89** (1984) 1-13
- [15] A. Bakker, J. J. Frijlink, Chem. Eng. Res. Des. **67** (1989) 208-210
- [16] J. Karcz, B. Mackiewicz, Chem. Pap. **63** (2009) 164-171
- [17] G. Taşkin, H. Wei, Chem. Eng. Sci. **58** (2003) 2011-2022
- [18] G. Taşkin, Chem. Eng. Sci. **61** (2006) 2871-2869
- [19] R. Wójtowicz, Ind. Eng. Chem. Res. **53** (2014) 13989-14001
- [20] K. Takahashi, S. Sasaki. J. Chem. Eng. Jpn. **32** (1999) 40-44
- [21] S. Xu, W. Z. Ren, X. M. Zhao, Chem. Eng. Tech. **24** (2001) 189-194
- [22] S. Xu, L.F. Feng, X.P. Gu, K. Wang, G.H. Hu, Chem. Eng. Tech. **23** (2000) 103-113
- [23] Y.Y. Bao, Z.G. Hao, Z.M. Gao, L.T. Shi, J.M. Smith, Chem. Eng. Sci. **60** (2005) 2283-2292
- [24] G. Micale, A. Brucato, F. Grisafi, AIChE J. **45** (1999) 445-464
- [25] F.L. Yang, S.J. Zhou, C.X. Zhang, Korean J. Chem. Eng. **32** (2015) 816-825
- [26] R. Zadghaffari, J.S. Moghaddas, J. Revstedt, Comput. Chem. Eng. **33** (2009) 1240-1246
- [27] A.R. Khopkar, G.R. Kasat, A.B. Pandit, V.V. Ranade, Ind. Eng. Chem. Res. **45** (2006) 4416-4428
- [28] M. Petitti, A. Nasuti, D.L. Marchisio, M. Vanni, G. Baldi, N. Mancini, F. Podenzani, AIChE J. **56** (2010) 36-53
- [29] G. Li, X.G. Yang, G.C. Dai, Chem. Eng. Sci. **64** (2009) 5104-5116
- [30] A. Tamburini, A. Cipollina, G. Micale, A. Brucato, M. Ciofalo, Chem. Eng. J. **223** (2013) 875-890
- [31] J.J. Derksen, AIChE J. **49** (2003) 2700-2714
- [32] M.A. Sattar, J. Naser, G. Brooks, Chem. Eng. Process. **70** (2013) 66-76
- [33] M.A. Sattar, J. Naser, G. Brooks, Chem. Eng. Sci. **94** (2013) 69-78
- [34] M.V. Sardeshpande, V.A. Juvekar, V.V. Ranade, AIChE J. **56** (2010) 2795-2804
- [35] M. Jahoda, L. Tomášková, M. Mošték, Chem. Eng. Res. Des. **87** (2009) 460-467
- [36] B.N. Murthy, R.S. Ghadge, J.B. Joshi, Chem. Eng. Sci. **62** (2007) 7184-7195
- [37] R. Panneerselvam, S. Savithri, G.D. Surender, Chem. Eng. Res. and Des. **86** (2008) 1331-1344
- [38] W. Feng, J. Wen, J. Fan, Q. Yuan, X. Jia, Y. Sun, Chem. Eng. Sci. **60** (2005), 6887-6898

- [39] A.R. Sarhan, J. Naser, G. Brooks, *Int. J. Miner. Process.* **146** (2016) 54-64
- [40] R. Achouri, I. Mokni, H. Mhii, P. Bournot, *Energy Convers. Man.* **64** (2012) 633-641
- [41] D. Wadnerkar, R.P. Utikar, M.O. Tade, V.K. Pareek, *Adv. Powder Technol.* **23** (2012) 445-453
- [42] R. Panneerselvam, S. Savithri, G.D. Surender, *Ind. Eng. Chem. Res.* **48** (2009) 1608-1620
- [43] L. Schiller, Z. Naumann, *Z. Ver. Dtsch. Ing.* **77** (1935) 318-325
- [44] S.E. Elgobashi, W. Abou-Arab, *Phys. Fluids* **26** (1983) 931-938
- [45] O. Simonin and P. L. Viollet, *Numer. Meth. Multiphase Flows* **91**(1990) 73-82
- [46] M. Spidla, V. Sinevic, M. Jahoda, V. Machon, *Chem. Eng. J.* **113** (2005) 73-82
- [47] Y.H. Zhang, C. Yang, Z.S. Mao, *AIChE J.* **5** (2008) 1963-1974
- [48] J.J. Derksen, *AIChE J.* **49** (2003): 2700-2714.

LIANGCHAO LI
BIN XU

Key Laboratory of Testing Technology
for Manufacturing Process of Ministry
of Education, School of Manufacturing
Science and Engineering, Southwest
University of Science and Technology,
Mianyang, Sichuan, China

NAUČNI RAD

SIMULACIJA MEŠANJA SISTEMA GAS-TEČNOST- -FLOTIRAJUĆE ČESTICE U SUDU SA MEŠALICOM POMOĆU PRORAČUNSKE DINAMIKE FLUIDA

Trofazni sistem gas-tečnost-flotirajuće čestice u sudu sa mešalicom je numerički proučavan pomoću proračunske dinamike fluida. U simulaciji je korišćen Eulerov višefluidni model zajedno sa standardnim modelom turbulencije k-ε. Za rešavanje rotacije mešalice korišćen je pristup višestrukog referentnog koordinatnog sistema. Prvo su određeni polje brzina i raspodele sadržaja gasa i čestica u sudu, a potom su istraženi efekti radnih uslova na disperziju gasa i suspenziju čestica. Rezultati simulacije pokazuju da se polja brzine čvrste i gasne faze u sudu prilično međusobno razlikuju. Flotirajuće čestice se lako akumuliraju u sredini površinskog područja, dok povećanje površinske brzine gasa favorizuje udaljavanje čestica od ovog područja. Sa povećanjem količine čvrstih čestica, disperzija gasa postaje sve gora, dok se relativna raspodela sadržaja čestica menja malo. Diskutovana su, takođe, ograničenja sadašnjeg modela i ponudjena su dalja istraživanja u budućnosti.

Ključne reči: trofazni tok, proračunska dinamika fluida (CFD), plutajuća čestica, sud sa mešalicom, numerička simulacija, višestruki referentni koordinatni sistem (MRF).

ZIXIA LI¹⁻³
YIN RAN²
WENQI ZHANG⁴
WEI SUN¹
TINGHAI WANG²

¹State Key laboratory for Oxo Synthesis and Selective Oxidation, Lanzhou Institute of Chemical Physics, Chinese Academy of Sciences, Lanzhou, China

²Lanzhou Petrochemical Research Center of Petrochina, Lanzhou, China

³University of Chinese Academy of Sciences, Beijing, China

⁴Petrochina Hohhot Petrochemical Company, Hohhot, China

SCIENTIFIC PAPER

UDC 665.633:665.644:66.094.522.091.8

INDUSTRIAL APPLICATION OF GASOLINE AROMATIZATION AND DESULFURIZATION TECHNOLOGY IN HOHHOT REFINERY

Article Highlights

- Ultraclean and high quality FCC gasoline can be obtained by GARDES technology
- Deep desulfurization can be achieved by removing sulfur compounds at different stage
- Olefin reduction with acceptable octane loss can be realized by hydroisomerization
- GARDES technology has more flexibility on the hydrodesulfurization unit of refinery

Abstract

*Gasoline aromatization and desulfurization (GARDES) technology is extensively used in refineries of Petrochina, aiming to produce high quality ultraclean fluid catalytic cracking (FCC) gasoline. This article introduces the industrial application results on the hydrodesulfurization unit of the Hohhot refinery, which plays an important role in guiding next round gasoline upgrading. The characteristics and the principle of GARDES technology were elaborated by analyzing the distribution of sulfur and hydrocarbon compounds in the feed and product. The analysis results proved that the presence of broad ranged sulfur types in the feed can be removed at different stages. Olefin can be decreased by saturation and conversion into *i*-paraffins and aromatics. The sulfur content of the blend product can be limited under 10 mg/kg, showing GARDES technology has excellent sulfur removal ability. The olefin reduction can also satisfy the ever-increasing severe requirement about the olefin limitation, while the loss of research octane number (RON) can be minimized to an acceptable level. Furthermore, according to the demand of gasoline upgrading, GARDES technology has great flexibility by adjusting operation condition without any further investment, which brings more economic benefits for refinery.*

Keywords: fluid catalytic cracking gasoline, hydrodesulfurization, olefin reduction, octane preservation.

With the ever-increasing stricter environmental regulations on transportation fuel, petroleum refineries over the world are required to speed up their technology to produce ultraclean gasoline. Effective 2017, the China national V standard (GB17930-2013) of gasoline for motor vehicles equivalent with Europe V standard requires the content of sulfur and olefin less than

10 mg/kg and 24 vol.%, respectively [1]. Depending on the refinery configuration, the gasoline pool is comprised of different distillates coming from reformat, isomerase and FCC gasoline, etc. [2,3]. In China, FCC gasoline containing 90% sulfur and olefin generally accounts for 70% of the gasoline pool, while other blending components such as reformat and isomerase containing negligible sulfur and olefin but high octane number only shares 20% of the gasoline pool [4]. It is significantly different from the configuration of United States and Europe wherein FCC gasoline contributes about 30% to the gasoline pool [5,6]. Consequently, Chinese refineries face more challenges in reducing sulfur and olefin due to the irrational configuration of the gasoline pool.

Correspondence: W. Sun, State Key laboratory for Oxo Synthesis and Selective Oxidation, Lanzhou Institute of Chemical Physics, Lanzhou, 730000, China; T.H. Wang, Lanzhou Petrochemical Research Center of Petrochina, Lanzhou, 730060, China.
E-mail: wsun@licp.cas.cn; wangtinghai@petrochina.com.cn

Paper received: 5 July, 2016

Paper revised: 3 October, 2016

Paper accepted: 17 October, 2016

<https://doi.org/10.2298/CICEQ160705053L>

Technologies based on the hydrodesulfurization are effective in the removal of sulfur compounds; however, always accompanying olefin saturation would result in the loss of octane number [7,8]. Among the existing technologies, selective hydrodesulfurization such as Prime G⁺ and SCANfining technology have been applied in refineries over the world [9-11]. However, because of the specification about the limitation of olefin content in the new regulation, such selective hydrodesulfurization processes are not suitable for the refineries that share a large part of FCC gasoline. Another hydrotreating technology such as OCT-Gain and UOP-INTEVEP's ISAL process combines deep hydrodesulfurization with octane recovery through isomerization of the paraffins, alkylation or cracking into high octane compounds [12-14]. However, the RON loss resulted from almost complete olefin saturation is difficult to compensate by isomerization and cracking approach. Furthermore, cracking into light products might lead to yield loss, which is also terrible for the economic benefits. To sum up, the clash between hydrodesulfurization and olefin reduction while minimizing the loss of octane number is becoming a great challenge.

In order to solve the above stated problem, the China University of Petroleum (Beijing) and Lanzhou Petrochemical Research Center of Petrochina have developed the FCC gasoline hydro-upgrading technology called GARDES, which has been applied in

seven hydrodesulfurization units of Petrochina. Three reactors and one splitter were cascaded in the process in order to achieve prehydrogenation, separation of the full range FCC gasoline, hydrodesulfurization of the heavy fraction and olefin directional conversion. Fan *et al.* have reported the laboratory results about the last two reactors [15], but lacking industrial data, which were always different from the lab test due to the amplification effects. This work aimed to find the characteristic and principle of GARDES technology based on the industrial application data. First, it was necessary to investigate the configuration of the gasoline pool and the properties of the FCC gasoline feed. Then, the hydrodesulfurization and olefin conversion ability were also studied by analyzing the sulfur distribution and the change of hydrocarbon composition at each step. Eventually, detailed industrial operation experiences for the other refineries were provided.

EXPERIMENTAL

Process of GARDES technology

Figure 1 shows the schematic of the GARDES process used in the hydrodesulfurization units of Hohhot refinery. First, the FCC full range gasoline was treated in the prehydrogenation reactor (Reactor I) to remove thiols compounds. Then, the product of prehydrogenation (Product I) was sent into a splitter to be separated into light fraction and heavy fraction, in

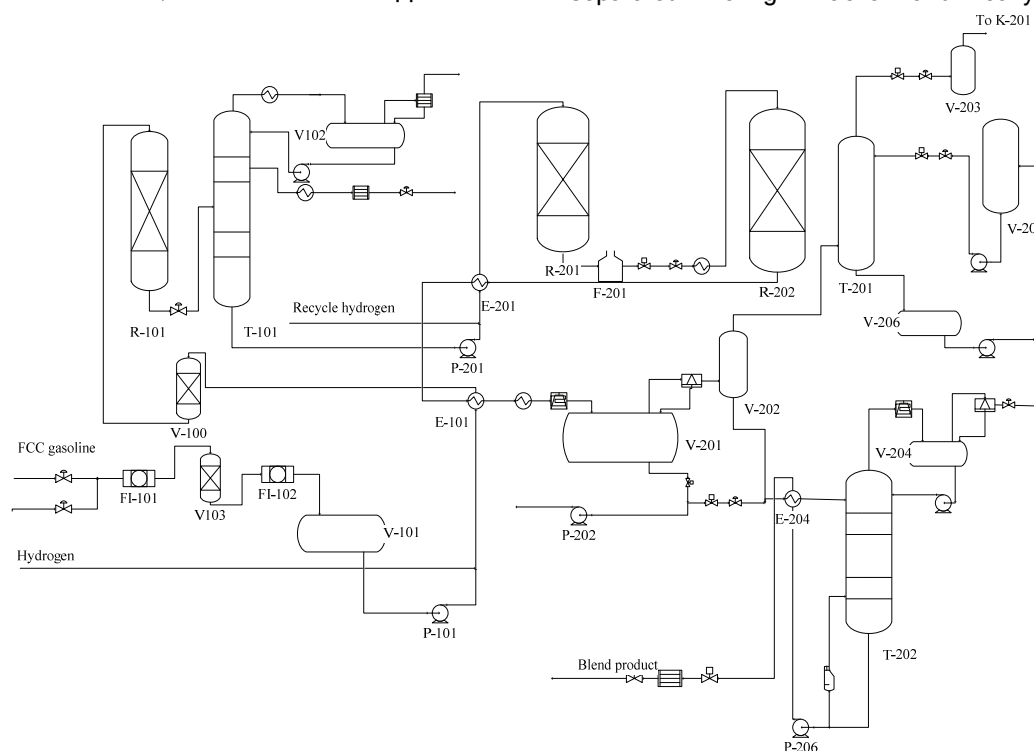


Figure 1. Diagram of FCC hydrodesulfurization units.

which the light fraction containing high olefins and few sulfur compounds was used to blend with the heavy fractions after hydrogenation. The heavy fraction containing less olefins and high sulfur compounds was continued to be hydrotreated in the hydrodesulfurization reactor (Reactor II) to remove part of the sulfur compounds. Following, the effluent of the hydrodesulfurization entered into the RON recovery reactor (Reactor III) where the rest of the sulfur compounds were eliminated, and on the other hand, olefin directional conversion into *i*-paraffins and aromatics were achieved. Finally, the product of heavy fraction (Product II) is blended with the light fraction to obtain ultra-clean FCC gasoline with acceptable loss of RON.

Operating condition of the hydrodesulfurization unit

GARDES technology included three reactors, one splitter and the corresponding catalysts. The three reactors were prehydrogenation, hydrodesulfurization and RON recovery reactor, represented by Reactor I, Reactor II and Reactor III. The corresponding product of Reactor I was referred as Product I. Product II was obtained by cascading Reactor II and Reactor III. The operating conditions and the properties of the corresponding catalysts are presented in Table 1.

Feed and product analysis

The hydrocarbon composition was characterized by PONA method using gas chromatography (Varian CP-3800), with accompanying software purchased from Research Institute of Petroleum Processing (RIPP). The di-olefin content was expressed as maleic anhydride value (MAV) using the UOP Method 326-07. Sulfur distribution was analyzed by gas chromatography (Agilent 7890A) using SCD 355 detector. Thiols content was tested by a Metrohm (916 Ti-Touch) potentiometric titrator using the GB/T 1792-1988 method.

Total sulfur content was determined by a sulfur and nitrogen analyzer (TSN-2000) using the SH/T 0689-2000 method. Distillation tests were performed using standard ASTM D86. RON was detected upon on an engine using the GB/T 5487-1995 method.

RESULTS AND DISCUSSION

Configuration and properties of the gasoline pool

The configuration and the composition of the commercial blend gasoline pool in Hohhot refinery reflected a typical feature for Chinese refineries. As shown in Figure 2, methyl tert-butyl ether (MTBE) containing high octane number took up only 4.26% of the gasoline pool. Another high octane distillate, reformate shared only 25.85% of the gasoline pool. FCC gasoline made up 69.89% of the blend pool, but contributed 98 mg/kg and 33.1 vol.% olefin. In the view of the gasoline pool, it was necessary to decrease sulfur less than 13 ppm, and decrease the olefin less than 35 vol.% for the FCC gasoline. In Table 2, ASTM analysis data of the feed showed that the initial boiling point (IBP) was 32.5 °C, and the final boiling point (FBP) was 195.3 °C. The RON was 90.0.

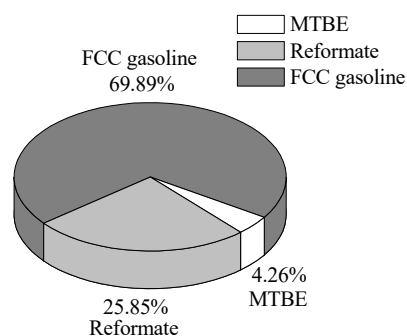


Figure 2. Configuration of the gasoline pool in Hohhot refinery.

Table 1. Operating condition and the properties of catalysts

Parameter	Reactor I	Splitter	Reactor II	Reactor III
Liquid space velocity, h ⁻¹	2.6	-	1.5	1.5
Volume ratio for H ₂ /Oil	7	-	300	300
Pressure, MPa	1.85	0.64	2.13	1.75
Temperature, °C	114	203	211	303
Reflux ratio	-	0.65	-	-
Properties of the corresponding catalysts				
Catalyst name	GDS-20	-	GDS-30	GDS-40
Shape	Tri-tubular	-	Tri-tubular	Tri-tubular
BET surface area, m ² /g	230	-	220	260
Support	Al ₂ O ₃	-	Al ₂ O ₃	Al ₂ O ₃ /ZSM-5
NiO (wt.%)	11.8	-	-	-
MoO ₃ (wt.%)	7.8	-	10.8	5.5
Co ₂ O ₃ (wt.%)	-	-	3.0	1.5

Table 2. Feed and product properties and sulfur distribution

Parameter	Feed	Product I	Light fraction	Heavy fraction	Product II	Blend product
Yield, %	-	-	42	58	-	-
Density, g/cm ³	0.7156	0.7150	0.6479	0.7701	0.7738	0.7226
MAV / gl/(100 g oil)	1.20	0.10	-	-	-	-
Sulfur, mg/kg	98	92	2	132	8	8.5
Thiols, mg/kg	16	3.29	4	4	10	9
RON*	90.0	89.4	-	86.3	82.5	88.5
ASTM distillation, °C						
IBP	32.5	36.5	27.6	83.6	84.6	34.7
10 vol. %	46.7	54.6	34.3	100.7	102.8	52.2
50 vol. %	87.6	99.5	45.3	125.8	127.8	90.1
90 vol. %	160.2	162	65.2	168.1	168.8	170
FBP	195.3	197.9	78.8	205.8	206.6	201.1
Sulfur distribution (mg/kg)						
Hydrogen sulfide	-	-	-	-	1.4	-
Methanethiol	1.4	-	-	-	-	-
Ethanethiol	3.1	-	-	-	-	-
Propanethiol	1.3	-	-	-	0.5	0.3
Thiophene	6.6	6.4	-	7.5	0.9	0.6
Methyl thiophene	13	12.6	-	16.0	0.8	0.4
Thiophane	2.4	1.7	-	1.2	-	-
Methyl thiophane	2.0	1.8	-	1.6	-	-
Ethyl thiophene	3.4	2.9	-	2.9	-	-
Dimethyl thiophene	6.3	6.3	-	8.4	0.6	0.4
Propyl thiophene	1.7	-	-	0.9	-	-
Methyl-ethyl thiophene	1.1	-	-	0.5	-	-
Trimethyl thiophene	2.8	2.7	-	3.6	0.6	0.4
Benzothiophene	4.2	3.9	-	5.1	-	-
Methyl benzothiophene	1.1	1.0	-	5.6	-	-
Unidentified	2.7	10.6	-	20.8	0.6	0.4

The detailed distribution of sulfur compounds is illustrated in Table 2. Five main types existed in the FCC gasoline feed, including thiols, thioethers, thiophenes, alkylthiophenes and benzothiophenes. It was an impossible to remove all kinds of sulfur compounds in a single reactor, indicating relayed sulfur removal in multiple reactors was necessary. As shown in Table 3, the type and quantity of hydrocarbon of the feed had been classified into five groups called, paraffins, *i*-paraffins, olefins, naphthenes and aromatics. The results showed that the major contribution of feed came from *i*-paraffins (36.9 vol.%) and olefins (33.1 vol.%). The feed also contained considerable aromatics which was 13.6 vol.%. The amount of *n*-paraffins (8.2 vol.%) and naphthenes (8.3 vol.%) was very low. Among the 36.9 vol.% of *i*-paraffins, *i*-pentane comprised the major amount of 11.2 vol.%, followed by *i*-hexane of 9.3 vol.%. *i*-paraffins of heptanes, octane and nonane were 5.3, 3.9 and 2.7 vol.%, respectively. Among the 33.1

vol.% olefins, the major amount was pentene (11.5 vol.%) followed by hexenes and heptenes. Higher carbon number olefins were negligible. The aromatic content was of 13.6 vol.%, with majority of C₉⁺ aromatics (8 vol.%), followed by xylenes (4.0 vol.%). The content of toluene was 1.7 vol.%. No benzene existed in the feed. Naphthene content in the feed was 8.3 vol.% with C₇ and C₈ as major followed by C₆ and C₉. The 8.2 vol.% *n*-paraffin in the feed consisted of 3.0 vol.% *n*-pentane, 1.3 vol.% *n*-hexane and 1.5 vol.% butane as major components. The detailed analysis of the hydrocarbon composition helped us to understand the mechanism of the sulfur and olefin conversion happened in the latter reactor.

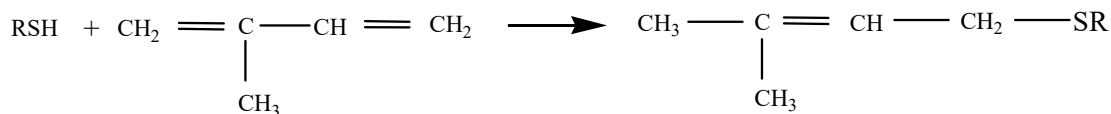
The product of prehydrogenation (Product I)

Reactor I was conducted to convert thiols to heavier sulfur compounds. The di-olefins reacted with

Table 3. Hydrocarbon composition (vol. %) of feed and product

Hydrocarbon type	Feed	Product I	Light fraction	Heavy fraction	Product II	Blend product
<i>n</i> -Paraffins	8.2	8.4	11.9	5.3	6.6	9.6
C4	1.5	0.8	2.1	-	-	0.9
C5	3.0	2.7	7.6	-	-	3.5
C6	1.3	1.7	2.2	-	-	1.8
C7	0.8	1.2	0.1	2.1	2.7	1.3
C8	0.9	1.2	-	2.0	2.3	1.1
C9	0.3	0.3	-	0.5	0.7	0.4
C10	0.2	0.2	-	0.4	0.5	0.3
C11	0.1	0.1	-	0.2	0.3	0.2
C12	0.1	0.1	-	0.1	0.2	0.1
<i>i</i> -Paraffins	36.9	36.6	45.7	29.5	33.0	39.4
C4	0.8	0.3	0.7	-	-	0.3
C5	11.2	8.5	25.0	0.1	0.1	11.4
C6	9.3	9.7	18.5	-	-	10.1
C7	5.3	6.4	1.5	10.1	11.2	6.2
C8	3.9	4.7	-	8.2	9.1	4.4
C9	2.7	3.0	-	5.1	5.9	3.1
C10	1.5	1.7	-	2.6	2.9	1.7
C11	1.1	1.1	-	1.8	2.1	1.2
C12	0.9	1.0	-	1.3	1.5	0.8
C13	0.1	0.2	-	0.3	0.3	0.2
Olefins	33.1	30.4	40.6	25.8	19.6	28.9
C4	3.0	1.4	3.7	-	-	1.6
C5	11.5	9.2	25.1	-	-	11.5
C6	8.6	8.7	11.2	6.7	3.8	7.5
C7	4.5	5.1	0.5	8.5	6.8	3.5
C8	2.1	2.5	-	4.7	3.7	1.7
C9	2.1	2.2	-	3.6	3.2	1.9
C10	0.7	0.8	-	1.3	1.2	0.7
C11	0.6	0.6	-	0.9	0.9	0.5
Naphthenes	8.3	9.5	1.7	14.3	15.4	8.8
C6	1.5	1.7	1.5	1.9	2.0	1.6
C7	2.3	2.9	0.2	4.9	5.5	2.7
C8	2.4	2.7	-	4.1	4.5	2.4
C9	1.5	1.6	-	2.6	2.6	1.5
C10	0.5	0.5	-	0.7	0.6	0.4
C11	0.1	0.1	-	0.2	0.2	0.1
Aromatics	13.6	15.2	-	25.2	25.4	13.4
C7	1.7	1.9	-	3.4	3.5	1.7
C8	4.0	4.5	-	7.7	7.7	3.9
C9	4.7	5.2	-	8.4	8.5	4.6
C10	2.5	2.6	-	4.3	4.3	2.4
C11	0.3	0.3	-	0.6	0.5	0.3
C12	0.5	0.6	-	0.8	0.8	0.5
Unidentified area, %	0.72	0.68	-	5.29	5.22	0.39

thiols to generate heavy thioethers, the typical chemical equation was as follows:



As shown in Table 2, the amount of di-olefins decreased from 1.2 to 0.1 g/100 g after reacting with thiols. The thiols content and thiols conversion of Product I are shown in Figure 3. During the 300 h run, the thiols content maintained at a low level, with an average of 3.29 mg/kg, and the thiols conversion reached above 85%. It was also proved in Table 2, thiols such as methanethiol, ethanethiol and propane-thiol disappeared in Product I. The unidentified sulfur components in Product I were supposed to be heavy thioethers, which was formed through chemical reaction between di-olefins and thiols, then condensed into heavy fraction.

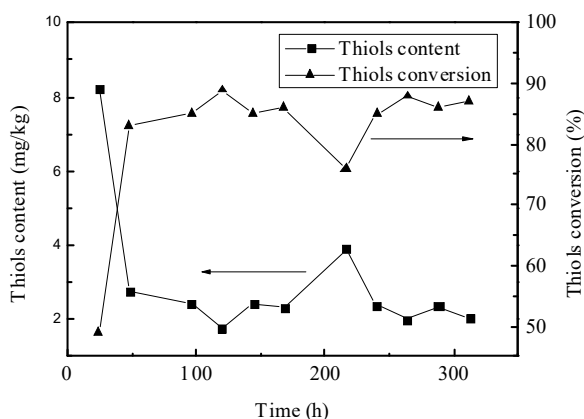


Figure 3. Thiols content and thiols conversion of the Product I as a function of time.

The hydrocarbon compositions of the feed and the Product I are compared in Table 3. The content of olefin decreased from 33.1 to 30.4 vol.%. The major source of olefin loss came from C₄ and C₅ olefin. However, the content of *n*-paraffins and *i*-paraffins changed a little, indicating the olefin loss did not result from olefin saturation, might from some alkenyl aromatics such as styrene and propenylbenzene were hydrogenated into ethylbenzene and propylbenzene. The increase of aromatics can prove this point. From the above information, the thiols can be removed effectively with a little olefin saturation, indicating that only a little octane number was lost in Reactor I. The RON lost 0.6 units.

Properties of the light and heavy fraction

Yields of the light and heavy fraction were 42 and 58 wt.%, respectively. Properties of the two fractions

can be read from Table 2. The ASTM data proved that the light and heavy fraction had been separated com-

pletely. The sulfur amount in the light and heavy fractions was 2 and 132 mg/kg, respectively. Heavy thioethers, thiophene, alkylthiophenes and benzothiophenes were condensed into the heavy fraction. The detailed compositional analysis of the two fractions is given in Table 3. The light fraction contained 45.7 vol.% *i*-paraffins, 40.6 vol.% olefins, followed by 11.9 vol.% *n*-paraffins and 1.7 vol.% naphthenes. The heavy fraction consisted of 29.5 vol.% *i*-paraffins, 25.8 vol.% olefins, 25.2 vol.% aromatics, followed by 14.3 vol.% naphthenes and 5.3 vol.% *n*-paraffins. Relative distribution of the various hydrocarbon types in the two fractions indicated existence of more *i*-paraffins and olefins in the light fraction, especially pentene and isopentane. More sulfur compounds and less olefin presented in the heavy fraction. One purpose of this stage was to preserve C₅ and C₆ olefins, another was to realize deep desulfurization by concentration all the heavy thioethers, thiophene, alkylthiophenes and benzothiophenes into the heavy fraction.

Product of the heavy fraction (Product II)

Total sulfur conversion (TSC) and olefin saturation (OS) were calculated as follows:

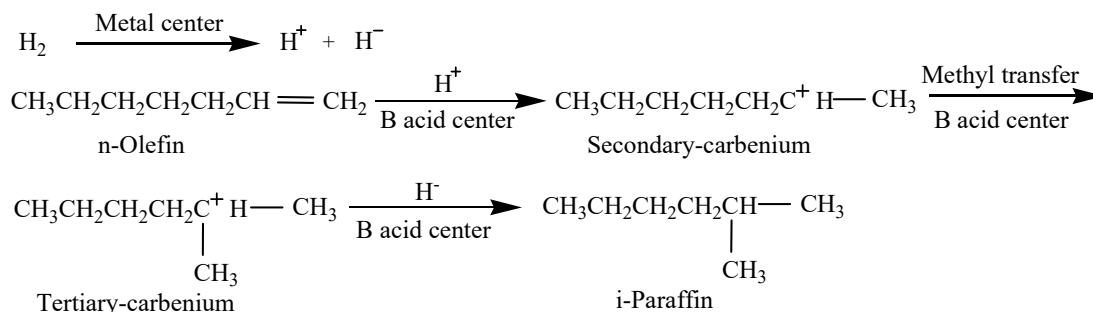
$$\text{Total sulfur conversion (\%)} = 100(S_f - S_p) / S_f \quad (1)$$

$$\text{Olefin saturation (\%)} = 100(O_f - O_p) / O_f \quad (2)$$

where S_f and S_p represent the mass fraction of total sulfur in the heavy fractions and products, respectively; O_f and O_p represent the volume fraction of olefin in the heavy fractions and products, respectively [16]. The properties of the Product II were shown in Tables 2 and 3. The total sulfur content was decreased from 132 to 8 mg/kg. The total sulfur conversion reached 94%. All the benzothiophenes, most heavy thioethers and alkylthiophenes compounds had been removed, leaving seldom alkylthiophenes including thiophene, methylthiophen, dimethylthiophene and trimethylthiophen compounds. The reactivity of these sulfur compounds can also be defined as follow, benzothiophenes, heavy thioethers and asymmetric alkylthiophenes such as ethyl thiophene, propyl thiophene and methyl-ethyl thiophene were more easily removed. However, alkylthiophenes with relatively symmetric structure such as thiophene, dimethyl thiophene and trimethyl thiophene were more difficult to remove

completely. In addition, thiophene was the hardest to remove due to its stable molecular structure. This result was consistent with the laboratory data [15]. Herein 0.4 mg/L propanethiol appeared again. H₂S was apt to react with olefins to form into thiols. Therefore, another purpose of this stage was to eliminate the regenerated thiols compounds.

On the other hand, the olefin content was decreased from 25.8 to 19.6 vol.%. The Olefin saturation was 24%. The amount of *i*-paraffin is increased from 29.5 to 33.0 vol.%. A slight increase for *n*-paraffin and naphthene amount was also observed. The aromatic amount changed little. It can be inferred that the majority of the reactive species was olefin. The decrease of olefin content indicated their conversion into *i*-paraffin, and saturation into *n*-paraffin and naphthene. Herein, different from the laboratory data, the directional olefin conversion into aromatic didn't happen due to the reaction temperature below 350 °C [17]. At relatively low reaction temperature, directional olefin conversion into *i*-paraffin can realize olefin reduction and make up the octane loss. The data given in Table 3 indicated that the increase in *i*-paraffins mainly came from the formation of C₇-C₉ *i*-paraffins. The decrease of C₇-C₉ olefins also supported their directional conversion into C₇-C₉ *i*-paraffins. The schematic diagram of the hydroisomerization can be explained as follows:



First, hydrogen is activated by the metal center of catalyst. This reaction results in the formation of H⁺ and H⁻. The activated hydrogen reacts with *n*-olefin to form into a secondary-carbenium ion on the B acid center of ZSM-5 zeolite. This ion is rapidly transformed into an energetically preferred tertiary-carbonium ion which would react with the activated hydrogen and desorb as *i*-paraffin from the surface. Overall, Reactors I and II were cascaded to behave superior sulfur conversion ability as well as acceptable octane loss by olefin directional conversion. The above results indicated that deep desulfurization happened in this stage of the GARDES process, while olefin reduction and octane preservation can also be realized.

Blend product analysis

Product II was blended with the light fraction to obtain the final product. The analysis results of the blend product are shown in Tables 2 and 3. The final composition of the blend product can be compared with the feed to see the compositional changes of the FCC gasoline. The total sulfur content of the blend product decreased from 98 to 8.5 mg/kg, the total sulfur conversion was 91%. The olefin content decreased from 33.1 to 28.9 vol.%. The RON loss was 1.5 units. There was an increase in *i*-paraffin, with little increase in *n*-paraffin and naphthene in the blend product. Hence, the overall change can be considered as the improving of FCC gasoline towards ultralow sulfur, less olefins and more *i*-paraffins with acceptable loss of octane number. As we mentioned in the configuration of the gasoline pool, the final product of FCC gasoline can satisfy the requirement of the deep desulfurization and olefin reduction.

CONCLUSION

GARDES technology has been applied to the hydrodesulfurization unit of Hohhot refinery. The operation results at two conditions were provided in the [supplementary material \(available from the author](#)

upon request). The results showed that:

1. Deep desulfurization can be completed by relayed removing different sulfur compounds in multiple reactors.
2. Olefin reduction with acceptable octane loss can be realized by directional olefin conversion into *i*-paraffins.
3. The energy consumption was 16.3 kgEo·t⁻¹, hydrogen consumption was 0.24%, total liquid yield was 98.98%.

With the above characteristics, GARDES technology has great capability and flexibility to produce ultraclean and high quality FCC gasoline.

Acknowledgement

This work was financially supported by Petro-China (2015F-0701(GF)).

REFERENCES

- [1] Y.B. Xi, D.Q. Zhang, Y. Chu, X.D. Gao, *China Pet. Process. Petrochem. Technol.* **17** (2015) 46-49
- [2] S.S. Shih, S. Mizrahi, L.A. Green, M.S. Sarli, *Ind. Eng. Chem. Res.* **31** (1992) 1232-1235
- [3] N. Viswanadham, B.S. Negi, M.O. Garg, M. Sundaram, B. Sairam, A.K. Agarwal, *Fuel* **86** (2007) 1290-1297
- [4] H. Liu, J. Yu, Y. Fan, G. Shi, X. Bao, *Pet. Sci.* **5** (2008) 285-294
- [5] H. Lasa, R.H. Enriquez, G. Tonetto, *Ind. Eng. Chem. Res.* **45** (2006) 1291-1299
- [6] J.T. Miller, W.J. Reagan, J.A. Kaduk, C.L. Marshall, A.J. Kropf, *J. Catal.* **193** (2000) 123-131
- [7] M. Toba, Y. Miki, T. Matsui, M. Harada, Y. Yoshimura, *Appl. Catal., B* **70** (2007) 542-547
- [8] C. Fontaine, Y. Romero, A. Daudin, E. Devers, C. Bouchy, S. Brunet, *Appl. Catal., A* **388** (2010) 188-195
- [9] M. Toba, Y. Miki, Y. Kanda, T. Matsui, M. Harada, Y. Yoshimura, *Catal. Today* **104** (2005) 64-69
- [10] S. Brunet, D. Mey, G. Pérot, C. Bouchy, F. Diehl, *Appl. Catal., A* **278** (2005) 143-172
- [11] P. Ghosh, A.T. Andrews, R.J. Quann, T.R. Halbert, *Energy Fuel* **23** (2009) 5743-5759
- [12] J. Hancsók, G. Marsi, T. Kasza, D. Kalló, *Top. Catal.* **54** (2011) 1102-1109
- [13] [H. González, J. Ramírez, *Ind. Eng. Chem. Res.* **40** (2001) 1103-1112
- [14] I.V. Babich, J.A. Moulijn, *Fuel* **82** (2003) 607-631
- [15] Y. Fan, G. Shi, X. Bao, *AIChE J.* **59** (2013) 571-581
- [16] M. Toba, Y. Miki, Y. Kanda, T. Matsui, M. Harada, Y. Yoshimura, *Catal. Today* **104** (2005) 64-69
- [17] Y. Fan, X.Y. Lin, G. Shi, H. Liu, X. Bao, *Microporous Mesoporous Mater.* **98** (2007) 174-181.

ZIXIA LI¹⁻³
YIN RAN²
WENQI ZHANG⁴
WEI SUN¹
TINGHAI WANG²

¹State Key laboratory for Oxo Synthesis and Selective Oxidation, Lanzhou Institute of Chemical Physics, Chinese Academy of Sciences, Lanzhou, China

²Lanzhou Petrochemical Research Center of Petrochina, Lanzhou, China

³University of Chinese Academy of Sciences, Beijing, China

⁴Petrochina Hohhot Petrochemical Company, Hohhot, China

NAUČNI RAD

INDUSTRIJSKA PRIMENA TEHNOLOGIJE AROMATIZACIJE I DESULFURIZACIJE BENZINA U RAFINERIJI HOHHOT, KINA

Tehnologija aromatizacije i desulfurizacije benzina (GARDES) se u velikoj meri koristi u rafinerijama kompanija Petrochine, sa ciljem da se proizvede visokokvalitetni ultra-čisti benzin fluid katalitičkim krekningom (FCC). Ovaj rad prikazuje rezultate industrijske jedinice za hidrodessulfurizaciju rafinerije Hohhot, koja igra važnu ulogu u daljem poboljšavanju kvaliteta benzina. Karakteristika i princip tehnologije GARDES su detaljno izloženi analizom distribucije sumpora i ugljovodoničnih jedinjenja u napojnoj smeši i proizvodu. Rezultati analize su potvrdili da se različite tipovavrste sumpora u napojnoj smeši mogu ukloniti u različitim fazama. Sadržaj olefin se može smanjiti zasićenjem i konverzijom u i-parafine i aromate. Sadržaj sumpora u smešanom proizvodu se može smanjiti ispod 10 mg/kg, što pokazuje da se sumpor odlično uklanja tehnologijom GARDES. Smanjenje olefina može, takođe, da zadovolji sve veći zahtev za ograničenje sadržaja olefina, dok se gubitak istraživačkog oktanskog broja može svesti na prihvatljiv nivo. Štaviše, prema zahtevima za poboljšanje kvaliteta benzina, tehnologija GARDES ima veliku fleksibilnost prilagodjavanjem uslova rada bez ikakvih daljih ulaganja, što donosi veću ekonomsku korist za rafineriju.

Ključne reči: benzin dobijen fluid katalitičkim krekningom, hidrodessulfurizacija, redukcija olefina, očuvanje oktana.

MUHAMMAD IMRAN DIN
KIRAN IJAZ
KHALIDA NASEEM

Institute of Chemistry, University of
Punjab, Lahore-54590, Pakistan

SCIENTIFIC PAPER

UDC 633.61:66.081.3:544.4

BIOSORPTION POTENTIALS OF ACID MODIFIED *Saccharum bengalense* FOR REMOVAL OF METHYL VIOLET FROM AQUEOUS SOLUTIONS

Article Highlights

- Removal of methyl violet dye from aqueous solution by acid modified *Saccharum bengalense*
- Adsorption reaction follows pseudo second order kinetics
- Langmuir adsorption isotherm is best followed by adsorption data
- Adsorption of dye molecules on the surface of adsorbent is in single layer

Abstract

In the present work, Saccharum bengalense (SB) was treated with sulfuric acid to enhance its efficiency. Methyl violet (MV), a cationic dye, was removed from aqueous medium using acid modified S. bengalense (A-SB). Different parameters like adsorbent dosage, stirring speed, temperature, contact time and effect of initial concentration of dye on rate of adsorption of dye from aqueous medium was studied. Experimental data obtained from adsorption of MV was analyzed by applying pseudo first order, pseudo second order and intra-particle diffusion models and it was found that the data best follows the pseudo-second order kinetics. Thermodynamic parameters indicate that adsorption reaction was spontaneous, feasible and endothermic in nature. Different adsorption isotherm models, like Langmuir, Freundlich, Dubinin-Radushkevich (D-R) and Temkin, were used to study the mechanism of adsorption process and experimental data was well fitted by the Langmuir adsorption isotherm.

Keywords: biosorption, Saccharum bengalense, kinetics, thermodynamics, dye.

During the last few years, industrial development has left deleterious effects on the environment. Dyes are used in many industries, especially in textile industry, Textile industries use different dyes for dyeing their products. Thus, as a result of poor dye fixation on fiber, 50% of dye is removed in water, which causes production of colored wastes, which are also contaminated with other organic pollutants [1]. Water contaminated with dyes affects people as this water is used for different purposes like drinking, washing and bathing [2]. Even low concentrations of dye, like 1.0

mg/L, can impart visible color to water, which makes it unfit for human use [3]. Dyes have the ability to absorb the specific wavelength of light so they interfere with sunlight to reach the water bodies, which causes harmful effects on the aquatic life. Dyes are highly carcinogenic, mutagenic and damage liver, kidneys, brain, central nervous system and reproductive system of human beings [4-6]. Due to high visibility and toxicity of dyes, their removal from contaminated water bodies has become very important [7].

Different techniques like chemical oxidation, membrane separation, coagulation, aerobic and anaerobic microbial degradation can be used for treatment of dye polluted wastewater but these methods have not attained much importance due to certain restrictions [8]. Among all these methods used for the treatment of wastewater, adsorption is preferred due to its high quality and the cheapness [9]. Wastewater

Correspondence: M.I. Din, Institute of Chemistry, University of Punjab, Lahore-54590, Pakistan.

E-mail: imrandin2007@gmail.com

Paper received: 17 December, 2015

Paper revised: 9 August, 2016

Paper accepted: 13 November, 2016

<https://doi.org/10.2298/CICEQ151217054D>

treated by using activated carbon in the adsorption process has become a very important aspect of recent research [10]. Therefore, effluent-containing wastewater is treated with activated carbon before its disposal in environment [11]. However, this method is not economically feasible due to requirements of the activated carbon regeneration and the decrease in its efficiency after recycling [12]. Presently, adsorption has become an economically suitable and realistic method for the removal of different pollutants like COD [13,14], gasses [15], heavy metals [16,17], phenol [18,19] and dyes [20-23] from aqueous media using the agricultural by-products as adsorbents. Literature studies showed that different researchers have used different methods for the activation of the adsorbent to enhance its adsorption capacity. Activation may be physical, such as carbonization, or chemical, by using chemical activating agents.

Xu *et al.* synthesized biochar from different crop residues and used it as an adsorbent for adsorption of methyl violet from aqueous medium [24]. They also showed that biochar have high ability to remove MV from aqueous medium. Tian *et al.* prepared nano-sized Fe₂O₃ modified baker yeast biomass and used it as efficient adsorbent for removal of MV from aqueous medium [25]. They also observed that adsorbent has capability to be removed from mixture magnetically due to presence of spherical nano-Fe₂O₃ on the surface of biomass. Ofomaja and his coworkers reported *Mansonia* wood sawdust as biosorbent for removal of MV from aqueous medium [26]. Effects of temperature and pH on the biosorption process were studied. They concluded from their experiment that biosorption process was strongly depending upon the pH of the medium and percentage removal efficiency of biosorbent was significantly high at pH > 7.

In our work, activated carbon was prepared from SB by chemical activation method and was used as adsorbent for removal of MV dye from aqueous medium. The novelty of our work is the use of acid modified *Saccharum bengalense* as biosorbent for removal of MV from aqueous medium, because researchers have not employed it as adsorbent for dye removal. Different parameters that affect the rate of adsorption of dye were also studied. The values of adsorbent dose, contact time temperature and stirring speed at which maximum adsorption rate was observed were used for further studies. Different models, such as pseudo-first order, pseudo-second order and intra-particle diffusion models were used to study the kinetics of adsorption of methyl violet on SB. Thermodynamic studies were done to estimate the nature and feasibility of the adsorption process. The mech-

anism of the adsorption process was studied using Langmuir, Freundlich, D-R and Temkin adsorption isotherms.

MATERIALS AND METHODS

Chemicals

Methyl violet (MV), sodium hydroxide (NaOH), sulfuric acid (H₂SO₄) and hydrochloric acid (HCl) were of analytical grade and obtained from Sigma Aldrich. All chemicals were used as received without any further treatment.

Methyl violet as adsorbate

Methyl violet (MV) was used as an adsorbate. It covers three compounds: MV-2B, MV-6B, and MV-10B, which differ in the number of methyl groups attached to amine. The change in color of dye depends upon the number of methyl groups present in it. In inks and paints, it is used as violet color, while in textile industry it is used as purple color dye. Methyl violet 6B is intermediate between 2B (less dark) and 10B (more dark) in color. Dipropylene, water and diethylene glycol are important solvent for this dye. We used methyl violet-6B (MV) as adsorbate and water as solvent for our work. 1 g of dye was dissolved in 1000 mL of deionized water to prepare stock solution of 1 g/1000 mL concentration. For experimental purposes, the concentration of dye was changed from 16 to 32 ppm and the optimum concentration of dye was found.

Acidic *S. Bengalense* as biosorbent

SB obtained from the bank of the river Ravi in Lahore, Pakistan, was washed with water to remove dust and unwanted particles. Then, the washed SB was dried under shade. After drying, the outer layer of samples was removed to obtain the inside pulp. A standard knife mill was used to mill the SB pulp and passed through 60-mesh screen. Milled SB was stored in air tight bottle for further use in experimental work. The weighed amount of SB was taken in a beaker and then H₂SO₄ (17 M) was added in it. The SB was dipped in acid for two hours. After that, it was washed with water and filtered. After filtration, the residue at the filter paper was dried in oven at 70 °C. After drying, the sample was ground with mortar so that all particles were of the same size and shape. These particles were placed in an airtight container for further use and labeled as A-SB.

Characterization of biosorbent

FTIR spectroscopy was used to analyze the SB and acid modified SB. FTIR analysis was done to find

the difference between vibrational frequencies of functional groups of SB and A-SB in range of 4000–400 cm^{-1} . For this purpose, samples were degassed for 2 h at 300 °C. The disc method was employed to analyze the samples by using a Tensor 27, Burker (Germany) FTIR spectrophotometer.

Biosorption experiments

Effect of adsorbent dose on the rate of adsorption of dye from aqueous solution was studied by varying the dose of adsorbent from 0.1 to 0.5 g in the adsorbent-adsorbate solution. The initial concentration of dye was kept constant while pH of solution was adjusted as 10. Solutions containing different adsorbent dose were stirred until equilibrium was established.

Effect of contact time on the rate of adsorption of dye was also studied by varying the shaking time from 10 to 70 min while the concentration of adsorbate-adsorbent was 0.2 g/50 mL at pH 10. After specific time interval, the solution was pipettes out from flasks, filtered and absorbance was measured using a 721 visible spectrophotometer (Shanghai Hansom Technology and Sales Limited, China)

Effect of temperature on the rate of adsorption of dye by biosorbent was studied by varying it in range of 10 to 60 °C while the concentration of adsorbent-adsorbate was 0.2 g/50 mL at pH 10 and contact time 50 min. Temperature was maintained during adsorption process until equilibrium was established and sample was pipette out for absorbance measurement. Rate of adsorption of dye was also studied by varying stirring speed from 100 to 175 rpm while all other parameters were kept constant. Stirring speed of 125 rpm at which maximum adsorption occur was found.

Effect of concentration of dye on the rate of adsorption process was also studied by changing its concentration from 16 to 32 ppm while all other factors were kept constant. Adsorbate-adsorbent solutions were stirred at optimum speed of 125 rpm to attain equilibrium and absorbance of relative solutions was found. Percentage removal efficiency was calculated for all parameters studied. It is the adsorption cap-

acity of adsorbent or amount of solute adsorbed on the adsorbent and can be represented as follows:

$$\text{Percentage removal } (R) = 100 \frac{C_o - C_e}{C_o} \quad (1)$$

where C_o (mg/L) and C_e (mg/L) are the concentration of solute in solution at start of adsorption process and at equilibrium, respectively, and q_e (mg/g) represents the biosorption capacity of SB at equilibrium and indicates the solute concentration adsorbed at the surface of adsorbent:

$$q_e = V \frac{C_o - C_e}{m} \quad (2)$$

RESULTS AND DISCUSSION

Fourier transform infrared spectroscopy (FTIR)

FTIR spectroscopy was used to study the structural hierarchies of SB and A-SB. Band positions for different functional groups present within SB and A-SB are given in Table 1. FTIR data indicates that SB and A-SB samples have common functional groups like amine and alcoholic groups. Secondary and tertiary alcoholic groups are present in SB while only tertiary alcoholic groups are present in A-SB samples. Both spectra also show that aromatic character is present in both samples. SB also has carbonyl groups. Literature survey shows that mostly FTIR spectra of SB have similar peaks which indicates the presence of different groups like hydroxyl group of alcohols, carbonyl group of aldehydes, ketones, ester and carboxylic acid and aromatic group [27,28].

Optimization of biosorption parameters

Effect of adsorbent dose

Percentage removal efficiency (R) of biosorbent increases with increase of biosorbent dose due to increase of availability of binding site as reported earlier [29]. It was observed that %R of biosorbent was increased with increase of adsorbent dose up to a certain limit. After that, further increase of adsorbent dose caused the overlapping of binding sites and adsorption capacity was decreased. Effect of adsorbent

Table 1. FT-IR analysis of SB and A-SB

Bond	Functional group	ν Range, cm^{-1}	SB, cm^{-1}	A-SB, cm^{-1}
v(C-N) s	Aliphatic amines	1020-1220	1035	1035
v(C-O) s	Secondary alcohols	1100	1104	-
v(C-O) s	Tertiary alcohols	1150-1200	1162	1167
v(C-O) s	Carbonyl group (acid)	1210-1320	1245	-
v(C-C) s	Aromatics	1400-1500	1508	-
v(C-H) s	Aromatics	860-900	900	874

dose on rate of adsorption was studied by varying adsorbent concentration from 0.1 to 0.5 g while all other factors were kept constant. Figure 1a shows the relation between adsorbent dose and its R . R of A-SB was increased with the increase of biosorbent dose and maximum R was attained at 0.2 g. At optimum dose (0.2 g/mL), R was 98.5%. Further increase of adsorbent dose decreased the value of R . Results

show that at high adsorbent concentration overlapping of binding sites occurs which decreases the value of R [29]. The results were in agreement with the previous work reported in literature [27,30].

Effect of contact time

Efficiency of adsorbent also depends upon the time duration of adsorbent-adsorbate contact. When

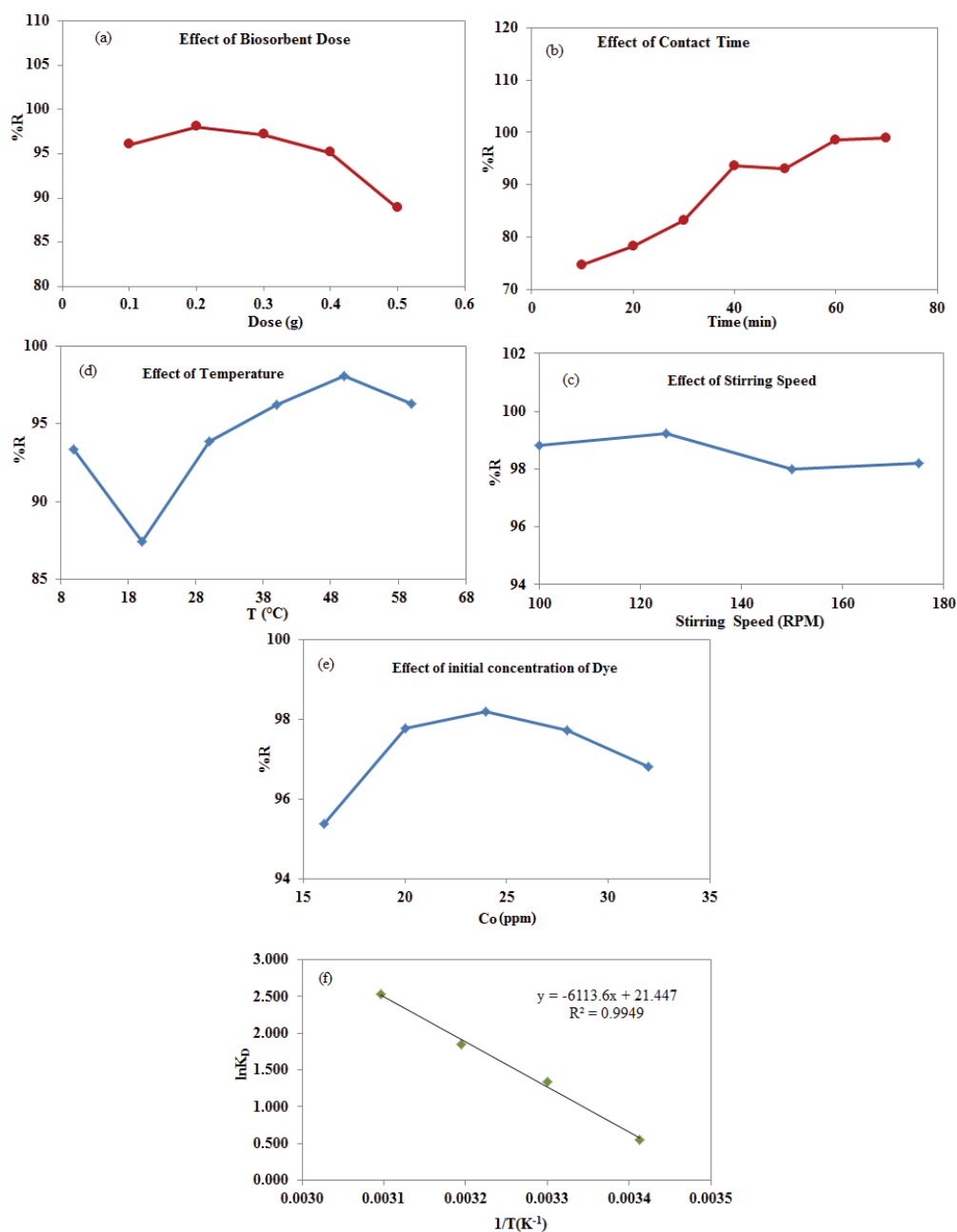


Figure 1. a) Effect of biosorbent dose (A-SB) for adsorption of MV at pH 10, $T = 323$ K, contact time = 50 min, stirring speed = 125 rpm; b) effect of contact time on biosorption of MV on A-SB at pH 10, $T = 323$ K and dose = 0.2 g/50 mL; c) effect of stirring speed on biosorption of MV on A-SB at $T = 313$ K, pH 10, dose = 0.2 g/50 mL, contact time = 50 min; d) effect of temperature on biosorption of MV on A-SB, pH 10, biosorbent dose = 0.2 g/50 mL, contact time = 50 min; e) effect of initial concentration of dye on adsorption of MV on A-SB, pH 10, biosorbent dose = 0.2 g/50 mL, contact time = 50 min, f) determination of thermodynamic parameters at pH 10, biosorbent dose = 0.2 g/50 mL, contact time = 50 min.

shorter time is required to attain equilibrium then efficiency of adsorbent to remove dyes from wastewater is high. At the start of contact time, rate of biosorption is high which becomes slower at the time near to the establishment of equilibrium. Different rate of adsorption during whole process is due to availability of active sites which are high at the start of reaction. Near equilibrium, molecules face inter repulsive forces as well as less binding sites are available so rate of adsorption becomes slow down [28]. The effect of contact time on R is leveled, continuous and single [31,32] as shown in Figure 1b. The R increases with increase of contact time but after some time it becomes constant. This stage is called equilibrium, at which all the binding sites of the adsorbent are occupied by the dye molecules and no further vacant sites are present for further adsorption of dye molecules [33,34]. The contact time of 50 min at which saturation occurs was used for further experimental work.

Effect of stirring speed

Literature survey shows that stirring speed has no significant effect on the value of R of adsorption during adsorption process. Effect of stirring speed was studied by varying its value from 100 to 175 rpm and all other parameters like biosorbent dose, contact time, temperature, pH and dye concentration were kept constant, as shown in Figure 1c. The value of R of A-SB increases slightly with the increase of stirring speed up to 125 rpm, but becomes constant with further increase in its value. Optimum stirring speed of 125 rpm, at which value of R was maximum, was used for further work.

Effect of temperature

Effect of temperature on the adsorption process indicates whether reaction is endothermic or exothermic. When adsorption capacity of adsorbate increases with increase of temperature it is called endothermic process. Increase in temperature may increase the movement of dye molecules or increase the number of active sites as a result R of adsorbent increases [35]. While in case of endothermic adsorption process, rate of adsorption decreases with increase of temperature because of decrease in attractive forces between the molecules of dye and active sites of adsorbate [36,37]. Figure 1d shows that when the temperature of the medium was increased from 10 to 60 °C, the value of R was increased up to 50 °C but further increase of temperature decreased the R of the adsorbent.

Effect of dye concentration

R of adsorbent for dye from aqueous solution also depends upon the initial dye concentration. R of

adsorbent for different concentration of dye decreases with increase of dye concentration due to saturation of binding sites of adsorbent as reported earlier [38]. When the concentration of dye is low, some binding sites are unoccupied and value of R increases. But with the increase of initial concentration of dye, availability of active site decreases because number of active sites remain fixed due to constant concentration of the adsorbent [39]. Dye concentration was varied between 16 to 32 ppm while all other parameters were kept constant to study its effect as shown in Figure 1e. It can be seen from Figure 1e that R increases with increase of dye concentration up to a specific value after which R decreases with increase of dye concentration. Results are compatible with previous reported work [40]. At high dye concentration, competition increases between its molecules for binding sites as a result R decreases [41].

Thermodynamic study

Different thermodynamic parameters for the biosorption of MV on the surface of A-SB were also studied by making use of following equations [42,43]:

$$\Delta G^\circ = \Delta H^\circ - T\Delta S^\circ \quad (3)$$

$$\Delta G^\circ = -RT \ln K_D \quad (4)$$

$$K_D = \frac{C_{AS}}{C_e} \quad (5)$$

$$\ln K_D = \frac{\Delta S^\circ}{R} - \frac{\Delta H^\circ}{RT} \quad (6)$$

where ΔG° and ΔH° are Gibbs free energy and enthalpy change respectively, T is temperature, ΔS° is the entropy change, while K_D is the distribution coefficient. C_{AS} and C_e are the total amount of adsorbate adsorbed and its amount at equilibrium, respectively.

The value of ΔH° , ΔG° and ΔS° was calculated by plotting a graph between $1/T$ and $\log K_D$ using Eq. (6), as shown in Figure 1f. The value of ΔH° was calculated from slope while the value of ΔS° was calculated from intercept of the graph. Different thermodynamic parameters like ΔH° , ΔG° and ΔS° calculated for biosorption of MV from the aqueous medium using A-SB are given in Table 2. The value of ΔG° was calculated at temperature 313 K using Eq. (3) because maximum amount of MV was adsorbed on SB at this temperature. The value of ΔG° shows the nature along with feasibility of biosorption process. The negative value of ΔG° in adsorption of MV shows that the reaction is spontaneous and energetically feasible [44]. The value of ΔH° can be posi-

Table 2. Thermodynamic parameters for biosorption of MV on A-SB

Thermodynamic parameter	Parameters value	Conclusion
$\Delta G^\circ / \text{J mol}^{-1}$ at 313 K	-6817.49	Negative sign indicates spontaneous and feasible nature
$\Delta H^\circ / \text{J mol}^{-1}$	50825	Endothermic process
$\Delta S^\circ / \text{J mol}^{-1} \text{K}$	178.25	Increase in randomness at the surface of solid-solution

tive or negative depending upon the nature of biosorption process. Here, positive value ΔH° for biosorption process shows that the reaction is endothermic in nature of reaction [45,46]. The value of ΔS° shows the change in randomness of atoms which are being adsorbed on the surface of adsorbent [47]. Its value can also be positive or negative. Positive value of entropy change for adsorption of MV by SB shows that adsorption rate increases with increase of randomness of reactant atoms [48].

Adsorption isotherms

Adsorption isotherms show the adsorption capacity of adsorbent and adsorption mechanism of how dye molecules interact with its active sites. Different isotherms - Temkin, Freundlich, Langmuir and D-R - were employed to analyze the data. These isotherms also explain whether the adsorption of MV molecules on the surface of SB was monolayer or multilayer. For this purpose, data was obtained by carrying the adsorption process at optimum conditions of temperature, pH, stirring speed, concentration of dye and contact time.

Langmuir adsorption isotherm

The Langmuir adsorption isotherm was presented by Irving Langmuir in 1916 to explain the mechanism of adsorption of gas molecules over the surface of activated carbon [49,50]. This isotherm also shows that adsorbate molecules do not interfere with each other during adsorption process and they are restricted to form a monolayer [50]. This isotherm also explains that once the dye molecule is adsorbed at one site then further adsorption does not occur at that site [55].

Graph was plotted between C_e/q_e and C_e as shown in Figure 2a. C_e (mg/L) and q_e mg/g represents the concentration of dye in solution and concentration of dye on adsorbent at equilibrium, respectively.

The value of q_m was found from the slope while the value of K_L was calculated from intercept of the graph shown in Figure 2a. Langmuir parameters for adsorption of MV on the surface of A-SB surface are given in Table 3. The value of correlation coefficient R^2 is 0.981 which is approximately equal to unity and

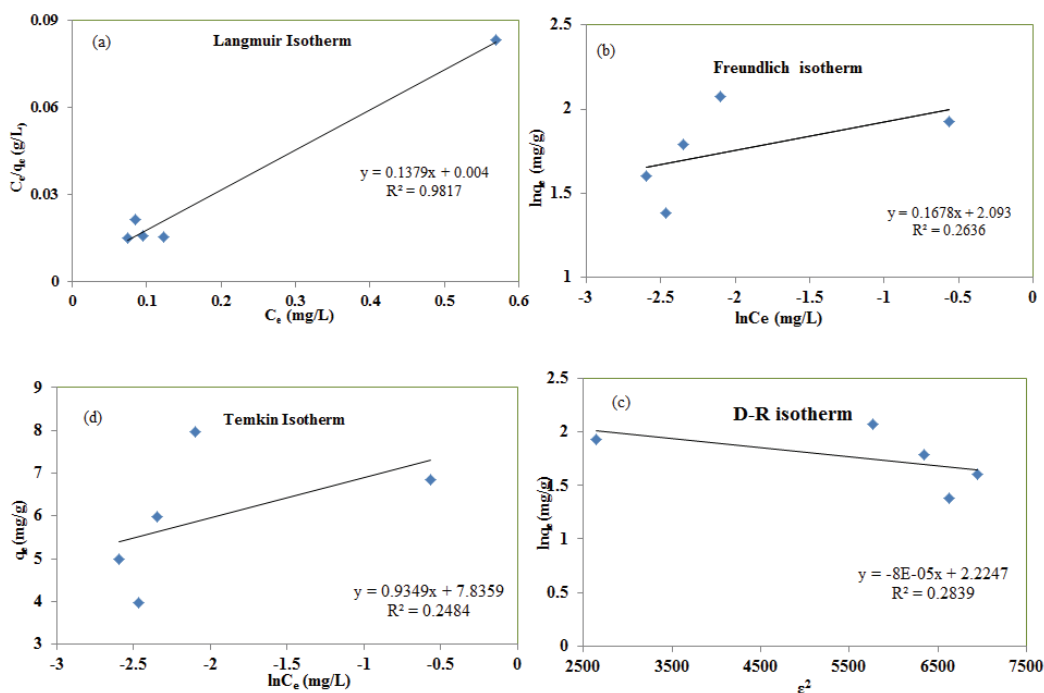


Figure 2. a) Langmuir, b) Freundlich, c) D-R and d) Temkin isotherm at pH 10, biosorbent dose 0.2 g/50 mL, contact time = 50 min, $T = 313 \text{ K}$ and stirring speed = 125 rpm.

indicates that Langmuir isotherm best explain the adsorption process of MV on the surface of A-SB. The calculated value of q_m is 7.299 mg/g. The validity of Langmuir isotherm indicates that monolayer adsorption of dye molecules occurs on the surface of SB while no interaction exists between adsorbed dye molecules. Ozdemir *et al.* found the adsorption capacity of Sepiolite for methyl violet as 2.55 mg/g at 50 °C temperatures by employing the Langmuir adsorption isotherm [34]. A comparison of q_m values for methyl violet to be adsorbed by different adsorbent using the Langmuir adsorption isotherm is given in Table 4.

Table 3. Parameters of different adsorption isotherms

Adsorption Isotherm	Parameters of adsorption isotherms		
Langmuir	$K_L / L\ m^{-1}$	$q_m / mg\ g^{-1}$	R^2
	34.25	7.299	0.981
Freundlich	K_F	n	R^2
	8.109	6.25	0.263
D-R	β	$q_m / mg\ g^{-1}$	R^2
	8×10^{-5}	9.24	0.283
Temkin	$K_T / g\ L^{-1}$	β	R^2
	4396	0.934	0.248

Table 4. A comparison for methyl violet (MV) capacity of different biosorbents

Adsorbent	MV capacity $q_m / mg\ g^{-1}$	Reference
Sepiolite	2.550	[34]
Sepiolite	2.330	[33]
Banana peel	12.20	[51]
Orange peel	11.50	[51]
Duckweed	332.5	[52]
<i>Artocarpus odoratissimus</i> skin	184.6	[53]
Water lettuce	267.6	[54]
Acid modified <i>S. bengalense</i>	7.299	Our study

Freundlich adsorption isotherm

Kuster and Freundlich presented a model in 1894 to explain the non-ideal and reversible adsorption process. They explain in their work that adsorption takes place on the heterogeneous surface in the form of multilayers [55]. The Freundlich adsorption isotherm is represented as follows:

$$\ln q_e = \ln K_f + \frac{1}{n} \ln C_e \quad (7)$$

In this equation, K_f is the dimensionless constant which represents the adsorption capacity while n represents the intensity of adsorption. q_e and C_e are

the equilibrium concentrations of adsorbate at adsorbent and in solution, respectively. Figure 2b shows the plot between $\ln q_e$ and $\ln C_e$ from which value of correlation coefficient was calculated which is not compatible with literature. It means experimental data cannot be explained by Freundlich adsorption isotherm and multilayer adsorption of MV dye molecules does not occur at the surface of A-SB. The values of correlation coefficient (R^2) for Langmuir and Freundlich isotherms indicate that adsorption of MV on the surface of A-SB follows the former isotherm as compares to the latter one.

Dubinini Radushkevich (D-R) isotherm

D-R model is represented by equation as follows [56]:

$$\ln q_e = \ln q_m - \beta \varepsilon^2 \quad (8)$$

where q_m (mg/g) and β ($\text{mol}^2\ \text{K}/\text{J}^2$) are theoretical saturation capacity and D-R constant, respectively, and ε in term of C_e is given as follows [42]:

$$\varepsilon = RT \ln \left(1 + \frac{1}{C_e} \right) \quad (9)$$

D-R model explains the nature of surface of adsorbent like heterogeneity or homogeneity [57]. A graph was plotted between $\ln q_e$ and ε^2 as shown in Figure 2c. The values of D-R parameter calculated from graph shown in Figure 2c are given in Table 3. Value of E_s (kJ/mol) can be calculated from [58]:

$$E_s = \frac{1}{\sqrt{\beta}} \quad (10)$$

Two factors are usually involved to decide whether data follows the D-R isotherm or not. The first one is the value of R^2 and the second is the comparative analysis of calculated and actual value of q_m for the adsorption process. Here, the value of R^2 is not close to unity and the value of q_m is not comparable to experimental value. Thus, the results show that adsorption of MV on the surface of SB does not follow the D-R model.

Temkin adsorption isotherm

This isotherm model shows that the value of heat of adsorption decreases linearly for the molecules that are present in the same layer during adsorbent-adsorbate interaction [59]. The equation for Temkin adsorption isotherm is as follows:

$$q_e = \beta \ln K_t + \beta \ln C_e \quad (11)$$

In this equation, K_t (1/g) and β are equilibrium binding constant and adsorption heat respectively.

Graph for Temkin adsorption isotherm is shown in Figure 2d and data is given in Table 3. The R^2 value shows that adsorption process does not follow Temkin adsorption isotherm.

Kinetics of methyl violet adsorption

Kinetics of adsorption of MV on the surface of SB was studied by employing different kinetic models as pseudo-first order, pseudo-second order and intra-particle diffusion model etc. Pseudo-first order was proposed by Lagergen in 1898. It is employed to observe the mechanism of adsorption of liquid or solid samples. It is represented by the following equation [60]:

$$\frac{dq_t}{dt} = k_1(q_e - q_t) \quad (12)$$

After integration, Eq. (12) becomes:

$$\ln(q_e - q_t) = \ln q_e - k_1 t \quad (13)$$

In this equation, k_1 is pseudo-first order rate constant while q_t (mg/g) is adsorption capacity at any time t . Graph was plotted between $\ln(q_e - q_t)$ vs. time to study the pseudo-first order kinetics of the adsorption of MV on the surface of SB as shown in Figure 3a and data is given in Table 5. The value of R^2 is small as compared to experimental predicted value which indicates that the adsorption of MV on the surface of A-SB does not follow pseudo first order kin-

etics. Also, the value of q_e is not comparable with literature.

Table 5. Kinetic parameters for biosorption of MV on A-SB

Kinetic Model	Parameters of kinetic models			
Pseudo-first-order	k_1	$q_e / \text{mg g}^{-1}$	$q_c / \text{mg g}^{-1}$	R^2
	34.25	6.18	2.07	0.29
Pseudo-second order	k_2	$q_e / \text{mg g}^{-1}$	$q_c / \text{mg g}^{-1}$	R^2
	0.022	6.18	6.72	0.99
Intraparticle diffusion model	K_{id}	$q_e / \text{mg g}^{-1}$	C	R^2
	0.325	6.18	3.558	0.95
Elovich kinetic model	$\alpha / \text{mg g}^{-1} \text{min}^{-1}$	$q_e / \text{mg g}^{-1}$	$\beta / \text{mg g}^{-1}$	R^2
	20.73	6.18	0.864	0.923

Pseudo-second order kinetic model was proposed on the basis that chemisorption are followed by the process of sorption [60].

The equation of pseudo second order is:

$$\frac{dq_t}{dt} = k_2(q_e - q_t)^2 \quad (14)$$

After integration, Eq. (14) becomes:

$$\frac{t}{q_t} = \frac{1}{k_1 q_e^2} + \frac{t}{q_e} \quad (15)$$

In this equation, k_2 (g/(mg min)) is pseudo-second order rate constant while q_t (mg/g) is the adsorption capacity of adsorbent at time t Figure 3b shows

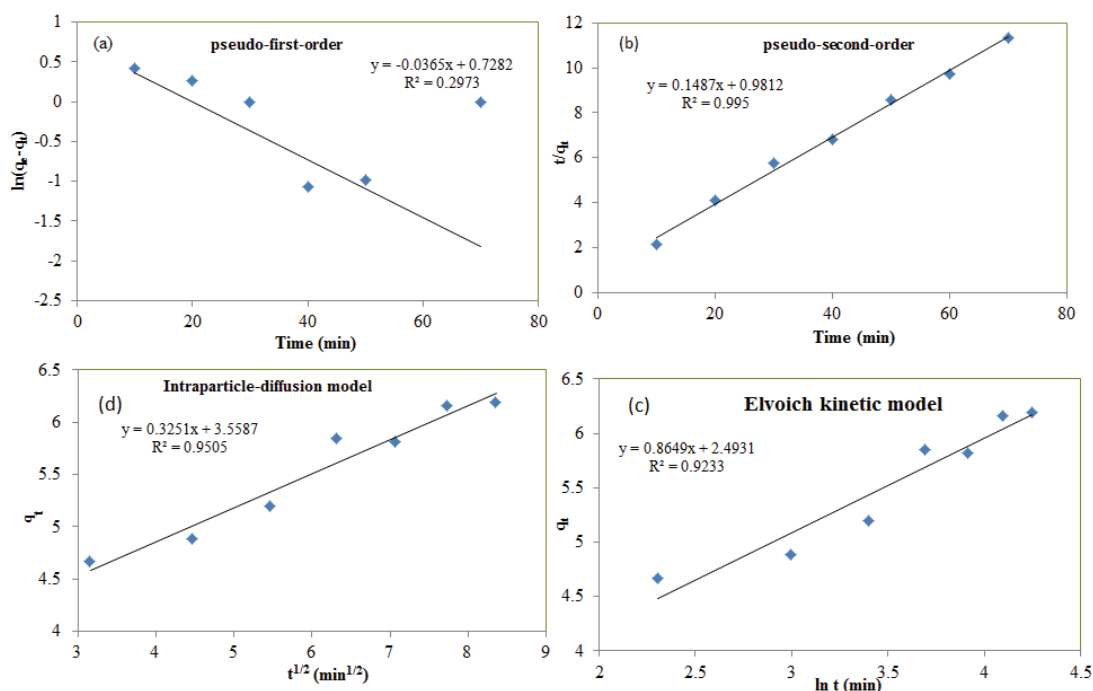


Figure 3. a) Pseudo-first-order, b) pseudo-second-order, c) Elovich and d) intra-particle diffusion kinetic model at pH 10, biosorbent dose = 0.2 g/50 mL, contact time = 50 min, $T = 323$ K, stirring speed = 125 rpm.

the graph between $\ln q_t$ and t to study pseudo-second order kinetics. Data for pseudo second order for the adsorption of MV on the surface of adsorbent is given in Table 5. Calculated value of R^2 for pseudo-second order is very close to unity as compared to other kinetic models. It shows that adsorption is best followed by pseudo second order kinetics. The calculated value of q_e is 6.72 mg/g while value of reported value of q_e is 6.18 mg/g which are approximately close to experimental ideal value. Hameed used sun flower seed hull as biosorbent for removal of MV dye from aqueous medium [61]. He reported that adsorption process best follow the pseudo-second order kinetic model as compared to pseudo-first order kinetic model because R^2 value exceeded 0.99 in case of former as compared to later one. He also showed that q_e value calculated from pseudo second order was more consistent to reported values. Similar results were found by other researchers for adsorption of methyl violet dye using different biosorbent [29,33,62,63].

Elovich kinetic model

This model is represented by:

$$\frac{dq_t}{dt} = \alpha \exp(-\beta q_t) \quad (16)$$

where α ($\text{mol g}^{-1} \text{min}^{-1}$) is sorption rate at the initial stage, and β (g mol^{-1}) is the desorption constant. The Elovich equation is converted to a simple form by supposing that $\alpha\beta t \gg 1$ and integrating. After applying the conditions above, the simple form becomes:

$$q_t = \beta \ln(\alpha\beta) + \beta \ln t \quad (17)$$

By plotting a graph between q_t and $\ln t$ a straight line is obtained with intercept $\beta \ln(\alpha\beta)$ and slope β which help to calculate the value of constants that are α and β . In order to check if the data fits this model or not, a graph was plotted between q_t and $\ln t$, which is shown in Figure 3c and calculated values are given in Table 5. Value of R^2 is very far from unity, which indicates that data is not well fitted with this model for adsorption process of MV over SB.

Intra-particle diffusion model

The intra-particle diffusion model is represented by:

$$q_t = K_{id} \sqrt{t} + C \quad (18)$$

In this equation, K_{id} ($\text{mg g}^{-1} \text{min}^{-1/2}$) is the inter-particle diffusion rate constant. A graph was plotted between q_t (mg/g) and $t^{1/2}$ to study the validity of model for adsorption of MV over the surface of SB adsorbent as shown in Figure 3d. Passing of straight line from origin of graph decides whether it is con-

trolling step or not. By using Figure 3d parameters of intra-particle diffusion model were calculated which are given in Table 5. The R^2 value for biosorption process was not close to unity, which means that it does not follow the intra-particle diffusion model.

CONCLUSION

The results showed that *Saccharum bengalense* (SB) is an effective biosorbent for the adsorption of methyl violet (MV) from aqueous solution. At 323 K temperature, 98% MV dye was removed using 0.2 g/25 mL of biosorbent while, pH and stirring speed were adjusted as 10 and 125 rpm, respectively. The results indicated that the time required to attain equilibrium was 50 min. Experimental data showed that adsorption process best followed the Langmuir adsorption isotherm. The dye molecules formed single layer over the binding sites of *S. bengalense* surface. Thermodynamic parameters showed that the adsorption process is endothermic, spontaneous and feasible, as the adsorption rate increases with increase of temperature of the medium.

Acknowledgment

This work was supported by University of the Punjab, Lahore, Pakistan, under a research project grant for the fiscal year 2015-2016.

REFERENCES

- [1] N. Mohan, N. Balasubramanian, C.A. Basha, J. Hazard. Mater. **147** (2007) 644-651
- [2] R. Malik, D. Ramteke, S. Wate, Waste Manage. **27** (2007) 1129-1138
- [3] K. Kadirvelu, C. Karthika, N. Vennilamani, S. Pattabhi, Chemosphere **60** (2005) 1009-1017
- [4] D. Shen, J. Fan, W. Zhou, B. Gao, Q. Yue, Q. Kang, J. Hazard. Mater. **172** (2009) 99-107
- [5] M. Sulak, E. Demirbas, M. Kobya, Bioresour. Technol. **98** (2007) 2590-2598
- [6] R. Qadeer, Colloids Surfaces.. A **293** (2007) 217-223
- [7] Y. Al-Degs, M. Khraisheh, S. Allen, M. Ahmad, G. Walker, Chem. Eng. J. **128** (2007) 163-167
- [8] M.K. Aroua, C.Y. Yin, F. Lim, W. Kan, W.M.A.W. Daud, J. Hazard. Mater. **166** (2009) 1526-1529
- [9] V.C. Srivastava, I.D. Mall, I.M. Mishra, Chem. Eng. J. **132** (2007) 267-278
- [10] M.H. El-Naas, S. Al-Zuhair, M.A. Alhijja, J. Hazard. Mater. **173** (2010) 750-757
- [11] A. Ahmad, B. Hameed, J. Hazard. Mater. **172** (2009) 1538-1543
- [12] M. Ahmad, W.W. Daud, M. Aroua, Colloids Surfaces, A **312** (2008) 131-135

- [13] M.E. Argun, S. Dursun, C. Ozdemir, M. Karatas, J. Hazard. Mater. **141** (2007) 77-85
- [14] M.K. Aroua, S. Leong, L. Teo, C.Y. Yin, W.M.A.W. Daud, Bioresour. Technol. **99** (2008) 5786-5792
- [15] N.H. Phan, S. Rio, C. Faur, L. Le Coq, P. Le Cloirec, T.H. Nguyen, Carbon **44** (2006) 2569-2577
- [16] N. El Hannafi, M. Boumakhla, T. Berrama, Z. Bendjama, Desalination **223** (2008) 264-268
- [17] C.-H. Weng, Y.-T. Lin, T.-W. Tzeng, J. Hazard. Mater. **170** (2009) 417-424
- [18] M. El-Halwany, Desalination **250** (2010) 208-213
- [19] M. Arulkumar, P. Sathishkumar, T. Palvannan, J. Hazard. Mater. **186** (2011) 827-834
- [20] V. Gupta, J. Environ. Manage. **90** (2009) 2313-2342
- [21] A. Demirbas, J. Hazard. Mater. **167** (2009) 1-9
- [22] D. Ghosh, K.G. Bhattacharyya, Appl. Clay. Sci. **20** (2002) 295-300
- [23] A.E. Ofomaja, Biochem. Eng. J. **40** (2008) 8-18
- [24] R.-K. Xu, S.-C. Xiao, J.-H. Yuan, A.-Z. Zhao, Bioresour. Technol. **102** (2011) 10293-10298
- [25] Y. Tian, C. Ji, M. Zhao, M. Xu, Y. Zhang, R. Wang, Chem. Eng. J. **165** (2010) 474-481
- [26] A.E. Ofomaja, Y.-S. Ho, Bioresour. Technol. **99** (2008) 5411-5417
- [27] M.I. Din, M.L. Mirza, Int. J. Bio. Macromol. **54** (2013) 99-108
- [28] M.I. Din, U. Farooq, M. Athar, M. Latif Mirza, Desalin. Water. Treat. **52** (2014) 5856-5868
- [29] I.D. Mall, V.C. Srivastava, N.K. Agarwal, Dyes. Pigm. **69** (2006) 210-223
- [30] M. Imran Din, M.L. Mirza, S. Ata, M. Athar, I.U. Mohsin, J. Chem. **2013** (2012)
- [31] T.C.R. Bertolini, J.C. Izidoro, C.P. Magdalena, D.A. Fungaro, J. Chem. **5** (2013) 179-191
- [32] M.I. Din, Z. Hussain, M.L. Mirza, M.M. Athar, A. Madni, S. Ahmad, Desalin. Water. Treat. **51** (2013) 5638-5648
- [33] M. Dogan, Y. Ozdemir, M. Alkan, Dyes. Pigm. **75** (2007) 701-713
- [34] Y. Ozdemir, M. Dogan, M. Alkan, Microporous. Mesoporous. Mater. **96** (2006) 419-427
- [35] F. Carrasco-Marin, M.A. Alvarez-Merino, C. Moreno-Castilla, Fuel **75** (1996) 966-970
- [36] M. Illan-Gomez, A. Garcia-Garcia, C. Salinas-Martinez de Lecea, A. Linares-Solano, Energy. Fuels. **10** (1996) 1108-1114
- [37] R. Ahmad, R. Kumar, Appl. Surf. Sci. **257** (2010) 1628-1633
- [38] F. Rozada, L. Calvo, A. Garcia, J. Martin-Villacorta, M. Otero, Bioresour. Technol. **87** (2003) 221-230
- [39] G. Calzaferri, D. Bruhwiler, S. Megelski, M. Pfenniger, M. Pauchard, B. Hennessy, H. Maas, A. Devaux, U. Graf, Solid. State. Sci. **2** (2000) 421-447
- [40] T. Robinson, B. Chandran, P. Nigam, Water. Res. **36** (2002) 2824-2830
- [41] Z. Eren, F.N. Acar, Desalination **194** (2006) 1-10
- [42] R.A. Anayurt, A. Sari, M. Tuzen, Chem. Eng. J. **151** (2009) 255-261
- [43] S. Suresh, V. Srivastava, I. Mishra, J. Chem. Eng. Data. **56** (2010) 811-818
- [44] S. Chowdhury, R. Mishra, P. Saha, P. Kushwaha, Desalination **265** (2011) 159-168
- [45] A.P. Vieira, S.A. Santana, C.W. Bezerra, H.A. Silva, J.A. Chaves, J.C. de Melo, E.C. da Silva Filho, C. Airoidi, J. Hazard. Mater. **166** (2009) 1272-1278
- [46] M. Horsfall Jnr, A.I. Spiff, Electron. J. Biotechnol. **8** (2005) 43-50
- [47] R. Prabakaran, S. Arivoli, Eur. J. Appl. Eng. Sci. **1** (2012) 134-142
- [48] O. Lawal, A. Sanni, I. Ajayi, O. Rabiun, J. Hazard. Mater. **177** (2010) 829-835
- [49] K. Foo, B. Hameed, Chem. Eng. J. **156** (2010) 2-10
- [50] T. Robinson, B. Chandran, P. Nigam, Water. Res. **36** (2002) 2824-2830
- [51] G. Annadurai, R.-S. Juang, D.-J. Lee, J. Hazard. Mater. **92** (2002) 263-274
- [52] L.B. Lim, N. Priyantha, C.M. Chan, D. Matassan, H.I. Chieng, M. Kooh, Arab. J. Sci. Eng. **39** (2014) 6757-6765
- [53] L.B. Lim, N. Priyantha, C. Hei Ing, M. Khairud Dahri, D. Tennakoon, T. Zehra, M. Suklueng, Desalin. Water. Treat. **53** (2015) 964-975
- [54] L.B. Lim, N. Priyantha, C.M. Chan, D. Matassan, H.I. Chieng, M.R.R. Kooh, Desalin. Water. Treat. **57** (2016) 8319-8329
- [55] H. Chen, J. Zhao, Adsorption **15** (2009) 381-389.
- [56] M.M. Montazer-Rahmati, P. Rabbani, A. Abdolali, A.R. Keshtkar, J. Hazard. Mater. **185** (2011) 401-407.
- [57] P. Mourao, P. Carrott, M.R. Carrott, Carbon **44** (2006) 2422-2429.
- [58] S.N. Milmile, J.V. Pande, S. Karmakar, A. Bansiwala, T. Chakrabarti, R.B. Biniwale, Desalination **276** (2011) 38-44
- [59] N. Ahalya, T. Ramachandra, R. Kanamadi, Res. J. Chem. Environ. **7** (2003) 71-79
- [60] E. Sabah, M. Turan, M. Celik, Water. Res. **36** (2002) 3957-3964
- [61] B. Hameed, J. Hazard. Mater. **154** (2008) 204-212
- [62] A.E. Ofomaja, Chem. Eng. J. **143** (2008) 85-95
- [63] S. Cengiz, L. Cavas, Mar. Biotechnol. **12** (2010) 728-736.

MUHAMMAD IMRAN DIN
KIRAN IJAZ
KHALIDA NASEEM

Institute of Chemistry, University of
Punjab, Lahore-54590, Pakistan

NAUČNI RAD

BIOSORPCIONI POTENCIJALI KISELINSKI MODIFIKOVANE *Saccharum bengalense* ZA UKLANJANJE METIL-VIOLETA IZ VODENIH RASTVORA

Šećerna trska Saccharum bengalense (SB) je tretirana sumpornom kiselinom radi povećanja njene sorpcione efikasnosti. Kationska boja, metil-violet (MV), je uklonjena iz vodenog rastvora pomoću kiselinski modifikovan trske (A-SB). Istraženi su različiti parametri, kao što su: doza adsorbenta, brzina mešanja, temperatura, vreme kontakta i početna koncentracija boje, na brzinu adsorpcije boje iz vodenog rastvora. Eksperimentalni podaci za adsorpciju MV analizirani su primenom modela pseudo-prvog reda, pseudo-drugog reda i unutra-čestične difuzije. Utvrđeno je da podaci najbolje prate kinetiku pseudo-drugog reda. Termodinamički parametri ukazuju na to da je reakcija adsorpcije spontana, izvodljiva i endotermna po prirodi. Za utvrđivanje mehanizma adsorpcionog procesa korišćeni su različiti izotermni modeli adsorpcije, kao što su: izoterme Lengmira, Frojndliha, Dubinin-Raduškeviča i Tjomkina, a eksperimentalni podaci se dobro slažu sa izotermom Lengmira.

Ključne reči: biosorpcija, Saccharum bengalense, kinetika, termodinamika, boja.

PETAR STOJANOVIC^{1,2}
MARIJA SAVIC²
DUSAN TRAJKOVIC²
JOVAN STEPANOVIC²
MIODRAG STAMENKOVIC²
MIRJANA KOSTIC³

¹Dunav a.d. Grocka, Grocka,
Serbia

²University of Niš, Faculty of
Technology, Leskovac, Serbia

³University of Belgrade, Faculty of
Technology and Metallurgy,
Department of Textile Engineering,
Belgrade, Serbia

SCIENTIFIC PAPER

UDC 677.494.674.02:66.03

THE EFFECT OF FALSE-TWIST TEXTURING PARAMETERS ON THE STRUCTURE AND CRIMP PROPERTIES OF POLYESTER YARN

Article Highlights

- Effect of false-twist texturing parameters on polyester yarn structure and properties were studied
- Texturing speed and heater temperature significantly affected yarn structure and crimp properties
- The effect of draw ratio and *D/Y* ratio on textured yarn structure and properties is less pronounced
- Texturing speed can be significantly increased comparing to industrial standard (1100 vs. 700 m/min)

Abstract

*In this paper, the effect of false-twist texturing parameters (texturing speed, heater temperature, draw ratio and disc-to-yarn speed ratio (*D/Y* ratio)) on the structure and crimp properties of polyester yarn has been studied using a high temperature heater and high texturing speeds. Textured yarn was analyzed and characterized in terms of the degree of crystallinity, degree of orientation and crimp properties (crimp contraction, crimp module and crimp stability). The most important parameters, significantly affecting yarn temperature and its uniformity and thus textured yarn structure and crimp properties, are texturing speed and heater temperature. Depending on these texturing parameters, the degree of crystallinity and orientation varied in the range of 24.48 to 36.66% and 0.371 to 0.595, respectively. The crimp characteristics increase with the increase in heater temperature, and decrease with the increase in texturing speed. The effect of draw ratio and *D/Y* ratio on the textured yarn structure and properties is less pronounced. Obtained results show that partially oriented polyester yarn used in this study can be textured at significantly higher texturing speed (up to 1100 m/min) than the standard texturing speed (up to 700 m/min) used for the yarn count examined.*

Keywords: crimp properties, false-twist texturing, fiber structure, high-temperature heater, polyester yarn.

Trends in the fiber sector are an important indicator of future trends in the textile industry and the global economy. The world fiber production rose to 92.7 million t in 2014. Not surprisingly, the 2014 rise was sustained mainly by growth in man-made fiber

production, which had reached 61.2 million t. Synthetic fibers accounted for most of the increase in man-made fiber production worldwide, and most of the increase in synthetic fiber production was due to growth in the production of polyester fibers. Polyester fiber, with a market share of about 50%, is the most used fiber in the world. The use of polyester fibers is growing very rapidly due to their desirable properties, including ease of processability, low cost, high-strength, thermostability, chemical and light resistance, silk-like hand, good elasticity, wear and tear property, etc. In 2002, polyester fiber demand passed that of cotton fiber and has continued to grow at a significantly faster rate than all

Correspondence: M. Kostic, University of Belgrade, Faculty of Technology and Metallurgy, Department of Textile Engineering, Karnegijeva 4, 11000 Belgrade, Serbia.

E-mail: kostic@tmf.bg.ac.rs

Paper received: 20 July, 2016

Paper revised: 27 October, 2016

Paper accepted: 15 November, 2016

<https://doi.org/10.2298/CICEQ160720055S>

other fiber types. That is how polyester came to claim a significant share from all other fibers, both man-made and natural, with polyester producers constantly looking at other fibers and their markets to determine if polyester can take further market share [1,2].

For this purpose, a considerable amount of work is being done to modify the existing polyester fibers in order to combine the above-mentioned superior properties of polyester with the features that are unique to natural fibers [3-5]. Texturing is one of the processes that give a crimped and bulky structure, a natural appearance, hand, warmth, stretch and bulk to filament yarns. Among different texturing processes, the false-twist texturing process is mostly used worldwide due to its higher texturing speeds and convenience [6-8].

The false-twist texturing process consists of softening a continuous-filament yarn by heating it above the glass transition temperature to make it more pliable, deforming the softened yarn by twisting, cooling the yarn in the twisted state to set the deformation, and then removing the inserted twist. The temporary twist is imparted to a moving yarn upstream of a twist applicator, such as magnetic spindle, Nip Twister (belt twisting), friction discs, etc. The friction disc twisting technology, introduced in the early 1970s, remains the most common means of twist insertion used in the industry today [6].

The most recent developments in the false-twist texturing process have shown that there is still considerable potential for improvement in that area. In order to increase the texturing speed and, hence, higher yarn speed, either the length or the temperature of the heater have to be increased in order to heat the yarn sufficiently. Since machine producers and users faced many problems with the heater and cooler length of up to 2.5 m, the texturing zone needed to be shortened in order to reduce the investment cost, and, more importantly, to decrease instabilities and to increase the production rate further, as well as to make the setting-up and operability of these machines easier. High-temperature (HT) heaters considerably reduce the residence time required to reach the setting temperature of the polymer. As the texturing zone is shortened, the yarn path is also improved [6-9].

The false-twist texturing process is a multi-parameter process. The most important parameters, considerably influencing textured yarn structure and properties, are: texturing speed, heater temperature, draw ratio and disc-to-yarn speed ratio (D/Y ratio). Studying the correlation between texturing process parameters and textured yarn structure and properties is the first step in process parameter optimization, which is aimed at satisfying product requirements and obtaining a con-

sistent yarn quality, as well as establishing good process performance. When using HT heaters, the operating window for optimizing the texturing process (in terms of filament structure uniformity, broken filament levels, process break-rate, and crimp stability) tends to be smaller than with conventional heaters. This is more pronounced in the case of polyester yarn since it heats up faster and responds more rapidly to heat-settings than polyamide, because of its lower specific heat (approximately 1800 J/(kg K) for polyester *versus* approximately 3300 J/(kg K) for polyamide [9]). Compared to fully oriented polyester yarn (FOY), partially oriented polyester yarn (POY), processed by simultaneous draw-texturing, responds even more rapidly to heat because of the following: the work of drawing and heat of crystallisation additionally raise the temperature of the yarn, and the undrawn POY yarn does not have the stable structure of FOY [6].

According to a literature review, the effect of false-twist texturing parameters on the structure and properties of POY polyester yarn textured using a HT heater and high texturing speeds was studied in smaller scope [10-11] and a comprehensive study about these effects is still missing. Previous approaches were limited to theoretical studies [8,9,12] or using texturing speeds of up to 700 m/min [13,14]. Furthermore, a significantly larger number of studies is dedicated to the texturing of FOY polyester yarn, which is characterized by a stable structure and is less sensitive to texturing parameter changes [15-18], or the texturing of POY polyester yarns, but using other texturing processes [16,18,19]. In this paper, the effect of false-twist texturing parameters (texturing speed, heater temperature, draw ratio and disc-to-yarn speed ratio (D/Y ratio)) on the structure and crimp characteristics of polyester yarn has been studied using a HT heater and high texturing speeds. POY polyester yarn was textured on an industrial false-twist texturing machine. Textured yarn was analyzed and characterized in terms of the degree of crystallinity, degree of orientation and crimp properties (crimp contraction, crimp module and crimp stability).

EXPERIMENTAL

Materials

Single end 167 dtex/36 filaments, polyester POY was used for the study. Chemicals were obtained from commercial sources and were of pro analysis purity.

Texturing conditions

The POY polyester yarn was textured on an industrial false-twist texturing machine FTF 15 HT (ICBT,

France) with a high temperature heater. To study the effect of false-twist texturing parameters (texturing speed, heater temperature, draw ratio and disc-to-yarn speed ratio (D/Y ratio)) on the structure and crimp characteristics of textured polyester yarn, two series of textured yarn samples were prepared at different texturing parameter levels. In the first series of experiments, the first heater temperature levels were 350, 400 and 450 °C. For each heater temperature, the samples were processed at different texturing speed levels: 500, 600, 700, 900, 1000 and 1100 m/min, by keeping other parameters constant at the level considered to be standard for the investigated yarn count (draw ratio of 1.675, D/Y ratio of 2.20 and the second heater temperature of 180 °C). In the second series of experiments, the effect of draw ratio (1.665, 1.675, 1.685) and D/Y ratio (2.15, 2.20, 2.25) on the structure and crimp properties of textured PET yarns were investigated only at higher texturing speeds: 900, 1000 and 1100 m/min, and constant heaters temperature (the first heater temperature 450 °C, and the second heater temperature 180 °C).

Crystallinity measurements

Owing to regular packing of the molecules, the crystalline phase has a higher density than the amorphous phase. Thus the total density of a fiber, i.e. semi-crystalline polymer, depends on the crystallinity of the sample. An accurate measurement of density can be used for estimating crystallinity.

The densities of the fibers/yarns were measured by the flotation method [20]. Short fragments of fibers, i.e., fiber bundles tied in a knot with loose ends snipped off, were immersed in a mixture of carbon tetrachloride and benzene solutions with different densities. After about half an hour they should come to rest at the level representing their density.

The degree of crystallinity is calculated by the following equation:

$$X(\%) = 100 \left[\frac{\rho - \rho_a}{\rho_c - \rho_a} \right] \frac{\rho_c}{\rho} \quad (1)$$

where X is the mass fraction of the crystalline phase in %; ρ , ρ_a and ρ_c are densities of the given sample, amorphous and crystalline phases, respectively. The literature values of ρ_a and ρ_c (i.e., the densities of a perfectly amorphous and a perfectly crystalline sample) for poly(ethylene terephthalate) are 1.335 and 1.515, respectively [21].

Birefringence measurements

The birefringence (Δn) was measured using a MIN 8 polarizing microscope, an average of 10 single

filaments were tested to maintain the reproducibility of the results. The birefringence was measured using the following relationship:

$$\Delta n = \Delta / d \quad (2)$$

where Δ is the ray-motion difference and d is the thickness of fiber in the compensation zone [22]. The optical orientation factor (f , in terms of Herman's orientation factor, can be calculated as the ratio of the birefringence of the fiber (Δn) to that of an ideal fiber (Δn_{\max}) in which the molecules are oriented in a perfectly parallel manner to the fiber axis. In the present study, a value of 0.24 has been used as the maximum birefringence value for the fully oriented poly(ethylene terephthalate) sample [23,24].

Morphology investigation

The yarn/filament morphology, i.e., the longitudinal view and cross section of filaments, was investigated by a light microscope (Kruess, Germany) in order to determine filament flattening and cross-sectional uniformity.

Yarn crimp measurement

Crimp contraction (CC), crimp module (CM) and crimp stability (CS) were determined in accordance with the standard DIN 53840-1 [25]. Briefly, a yarn hank of 2500 dtex was dry heated at 120 °C for 10 min and then conditioned in the standard atmospheric conditions before length measurement on the Texturmat instrument. Crimp contraction, crimp module and crimp stability were calculated from the following equations:

$$CC(\%) = 100 \frac{l_0 - l_1}{l_0} \quad (3)$$

$$CM(\%) = 100 \frac{l_0 - l_2}{l_0} \quad (4)$$

$$CS(\%) = 100 \frac{l_0 - l_3}{l_0 - l_1} \quad (5)$$

where l_0 is the length with loading at 500 cN, l_1 is the length with loading at 2.5 cN, l_2 is the length with loading at 25 cN, and l_3 is the length with loading first at 2500 cN for 10 s, followed by unloading to 2.5 cN.

RESULTS AND DISCUSSION

Effect of heater temperature and texturing speed on the yarn structure and crimp properties

Characterisation of the structure in the bulk state is essential for the process conditions-structure-property correlation of polymers and fibers. The packing of long polymer chains in a three-dimensional structure is

largely governed by their molecular characteristics (such as flexibility, structural regularity, etc), intermolecular interactions and external constraints (such as temperature, stress, etc.) [21,26].

POY polyester (polyethylene terephthalate) yarn used in this study is partially orientated yarn with a very low degree of crystallinity (less than 5%) and thus its structure and properties can be varied through manipulation of the texturing process parameters. The most important parameters are texturing speed and heater temperature, both of them affecting yarn temperature and its uniformity, and thus textured yarn structure. The effect of texturing speed and heater temperature on the structure of false-twist textured yarn, *i.e.*, degree of crystallinity and birefringence of textured polyester yarn is shown in Figure 1. The texturing speed and heater temperature have been varied between 500 to 1100 m/min and 350 to 450 °C, respectively, while other texturing parameters have been kept constant. The degree of crystallinity of POY polyester false-twist textured filament yarn varies in the range of 24.48 to 36.66% depending on the texturing parameters. It can be seen that the degree of crystallinity increases with the increase in heater temperature and texturing speed up to 900 m/min. However, in this study, the degree of crystallinity decreases after peak point, and starts to increase again with increasing the texturing speed. At lower texturing speeds, increase in the degree of crystallinity can be explained by the re-crystallization process at an elevated temperature. As the yarn temperature increases, the intermolecular forces become weak, facilitating the mobility and flexibility of the macromolecular chains and structural elements, allowing the crystallites to align more easily. The observed decrease in crystallinity can be explained by the facts that during the false-twist texturing process POY polyester yarn is subjected to externally applied forces, namely

drawing and twisting forces, and internal stress, *i.e.*, contraction stresses due to relaxation processes and increased molecular mobility with increasing temperature. The ability of the yarn to resist these forces depends on changes in the yarn temperature, which is determined by both texturing speed and heater temperature. The effect of these two parameters on the yarn stress is opposite. The increasing temperature interrupts more and more molecular interactions and softens the material; as a consequence, the yarn stress diminishes. On the other hand, the increase of texturing speed increases both externally applied forces and internal yarn stress [10,27].

The birefringence values of POY polyester false-twist textured filament yarn are shown in Figure 1b. The birefringence values vary in the range of 0.089 to 0.143, depending on the texturing parameters. Since the birefringence is a measure of overall orientation, the increase in birefringence values shows that the orientation also increases; the optical orientation factor varies in the range of 0.371 to 0.595, depending on the texturing parameters. From the data obtained, it is clear that the birefringence shows tendency to increase with increasing temperature. This can also be explained, as in the case of the degree of crystallinity, by the fact that higher yarn temperature facilitates the mobility and flexibility of the macromolecular chains and structural elements, wherefore they are oriented more easily. Concerning the effect of texturing speed on the birefringence, an increase in the texturing speed, which corresponds to a decrease in contact time in the heater, decreases the birefringence and orientation; however, there is no clear correlation since at higher texturing speed an increase in birefringence and orientation has been again observed. This can be explained by the fact that, in addition to yarn temperature, there are two more factors influencing the degree of

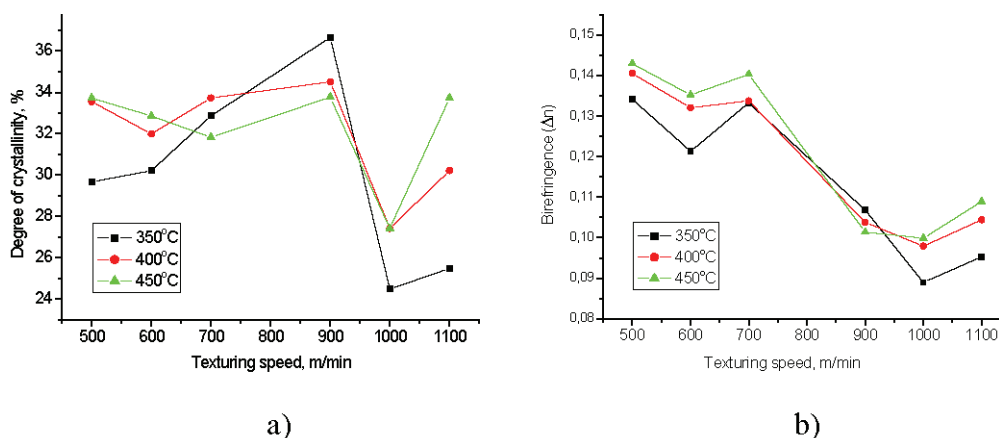


Figure 1. Effect of texturing speed and heater temperature on: a) degree of crystallinity and b) birefringence of textured polyester yarn (draw ratio of 1.675, D/Y ratio of 2.20).

orientation of textured yarn: the torsional stresses that help to disorient the macromolecules chains, and the tensile stresses that orient crystalline and amorphous sections of the chains further [6,7]. In general, POY PET yarn textured at the lowest texturing speed (*i.e.*, 500 m/min) and highest temperature (450 °C) shows the highest birefringence and consequently orientation, possibly due to the fact that at a higher temperature and lower texturing speed segments of macromolecules have higher mobility and sufficient time for orientation under the tensile stresses.

The yarn/filament morphology investigation revealed differential crimp existing in the individual filaments (Figure 2a and b), relatively straight and deformed in a purely torsional way the filament parts staying on the yarn axis (Figure 3a), the filament flattening and filament fusion (Figure 3b and c), as well as the filament cross-sectional non-uniformity (Figure 3d). Observed morphological non-uniformities can be explained by the fact that texturing of the multifilament yarn with a large number of filaments leads to obtaining a more compacted, denser filament bundle before its entry into the heater. As a consequence, proper migration of constituent filaments within the twisted bundle in the texturing zone is difficult due to the high number of filaments, resulting in yarn temperature cross-sectional non-uniformity (filaments on the outside of the bundle receive more heat than those on the inside) and an asymmetric distribution of tensile and twisting forces, which also affects the amount of crimp development in the different individual filaments and the filament cross-section shape uniformity [6,7].

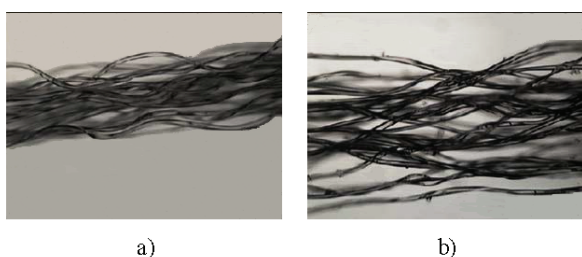


Figure 2. Longitudinal view of yarn textured at 700 m/min, draw ratio 1.665, D/Y ratio 2.15 and heater temperature: a) 400; b) 350 °C (magnification 40 \times).

Filament damage (*i.e.*, filament flattening and filament fusion), mainly observed during texturing at higher heater temperature and lower texturing speed, occurs on the filaments located on the outside of the twisted bundle as a result of their contact with higher surface temperatures on the HT heater. Figure 3d shows the textured filament cross-section deviation from the round cross-section of the parent POY yarn. The polygonal or elliptical form of these filaments is a

result of their deformation in the twisting unit, and it will also affect filament optical properties.

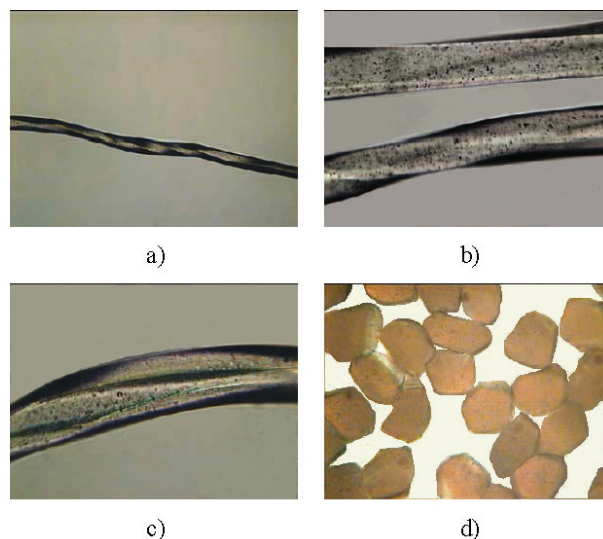


Figure 3. Longitudinal view of single filament textured at 700 m/min (a and b), heater temperature 350 °C, draw ratio 1.685, D/Y ratio 2.25 (magnification 100 and 400 \times , respectively); c) single filament textured at 500 m/min, heater temperature 400 °C, draw ratio 1.685, D/Y ratio 2.25 (magnification 400 \times); d) cross-section of yarn textured at 600 m/min, heater temperature 350 °C, draw ratio 1.675, D/Y ratio 2.25 (magnification 400 \times).

Discussed differential crimp existing in the individual filaments and the structural changes in the polymer and filament yarn developed during the texturing process both affect crimp properties of the textured yarn. Crimp properties are a measure of the structural stability and relaxation of yarn tensions remaining from previous treatment steps that affect textured yarn performance during further processing (knitting, warping, weaving or tufting) and, knowing them, it is possible to predict how a yarn will perform during fabric formation and finishing [6,7]. The obtained results for crimp contraction, defined as the reduction in length of a textured filament yarn as a result of its crimped structure when the crimp is developed; crimp module, which characterises the elongation behavior of the textured yarn in the range of crimp elasticity; and crimp stability, defined as the ratio of the retraction of a hank of yarn after and before defined loading; are shown in Figure 4. The results indicate that in general the crimp contraction, crimp module and crimp stability increase as the heater temperature increases. On the other hand, the crimp contraction, crimp module and crimp stability decrease as the texturing speed increases. This can be explained by yarn instability and decrease in orientation (Figure 1a). Furthermore, the absence of a clear correlation between crimp properties and texturing speed could be

explained by different types of deformation imposed on the twisted continuous yarns: the tension occurring above glass transition temperatures which inhibits macromolecule mobility and consequently lowers the yarn's ability to relax during texturing; the twist along the length of the filaments, resulting, as it has been mentioned, in relatively straight filaments deformed in a purely torsional way; and, finally, the bending of some filaments, which thus follow a helical path about the yarn axis [11].

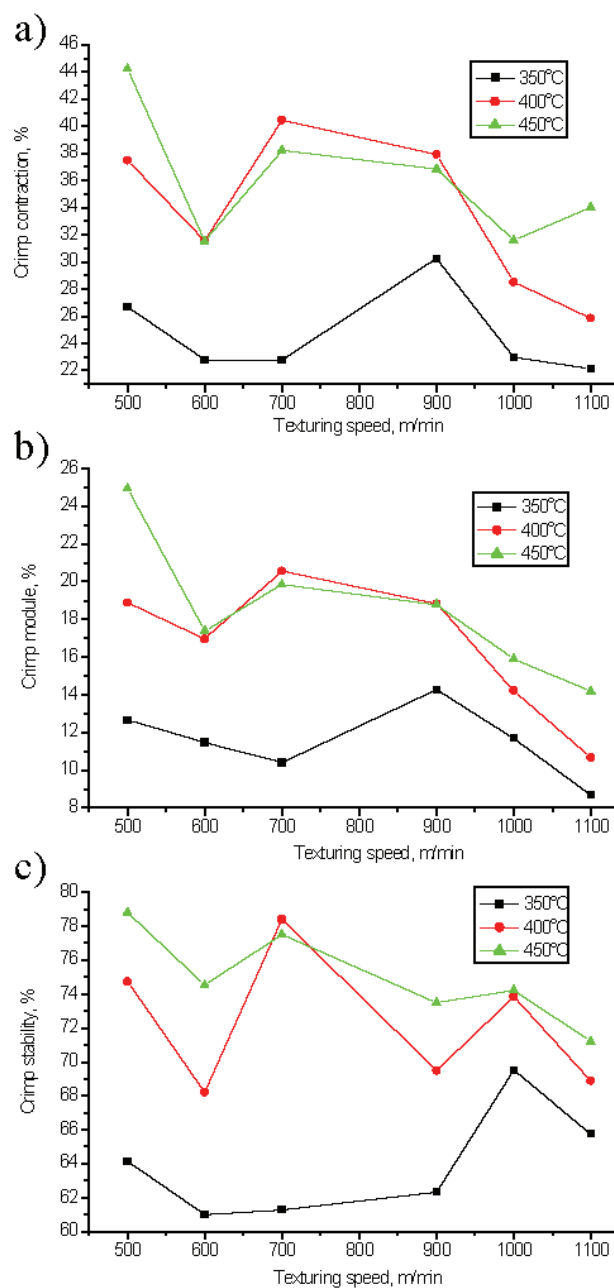


Figure 4. Effect of texturing speed and heater temperature on: a) crimp contraction, b) crimp module and c) crimp stability of textured polyester yarn (draw ratio of 1.675, D/Y ratio of 2.20).

The results obtained in the first set of experiments aimed at satisfying product requirements and establishing good process performance at a higher texturing speed (up to 1100 m/min), clearly show that by increasing the heater temperature (from 350 to 450 °C), it is possible to obtain textured polyester yarn with improved crimp properties (*i.e.*, increased CC , CM and CS parameters).

Effect of draw and D/Y ratio variations on yarn structure and crimp properties

The second part of the study has been conducted in order to clarify effects of small changes of texturing parameters (draw and D/Y ratios) on structure and crimp properties of polyester yarn textured at a higher texturing speed (900–1100 m/min), but also to explore the possibility of improving textured yarn properties by varying these two parameters. The degree of changes of these parameters has been governed by the stability of the process on the texturing machine. The draw and D/Y ratios have been varied in the range of 1.665 to 1.685 and 2.15 to 2.25, respectively, while other texturing parameters have been kept constant. The effect of false-twist texturing parameters: draw and D/Y ratios on the structure, *i.e.*, degree of crystallinity and birefringence of textured polyester yarn is shown in Figure 4. The degree of crystallinity varies in the range of 25.48 to 34.51%, while birefringence varies in the range of 0.0842 to 0.1089, depending on the texturing parameters. Increasing the draw ratio means that more tensile stress is generated into the yarn, while increasing the D/Y ratio means that the discs are rotating faster and more twist is inserted into the yarn [7]. Furthermore, if the D/Y ratio is low, the yarn tension before the twisting unit will be low and the tension after twisting unit will be high, which can cause yarn damage [13]. Figure 5a gives a clear indication of the effect of draw ratio on the crystallinity and orientation of the textured yarn, *i.e.*, extending the yarn below or above the optimum value (draw ratio of 1.675) results in decrease of both structural parameters. It should be noted that the D/Y ratio has a similar effect on these two structural parameters of textured yarns (Figure 5b).

The discussed structural changes in the polymer and filament yarn occurred during the texturing process have a surprisingly minor effect on the crimp properties of the textured yarn, as it is shown in Figure 6. According to literature [7], increases in orientation should reduce the capability of polymer chains to buckle and deform in the friction unit, thereby restricting the degree of crimp that can be developed in the yarn. Polyester yarn textured at a texturing speed of 900 m/min shows the highest crimp characteristics

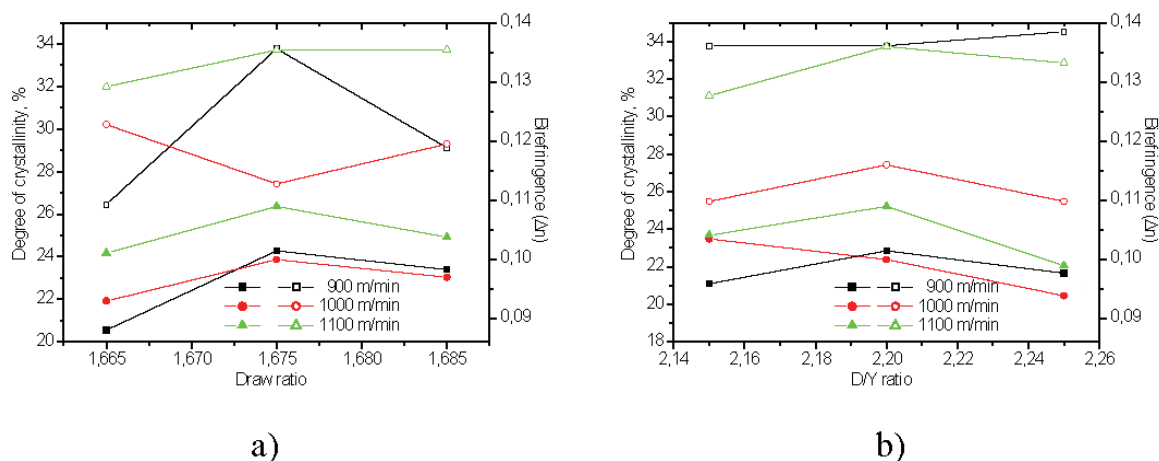


Figure 5. a) Effect of texturing speed and draw ratio on degree of crystallinity (empty symbol) and birefringence (solid symbol) of textured polyester yarn (heater temperature 450 °C, D/Y ratio of 2.20) and b) effect of texturing speed and D/Y ratio on degree of crystallinity (empty symbol) and birefringence (solid symbol) of textured polyester yarn (heater temperature 450 °C, draw ratio of 1.675).

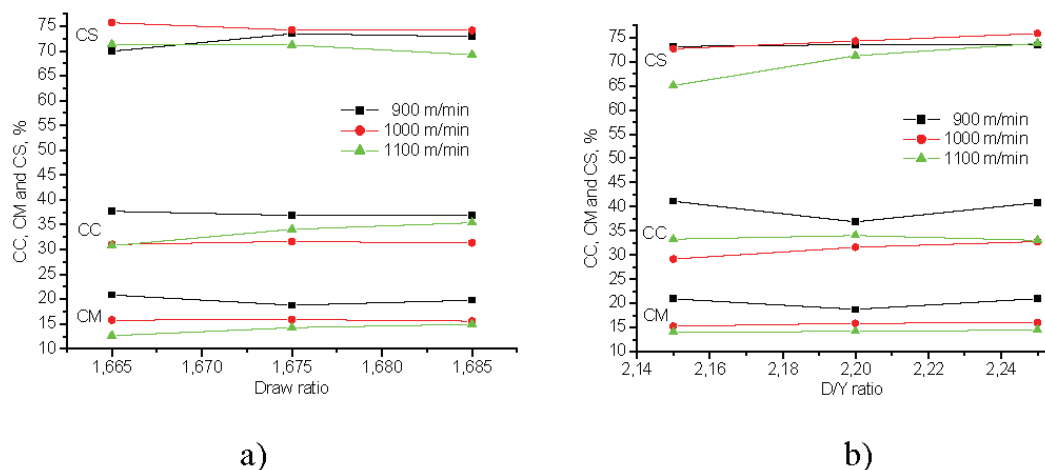


Figure 6. a) Effect of texturing speed and draw ratio on crimp contraction, crimp module and crimp stability of textured polyester yarn (heater temperature 450 °C, D/Y ratio of 2.20) and b) effect of texturing speed and D/Y ratio on crimp contraction, crimp module and crimp stability of textured polyester yarn (heater temperature 450 °C, draw ratio of 1.675).

over almost all texturing conditions. It is important to note that the increases in draw ratio can be used to increase crimp contraction, while the increases in D/Y ratio can be used to increase crimp stability at the highest texturing speed applied in this research. In such instances, texturing parameters have to be compromised, mainly taking into account texturing speed and yarn crimp properties. Our results show that POY polyester yarn fineness of 167 dtex f36x1 used in this study can be textured at significantly higher texturing speeds than the standard texturing speed for the yarn count examined (up to 700 m/min).

CONCLUSION

The false-twist texturing of POY polyester yarn is a process that includes close interactions between

process parameters and textured yarn structure and properties. The most important parameters are texturing speed and heater temperature, both of them affecting textured yarn structure and crimp properties. The degree of crystallinity increases with the increase in heater temperature and texturing speed reaching peak point at 900 m/min. The birefringence and orientation show a tendency to increase with increasing temperature, while an increase in the texturing speed decreases the birefringence and orientation. At a higher texturing speed, above 1000 m/min, an increase in birefringence and orientation has been observed. A similar tendency has been observed for crimp properties, they increase as the heater temperature increases and decrease as the texturing speed increases. Small changes of draw and D/Y ratios affect to a higher extent the structure of the textured polyester yarn,

while their effect on the crimp properties is surprisingly minor. Obtained results show that texturing parameters have to be compromised, mainly taking into account the texturing speed and yarn crimp properties. POY polyester yarn used in this study can be textured at significantly higher texturing speeds than the standard texturing speed used for the yarn count examined, while maintaining the same textured yarn characteristics.

Acknowledgments

The authors are grateful to Mr. M. Filipovic from Dunav a.d. Grocka and Mrs. N. Tadic from Univesity of Belgrade, Faculty of Technology and Metallurgy, for technical assistance. Authors would also like to thank the Ministry of Education, Science and Technological Development of the Republic of Serbia for financial support through the Projects „The Development of New and the Improvement of the Existing Technological Processes for the Production of Technical Textiles“, No. TR 34020.

REFERENCES

- [1] P. Simpson, *Textile Outlook International*, 2015/175, 2015, pp. 67-82
- [2] CIFRS, *World Man-Made Fibres Production*, <http://www.cifrs.org/KeyStatistics/WorldManMadeFibresProduction.aspx> (accessed 20 June 2016)
- [3] K.E. Perepelkin, *Fibre Chem.* **33** (2011) 333-339
- [4] M. Jaffe, A.J. East, in *Handbook of Fiber Chemistry*, M. Lewin Ed., 3rd ed., CRC Press, Taylor & Francis Group, Boca Raton, FL, 2007, p. 1
- [5] V.B. Gupta, A.K. Mukherjee, S.S. Cameotra, in *Manufactured Fibre Technology*, V.B. Gupta, V.K. Kothari Eds., Chapman & Hall, London, 1997, p. 271
- [6] C. Atkinson, *False Twist Textured Yarns: Principles, Processing and Applications*, Woodhead Publishing Ltd., Cambridge, 2012
- [7] J.W.S. Hearle, L. Hollick, D.K. Wilson, *Yarn Texturing Technology*, Woodhead Publishing Ltd, Cambridge, 2001
- [8] E.A. Silva, A.P. Paiva, P.P. Balestrassi, C.E.S. Silva, *Fibres Text. East. Eur.* **17** (2009) 57-62
- [9] N. Eskin, *Energy Conv. Manage.* **44** (2003) 2531-2547
- [10] H. Canbaz Karakaşa, H. Dayioğlu, *Indian J. Fibre Text. Res.* **30** (2005) 37-41
- [11] S. Canoglu, *Fibres Text East. Eur.* **17** (2009) 35-39
- [12] B. Azimi, M.A. Tehran, M.R.M. Mojtahedi, *J. Eng. Fiber Fabr.* **8** (2013) 97-101
- [13] K. Yildirim, S. Altun, Y. Ulcay, *J. Eng. Fiber Fabr.* **4** (2009) 26-32
- [14] M.A. Tehran, B. Azimi, M.R.M. Mojtahedi, *J. Eng. Fiber Fabr.* **6** (2011) 54-62
- [15] P. Celik, N. Ozdil, G. Supure, *Ind. Text.* **62** (2011) 38-43
- [16] S.S. Bhattacharya, T.N. Shaikh, A. Pratap, *AIP Conf. Proc.* **1249** (2010) 67-74
- [17] T.N. Shaikh, S.S. Bhattacharya, *Text. Res. J.* **80** (2010) 483-486
- [18] T.N. Shaikh, S.S. Bhattacharya, *Text. Res. J.* **81** (2011) 1995-2005
- [19] S.S. Mahish, S.K. Punj, V.K. Kothari, *Fiber. Polym.* **11** (2010) 932-940
- [20] AATCC Test Method 20-2007, *Fiber Analysis: Qualitative*, 2007
- [21] A.K. Gupta, in: *Manufactured Fibre Technology*, V.B. Gupta, V.K. Kothari Eds., Chapman & Hall, London, 1997, p. 203
- [22] A. Koblyakov, *Laboratory Practice in the Study of Textile Materials*, Mir Publishers, Moscow, 1989, p. 200
- [23] A.A. Hamza, T.Z.N. Sokkar, K.A. El-Farahaty, H.M. El-Dessouky, *Polym. Test.* **23** (2004) 203-208
- [24] I. Karacan, *Fiber. Polym.* **6** (2005) 186-199
- [25] DIN 53840-1, *Determination of parameters for the crimp of textured filament yarns; filament yarns with a linear density exceeding 500 dtex*, 1983
- [26] A. Ziabicki, *Fundamentals of Fibre Formation*, John Wiley & Sons, London, 1976
- [27] V.B. Gupta, M. Kumar, *Tex. Res. J.* **45** (1975) 382-388.

PETAR STOJANOVIĆ^{1,2}
MARIJA SAVIĆ²
DUŠAN TRAJKOVIĆ²
JOVAN STEPANOVIĆ²
MIODRAG STAMENKOVIĆ²
MIRJANA KOSTIĆ³

¹Dunav a.d. Grocka, Bulevar Revolucije
15, 11306 Grocka, Srbija

²Univerzitet u Nišu, Tehnološki fakultet,
Bulevar Oslobođenja 124, 16000
Leskovac, Srbija

³Univerzitet u Beogradu, Tehnološko-
metalurški fakultet, Katedra za tekstilno
inženjerstvo, Karmegijeva 4, 11000
Beograd, Srbija

NAUČNI RAD

UTICAJ PARAMETARA PROCESA TEKSTURIRANJA LAŽNIM UPREDANJEM NA STRUKTURU I KARAKTERISTIKE KOVRDŽAVOSTI TEKSTURIRANOG POLIESTARSKOG PREDIVA

U ovom radu proučavan je uticaj parametara tekstuiranja lažnim upredanjem (brzina tekstuiranja, temperatura grejača, stepen istezanja, kao i odnos površinske brzine diska i linearne brzine prediva (D/Y odnos)) na strukturu i karakteristike kovrdžavosti poliestarskog prediva tekstuiranog uz korišćenje visokotemperaturnog grejača i pri velikim brzinama tekstuiranja. Tekstuirano predivo je okarakterisano sa aspekta novodobijene strukture (stepen kristalnosti i stepen orijentisanosti) i karakteristika kovrdžavosti (stepen kovrdžavosti, karakteristična kovrdžavost i stabilnost kovrdža). Najznačajniji parametri, koji u najvećem stepenu utiču na temperaturu prediva i njenu ravnomernost, a samim tim i na strukturu i svojstva kovrdžavosti tekstuiranog prediva, su brzina tekstuiranja i temperatura grejača. Zavisno od ovih parametara tekstuiranja, stepen kristalnosti i stepen orijentacije varirali su u rasponu od 24,48 do 36,66% i 0,371 do 0,595, redom. Karakteristike kovrdžavosti se povećavaju sa povećanjem temperature grejača, a smanjuju sa povećanjem brzine tekstuiranja. Uticaj stepena istezanja i D/Y odnosa na strukturu i svojstva tekstuiranog prediva je manje izražen. Dobijeni rezultati su pokazali da se delimično orijentisano poliestersko predivo, korišćeno u ovom radu, može tekstuirati pri značajno većim brzinama tekstuiranja (do 1100 m/min) u odnosu na standardne brzine tekstuiranja (do 700 m/min) koje se koriste za preradu prediva ispitivane finoće.

Ključne reči: poliestarsko predivo, struktura vlakana, svojstva kovrdžavosti, tekstuiranje lažnim upredanjem, visokotemperaturni grejač.

MENG PENG
XIAOJUN YANG
JIAXIONG WU
HUA YUAN
CHAOFAN YIN
YUANXIN WU

Key Laboratory for Chemical
Process of Ministry of Education,
Wuhan Institute of Technology,
Wuhan, China

SCIENTIFIC PAPER

UDC 546.88:54:66.095.6:66.097.3

APPLICATION OF VANADIUM-INCORPORATED PHOSPHOMOLYBDATE SUPPORTED ON THE MODIFIED KAOLIN IN SYNTHESIS OF DIPHENYL CARBONATE BY OXIDATIVE CARBONYLATION WITH PHENOL

Article Highlights

- This kind of catalyst is reported for the first time
- Both the conversion of phenol and the DPC yield are the highest levels that have been reported
- With the increase of the number of vanadium atoms, the activity is enhanced
- The catalyst can be regenerated and reused for several runs

Abstract

Keggin-type molybdophosphoric acid, molybdophosphoric salt and vanadium incorporated molybdophosphoric salt supported on the modified kaolin (MK) were investigated as redox co-catalysts for the oxidative carbonylation of phenol to diphenyl carbonate (DPC) in the absence of solvent. The 20 wt.% of MnAMPV₅ (one kind of vanadium incorporated molybdophosphoric salt) loaded on MK showed the highest catalytic activity with the yield of 24.68% and a TON of 306, while the selectivity amounts to nearly 100% in all the carbonylation reactions. The catalysts were characterized by XRD, BET, XPS and H₂-TPR. The reusability study showed that the catalysts were stable and active.

Keywords: vanadium, molybdophosphoric, oxidative carbonylation, catalyst, diphenyl carbonate.

Diphenyl carbonate is a versatile chemical intermediate as well as the main raw material for the cleaner production of polycarbonate (PC) [1]. The main synthetic methods of DPC are phosgene method, transesterification method and oxidative carbonylation method. Phosgene method gradually dies out due to serious environmental pollution problems [2]. The transesterification reaction of DPC by phenol and DMC is limited by the thermodynamic conditions, the equilibrium constant of which is small leading to the lower catalytic efficiency [3]. The most attractive method is oxidative carbonylation of phenol using monoxide and oxygen in one-step [4], in which H₂O is the sole by-

-product and the use of highly toxic and corrosive phosgene can be avoided. Compared to homogeneous catalysts, the heterogeneous catalysts are easy to be separated [5]. Thus, it is essential to decrease the intraparticle diffusion resistance and improve catalytic activity of heterogeneous catalysts in oxidative carbonylation of phenol to DPC.

The formula of the Keggin-type heteropolyacids (HPAs) is H_{8-x}[XM₁₂O₄₀], where X refers to the heteroatom (most frequently P⁵⁺ or Si⁴⁺), *x* refers to its oxidation state, and M means the addenda atom (usually W⁶⁺ or Mo⁶⁺). The Keggin-type HPA is a promising acid catalyst as well as a nice oxidation/reduction catalyst and a good bifunctional catalyst (acid catalyst and oxidation/reduction catalyst) [6] for its adjustment of architecture [7], oxidation resistance, thermal stability and low corrosivity. Compared to heteropolytungstates, heteropoly molybdates are better catalysts for most of oxidation reactions [8]. Furthermore, the high solubility in polar solvents, low surface area and thermal stability of the HPAs can be enhanced by exchan-

Correspondence: Y. Wu, Key Laboratory for Chemical Process of Ministry of Education, Wuhan Institute of Technology, Wuhan 430073, China.

E-mail: wyx@mail.wit.edu.cn

Paper received: 1 July, 2016

Paper revised: 5 November, 2016

Paper accepted: 16 November, 2016

<https://doi.org/10.2298/CICEQ160701056P>

ging the proton with metal, converting into salts or dispersing them on suitable support [9]. The activity of HPAs in oxidation can be improved by partial substitution of redox metal ions in the Keggin structure [10]. Vanadium incorporated molybdophosphoric acid (HAMPV) catalysts show unique catalytic features in oxidation due to the bifunctional character—the good redox nature of vanadium and the oxidation/acidic character of the molybdophosphoric acid [11]. Authors have investigated V-incorporated molybdophosphoric acid catalysts through the way of replacing 1-3 Mo atoms with the corresponding number of V atoms [12,13]. The acidity, redox and thermal stability of the HAMPV catalysts are influenced by the degree of V substitution [14]. It is helpful to increase the surface area by loading modified HPAs on support. It is always advantageous to use supports such as Nb₂O₅, TiO₂, SiO₂ and Al₂O₃, all of which are capable of releasing oxygen by the mobility of lattice oxygen and form oxygen vacancies [15]. Acidified and modified cross-linked kaolin with the porous structural [16] has been widely applied for industrial catalysts [17] and carriers [18] owing to its acidity and high surface area itself.

Some research groups focus on Pd/Mn system because the potentials of MnO₂/Mn²⁺ pair are between the potentials of Pd²⁺/Pd and O₂ + H⁺/H₂O pairs. Therefore, Mn⁴⁺ of MnO₂ can oxidize Pd to form Pd²⁺ and Mn²⁺, then the latter one could be reoxidized by O₂ to Mn⁴⁺. Manganese oxide has been studied for the first time as co-catalyst and support by Min [19], which made it easy for the metallic parts of the catalytic system to separate. But the yield of DPC was only 10.7% [19]. Xiaojun prepared palladium supported on Pb-cation-doped manganese oxide octahedral molecular sieves as heterogeneous catalysts and the yield of DPC increased to 18.1% [20]. The spinel ferrite MnFe₂O₄ has been prepared by Zhang in the sol-gel method as a catalyst support applied in oxidative carbonylation of phenol to diphenyl carbonate. It cannot be reused although the single pass yield of DPC reached 33.12% and TOF was 70.56 mol DPC (mol Pd·h)⁻¹ [21].

In this work, heteropoly salts (MPAs) loaded on the modified kaolin as a co-catalyst is applied in the synthesis of diphenyl carbonate by oxidative carbonylation of phenol. In addition, the influence of V replacing Mo in heteropoly salts on the catalytic activity in the reaction is also studied.

EXPERIMENTAL

The preparation of the Keggin-type heteropoly salt

Keggin-type molybdophosphoric acid, molybdophosphoric salt and vanadium-incorporated molybdophosphoric salt have been successfully synthesized based on the synthesis procedure reported previously [22].

Synthesis of H₄PMo₁₁VO₄₀

1.56 g Na₂HPO₄·12H₂O (0.01 mol) was dissolved in 50 ml deionized water. 26.64 g NaMoO₄·2H₂O (0.11 mol) was dissolved in 60 ml deionized water. Then the two solutions were mixed together and heated with stirring until it boiled to reflux for about 30 min and 1.53 g NaVO₃·2H₂O (0.01 mol) was added into it. Then the mixture was heated with reflux at 110 °C for 30 min. The pH was adjusted to 2 with sulfuric acid in a mole ratio of 1:1 until it turned to scarlet. It was cooled down to room temperature and transferred into a 500 ml tap funnel. 50 ml diethyl ether was added and shaken until the solution was divided into two layers. Then 1:1 sulfuric acid (about 30 ml) was dropped and shaken until red granular objects sank into the solution. When the solution was divided into three layers, the upper was diethyl ether, the middle was aqueous solution, the lower reddish-brown oil was ether compounds of heteropolyacids and ether, which was taken for vacuum drying to obtain brown-red powder - H₄PMo₁₁VO₄₀ (HAMPV).

The preparation of HAMPV₃ and HAMPV₅ was the same as the way above with the different mixing ratios.

Synthesis of the Keggin-type heteropoly salt

1g desiccative HAMPV prepared above was dissolved in 5 ml deionized water. 0.1392 g Mn(NO₃)₂·4H₂O was dissolved in 5 ml deionized water. The two solutions were mixed, stirred for 30 min at a magnetic stirrer and placed in a vacuum oven, dried at 70 °C for 6 h. The mixture was cooled down to the room temperature, transferred to a small mug and calcined at 200 °C for 4 h in a muffle furnace. It was cooled down to the room temperature to obtain a powder—MnAMPV.

CuCl₂·2H₂O, Co(NO₃)₂·6H₂O, Pb(NO₃)₂, Ce(NO₃)₃·6H₂O or FeCl₃·6H₂O took the place of Mn(NO₃)₂·4H₂O to prepare different heteropoly salts.

Pretreatment of kaolin carrier

The kaolin was purified by immersing in deionized water and stirred at room temperature for 6 h. It was filtrated, dried at 110 °C, ground and calcined at 300 °C for 2 h, after which it was immersed in 20 wt.%

H₂SO₄, activated at 100 °C for 4 h. The solution was cooled down to room temperature, washed with deionized water, filtrated to neutral state and finally dried at 120 °C for 8 h. The modified kaolin was prepared for later use.

The supported of heteropoly salt

0.3 g MnAMPV was dissolved into 80 ml solution mixed with anhydrous ethanol and distilled water in volume ratio 1:1. 1 g modified kaolin was added into the mixed solution above and stirred in hot reflux for 8 h. Then it was dried at 100 °C for 6 h, calcined it in the muffle furnace at 300 °C for 3 h and cooled down to the room temperature to prepare 30 wt.% MnAMPV/MK co-catalyst.

10 wt.% MnAMPV/MK and 20 wt.% MnAMPV/MK could be obtained by changing the ratio of MnAMPV and MK.

Supporting the PdCl₂

The active component PdCl₂ was loaded on the support by coprecipitation method. PdCl₂ was dissolved into 50 ml distilled water with hydrochloric acid of proper volume completely. 5 g support was dipped into the PdCl₂ solution in order to have a palladium loading of 1 wt.%. The NaOH solution as a precipitant was then added into the solution to keep pH value at 9-10 with stirring. Filtrated, dried and finally calcined it at 300 °C for 3 h to obtain the catalysts.

Characterization

The phase identification and crystalline structure analysis were characterized by the X-ray diffractometer (XRD, D8 Advance, Germany) operating at 40 kV and 40 mA using CuK α radiation and Ni filter. The scanning rate is 4°·min⁻¹ in the 2 θ range 5-80°. BET surface area measurement was done by applying the Quantachrome Instruments Nova2000e. The chemical shift and valence of element on surface were studied by X-ray photoelectron spectra (XPS) in a Perkin-Elmer PHI 1600 ESCA system with MgK α X-ray radiation (1253.6 eV, 250 W). Temperature-programmed reduction (H₂-TPR) experiments were performed in a quartz reactor using a thermal conductivity detector (TCD) as detector on Micromeritics AutoChem2920 (USA) instrument.

Catalytic activity test

DPC synthesis by oxidative carbonylation of phenol was carried out in a stainless steel autoclave of ca. 250 ml of capacity provided with a magnetic stirrer. Typical reaction conditions were as follows: $t = 65$ °C, $p = 5$ MPa, CO/O₂ = 93/7 mole ratio, phenol, 20 g, 1.0 g catalyst (Pd/carrier = 1/100 mass ratio),

tetrabutylammonium bromide (TBAB) 1 g, 4A molecular sieve as drying agent, reaction time 8 h. Then the autoclave was pressurized with the mixture of carbon monoxide and oxygen, and the reaction autoclave was cooled down to room temperature and vented in the end.

The reaction products were identified and quantified by gas chromatography with a flame ionization detector (FID, GC4000A of EAST&WEST Analytical Instruments made in China).

RESULTS AND DISCUSSION

Catalyst characterization

XRD and BET characterization

The heteropolyanion of the Keggin-type absorption peaks generally appear at 8.28, 8.90, 9.10, 27.9 and 28.9°, which are basically identical with the characteristic peaks of MnAMPV (Figure 1). Therefore, the prepared heteropoly salt belongs to Keggin-type heteropoly compound. From the XRD pattern of MK, it is known that the absorption peak of MK is consist with the characteristic peak of the kaolin at around 26.3°. The absorption peak of heteropolyanion is gradually enhanced with the increase of heteropoly salt loading, the intensity of which is weaker than pure molybdovanadophosphoric heteropoly salt. It indicates that molybdovanadophosphoric heteropoly salt has good dispersion on the carriers instead of aggregation. The characteristic peak of Pd is hard to be found for its content of merely 1%.

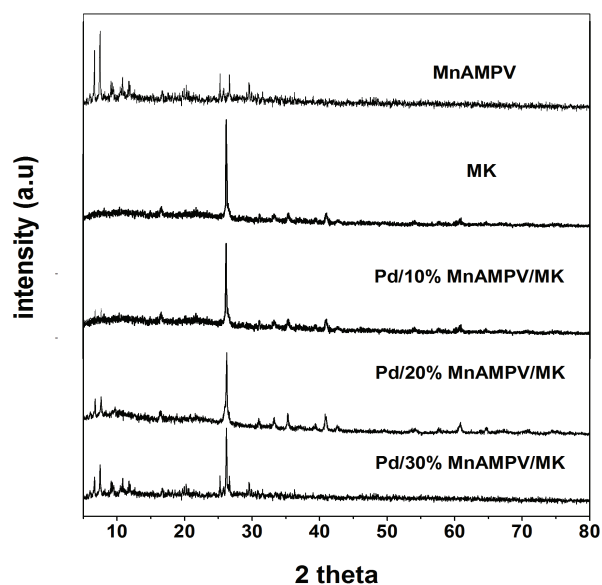


Figure 1. XRD patterns of different samples.

Comparison of the surface areas and pore volumes of MnAMPV, Pd/10%MnAMPV/MK, Pd/20%MnAMPV/MK, Pd/30%MnAMPV/MK and MK (Table 1) indicates that surface area and pore volume of MnAMPV supported on MK are larger than that of pure MnAMPV. Surface area and pore volume of the catalysts decrease with the increase of MnAMPV loading on MK (10–30 wt.%). For instance, Pd/10%MnAMPV/MK has the surface area of 45 m²/g and the total pore volume of 0.23 cm³/g. The surface area of Pd/30%MnAMPV/MK decreases to 27 m²/g, the total pore volume reduces to 0.15 cm³/g. The surface area and the total pore volume of the pure MnAMPV are only 8 m²/g and 0.04 cm³/g, respectively. The decrease of surface areas attributed to the subsequent filling of support pores by active component.

XPS characterization

XPS spectra shows more information on the structure of different catalysts (Figure 2a). Pd/20%MnAMPV/MK, Pd/20%MnAMPV₃/MK, Pd/20%MnAMPV₅/MK

are selected as target samples for the optimum result of activity test. It is observed that no change in binding energy of Pd species. The Pd 3d binding energies at 337.5 and 343.0 eV corresponding to the Pd²⁺ are almost the same in catalysts at varying quantities of V.

Table 1. BET surface areas and pore volumes of different samples

Catalyst	BET surface area m ² /g	Total pore volume cm ³ /g
MnAMPV	8	0.04
Pd/10%MnAMPV/MK	35	0.23
Pd/20%MnAMPV/MK	28	0.20
Pd/30%MnAMPV/MK	23	0.15
MK	39	0.25

The strong interaction between the active component and the carrier of the supported catalyst, the SMSI effect, leads to the transfer of electrons between them resulting in the binding energy shift. If the active component transfer electrons to the carrier, the binding energy will increased, and *vice versa* red-

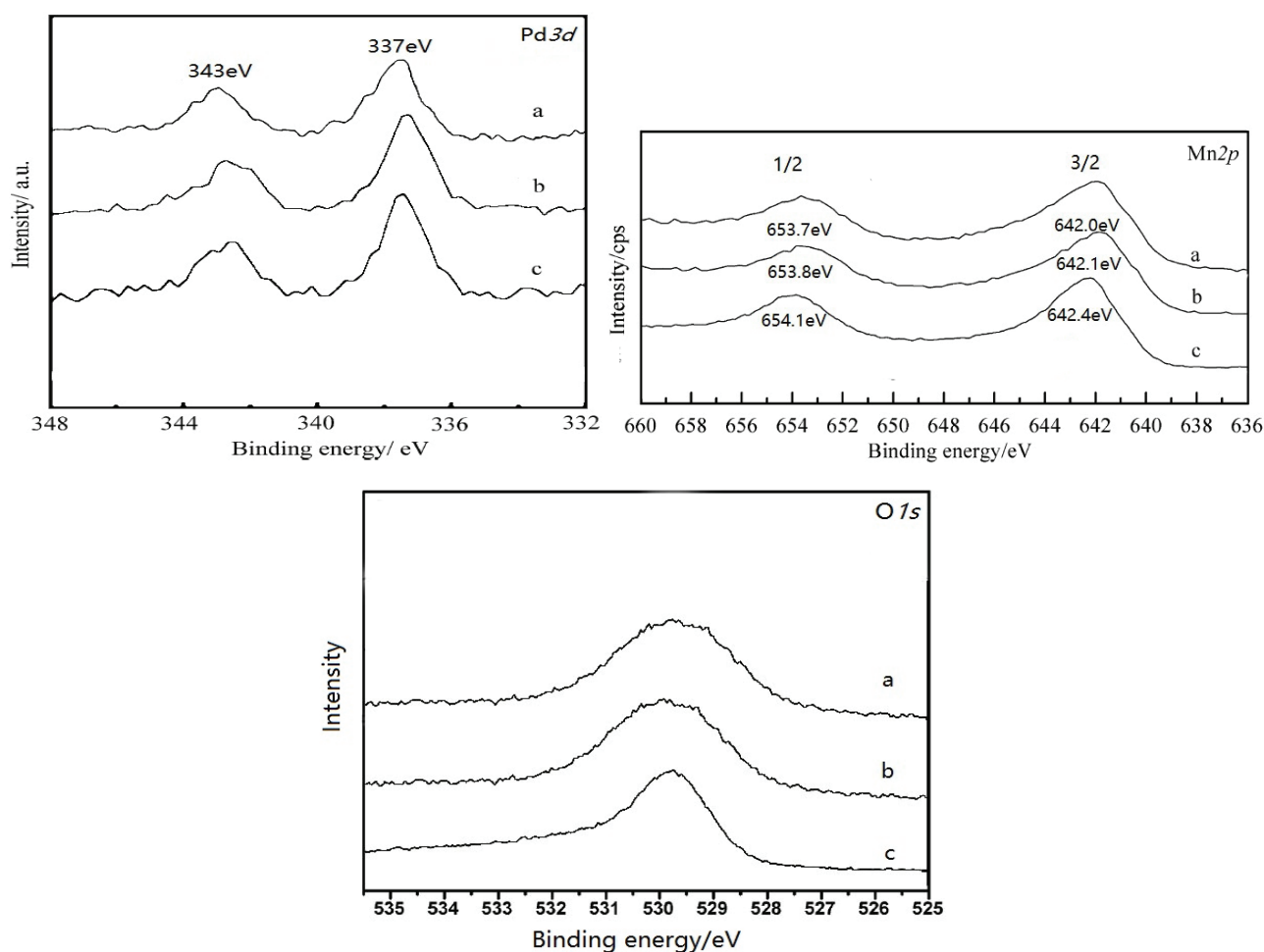


Figure 2. XPS spectra of Pd3d, Mn2P and O1s of: a) Pd/20%MnAMPV/MK, b) Pd/20%MnAMPV₃/MK and c) Pd/20%MnAMPV₅/MK.

uced. XPS spectrum of Mn2p (Figure 2b) shows that the binding energies of V-incorporated catalysts are increasing with the rise of the V number. Pd/20%MnAMPV₅/MK is about 0.4 eV higher than that of Pd/20%MnAMPV₁/MK catalysts. This small shift suggests the decrease of Mn atoms electronic densities owing to the transferring of electrons from active component to carrier makes the high-valence Mn species increase. Mn²⁺ transforms to Mn³⁺ in five atoms of V-incorporated catalysts. It is known that the lattice is strained when the tunnels Mo⁵⁺ is exchanged with smaller radius ions. As a result, it is confirmed that the lattice strain and the increase of Mn³⁺ sites is owing to the substitution of Mo⁵⁺ (0.139 nm) with relatively smaller ionic radius of V⁵⁺ (0.134 nm) [23]. Since Mn³⁺ is more easily oxidized than Mn²⁺, the increase of Mn³⁺ is beneficial to the supplement of reduced Mn⁴⁺ in redox cycle and leads to the increasing activities of five atoms of V incorporated catalysts.

Figure 2c, O1s, shows the corresponding XPS spectra of oxygen species and Table 2 indicates that the proportion of different oxygen species originates from fitted O1s spectrum, which refers to the XPS results obtained by Peluso [24]. Mn³⁺ sites could form a weak Mn-O bond, which makes active oxygen species come into being in the lattice [24]. Two photo-emission peaks correspond to two distinct oxygen species. The high binding energy (about 531.3 eV) indicates strongly adsorbed molecular oxygen, and the line with low binding energy (about 529.5 eV) indicates the crystal lattice oxygen (O²⁻) [24]. With the rise of V number in catalysts, the lattice oxygen content decreases, which originates amounts of oxygen vacancies and the adsorption of oxygen increases in the crystal phase. Therefore, the catalysis with five V might possess good low-temperature oxidation performance.

TPR characterization

For the oxidation cycle regeneration efficiency of the active Pd source is the important factor in the catalytic reaction, the oxides supporters must be activated in a reducing atmosphere. To study this activation process, the reducibility of 20%MnAMPV_x/MK systems is tested by temperature-programmed reduction and the reduction profiles are displayed in Figure 3. It is observed that the TPR flows from the diverse vanadium containing samples. There is a

main reduction peak within the range of 650-750 °C of all the samples. The reduction peaks during 650-750 °C may result from the reduction of free metal oxides produced by the decomposition of the Keggin anion decomposing above 540 °C [25]. The reduction peaks below 500 °C may originate from the reduction of vanadium in the primary structure of the Keggin ion. The increasing reduction peak with enhancement in vanadium content especially in Pd/20%MnAMPV₅/MK illustrates the vanadium expulses from main structure. In the case of Pd/20%MnAMPV₁/MK, the intact vanadium that containing the Keggin ion has reduced at around 650 °C. The expulsion of vanadium is expected for the catalysts with more vanadium atoms as resulting metal oxides being reduced at high temperatures. On the one hand, the V-incorporated catalyst possesses the low reduction temperature, which corresponds to the results of XPS. On the other hand, the lattice oxygen in its primary or secondary structure of the catalyst with V is more reactive than one with no V. These might be two reasons for high activity of the catalyst with V compared to catalyst without V.

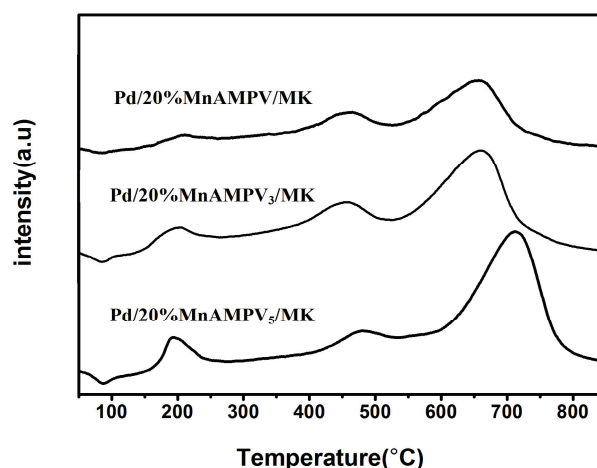


Figure 3. Temperature-programmed reduction profiles of Pd/20%MnAMPV_x/MK.

Efficiency of oxidative carbonylation with various catalysts

Under high pressure of a closed system, the Keggin type heteropolyacids, heteropoly salts and the modified kaolin supported heteropoly salts have been investigated as the redox co-catalysts for the oxidative carbonylation of phenol to DPC in the absence

Table 2. Different oxygen species content (%) on different catalysts

Oxygen species	Pd/20%MnAMPV ₁ /MK	Pd/20%MnAMPV ₃ /MK	Pd/20%MnAMPV ₅ /MK
O ²⁻	42.2	36.5	31.7
O ₂	9.2	15.3	19.6

of solvent. The results are shown in Table 3. Pd/HAMP catalyst is hardly active for the oxidative carbonylation of phenol to DPC, although the yield of DPC reaches only 0.58% based on phenol with a *TON* of 7 after 8 h (entry 1). Pd/HAMPV has higher activity than Pd/HAMP. The activity can be improved to 2.30% with a *TON* of 29 (entry 2). This result shows that HAMP is inactive as the co-catalyst. In other words, V-incorporated catalyst can improve the reaction activity. All of the Pd/MPAs catalysts are more active than Pd/HPAs. The main reason is that the cation substitutes HPAs as a counter ion [26,27]. There are two kinds of counter ion, one has a large ionic radius with stability [28], who can make the dispersion of the active center, keep the active phase and improve the stability of the catalyst as well as the integrity (it includes surface area, porosity, and framework flexibility). Another is the multivalent metal with the use of improving the activity of catalyst in oxidation-reduction by charge transfer of atom with redox electron pair and heteropolyanion [29]. However, Pd/MnAMPV is more active than the others among Pd/MPAs catalysts, whose yield can be improved to 12.02% with a *TON* of 144 (entry 3). There are two reasons. On the one hand, the Mn atoms with suitable ionic radius can disperse active center well and enhance the catalyst stability. On the other hand, Mn is the multivalent metal and its electron transfers to the atom of heteropolyanion so as to improve the activity of the catalyst.

Under the same condition, the yield of the unmodified kaolin is lower (entry 9). It is necessary to modify the kaolin since the alkalinity of Al_2O_3 in the

kaolin is stronger enough to neutralize acid parts of heteropoly acid to affect the yield of carbonylation reaction. In this experiment, the kaolin will be modified by immersion in 20% H_2SO_4 and then activating treatment under 100 °C. Besides, the modified kaolin may release oxygen attributed to the mobility of lattice oxygen and the formation of the oxygen vacancies [20]. It is beneficial for the conversion of Pd to active Pd^{2+} and the increase of the DPC yield. It is showed that the DPC yields changed with the different loading of MnAMPV. When the loading of MnAMPV is 20 wt.%, the DPC yield is up to 17.88%, it indicates the best catalytic activity. The reasons for high activity and selectivity of Pd/20%MnAMPV/MK catalyst can be explained based on the observation made from characterization results. The catalysts show well-dispersed MnAMPV at 20 wt.% and beyond that crystalline nature of AMPV is observed. The high activity is due to well-dispersed Keggin ion in MK.

As the Pd/20%MnAMPV catalyst shows the best activity, this loading is optimum. Catalysts with V atoms in place of one, three and five Mo atoms in the primary structure of the Keggin ion are prepared by keeping the MnAMPV_x content as 20 wt.% on the modified kaolin. The results show that the activity is enhanced with the increase of the number of vanadium atoms and the maximum activity is obtained (entry 14) for the catalyst with five vanadium atoms in the Keggin structure. The catalysts without any V, *i.e.*, Pd/HAMP show slight activity. The obvious increase of activities is due to V replacing Mo in the primary structure of molybdophosphoric acid and the redox property of vanadium. The V atom substituting Mo

Table 3. Oxidative carbonylation of phenol to DPC with various catalysts

Entry	Catalyst	Yield of DPC, %	Selectivity of DPC, %	<i>TON</i> , mol DPC/mol Pd
1	Pd/HAMP	0.58	96.82	7
2	Pd/HAMPV	2.30	97.21	29
3	Pd/MnAMPV	12.02	99.14	144
4	Pd/CuAMPV	3.41	98.01	41
5	Pd/CoAMPV	2.28	97.28	28
6	Pd/PbAMPV	4.66	99.04	56
7	Pd/CeAMPV	6.81	98.87	82
8	Pd/FeAMPV	4.16	96.56	50
9	Pd/10%MnAMPV/K	3.23	97.21	40
10	Pd/10%MnAMPV/MK	13.74	98.88	170
11	Pd/20%MnAMPV/MK	17.88	99.22	222
12	Pd/30%MnAMPV/MK	14.15	98.72	176
13	Pd/20%MnAMPV ₃ /MK	19.27	99.28	239
14	Pd/20%MnAMPV ₅ /MK	24.68 ^a	99.13	306
15		15.90 ^b	98.16	191
16		10.81 ^c	98.02	130

^a1st run; ^b2nd run; ^c3rd run

atom is beneficial for the conversion of Pd to active Pd^{2+} [30]. In the reaction, the V atoms occupy the position of the cross-linked cation on the proton position, or are extruded from the Keggin structure, forming an independent structure [31]. That should be V^{5+} , and under the influence of oxygen, the oxidation and the reduction state of V is easy to the mutual conversion. Meanwhile, compared to the redox potential of $\text{H}_3\text{PMo}_{12}\text{O}_{40}$ 0.52 V [32], the redox potential of $\text{H}_4\text{PMo}_{11}\text{VO}_{40}$ increases to 0.65 V [31], so the ability of Pd oxidation to Pd^{2+} is enhanced, which accelerated the catalytic cycle and increased the yield of DPC.

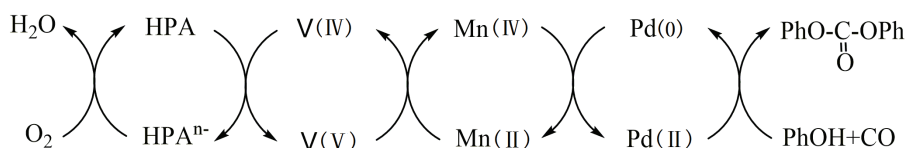


Figure 4. A possible mechanism for the oxidative carbonylation of phenol with CO and oxygen with Pd-Mn-AMPV catalyst system.

Recyclability of the catalysts

The regeneration of the catalysts was done by filtration after 8 h reaction, washing with conductivity water for several times followed by drying at 80 °C in an air oven and they were used in the oxidative carbonylation reactions with a fresh reaction mixture. As a typical example, the catalyst Pd/20%MnAMPV₅/MK showing (Table 3) yield of 24.68% in the first run decreased to about 15.90% (entry 15) in the second run and 10.81% (entry 16) in the third run, respectively. The *TON* also decreased with subsequent reuse. This decrease in catalytic activity was attributed to the leaching of HPA (of about 3-5%) and the loss of Pd ion from the support into the liquid phase during the catalytic reactions, which was confirmed by the well-known ascorbic acid test [33]. A hot filtration technique promoted the percolate of catalyst into the reaction mixture in process of the reaction too. Under optimized reaction conditions for 8 h, we used fresh Pd/20%MnAMPV₅/MK catalyst. After 8 h, the filtration separated the catalyst, then stirring the hot filtrate for 2 h under the same reaction conditions. It can be observed that in defect of the catalyst the conversion was increased about 3%. What is more, it indicated the presence of some amount of HPA and Pd ion in the reaction mixture. The catalyst was washed after filtration to remove all the adsorbed reactants and products, while some of the adsorbed reactants and products species still remained, which might cause the blockage of active sites and a decrease in catalytic activity. Therefore, the activity would reduce when we reused the catalyzer. Yet, the selectivity remained little changed, *i.e.*, 98.16 to 98.02%.

Multistep electron transfers catalytic cycle

The results in Table 2 show that there is a synergistic effect existing between vanadium incorporated molybdophosphoric salts loaded on MK for the regeneration of the Pd(II) species. A possible mechanism of the multistep electron transfer is proposed in Figure 4. The Pd(II) species would be reduced to Pd during the DPC formation from two molecules of phenol and one molecule of CO. The Pd would be reoxidized by Mn(IV) to form Pd(II) and Mn(II), and in turn Mn(II) would be reoxidized to Mn(IV) by V(V)

which is reduced to V(IV), then V(IV) be reoxidized to V(V) by HPA which is reduced to HPAⁿ⁻. Finally, HPAⁿ⁻ would be oxidized to HPA by O₂. The modified kaolin as a carrier of solid acid catalyst for its suitable pH can make the surface area of the heteropoly salts become larger, stability improve, activity component disperse well and electron transfer accelerate, all of which can promote catalytic cycle.

CONCLUSION

Vanadium incorporated molybdophosphoric salt supported on modified kaolin acts as efficient stable solid acid co-catalysts for synthesis of diphenyl carbonate by oxidative carbonylation with phenol. The high catalytic activity is attributed to the increase of surface area, the presence of the counter ion, the well-dispersed Keggin ion and Brønsted acid sites of the co-catalysts. Selectivity of all the carbonylation reactions is nearly 100% while the highest yield of DPC is 24.68% with a *TON* of 306 for the Pd/20%MnAMPV₅/MK catalyst in the absence of solvents. The catalyst can be regenerated and reused for several times. A new, more active and reusable heterogeneous catalyst for oxidative carbonylation of phenol to diphenyl carbonate is proposed in the research, which may be suitable for industrial experiments in the future.

Acknowledgement

This work was supported financially by the National Natural Science Foundation of China (Grant No. 21276201). We would like to thank The Centre of

Analysis and Measurement, Huazhong Normal University for the XRD analyses.

REFERENCES

- [1] Y. Kim, K.Y. Choi, *J. Appl. Polym. Sci.* **49** (1993) 747-764
- [2] J.L. Gong, X.B. Ma, S.P. Wang, *Appl. Catal., A: Gen.* **316** (2007) 1-21
- [3] Z.P. Du, W.K. Kang, T. Cheng, J. Yao, G.Y. Wang, *J. Mol. Catal., A: Chem.* **246** (2006) 200-205
- [4] A.G. Shaikh, S. Sivaram, *Chem. Rev.* **96** (1996) 951-976
- [5] H.Y. Song, E.D. Park, J.S. Lee, *J. Mol. Catal., A: Chem.* **154** (2000) 243-250
- [6] I. V. Kozhevnikov, *Catal., A: Gen.* **256** (2003) 3-18
- [7] J. Haber, K. Pamin, L. Matachowski, D. Mucha, *Appl. Catal., A: Gen.* **256** (2003) 141-152
- [8] M.T. Pope, *Heteropoly and Isopoly Oxometalates*, Springer, Berlin, 1983
- [9] N. Dimitratos, J. C. Védrine, *Catal. Today* **81** (2003) 561-571
- [10] N. Mizuno, M. Misono, *Chem. Rev.* **98** (1998) 199-218
- [11] D. Casarin, G. Centi, P. Jiro, V. Lena, Z. Tvaruzkova, *J. Catal.* **143** (1993) 325-344
- [12] J.K. Lee, J. Melsheimer, S. Berndt, G. Mestle, R. Schlogl, K. Kohler, *Appl. Catal., A: Gen.* **214** (2001) 125-148
- [13] H. Liu, E. Iglesia, *J. Phys. Chem., B.* **107** (2003) 10840-10847
- [14] M. Sopa, A. Waclaw-Held, M. Grossy, J. Pijanka, K. Nowinska, *Appl. Catal., A: Gen.* **285** (2005) 119-125
- [15] H. Liu, E. Iglesia, *J. Catal.* **223** (2004) 161-169
- [16] Kumar, Sachin, Panda, A. Kumar, R.K. Singh, *Bull. Chem. Reac. Eng. Catal.* **8** (2013) 61-69
- [17] A.M. George, US Patent 2 466 051 (1949)
- [18] B.K. Speronello, US Patent 4 628 042 (1986)
- [19] M. Liu, Y.X. Wu, Z.P. Du, H. Yuan, J.W. Ge, *Shiyou Huagong* **37** (2008) 672-675
- [20] X.J. Yang, J.Y. Yu, Z.P. Du, H. Yuan, F. Jin, Y.X. Wu, *Catal Commun* **11** (2010): 643-646
- [21] L.F. Zhang, J. Ji, Y.X. Wu, *Chem. Ind. Chem. Eng. Q.* **21** (2015) 45-51
- [22] D. Casarini, G. Centi, P. Jiru, *J. Catal.* **143** (1993) 325-344
- [23] V.D. Makwana, L.J. Garces, J. Liu, J. Cai, Y.C. Son, *Catal. Today* **85** (2003) 225-233
- [24] M.A. Peluso, L.A. Gambaro, E. Proncato, D. Gazzoli, H. J. Thomas, J. E. Sambeth, *Catal. Today* **133** (2008) 487-492
- [25] N. Dimitratos, J.C. Védrine, *Appl. Catal., A: Gen.* **256** (2003) 251-263
- [26] M. Langpape, J.M.M. Millet, *Appl. Catal., A: Gen.* **200** (2000) 89-101
- [27] S.A. Borshch, H. Duclusaud, J.M.M. Millet, *Appl. Catal., A: Gen.* **200** (2000) 103-108
- [28] C. Marchal-Roch, J.M.M. Millet, *Comptes Rendus de l'Académie des Sciences-Series IIC-Chemistry* **4** (2001) 321-329
- [29] I.K. Song, M.A. Barteau, *J. Mol. Catal., A: Chem.* **212** (2004) 229-23
- [30] P. Villabrilie, G. Romanelli, P. Vazquez, C. Caceres, *Appl. Catal., A: Gen.* **270** (2004) 101-111
- [31] T. Murtha, P. Timothy. *Catalysts US*, 4507507, 1 985 03 26
- [32] K. Eguchi, T. Seiyama, N. Yamazoe, S. Katsuki, H. Taketa, *J. Catal.* **111** (1988) 336-344
- [33] G.D. Yadav, V.V. Bokade, *Appl. Catal., A: Gen.* **147** (1996) 299-323.

MENG PENG
XIAOJUN YANG
JIAXIONG WU
HUA YUAN
CHAOFAN YIN
YUANXIN WU

Key Laboratory for Chemical Process
of Ministry of Education, Wuhan
Institute of Technology, Wuhan, China

NAUČNI RAD

PRIMENA FOSFOMOLIBDATA SA INKORPORIRANIM VANADIJUMOM NANETIM NA MODIFIKOVANOM KAOLINU U SINTEZI DIFENIL-KARBONATA OKSIDATIVNOM KARBONILACIJOM FENOLA

Molibdofosforna kiselina Kegginovog tipa, njena so i molibdofosforna so sa inkorporiranim vanadijumom koja je naneta na modifikovani kaolin (MK) kотиšćeni su kao redoks katalizatori za oksidativnu karbonilaciju fenola do difenil karbonata (DPC) u odsustvu rastvarača. MnAMPV5 (jedna molibdofosforme soli sa inkorporiranim vanadijumom) koja je naneta na MK pokazala je najveću katalitičku aktivnost sa prinosom od 24,68% i molskim odnosom DPC/Pd od 306, dok je selektivnost skoro 100% u svim reakcijama karbonilacije. Katalizatori su okarakterisani tehnikama XRD, BET, XPS i H₂-TPR. Provera ponovne upotrebe pokazala je da su katalizatori stabilni i aktivni.

Ključne reči: vanadijum, molibdofosforna kiselina, oksidativna karbonilacija, katalizator, difenil-karbonat.

MOHSEN BEIGI

Department of Mechanical
Engineering, Tiran Branch, Islamic
Azad University, Tiran, Iran

SCIENTIFIC PAPER

UDC 635.21:66.047:519.87:66

NUMERICAL SIMULATION OF POTATO SLICES DRYING USING A TWO-DIMENSIONAL FINITE ELEMENT MODEL

Article Highlights

- A two-dimensional finite element model was developed
- The model was programmed in Compaq Visual Fortran, version 6.5
- Dynamic drying curves were predicted by the methodology very well

Abstract

An experimental and numerical study was conducted to investigate the process of potato slices drying. For simulating the moisture transfer in the samples and predict the dehydration curves, a two-dimensional finite element model was developed and programmed in Compaq Visual Fortran, version 6.5. The model solved the Fick's second law for slab in a shrinkage system to calculate the unsteady two-dimensional moisture transmission in rectangular coordinates (x,y). Moisture diffusivity and moisture transfer coefficient were determined by minimizing the sum squares of residuals between experimental and numerical predicted data. Shrinkage kinetics of the potato slices during dehydration was determined experimentally and found to be a linear function of removed moisture. The determined parameters were used in the mathematical model. The predicted moisture content values were compared to the experimental data and the validation results demonstrated that the dynamic drying curves were predicted by the methodology very well.

Keywords: finite element, moisture diffusivity, mass transfer coefficient, shrinkage, Fick's second law, Fortran.

Mathematical modelling and computer simulation are widely used in research to predict dehydration behaviour of materials, design new dryers, and even to control the process [1]. The main proposed mathematical models used to describe the drying process are categorized as theoretical, semi-theoretical and empirical models [2]. Although these models give good fitting to the experimental data parameters, finally they do not offer any physical meaning [3]. The parameters depend on the product, drying technology and processing condition, and hinder the understanding of the mechanism that governs the water removal. Despite of the empirical and semi-theoretical models, theoretical models are built based on the understanding of the

fundamental heat and mass transfer mechanisms that occur during drying. Some studies like Zare *et al.* (2006) [4], Zhao and Chen (2011) [5], Mabrouk *et al.* (2012) [6], Nilnont *et al.* (2012) [7], Askari *et al.* (2013) [8] and Lemus-Mondaca *et al.* (2013) [9] have reported computational simulation of various agricultural and food products drying with a remarkable agreement between the theoretical and experimental results.

Theoretical models are realistic and give an accurate explanation of the drying process. However, they require a computing tool and also substantial information about physicothermal properties of drying material such as moisture diffusivity, mass transfer coefficient and shrinkage. Therefore, perfect understanding of these parameters and applying an appropriate numerical method are essential for precise prediction of the process [10].

Among the various types of dryers reported in the literature, convective hot air dryers have been to date

E-mail: mohsenbeigi59@gmail.com

Paper received: 30 May, 2016

Paper revised: 13 November, 2016

Paper accepted: 21 November, 2016

<https://doi.org/10.2298/CICEQ160530057B>

the most common dryers employed for dehydrating agricultural and food products. Convective drying is considered a simultaneous heat and mass transfer phenomenon wherein moisture transfer occurs in two forms of internal vapour evaporation and surface evaporation. During this process, water is transferred from the product inside to its surface by diffusion and carried from the surface to the air by convection [11].

The moisture diffusivity is a system specific function which represents all moisture gradient driven transfer mechanisms including liquid diffusion, migration in the adsorbed layer, vapour condensation and true diffusion of vapour in the air [12]. For foods, in the falling rate period, it is assumed that moisture transport is controlled by the liquid diffusion [13]. Extensive studies have been conducted to determine the moisture diffusivity for various foodstuff [2,14-18]. Mass transfer between liquid or solid and a gas interface is an important phenomenon for various engineering processes. Convective mass transfer coefficient is often used to describe and calculate the mass transfer rate at these interfaces [19]. Convective mass transfer of various materials has been reported in the literature [9,20,21,22].

Due to moisture evaporation, most of fruits and vegetables undergo considerable changes in volume during drying process. Since volumetric shrinkage influences drying behavior of products, it has to be taken into account in mathematical modelling of such processes for proper prediction of drying curves [7,23,24]. In the literature, several studies of volumetric shrinkage in biological materials have been reported [25,26].

Among the numerical methods available in simulation studies, finite difference method and finite element method are the main methods applied to model heat and mass transfer. The finite difference method simply formulates the discretized equations set from the transport differential equations in a differential manner and normally is used for simple and regular geometries [27]. The finite element method has better performance in comparison to finite difference method when solving problems with irregular geometries, complex boundary conditions and heterogeneous materials [28].

The aim of the present study was to experimentally and numerically study drying process of potato slices, implementing a two-dimensional finite element model with a computer code and using experimentally determined moisture diffusivity, mass transfer coefficient and shrinkage of the samples.

EXPERIMENTAL

Dryer set-up

To carry out the drying experiments, a laboratory-scale convective hot air dryer was fabricated (Figure 1). A centrifugal fan was used to blow the air into an electrical heater and pass it to the drying chamber. Temperature of the drying air was measured by a thermometer (PT100, 0.1 °C resolution) in the drying chamber inlet and controlled by using a microcontroller. The air flow rate was measured by a portable hot wire anemometer (Lutron, AM-4204 model, Taiwan) and controlled by using a frequency inverter (TECO, 7300 CV model, Taiwan). Three trays were placed in the drying chamber. During the drying experiments, one of the trays was used to monitor dehydration behaviour (weighting tray) and the others were used to determine shrinkage kinetic (sampling trays) of the samples.

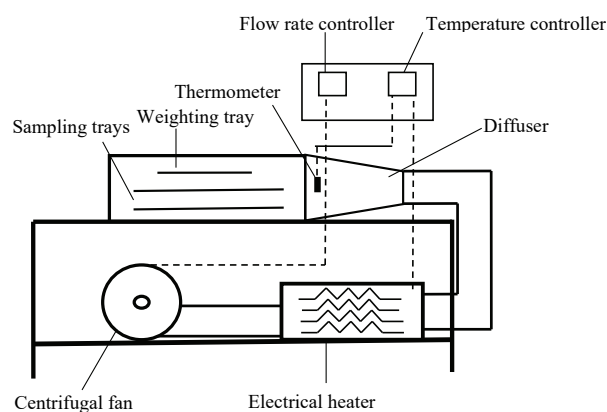


Figure 1. A scheme of the dryer set-up.

Drying experiments

The fresh potatoes used in the presented study were purchased from a local market in Isfahan (central Iran) and stored in a refrigerator at 4–6 °C until the experiments were started. The initial moisture content of the samples was determined by dehydration of about 5 g of the fresh potatoes at 103 °C until constant weight [29], and approximately calculated to be 4.65 kg_{water}/kg_{dry matter}. Prior to each experiment, the samples were placed at room temperature for about 2 h to reach thermal equilibrium with the environment. The potatoes were washed with water, hand peeled and cut into slabs (40 mm×25 mm×10 mm). For each drying experiment, approximately 200 and 2000 g of the samples were spread as a monolayer on the weighting tray and sampling trays, respectively. The drying experiments were conducted at constant drying air velocity of 1.2 m s⁻¹ and temperatures of 50, 60, 70 and 80 °C. During

the experiments, relative air humidity remained approximately at constant level of 30% using an ultrasonic humidifier equipped with a microcontroller.

The sample mass was monitored by a digital balance, accuracy of 0.001 g (ViBRA, model AJ-320E, Japan) and the instantaneous moisture content was calculated using Eq. (1) [22]:

$$M = \left(\frac{(M_o + 1)W}{W_o} - 1 \right) \quad (1)$$

where M and M_o are the moisture content at any given time ($\text{kg}_{\text{water}}/\text{kg}_{\text{dry matter}}$) and the initial moisture content ($\text{kg}_{\text{water}}/\text{kg}_{\text{dry matter}}$), respectively and W and W_o are the mass of samples at any given time (g) and the initial mass of fresh samples (g), respectively.

At each drying temperature, the experiments were replicated three times and the average values were used.

Drying rate was computed using Eq. (2):

$$DR = - \frac{M_{t+dt} - M_t}{dt} \quad (2)$$

where DR is the drying rate ($\text{g}_{\text{water}}/(\text{g}_{\text{dry matter s}}$), M_t and M_{t+dt} are the moisture contents at t and $t+dt$ respectively, and t is the drying time (s).

Uncertainty analysis

To prove the accuracy of the experiments the uncertainty analysis is needed. During experiments, uncertainties and errors could arise from factors such as instrument selection, instrument condition, observation, reading and test planning. In the present study, the drying temperatures, and sample thickness and weights were measured using appropriate instrumentation. The total uncertainties of these parameters are presented in Table 1. The method described by Holman was used to perform uncertainty analysis [32]:

$$E = \left[\left(\frac{\partial F}{\partial y_1} E_1 \right)^2 + \left(\frac{\partial F}{\partial y_2} E_2 \right)^2 + \dots + \left(\frac{\partial F}{\partial y_n} E_n \right)^2 \right]^{1/2} \quad (3)$$

where E is the uncertainty and y is the independent variable.

Table 1. Uncertainties in measurement of parameters during drying of potato slices

Parameter	Unit	Range	Estimated uncertainty
Drying air temperature	°C	From 200 to 850	±1
Drying air velocity	m s^{-1}	From 0.2 to 20	0.1
Sample weight	g	0-620	0.001

THEORETICAL APPROACH

A scheme of the potato samples is presented in Figure 2 for unsteady two-dimensional mass transfer during convective drying.

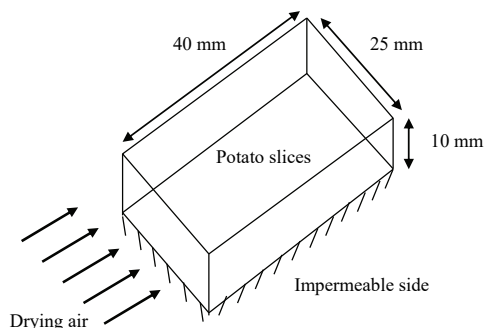


Figure 2. A scheme showing the geometry of the potato slice and drying air flow.

To define the mass transfer process, by assuming isotropic behavior of the samples in regards to the water diffusivity, Fick's second law could be used:

$$\frac{\partial M}{\partial t} = \text{Div} (D_{\text{eff}} (\text{grad } M)) \quad (4)$$

The mathematical analysis was based on the following certain assumptions:

- heat generated inside the object is negligible,
- two dimensional equations sufficiently describe the process for small thickness of the product,
- initial field of moisture content inside the sample is homogeneous,
- effective diffusivity of the product depends on drying air temperature and
- convective mass transfer coefficient depends on drying time and air temperature.

Under listed assumptions, governing mass transfer equation for unsteady drying process in rectangular coordinates (x, y) becomes [28]:

$$\frac{\partial M}{\partial t} = D_{\text{eff}}(T) \left(\frac{\partial^2 M}{\partial x^2} + \frac{\partial^2 M}{\partial y^2} \right) \quad (5)$$

Initial and boundary conditions to solve the mass transfer equation are given as Eqs. (6) and (7), respectively:

$$M = M_o, \quad t = 0 \quad (6)$$

$$-D_{\text{eff}}(T) \frac{\partial M}{\partial n} = h_m(T, t) [M_{\text{surf}} - M_{\text{eq}}], \quad t > 0 \quad (7)$$

where h_m is the mass transfer coefficient (m s^{-1}), M_{eq} and M_{surf} are the equilibrium and surface moisture

content of the samples ($\text{kg}_{\text{water}}/\text{kg}_{\text{dry matter}}$). Also, n is the magnitude of normal vector to the surface.

To solve finite element problems, Galerkin method is widely used. Using Galerkin method, Eq. (5) can be written as:

$$\int_{\Omega} [N]^T \left[D_{\text{eff}}(T) \left(\frac{\partial^2 M}{\partial x^2} + \frac{\partial^2 M}{\partial y^2} \right) - \frac{\partial M}{\partial t} \right] d\Omega = 0 \quad (8)$$

The interpolation functions do not have continuous derivatives between elements and it is necessary to replace them in the Eq. (8) by first derivatives. In order to obtain lower-order derivative, it is better to apply integration by parts to the integral expression. Concentrating on the first integral of Eq. (9):

$$\begin{aligned} & \int_{\Omega} [N]^T D_{\text{eff}}(T) \left(\frac{\partial^2 M}{\partial x^2} \right) d\Omega = \\ & = \int_{\Omega} \frac{\partial}{\partial x} \left([N]^T D_{\text{eff}}(T) \frac{\partial M}{\partial x} \right) d\Omega - \\ & - \int_{\Omega} D_{\text{eff}}(T) \left(\frac{\partial [N]^T}{\partial x} \frac{\partial M}{\partial x} \right) d\Omega \end{aligned} \quad (9)$$

Using Gauss's divergence theorem, the first integral on the right-hand side of Eq. (9) can be replaced by an integral around the boundary and gives:

$$\begin{aligned} & \int_{\Omega} \frac{\partial}{\partial x} \left([N]^T D_{\text{eff}}(T) \frac{\partial M}{\partial x} \right) d\Omega = \\ & = \int_L D_{\text{eff}}(T) [N]^T \left(\frac{\partial M}{\partial x} \right) n_x dL \end{aligned} \quad (10)$$

By performing a similar operation for the second term, Eq. (8) becomes as:

$$\begin{aligned} & \int_{\Omega} D_{\text{eff}}(T) \left(\frac{\partial [N]^T}{\partial x} \frac{\partial M}{\partial x} + \frac{\partial [N]^T}{\partial y} \frac{\partial M}{\partial y} \right) d\Omega = \\ & = \int_L D_{\text{eff}}(T) [N]^T \left(\frac{\partial M}{\partial x} n_x + \frac{\partial M}{\partial y} n_y \right) dL \end{aligned} \quad (11)$$

In Eq. (11), the unknown M can be expressed as:

$$M = [N] \{M\} \quad (12)$$

Therefore, it can be written as:

$$\frac{\partial M}{\partial x} = \frac{\partial [N]}{\partial x} \{M\} \quad \text{and} \quad \frac{\partial M}{\partial y} = \frac{\partial [N]}{\partial y} \{M\} \quad (13)$$

Substituting of these equations into Eq. (11) yields:

$$\begin{aligned} & \int_{\Omega} D_{\text{eff}}(T) \left(\frac{\partial [N]^T}{\partial x} \frac{\partial [N]}{\partial x} + \frac{\partial [N]^T}{\partial y} \frac{\partial [N]}{\partial y} \right) d\Omega \{M\} = \\ & = \int_{\Omega} D_{\text{eff}}(T) [B]^T [B] d\Omega \{M\} \end{aligned} \quad (14)$$

where $[B]$ is the gradient matrix of triangular elements in the finite element mesh and defined as:

$$[B] = \begin{bmatrix} \frac{\partial N_1}{\partial x} & \frac{\partial N_2}{\partial x} & \frac{\partial N_3}{\partial x} \\ \frac{\partial N_1}{\partial y} & \frac{\partial N_2}{\partial y} & \frac{\partial N_3}{\partial y} \end{bmatrix} \quad (15)$$

By writing the surface integral in terms of flux $\partial M / \partial n$ along the boundary, Eq. (11) can be expressed as:

$$\begin{aligned} & \int_{\Omega} D_{\text{eff}}(T) \left(\frac{\partial [N]^T}{\partial x} \frac{\partial M}{\partial x} + \frac{\partial [N]^T}{\partial y} \frac{\partial M}{\partial y} \right) d\Omega = \\ & = \int_L D_{\text{eff}}(T) [N]^T \left(\frac{\partial M}{\partial n} \right) dL \end{aligned} \quad (16)$$

where n is the outward normal to the surface.

Using Eq. (7), the right-hand side of Eq. (16) can be expressed as follows:

$$\begin{aligned} & \int_L D_{\text{eff}}(T) [N]^T \left(\frac{\partial M}{\partial n} \right) dL = \\ & = -h_m \int_L [N]^T [N] \{M\} dL + h_m \int_L [N]^T M_{\text{eq}} dL \end{aligned} \quad (17)$$

where the gradient matrix $[B]$ can be defined as:

$$[B] = \frac{1}{2A} \begin{bmatrix} b_i & b_j & b_k \\ c_i & c_j & c_k \end{bmatrix} \quad (18)$$

where A is area of the triangular element and:

$$\begin{aligned} b_i &= Y_j - Y_k, \quad b_j = Y_k - Y_i, \quad b_k = Y_i - Y_j, \quad c_i = X_j - X_k, \\ c_j &= X_k - X_i, \quad c_k = X_i - X_j \end{aligned} \quad (19)$$

where X and Y are nodal coordinates of an element and the suffixes i, j and k indicate the nodal points of a triangle.

Keeping $\{M\}$ aside, the right-hand side of Eq. (14) can be written as:

$$\begin{aligned} & \int_{\Omega} D_{\text{eff}}(T) [B]^T [B] d\Omega = \\ & = \int_{\Omega} D_{\text{eff}}(T) \frac{1}{4A} \begin{bmatrix} b_i & c_i \\ b_j & c_j \\ b_k & c_k \end{bmatrix} \begin{bmatrix} b_i & b_j & b_k \\ c_i & c_j & c_k \end{bmatrix} d\Omega \end{aligned} \quad (20)$$

Since the thickness is assumed to be unity for a two-dimensional model, $d\Omega$ could be replaced by dA . Also, from the Eq. (20), it is evident that for any element all terms are constant. Therefore, the Eq. (20) can be expressed as:

$$\int_{\Omega} D_{\text{eff}}(T)[B]^T [B]d\Omega = \int_A D_{\text{eff}}(T)[B]^T [B]dA \quad (21)$$

Equation (21) is defined as the element stiffness matrix $[k]$.

The matrix obtained by integrating the first term on the right-hand side of Eq. (16) should be added to matrix $[k]$. Keeping $\{M\}$ aside as before, this surface integral is expressed as:

$$h_m \int_L [N]^T [N]dL = h_m \int_L \begin{bmatrix} N_{ii} & N_{ij} & N_{ik} \\ N_{ji} & N_{jj} & N_{jk} \\ N_{ki} & N_{kj} & N_{kk} \end{bmatrix} dL \quad (22)$$

Assuming L_1 , L_2 and L_3 are measured from opposite nodes i , j and k , respectively; the N_s in the coordinate system can be replaced as follows:

$$L_1 = N_i, \quad L_2 = N_j, \quad L_3 = N_k \quad (23)$$

Therefore, in Eq. (22), there are two types of products: 1) L_1 , L_2 and L_3 and 2) L_{12} , L_{13} and L_{23} . Considering, for example, nodes i and j on the surface, the integrals of the square products and the cross-product are given, respectively:

$$\int_{L_{ij}} L_{ij}^2 dL = \int_{L_{ij}} L_2^2 = \frac{2!0!L_{ij}}{(2+0+1)!} = \frac{L_{ij}}{3} \quad (24)$$

$$\int_{L_{ij}} L_i L_j dL = \frac{1!1!0!L_{ij}}{(1+1+0)!} = \frac{L_{ij}}{6} \quad (25)$$

where the L_{ij} is the length of the side between nodes i and j of the under consideration surface element.

For an integration over an element, the general forms of Eqs. (24) and (25) can be modified as follows, respectively:

$$\int_A L_i^2 dA = \int_A L_i^2 L_j^0 L_k^0 dA = \frac{2!0!0!}{(2+0+0+2)!} 2A = \frac{A}{6} \quad (26)$$

$$\int_A L_i L_j dA = \int_A L_i^0 L_j^1 L_k^1 dA = \frac{0!1!1!}{(0+1+1+2)!} 2A = \frac{A}{12} \quad (27)$$

The second term in Eq. (17) can be expressed as:

$$h_m = \int_L [N]^T M_{\text{eq}} dL = h_m \int_L \begin{bmatrix} N_i \\ N_j \\ N_k \end{bmatrix} M_{\text{eq}} dL = \quad (28)$$

$$= h_m \int_L \begin{bmatrix} L_1 \\ L_2 \\ L_3 \end{bmatrix} M_{\text{eq}} dL$$

The solution of Eq. (28) is as follows:

$$h_m \int_L \begin{bmatrix} L_1 \\ L_2 \\ L_3 \end{bmatrix} M_{\text{eq}} dL = \frac{h_m M_{\text{eq}}}{2} \begin{bmatrix} L_{12} \begin{Bmatrix} 1 \\ 1 \\ 0 \end{Bmatrix} \\ L_{23} \begin{Bmatrix} 0 \\ 1 \\ 1 \end{Bmatrix} \\ L_{13} \begin{Bmatrix} 1 \\ 0 \\ 1 \end{Bmatrix} \end{bmatrix} \quad (29)$$

Also, by using Eq. (12), the last term of Eq. (8) can be written as follows:

$$\int_{\Omega} [N]^T \frac{\partial M}{\partial t} d\Omega = \int_{\Omega} [N]^T [N] \frac{\partial \{M\}}{\partial t} d\Omega \quad (30)$$

Since the time derivative of moisture inside the drying samples ($\partial M / \partial t$) is independent of the sample domain (Ω) coordinates, the Eq. (30) can be expressed as:

$$\int_{\Omega} [N]^T [N] \frac{\partial \{M\}}{\partial t} d\Omega = \left(\int_{\Omega} [N]^T [N] d\Omega \right) \frac{\partial M}{\partial t} \quad (31)$$

The integral within the bracket on the right-hand side of Eq. (31) is the element capacitance matrix $[c]$. This matrix can be solved using Eqs. (26) and (27).

Combining Eqs. (17), (21) and (31), the following first-order differential equation can be obtained as:

$$[k]\{M\} + [c] \frac{d\{M\}}{dt} = \{f\} \quad (32)$$

where $\{f\}$ is the element load force vector.

By using direct stiffness procedure to incorporate the element matrixes into final system of equations, the final result of the system can be obtained in terms of first order differential equation as follows:

$$[C] \left\{ \frac{\partial M}{\partial t} \right\} + [K]\{M\} = \{F\} \quad (33)$$

where $[C]$ is the global capacitance matrix, $[K]$ is the global stiffness matrix and $\{F\}$ is the global load force vector.

Solving by finite difference scheme, Eq. (33) can be written as [29]:

$$\left[\frac{[C]}{\Delta t} + \beta[K] \right] \{M\}_{t+\Delta t} = \left[\frac{[C]}{\Delta t} - (1-\beta)[K] \right] \{M\}_t + \{F\} \quad (34)$$

where β is a weighting factor and should be in the range of 0 to 1. Choosing different values of β , different schemes of finite difference equation can be obtained. In this study, backward method ($\beta = 1$) was used.

Thermo-physical properties

Effective diffusion

Crank (1975) has given an analytical solution for Eq. (3) for different solid geometries, which for an infinite slab are written as Eq. (35) [30]:

$$MR = \frac{8}{\pi^2} \sum_{n=0}^{\infty} \frac{1}{(2n+1)^2} \exp\left(-\frac{(2n+1)^2 \pi^2 D_{\text{eff}} t}{4H^2}\right) \quad (35)$$

where D_{eff} is the effective diffusivity ($\text{m}^2 \text{s}^{-1}$), and MR is the moisture ratio and defined as follows:

$$MR = \frac{M - M_{\text{eq}}}{M_0 - M_{\text{eq}}} \quad (36)$$

For long drying periods, Eq. (35) can be simplified to only the first term of the series and written in logarithmic form as Eq. (37) [18]:

$$\ln MR = \ln \frac{8}{\pi^2} - \left(\frac{\pi^2 D_{\text{eff}} t}{4H^2} \right) \quad (37)$$

By plotting experimental data in term of $\ln MR$ against drying time, a straight line was obtained and the moisture diffusivity was calculated as follows:

$$D_{\text{eff}} = -\left(\frac{4H^2}{\pi^2} \right) \times \text{Slope} \quad (38)$$

The convective mass transfer coefficient (h_m) in the surface of the samples was determined by using the procedure described by [31]:

$$h_m = \frac{V}{St} \ln MR \quad (39)$$

where V and S are volume (m^3) and area (m^2) of the samples, respectively.

Shrinkage

During the drying experiments, the shrinkage kinetic of the potato slices was determined using toluene displacement method [17]. Three potato slices were randomly taken from the sampling trays and

weighed (m_1), accuracy of 0.001 g (Shimadzu, model AUW220D, Japan). The samples were placed into an empty 250 ml flask, filled up with toluene and weighed again (m_2). The instantaneous volume of the samples was determined as:

$$V_i = 250 - \frac{(m_2 - m_1)}{\rho_{\text{toluene}}} \quad (40)$$

where V_i is the instantaneous volume of the samples (m^3) at any sampling time.

The density of toluene (ρ_{toluene}) is 0.87 g cm^{-3} at 20°C .

After determination of the sample volumes, the volume ratio was calculated as follows:

$$V_r = \frac{V_i}{V_0} \quad (41)$$

where V_r and V_0 represent instantaneous volume ratio and initial volume of the fresh potato slices (m^3), respectively.

The initial volume of the fresh samples was determined using its dimensions.

RESULTS AND DISCUSSION

Drying characteristics of the samples

Variation in drying rate in respect to the moisture content for the samples at the applied air temperatures is shown in Figure 3. As the results show, the entire drying process occurred in the falling rate period and no constant rate period was observed. Drying processes in falling rate period indicated that diffusion is the dominant physical mechanism controlling the moisture movement in the potato slices [17]. During this period, water migration from the interior to the product

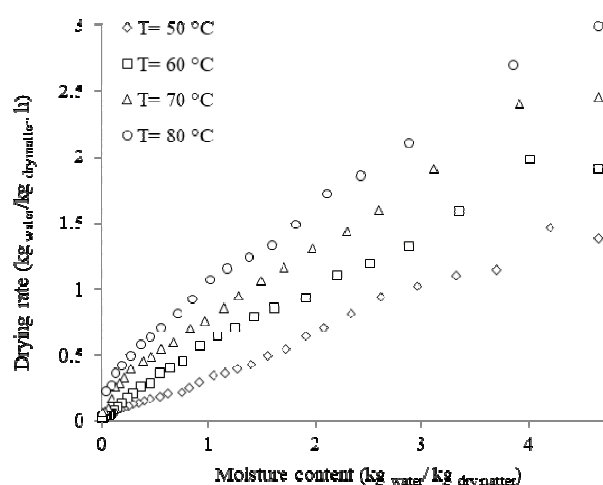


Figure 3. Variation of drying rate with moisture content for the potato slices at the applied drying air temperatures.

surface is controlled by molecular diffusion where water moves based on moisture content gradient from the zones with higher moisture content to the lower moisture zones. In addition, drying rate increased considerably with an increase in the drying air temperature. This agrees well with results regarding the influence of drying air temperature on dehydration rate of samples reported in the literature [14,32]. Some factors such as indigenous properties, initial and final moisture content of the product, drying method and drying conditions can affect the drying rate of the agricultural materials. At higher temperatures, the heat transfer rate between thermal source and the material is higher leading to the faster moisture evaporation and lower drying time [17].

Effective diffusivity and convective mass transfer coefficient

The effective moisture diffusivity of the potato slices was calculated using Eq. (38) and the obtained values for the applied air temperatures are shown in Table 2. As the results show, the values ranged from 4.32×10^{-9} to $6.11 \times 10^{-9} \text{ m}^2 \text{ s}^{-1}$ that generally is within the range given for food material moisture diffusion (10^{-11} to $10^{-6} \text{ m}^2 \text{ s}^{-1}$). These results were found to be in agreement with the values reported in literature for different vegetables and fruits. Tulek (2011) reported the effective moisture diffusivity ranged from 9.619×10^{-10} to $1.556 \times 10^{-9} \text{ m}^2 \text{ s}^{-1}$ for mushroom slices dried at temperatures of 50, 60 and 70 °C and constant air flow rate of 0.2 m s^{-1} [32]. Singh and Pandey (2012) dried sweet potato in a convective dryer under five air temperatures (50, 60, 70, 80 and 90 °C), five air velocities (1.5, 2.5, 3.5, 4.5 and 5.5 m s^{-1}) and three different thicknesses for the samples (5, 8 and 12 mm) and determined the diffusivity values to be in the range of 1.258×10^{-9} to $8.156 \times 10^{-9} \text{ m}^2 \text{ s}^{-1}$ [33].

Table 2. Values of the obtained effective diffusivity for potato samples at the applied drying air temperatures

Drying air temperature, °C	Effective diffusivity $\times 10^9, \text{ m}^2 \text{ s}^{-1}$
50	4.32
60	5.09
70	5.64
80	6.11

In addition, it was observed that an increment in drying temperature increased the effective diffusivity value. In fact, an increase in temperature causes a decrement in water viscosity and increases the activity of water molecules. These phenomena facilitate diffusion of water molecules in object capillaries and consequently, increase the moisture diffusivity. The effect

of drying air temperature on the moisture diffusivity can be discussed as shown in Figure 4. As the results show, the moisture diffusivity of potato slices can be expressed as a function of temperature using an exponential equation:

$$D_{\text{eff}}(T) = 1.864 \times 10^{-9} \exp(0.01617T), R^2 = 0.9979$$

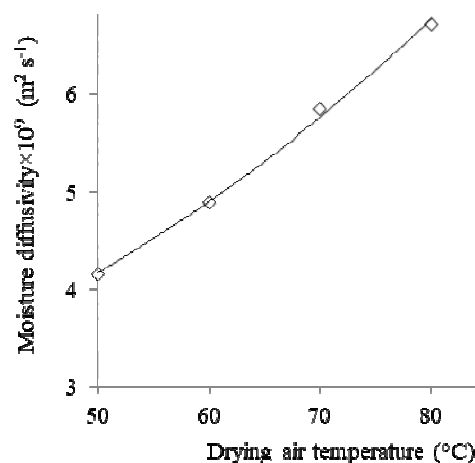


Figure 4. Air temperature effect on effective moisture diffusivity for the potato slices.

Fit goodness of the equation was assessed based on the coefficient of determination (R^2) which is defined as follows:

$$R^2 = 1 - \frac{\sum_{i=1}^n (\text{Value}_{\text{exp},i} - \text{Value}_{\text{pre},i})^2}{\sum_{i=1}^n (\text{Value}_{\text{exp},i} - \bar{\text{Value}})^2} \quad (42)$$

A model was considered acceptable if the R^2 values are higher than 0.90 [34]. As the results show, the equation is capable to predict the experimental effective moisture diffusivity data.

Mass transfer between the interface of a liquid or a solid and a gas is an important phenomenon and often is described by a convective mass transfer coefficient. Results reported in the literature indicated an improvement in heat and mass transfer equation using unsteady heat and mass coefficients in comparison to values remaining constant in time and in space for each surface [9]. The values of convective mass transfer obtained from Eq. (39) ranged from 1.303×10^{-7} to $2.665 \times 10^{-7} \text{ m s}^{-1}$ for the drying temperature between 50 and 80 °C. The obtained results agree well with the values reported for different products and drying conditions in the literature [7,9,21].

In the presented study, the determined convective mass transfer coefficient was given as a function of

drying time for each air temperature based on the regression analysis, as follows:

$T/^\circ\text{C}$	Equation	R^2
50	$h_m(t) = 10^{-13}t^2 - 6 \times 10^{-11}t + 10^{-7}$	0.9252
60	$h_m(t) = 4 \times 10^{-13}t^2 - 10^{-10}t + 2 \times 10^{-7}$	0.9285
70	$h_m(t) = 10^{-12}t^2 - 5 \times 10^{-10}t + 3 \times 10^{-7}$	0.9637
80	$h_m(t) = 6 \times 10^{-16}t^2 - 10^{-11}t + 3 \times 10^{-7}$	0.9807

Shrinkage of samples

Shrinkage kinetic of the potato slices was determined experimentally and, based on the regression analysis, found to be a function of removed moisture from the slices ($M_0 - M_i$):

$T/^\circ\text{C}$	Equation	R^2
50	$\frac{V_i}{V_0} = -0.1917(M_0 - M_i) + 1.0204$	0.9935
60	$\frac{V_i}{V_0} = -0.1788(M_0 - M_i) + 1.00057$	0.9952
70	$\frac{V_i}{V_0} = -0.1862(M_0 - M_i) + 1.0274$	0.9903
80	$\frac{V_i}{V_0} = -0.1773(M_0 - M_i) + 0.9802$	0.9912

Same results have been reported for shrinkage decrement during drying process for potato [12], mango [28], coffee beans [7], and banana and carrot [23].

Verification of the finite element solution

To predict the moisture content changes of the potato slices by the implemented finite element scheme presented in Eq. (34), the experimentally

obtained diffusivity, mass transfer coefficient and shrinkage of the samples were used and a computer program was written in Compaq Visual Fortran, version 6.5. Sub-routines for initial and boundary conditions, grid information, properties and matrix solution have been included in the program. In addition, the written program could generate the two-dimensional grid data automatically if dimensions of the object were given as an input.

The variation of average moisture content of the potato samples with respect to the drying time for the experiments along with the computed results at the air temperature of 50 °C, are presented in Figure 5. For the other drying air temperatures, the same results were observed.

The accuracy of the elaborated model was evaluated by comparing computed and experimental data by calculating the relative error (%RE) and the mean relative error (%MRE):

$$\%RE = 100 \frac{|M_{\text{exp},i} - M_{\text{pre},i}|}{M_{\text{exp},i}} \quad (43)$$

$$\%MRE = \frac{100}{N} \sum_{i=1}^N \frac{|M_{\text{exp},i} - M_{\text{pre},i}|}{M_{\text{exp},i}} \quad (44)$$

Relative error of 10-15% is usually reported to be satisfactory for drying simulation. Also, a mean relative error of less than 10% is generally considered as a good degree of agreement between predicted and experimental data for drying process [35]. The values of mean and maximum relative error at the applied air temperatures are shown in Table 3.

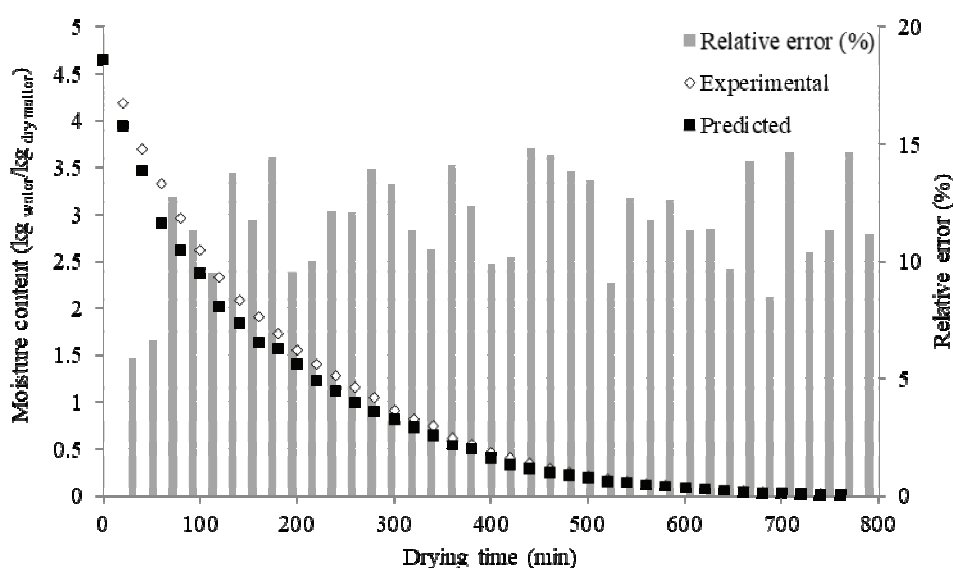


Figure 5. Variations of the experimental and predicted average moisture content for the potato slices with relative error values at air temperature of 50 °C.

Table 3. Mean relative error (%MRE) and maximum relative error (%RE_{max}) for predicting moisture content at various air temperatures

Drying air temperature, °C	%MRE / %	%RE _{max} / %
50	8.91	14.71
60	8.64	13.73
70	7.56	12.14
80	9.04	13.35

As the validation results show, the implemented model and the solution could describe drying process of the potato slices with a high accuracy, where the obtained mean relative error and the maximum relative error values were in the range of 7.56 to 9.04% and 12.14 to 14.71%, respectively. The reasons could be due to the following:

- Experimentally determined moisture diffusivity and mass transfer coefficient for the potato slices were accurate enough,
- Shrinkage kinetic of the samples during dehydration process was determined and taken into account,
- Two-dimensional finite element model had enough flexibility to describe the geometry of the samples and
- The developed numerical simulation and the written program had good capability to describe the mass transfer phenomenon during the experiments.

CONCLUSIONS

In this study, convective drying of potato slices was investigated experimentally and numerically. Drying rate, moisture diffusivity and mass transfer coefficient of the samples were found to increase with increase in the drying air temperature increment. No constant rate period was observed and the entire drying process of the potatoes occurred in the falling rate period at the applied air temperatures. The diffusivity of the samples was determined to be in the range of 1.68×10^{-9} to 2.81×10^{-9} $\text{m}^2 \text{s}^{-1}$ and described using an exponential equation as a function of air temperature. For each drying temperature, mass transfer coefficient and shrinkage of the samples were determined experimentally and found to be functions of the process time and moisture removal, respectively.

A two-dimensional finite element model was developed for the sample drying and programmed in Compaq Visual Fortran, version 6.5, to simulate the process and predict the drying curves. The predicted moisture content values were compared to the experimental data and the results indicated that the imple-

mented model could describe drying kinetics with a high accuracy.

Nomenclature

A	Area of element
$[A]$	Intermediate parameter matrix
$[B]$	Gradient matrix
$[C]$	Global capacitance matrix
$[c]$	Element capacitance matrix
D_{eff}	Effective moisture diffusivity ($\text{m}^2 \text{s}^{-1}$)
DR	Drying rate ($\text{kg}_{\text{water}}/(\text{kg}_{\text{dry matter}} \text{s})$)
E	Uncertainty
$\{F\}$	Global load force vector
$\{f\}$	Element load force vector
H	Half thickness of the samples (m)
h_m	Moisture transfer coefficient (m s^{-1})
$[K]$	Global stiffness matrix
$[k]$	Element stiffness matrix
L	Boundary line
M	Moisture content ($\text{kg}_{\text{water}}/\text{kg}_{\text{dry matter}}$)
M_{eq}	Equilibrium moisture content ($\text{kg}_{\text{water}}/\text{kg}_{\text{dry matter}}$)
M_0	Initial moisture content ($\text{g}_{\text{water}}/\text{g}_{\text{dry matter}}$)
M_{surf}	Moisture content at surface of sample ($\text{kg}_{\text{water}}/\text{kg}_{\text{dry matter}}$)
MR	Moisture ratio
$MR_{\text{exp},i}$	The i -th experimental moisture ratio (-)
$MR_{\text{pre},i}$	The i -th predicted moisture ratio (-)
MRE	Mean relative error (%)
$\{M\}$	Vectors of unknown moisture content
n	Magnitude of the outward normal vector to the surface
$[N]$	Matrix of interpolation function
R^2	Coefficient of determination
RE	Relative error (%)
S	Area of samples (m^2)
t	Drying time (s)
T	Temperature ($^{\circ}\text{C}$)
V_i	Instantaneous volume of the samples (m^3)
V_r	Volume ratio
V_0	initial volume of the fresh samples (m^3)
W	Mass of samples at any given time (kg)
W_0	Initial mass of fresh samples (kg)
y	Independent variable
ρ_{toluene}	Density of toluene (kg m^{-3})
β	Weighting factor for the determination of the finite difference method
Ω	Sample domain

REFERENCES

- [1] Z. Naghavi, A. Moheb, S. Ziaei-rad, Energy Conv. Manage. **51** (2010) 258-264

- [2] C.L. Hii, C.L. Law, M. Cloke, J. Food Eng. **90** (2009) 191-198
- [3] S. Simal, A. Femenia, M.C. Garau, C. Rosselló, J. Food Eng. **66** (2005) 323-328
- [4] D. Zare, S. Minaei, M. Mohamad Zadeh, M.H. Khosh-taghaza, Energy Conv. Manage. **47** (2006) 3241-3254
- [5] F. Zhao, Z. Chen, Drying Technol. **29** (2011) 1404-1415
- [6] S.B. Mabrouk, E. Benali, H. Oueslati, Food Bioprod. Process. **90** (2012) 719-728
- [7] W. Nilnont, S. Thepa, S. Janjai, N. Kasayapanand, C. Thamrongmas, B.K. Bala, Food Bioprod. Process. **90** (2012) 341-350
- [8] G.R. Askari, Z. Emam-Djomeh, S.M. Mousavi, Food Bioprod. Process. **91** (2013) 207-215
- [9] R.A. Lemus-Mondaca, C.E. Zambra, A. Vega-Gálvez, N. O. Moraga, J. Food Eng. **116** (2013) 109-117
- [10] P.N. Sarsavadia, R.L. Sawhney, D.R. Pangavhane, S.P. Singh, J. Food Eng. **40** (1999) 219-226
- [11] Z. Sahin, I. Dincer, J. Food Eng. **71** (2005) 119-126
- [12] L. Hassini, S. Azzouz, R. Peczkalski, A. Belghith, J. Food Eng. **79** (2007) 47-56
- [13] G.P. Sharma, S. Prasad, J. Food Eng. **65** (2004) 609-617
- [14] S. Kaleemullah, R. Kailappan, J. Food Eng. **76** (2006) 531-537
- [15] D. Evin, Food Bioprod. Process. **90** (2012) 323-332
- [16] M. Foroughi-Dahr, M. Golmohammadi, R. Pourjamshidian, M. Rajabi-Hamaneh, S. J. Hashemi, Chem. Eng. Commun. **202** (2015) 1024-1035
- [17] M. Beigi, Heat Mass Transfer, 2015, doi:10.1007/s00231-015-1646-8
- [18] M. Torki-Harchegani, M. Ghasemi-Varnamkhasti, D. Ghanbarian, M. Sadeghi, M. Tohidi, Heat Mass Transfer **52** (2016) 281-289
- [19] H.-J. Steeman, C. T'Joel, M. Van Belleghem, A. Janssens, M. De Paepe, Int. J. Heat Mass Transfer **52** (2009) 3757-3766
- [20] W.A.M. Mcminn, M.A.M. Khraisheh, T.R.A. Magee, Food Res. Int. **36** (2003) 977-983
- [21] A. Kaya, O. Aydin, I. Dincer, J. Heat Mass Transfer **49** (2006) 3094-3103
- [22] M. Torki-Harchegani, D. Ghanbarian, M. Sadeghi, Heat Mass Transfer **51** (2015) 1121-1129
- [23] J. Madiouli, J. Sghaier, D. Lecomte, H. Sammouda, Food Bioprod. Process. **90** (2012) 43-51
- [24] A. Brasiello, G. Adiletta, P. Russo, S. Crescitelli, D. Albanese, M. Di Matteo, J. Food Eng. **114** (2013) 99-105
- [25] ATalla, J.R. Puiggali, W. Jomaa, Y. Jannot, J. Food Eng. **64** (2004) 103-109
- [26] Z. Yan, M.J. Sousa-Gallagher, F.A.R. Oliveira, J. Food Eng. **84** (2008) 430-440
- [27] L. Wang, D.W. Sun, Trends Food Sci. Technol. **14** (2003) 408-423
- [28] S. Janjai, N. Lamlet, P. Intawee, B. Mahayothee, M. Haewsungcharern, B.K. Bala, J. Müller, Biosyst. Eng. **99** (2008) 523-531
- [29] K. Schössler, H. Jäger, D. Knorr, J. Food Eng. **108** (2012) 103-110
- [30] J. Crank, The Mathematics of Diffusion, Clarendon Press, Oxford, 1975
- [31] A. Kaya, O. Aydin, C. Demirtas, J. Food Process Eng. **30** (2007) 546-577
- [32] Y. Tulek, J. Agric. Sci. Technol. **13** (2011) 655-664
- [33] N.J. Singh, R.K. Pandey, Food Bioprod. Process. **90** (2012) 317-322
- [34] B. Koç, I. Eren, F. K. Ertekin, J. Food Eng. **85** (2008) 340-349
- [35] M. Torki-Harchegani, M. Sadeghi, A. Moheb, Z. Naghavi, Heat Mass Transfer **50** (2014) 1717-1725.

MOHSEN BEIGI

Department of Mechanical
Engineering, Tiran Branch, Islamic
Azad University, Tiran, Iran

NAUČNI RAD

NUMERIČKA SIMULACIJA SUŠENJA KRIŠKI KROMPIRA POMOĆU DVODIMENZIONALNOG MODELA KONAČNIH ELEMENATA

Sušenje kriški krompira je proučavano eksperimentalno i numerički. Za simulaciju prenosa vlage u uzorcima i predviđanje krivih sušenja, razvijen je dvodimenzionalni model konačnih elemenata, koji je rešavan primenom programa napisanog u Compak Visual Fortran, verzija 6.5. Model rešava drugi Fickov zakon za ploču koja se skuplja za izračunavanje nestacionarnog dvodimenzionalnog prenosa vlage u pravouglom koordinatnom sistemu. Difuzivnost i koeficijent prenosa vlage u uzorcima određen je minimiziranjem kvadrata odstupanja između eksperimentalnih i izračunatih vrednosti. Kinetika skupljanja kriški krompira tokom sušenja određena je eksperimentalno. Utvrđena je da je linearna funkcija uklonjene vlage. Određeni parametri korišćeni su u matematičkom modelu. Predviđene vrednosti sadržaja vlage upoređene su sa eksperimentalnim podacima i rezultati validacije su pokazali da su razvijene dinamičke krive sušenja vrlo dobro slažu sa eksperimentom.

Ključne reči: konačni element, difuzivnost vlage, koeficijent prenosa mase, skupljanje, Fickov drugi zakon, Fortran.